The myofilament basis of striated muscle function: Experimental and computational models

Joseph D. Powers

A dissertation

submitted in partial fulfilment of the

requirements for the degree of

Doctor of Philosophy

University of Washington

2018

Supervisory Committee:

Michael Regnier (Co-chair)

Thomas L. Daniel (Co-chair)

Jennifer Davis

Charles Asbury

Program Authorized to Offer Degree:

Department of Bioengineering

University of Washington

ABSTRACT

The myofilament basis of striated muscle function: Experimental and computational models

Joseph D. Powers

Co-chairs of Supervisory Committee:
Michael Regnier, Ph.D.
Thomas L. Daniel, Ph.D.
Department of Bioengineering

For over a century, understanding the subcellular mechanisms that regulate striated muscle function has been of great interest to biophysicists and physiologists. During contraction-relaxation cycles, both skeletal and cardiac myocytes undergo tremendous structural and geometrical dynamics that are driven by complex sarcomere-level regulatory processes. Yet, despite much effort, many sarcomere-based mechanisms of the regulation of muscle function have remained unresolved. The body of work presented here is aimed at revealing such mechanisms by leveraging recent advances in structural, mechanical, and computational biology. Specifically, we integrate: (*i*) experimental techniques to study sarcomere mechanics *in situ*, (*ii*) high-resolution X-ray diffraction-based imaging modalities of myofilament and sarcomere structure, (*iii*) spatially explicit computational models of sarcomere mechanics and energetics, and (*iv*) genetic engineering of murine models of heart failure harboring cardiomyopathy-associated myofilament protein mutations. In doing so, we provide insight into the molecular mechanisms that govern the regulation (and dysregulation) of straited muscle function.

Moreover, this work focusses on uncovering contributions to regulatory mechanisms of muscle function from each of the three main myofilaments of the sarcomere: the myosin-

containing thick filament, the actin-containing thin filament, and the giant filamentous protein titin. First, we describe a spatially explicit computational model that explores how titin stiffness affects contractile mechanics and energetics. We find that increasing titin stiffness inhibits the ability of myosin motors to energetically compete with the added titin-based strain in the thick filament and are therefore less efficient in generating force compared with motors in series with compliant titin. Second, we measure the contributions of titin to the elasticity of the sarcomere *in-situ* in single intact skeletal muscle fibers throughout the duration of isometric tetanus. We show that titin the I-band region of titin has a dynamic stiffness that is tuned to the length of the sarcomere, likely mediated by load-dependent structural dynamics of the I-band-specific domains. Third, we present multiple studies that harness high-intensity synchrotron light to enable Angstrom-level X-ray diffraction-based measurements of the myofilament structure in cardiac muscle. Through this technique, we investigate the structural dynamics of myosin motors in resting and activated cardiac muscle and find that some positively inotropic interventions have no effect on resting sarcomere structure, whereas others perturb the resting state of the thick filament to potentiate the ensuing contraction. Lastly, we use a transgenic murine model harboring a loss-of-function tropomyosin mutation that causes dilated cardiomyopathy. We show that both sarcomere-level and tissue-level dysfunction can be prevented by rationally designing filament-specific interventions.

To summarize, the work presented here highlights results from an integrative approach that aims to understand myofilament-specific mechanisms that govern regulation of both cardiac and skeletal muscle function. As a result, we answer questions that range from a basic understanding of molecular-level regulation of muscle function to developing potential therapeutics that may translate to the clinic for patients with specific types of congenital heart failure.

TABLE OF CONTENTS

LIST OF FIGURES

LIST OF TABLES

ACKNOWLEDGEMENTS

The work presented in this dissertation could not have been done without the guidance, mentorship, and support from people all around the world. First, I am immensely appreciative for my advisors Mike Regnier and Tom Daniel, whose guidance and leadership has had a significant impact on me throughout my PhD. I could not have asked for better advisors. Mike offered unfaltering generosity and support during my time in his lab, and he taught me the value of saying 'yes' to new and challenging endeavors. Tom led by example, demonstrating the values of strong leadership, scientific curiosity, and research integrity, while offering exceptional personal mentorship. I am also grateful to Jen Davis for offering her intellect during discussions about experimental development, design, and interpreting results. Through these discussions, she became a strong role model and an exemplar of a how to pave a successful career path in academia.

Secondly, I am thankful to have worked with the group at the University of Florence in Italy, led by Vincenzo Lombardi and Gabriella Piazzesi, where I spent over a year learning their muscle mechanics and X-ray diffraction techniques. My friends and colleagues there, especially the Marcos (Caremani and Linari), Francesca, Irene, Valentina, and Massimo, were together a tremendous support system in the lab, and taught me invaluable experimental techniques and how to be a successful experimentalist. Most of all, however, the mentorship and friendship of Vincenzo and Gab was beyond expectation, and provided a rich and supportive environment during my time working in their lab.

In addition, the experiments described in this work involving X-ray diffraction were carried out through collaborations at the Advanced Photon Source (APS) at the Argonne National Laboratory in Illinois, and the European Synchrotron Radiation Facility (ESRF) in Grenoble,

France. I am appreciative of the technical assistance and scientific discussions with Tom Irving and Weikang Ma at APS, and Theyencheri Narayanan at ESRF.

Lastly, I am forever indebted to my friends and family for their support and companionship. In particular, the constant love and praise from my mom, dad, and sister were of most significance to me. Their unwavering support, patience, and encouragement has kept me upright my whole life. I don't know where I'd be without them.

For Sarah.

Chapter 1

Striated muscle physiology, morphology, and molecular mechanisms of its regulation: Knowns and unknowns

1.1. Overview and Significance

Straited muscle is a critical driver of human life and movement. Consequently, dysregulation of muscle function can have a devastating impact on an individual's health and mobility. Thus, understanding the many fundamental molecular mechanisms that regulate muscle function is essential for our ability to prevent dysfunction or restore proper muscle function in individuals with life-threatening muscular diseases. The work presented here highlights an integrative approach towards understanding myofilament-specific mechanisms that govern the regulation of both cardiac and skeletal muscle function. This work is aimed at answering questions that range from a basic understanding of molecular-level regulation of muscle function to developing potential therapeutics that may translate to the clinic for patients with specific types of congenital heart failure.

1.2. Striated muscle at the cellular and subcellular scale

Across all animal taxa, striated muscles show markedly different properties that reflect a stunningly diverse array of functions, from the slow, energy-saving molluscan catch muscles (1), to exceedingly rapid stretch-activated asynchronous flight muscles, (2), to vertebrate cardiac muscle regulating systemic blood supply on a beat-to-beat basis (3). Many of the functional

differences between various muscles types are associated with their cellular and subcellular ultrastructure, and the immense diversity of muscle geometry observed in biology presents exciting opportunities to relate basic biophysics of muscle to function (4).

Mammalian striated muscle (*i.e.*, skeletal and cardiac muscle) each possess unique, morphological characteristics. Skeletal muscle is comprised of long, multinucleated myocytes that are organized with a high degree of myofibrillar alignment throughout the cell (Figure 1.1 A). Cardiac muscle, conversely, is more disorganized, comprised of much shorter, mononucleated myocytes that branch and link together end-to-end (mechanically, electrically, and chemically) via intercalated disks, forming a complex three-dimensional cellular mesh (Figure 1.1 B). However, at the microscopic level, skeletal and cardiac myocytes have similar distinct striations that arise from dense, repeating protein networks called sarcomeres (Figure 1.1 C).

The sarcomere is often described as the basic unit of contraction of striated muscle and is the source of the molecular machinery that converts electrical and chemical energy into the mechanical force that drives human movement and every beat of the heart. Figure 1.1D shows an illustration of the half-sarcomere. It is made up of interdigitated thick and thin filaments that each contain various regulatory proteins. This pseudo-crystalline ensemble of proteins is what is responsible for the finely tuned regulation of striated muscle function, and the vast molecular mechanisms operating within it continue to be a major focus area of research. A detailed description of what is currently known and unknown about the structure and function of the sarcomere myofilaments is in the sections to follow.

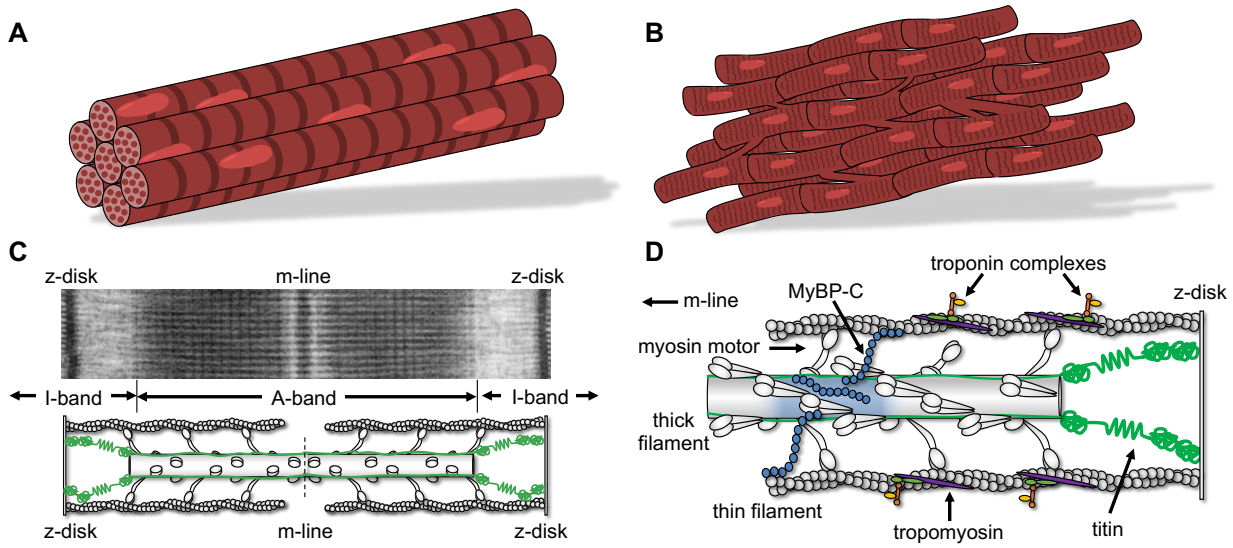

Figure 1.1. Striated muscle, the sarcomere, and its constituents.

Despite macroscale differences in morphology, both skeletal (**A**) and cardiac (**B**) muscle have similar subcellular structure. The dense network of proteins that give myocytes their straited appearance are sarcomeres (**C**), which contain interdigitated thick (myosin) and thin (actin) filaments each decorated with various regulatory proteins. An example of a sarcomere is shown by the electron micrograph (image from sarcomere.org) with a cartoon depicting the arrangement of filaments below. The sarcomeres are capped by z-disks on each end, which is the center of the I-band. The I-band contains mainly actin and titin, as opposed to the A-band, which also contains the myosin filaments. (**D**) Schematic of the half-sarcomere with its various regulatory proteins. The thick filament is made up mostly of myosin, but also includes the A-band region of titin (green) and myosin-binding protein C (MyBP-C; blue) which is localized to the 'C-zone' in the central third of the half-A-band (blue shaded region). The thin filament consists of F-actin decorated with 'regulatory units' that include tropomyosin (purple) and troponin complexes made up of three subunits: troponin C (orange) troponin I (yellow) and troponin T (green). The I-band region mainly consists of the spring-like domains of titin (green) and binds to the z-disk. For clarity, only proteins relevant to the work presented here are depicted.

1.3. Myofilament proteins in skeletal and cardiac muscle and variations in regulatory mechanisms between muscle types

The sarcomere is comprised of interdigitating thick (myosin-containing) and thin (actin-containing) filaments that are each decorated with various regulatory and structural proteins. (Figure 1.1 C & D). The arrangement of the thick and thin filaments gives rise to the distinctive striation pattern of the myocytes, which is a series of dark and light bands called the A-band and I-band (respectively). The A-band is the region where thick and thin filament overlap, whereas the I-band contains mainly the thin filaments and titin (Figure 1.1 C). Each end of the sarcomere is capped by a dense protein mesh in the I-band called the z-disk, and it is to this network of proteins that the thin filaments and titin are anchored. Each filament and various regulatory proteins in the sarcomere of cardiac and skeletal muscle are described in more detail in the sections below.

1.3.1. The thin filament and associated regulatory proteins

The main site for calcium-based regulation of muscle function is the thin filament of the sarcomere, which is mainly comprised of polymerized actin monomers in a helical coiled-coil. Different muscle types express different thin filament lengths—in rat cardiac papillary muscle, the actin filament of the sarcomere was recently measured at 1.04 ± 0.03 μm, while it was found to be 0.94 ± 0.01 μm in sartorius muscle from a frog (5). In each muscle type, however, various regulatory proteins are bound to the actin filaments, grouped into protein complexes (approximately every 7 actin monomers) often referred to as 'regulatory units' (3). The regulatory units are made up of the long, filamentous protein tropomyosin (Tpm) and the troponin (Tn) complex, which contains three subunits: troponin C, I, and T (abbreviated as TnC, TnI, and TnT, respectively).

Troponin C is the major calcium receptor of the thin filament in both cardiac and skeletal muscle. The skeletal muscle isoform of TnC contains two possible calcium binding sites, whereas cardiac muscle (and slow skeletal muscle) isoforms have only a single calcium binding site (3). Upon calcium release into the cytosol, calcium binds to TnC, which induces a conformational change throughout the troponin complex, which strongly depends on the interactions between the troponin subunits. This conformational change in troponin alters the interaction between TnT and tropomyosin such that tropomyosin is azimuthally displaced, resulting in exposure of myosin binding sites on actin along the thin filament (3). Thus, calcium-mediated displacement of tropomyosin via structural changes in troponin is a key determinant and regulator of muscle activation.

Tropomyosin is often referred to as the 'gate-keeper' of muscle contraction (6–8), as its position on the actin filament dictates the degree to which myosin can interact with actin. It is widely accepted that tropomyosin's position on the thin filament is a dynamic equilibrium between three possible states, each of which are associated with different degrees of activation. This model of thin filament activation was originally proposed in the seminal work by McKillop and Geeves (9), and defines these three tropomyosin positions, or states, as the 'blocked,' 'closed,' and 'open' states. In the absence of calcium, tropomyosin favors the 'blocked' state, in which it is lying in the groove created by the actin filament helix, covering the myosin binding sites on actin sterically inhibiting actin-myosin interactions (10). The 'closed' state occurs in the presence of calcium, and is the result of partial tropomyosin displacement, permitting mainly weak actin-myosin interaction. When calcium is bound to TnC *and* myosin motors are weakly interacting with the thin filament, tropomyosin can be pushed into the 'open' state, in which myosin binding sites on actin are fully exposed and strong, force-generating actin-myosin interactions are possible.

The transition of tropomyosin form one state to another is therefore a key determinant of striated muscle activation and force generation. For example, different troponin isoforms may interact differently with tropomyosin which may alter the sensitivity of calcium to tropomyosin displacement. An extreme-case example of this was recently reported using cryo-EM to investigate the position of either cardiac muscle or smooth muscle tropomyosin of F-actin (11). The authors found that cardiac tropomyosin is less likely to occupy a 'closed' (partially activated) position than smooth muscle tropomyosin, which they attribute to cardiac tropomyosin interacting with troponin to maintain equilibrium between the three states while smooth tropomyosin does not interact with troponin. Additionally, the stiffness of tropomyosin is likely an important factor in modulating thin filament activation, changes in tropomyosin rigidity due to mutations may be an underlying cause for various forms of cardiomyopathy (12, 13). It was recently suggested that point mutations associated with hypertrophic cardiomyopathy alter the energetic landscape the tropomyosin-actin system in such a way as to diminish cooperative inhibition of neighboring regulatory units on the thin filament (14). The authors attributed this to the hypercontractility seen with the same mutations experimentally on demembranated cardiac muscle preparations. Moreover, others have focused on the head-to-tail overlap region of tropomyosin as a location of interest, as there have been several mutations in this region associated with cardiomyopathies (15, 16). It is possible that these mutations also influence the rigidity of serially linked tropomyosin molecules, thereby affecting the cooperativity of thin filament activation.

1.3.2. The thick filament, myosin, and myosin-binding protein C

The thick filament is mainly comprised of the motor protein myosin, which polymerizes into a helical, bipolar filament. With this arrangement of myosin motors, each half of the myosin

filament contributes to sarcomere shortening by pulling the Z-disks toward one another via myosin-actin cross-bridges. The α-helical coiled-coils of the myosin tails form the backbone of the thick filament, and the myosin heads (two per molecule) extend outward radially from the surface of the backbone (17). The central portion of the thick filament (the m-line) is bare of myosin motors and contains unique titin protein domains (see section 1.2.3 below). The myosin motors are arranged on the thick filament as 'crowns' of three heads rotated azimuthally by 120° within each crown (18–20). Subsequent crowns along the axis of the thick filament are separated by ~14.3 – 14.5 nm and rotated azimuthally by 40° such that the thick filament helical periodicity is ~43 nm (Reconditi, 2006 and references therein) (19).

Myosin motors are the primary molecular drivers of muscle contraction, powering filament sliding via ATP-driven cyclical actin-myosin interactions. The structural and chemo-mechanical properties of muscle myosin have been a major focus of muscle research for decades, and remarkable progress has been made towards elucidating myosin's exact functional properties in both skeletal and cardiac muscle. Structural advances using X-ray diffraction techniques have characterized the power-stroke (or working stroke) of myosin *in situ* in skeletal muscle (21–24), and find that each myosin motor undergoes a powerstroke of about 6 nm, producing about 6 pN of force (25). However, different muscle types express different myosin heavy chain isoforms, which dictate the ATPase rate of each myosin head. In adult humans, for example, cardiac muscle is comprised mainly of slow-twitch myosin isoforms (beta-myosin, expressed from the MYH7 gene) while skeletal muscle is comprised of either slow-twitch or fast-twitch (alpha-myosin, expressed by the MYH6 gene).

In addition to myosin motors, the thick filament also contains myosin-binding protein-C (MyBP-C), which is localized to the central third of the A-band region of the sarcomere [depicted

in Figure 1.1 D by the blue shaded region; (26)]. It is present in three isoforms: slow-skeletal, fast-skeletal, and cardiac, and the functional role varies between each isoform depending on the tuning of the sarcomere (27). While it is generally accepted that MyBP-C directly links the thick and thin filaments together in striated muscle, it's function and regulatory role in the sarcomere is still debated (28, 29). When myosin motors are in their resting conformation, MyBP-C may act to stabilize this conformation and then release motors upon activation. Additionally, although MyBP-C is mainly associated with the thick filament, recent evidence has emerged that it can also interact with actin to facilitate thin filament activation (30–32). Recent work by Risi and colleagues has demonstrated that specific N-terminal domains of cardiac MyBP-C interact with tropomyosin on to aid in thin filament activation (33). However, other studies have shown that ablation of MyBP-C increases cross-bridge binding and cycling rates, likely by removing the physical constraints of MyBP-C on the myosin motors (34). This mechanism has also been explored as a potential treatment for diminished cardiac contractile function in dilated cardiomyopathy (35).

1.3.3. Titin

Titin is the largest known protein at present (3–4 MDa), and spans the entire length of the half-sarcomere from the m-line to the z-disk (36, 37). (The illustration in Figure 1D depicts titin spanning the half-sarcomere in green.) Titin is composed of many serially linked unique domains that have specialized tasks in the sarcomere, and the biophysical an biochemical properties of the different regions of titin have been a major focus area in muscle biophysics for over a decade [for comprehensive reviews, see references (36–39)]. Historically, titin was believed to be mainly a structural protein that connected thick filaments to the z-disks and was previously called connectin (40). Now, however, it is generally accepted that titin plays a much bigger role in muscle function

and regulation than simply sarcomeric structural stability, including a potentially major role in heart failure.

The C-terminal of titin associates with the M-band region of the sarcomere (the 'bare zone' of the myosin filament) and has various signaling pathway effectors including a kinase domain and phosphorylation sites in cardiac muscle (41). Additionally, many titin-associated ligands interact with the M-band region of titin, such as calmodulin, lamin, and obscurin (41). Furthermore, the M-band region of titin interacts with muscle-specific RING-finger prteins-1/-2 (MURF1/2), which binds to microtubules and helps maintain their stability (36, 41). Lastly, myomesin interacts with the M-band region of titin, which links thick filaments to one another (39).

The majority of the A-band region of titin interacts mainly with myosin and MyBP-C (41) and may play a role in regulating thick filament-based mechanisms of activation in both cardiac and skeletal muscle (42, 43). Notably, the A-band region is also highly associated with cardiomyopathy-causing mutations. In fact, 25% of patients with end-stage dilated cardiomyopathy have titin-associated truncating mutations (44, 45), many of which are located in the A-band region of titin. However, the functionality of this region of titin and why it is so prone to cardiomyopathy-associated mutations remains largely unknown and, consequently, currently remains a very significant area of cardiac muscle research.

The I-band region of titin provides the major source of passive tension when striated muscle fibers are stretched (46) and has been studied extensively in both cardiac and skeletal muscle. It is comprised of serially linked immunoglobulin-like (Ig) domains that flank a unique region known as the PEVK segment, because it is rich in proline, glutamine, valine, and lysine (41). By putting titin antibodies on both proximal and distal (*i.e.*, towards the Z-disk and A-band,

respectively, relative to the PEVK region), Linke and colleagues measured (using immunoelectron micrographs) the extensibility of the different I-band titin regions as they increased the sarcomere length of single rabbit psoas myofibrils (47). The authors found that the PEVK region of titin behaves as a pure entropic spring at small sarcomere extensions, while it behaves as an entropic-enthalpic spring at higher (but still physiologically relevant) sarcomere extensions. Importantly, they also found that both the proximal and distal poly-Ig domains extend at much lower forces than the PEVK region, due to their high bending rigidity compared to PEVK region.

These results led to a more recent investigation of the Ig domain extensibility, in which Rivas-Pardo and colleagues used single-molecule tracking of labeled myofibrils of rabbit psoas and examined the time-resolved structural transitions of I-band titin after sarcomere stretches (48). With this technique, the authors could directly measure the load-dependent folding/unfolding kinetics of the poly-Ig domains that flank the PEVK region. They found that at forces between 4–6 pN per titin filament, the probability of any Ig domain being in its native, folded conformation drops from 1 to 0, and that this was independent of whether the Ig domain is proximal or distal to the PEVK region. Thus, there are significant load-dependent structural dynamics of the I-band region of titin that may play an appreciable role in the regulation of contraction.

1.3.4. Muscle-specific length-tension relations and regulators thereof

Understanding the complex mechanisms that originate in the sarcomere to regulate muscle function has been a major focus in physiology since the 1950's (20, 49). The sliding filament theory, pioneered by Nobel laureate Andrew Huxley and Hugh Huxley (no relation to Andrew Huxley) in two independent papers in 1954 (50, 51), states that ATP-driven myosin motors slide the thin filaments relative to the thick filaments, and provide sarcomere and muscle shortening

during contraction. Since the birth of this theory, a tremendous amount of work has been done to uncover the vast molecular mechanisms that regulate this process, as well as characterizing the differences between skeletal and cardiac muscle.

Despite similarities between skeletal and cardiac muscle from a structural point of view at the sarcomere level, the regulatory processes governing the function of each muscle type vary drastically. Both skeletal muscle fibers and cardiomyocytes undergo tremendous geometrical and structural dynamics during contraction-relaxation cycles, and these cellular level dynamics translate to the level of the sarcomere as changes in sarcomere length (SL) and interfilament lattice spacing (52). While finely tuned contractile responses to changes in SL are a common feature of cardiac and skeletal muscle—upon which each muscle type relies for proper function—the properties of the force-SL relation are necessarily quite different between muscle types. That is, with regards to passive and active force generation, cardiac and skeletal muscle do not respond to changes in sarcomere length in the same way, giving rise to unique, muscle-specific sarcomere length-tension relationships that provide each muscle type with different contractile properties.

Hinging on the sliding filament theory, the force–SL relation in skeletal muscle was first characterized in detail in seminal work by Albert Gordon and colleagues in 1966 (53). The length-tension relation consists of a steep ascending portion, rising from nearly no isometric tension to maximum tension between sarcomere length ~1.25 – 2.0 μm (in skeletal muscle from frogs). Between sarcomere length ~2.0 and 2.25 μm is the 'plateau' region, at which maximum isometric tension is generated due to the optimal degree of inter-myofilament overlap for this range of SL. As sarcomere length increases beyond ~2.25 μm, the degree of filament overlap reduces, causing a proportional reduction in tetanic force.

Mammalian cardiac muscle, on the other hand, has a different force–SL relation, in which twitch force rises steadily between SL 1.8–2.3 μm, at which point it plateaus. At the organ level, the SL dependence of twitch force manifest as the Frank-Starling law of the heart, which states that cardiac output is determined by venous return such that sufficient systemic blood supply is maintained on a beat-to-beat basis. In skeletal muscle, the force-SL relation also dictates the power output and efficiency of contraction.

Despite much recent effort, many of the sarcomere length-sensitive molecular underpinnings of the regulation of muscle function have remained unresolved. Many molecular mechanisms originating in the skeletal and cardiac muscle sarcomere have been attributed to contributing to the force-SL relation of each muscle type. A key reason for the difference in the response of skeletal muscle versus cardiac muscle to changes in SL may be in the calcium handling properties. Skeletal muscle has different calcium handling properties than cardiac muscle, such as: (*i*) more efficient calcium-mediated thin filament activation due to the two calcium binding sites on the skeletal isoform of troponin C, as opposed to the single site on cardiac troponin C, and (*ii*) the fact that a couple of milliseconds after the stimulus in skeletal muscle has maximum intracellular calcium concentration (54), while the calcium transient at the peak of a twitch in cardiac muscle is far below saturating levels (55). For this reason (at least in part), cooperative activation mechanisms may become more relevant at long sarcomere lengths in cardiac muscle that may contribute to the unique force-SL relation. For example, tropomyosin-tropomyosin interactions may activate neighboring regulatory units along the thin filament (56). Similarly, cross-bridges can then recruit more cross-bridges through nearest-neighbor interactions (57). Moreover, the intrinsic compliance of the myofilaments have also been suggested to play a role in the cooperative mechanisms of activation (58) and may alone regulate isometric tension

development in striated muscle (58–60). It is likely that a combination of these mechanisms contributes to the overall force–SL relation for cardiac muscle.

1.4. Current open questions regarding the regulation of striated muscle function and motivation for this work

1.4.1. What drives a given cardiomyopathy phenotype, and can it be prevented through rationally designed and genetically engineered intervention?

There is an emphatically growing interest in cardiac biology and medicine to understand the molecular underpinnings of inherited forms of cardiomyopathy. Broadly, cardiomyopathy is defined as pathological changes in myocardial morphology, and genetic forms can be caused by mutations in genes encoding proteins in the sarcomere, the mitochondria, and the cytoskeleton (61, 62). Two of the most common clinical phenotypes include hypertrophic cardiomyopathy (HCM), which is associated with a thickening of the ventricular walls and diastolic dysfunction, and dilated cardiomyopathy (DCM), which is associated with thinning of the ventricular walls and systolic dysfunction (Figure 1.2).

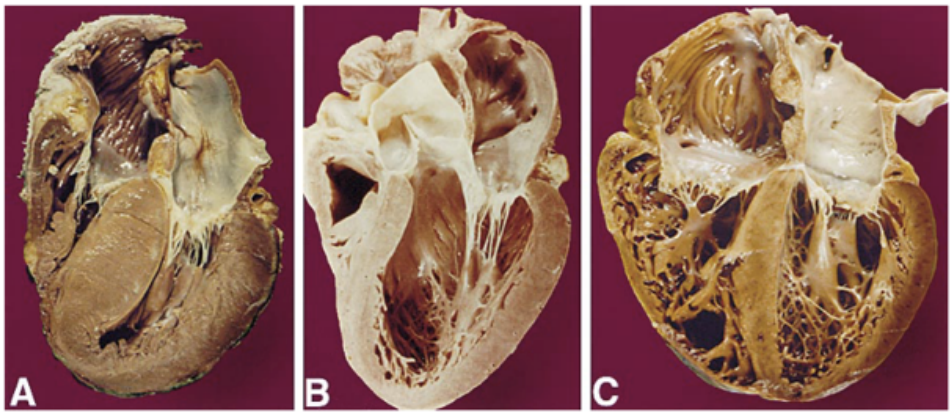

Figure 1.2. Examples of myocardial remodeling due to cardiomyopathies.
Hypertrophic cardiomyopathy (**A**) is associated with pathological thickening of the ventricular and atrial walls compared to a normal heart (**B**), whereas dilated cardiomyopathy (**C**) is associated with thinning of the ventricular walls. Image adapted from reference (62).

These deadly cardiac disorder affect approximately 1 in 500 individuals in the general population (61), and, to date, the only effective treatment option for patient with cardiomyopathy is cardiac transplantation (63). Furthermore, the development of new pharmacological therapeutic options (e.g. inotropes) has also been largely unsuccessful thus far. Consequently, there is a pressing need to elucidate the mechanisms by which specific cardiomyopathy-linked mutations drive disease progression, and how to prevent pathological myocardial remodeling in mutation-specific failing hearts with targeted and rational approaches. [Depressed F-S mechanism in DCM - (64)].

As discussed in the preceding section, the cardiac sarcomere is a finely tuned molecular machine reliant on cooperative regulatory mechanisms for proper function, and the importance of these mechanisms is highlighted by the mutations in sarcomere proteins that cause cardiomyopathy. There have already been nearly 1,500 mutations in sarcomere proteins associated

with inherited cardiomyopathies (61), making the sarcomere a primary focus of genetic cardiomyopathies (63). Our inability to restore function (or prevent dysfunction) of failing hearts due to sarcomere-based inherited cardiomyopathies is likely due to the complexity of the fundamental regulatory mechanisms operating within the sarcomere that are disrupted by mutations, as well as the vast diversity of sarcomere mutations that have already been linked to either the HCM or DCM phenotype. As such, the most effective form of treatment likely varies from patient to patient depending on the underlying mutation, further complicating therapeutic intervention. Moreover, the divergence of phenotype (*e.g.* DCM versus HCM) from genotypically similar sarcomere mutations suggests that the molecular mechanisms driving the resultant phenotype are extremely sensitive to the nature of the mutation. Elucidating such specific patho-mechanisms remains a major challenge in cardiac research.

Because genetic cardiomyopathy is a progressive disease, it may be possible to prevent myocardial remodeling before it reaches pathological stages. This, of course, requires adequate knowledge about not only about the mechanisms underlying the dysfunction, but also proper insight into how the sarcomere operates under normal conditions in order to apply the appropriate intervention. Recent work by Jennifer Davis and colleagues has uncovered a predictive metric for determining the type and severity of myocardial remodeling based on the contractile properties of the cardiomyocytes with various HCM– and DCM–associated mutations (65, 66). The authors found that sarcomere mutations that alter in the twitch force and calcium handling in cardiomyocytes from HCM or DCM mouse hearts manifest as a quantifiably consistent difference in twitch force–time integral as compared to wild-type cardiomyocytes. Thus, this metric, which they termed the 'twitch index,' is correlated with the degree and morphology of myocardial remodeling for each case, providing a biophysical link between the subcellular mechanical

properties and the organ-level morphology. Moreover, this metric was also able to predict human cardiac phenotypes from human induced pluripotent stem cell-derived cardiomyocytes from patients with genetic cardiomyopathy. However, the twitch data upon which the predictive metric is based relied on computationally simulated twitches based on biochemical and biophysical rates in the excitation contraction properties of the cardiomyocytes. Therefore, it is uncertain whether an analogous measurement based on twitches from cardiac mechanics experiments on intact myocardial preparations will provide a similarly robust predictive metric.

Nonetheless, the elegant work of Davis *et al.* has provided a platform from which we can begin investigating methods to prevent pathological myocardial remodeling in genetically engineered animal models of cardiomyopathy. Synthesizing the multitude of research done on the various sarcomere protein mutation-based cardiomyopathy may be a fruitful first step towards a holistic answer. We posit that systematic characterization of certain mutations may elucidate the underlying mechanisms driving cardiomyopathy pathogenesis, and that understanding how the regulatory processes within the sarcomere operate under normal conditions may enable us to make precision medicine models of treatment on a patient-to-patient basis. This remains a current major focus in cardiac research, and steps we have taken towards an answer are presented in Chapter 6.

1.4.2. What are the mechanical cues of thick filament activation in striated muscle?

As discussed above, the canonical mode of muscle activation typically focuses on calcium-based regulatory mechanisms involving proteins associated with the thin filament. However, in resting muscle, most of the myosin motors on the thick filament are in the 'off' state and packed into helical tracks with 43 nm periodicity on the surface of the thick filament backbone (67–69), making them unavailable for actin interactions and ATP hydrolysis (70). This observation has

brought into question the mechanisms by which myosin motors are released from their resting conformation to an activated, force-generating conformation, and what regulatory factors might influence these mechanisms [for a comprehensive review, see reference (71)].

In both skeletal and cardiac muscle, individual myosin motors may be in multiple different conformations that largely depend on whether the muscle is activated, at rest, or under passive tension (68, 72). In resting muscle, the majority of the myosin heads are in a 'relaxed' conformation, in which they lay on the surface of the thick filament backbone with their heads toward the m-line of the sarcomere (68). Upon activation, more motors switch to an 'ON' conformation, in which they extend farther from the backbone and interact with actin on the thin filament [(18) and references therein]. However, the mechanism(s) by which myosin motors transition from a resting conformation (favoring thick filament backbone interactions) to an active conformation (favoring actin interactions) have only recently been elucidated in skeletal muscle. Linari and colleagues have demonstrated using tie-resolved X-ray diffraction techniques that myosin heads are switched from a relaxed position to an active position via a mechanosensing-based mechanism in the thick filament backbone (72). According to the proposed mechanism, in a tetanically stimulated skeletal muscle fiber, a few constitutively activated myosin motors interact with actin to initiate contraction upon calcium-mediated thin filament activation. This induces a strain in the thick filament backbone that causes the resting conformation of myosin motors to be less favorable, resulting in more motors becoming activated and interacting with actin (Figure 1.3).

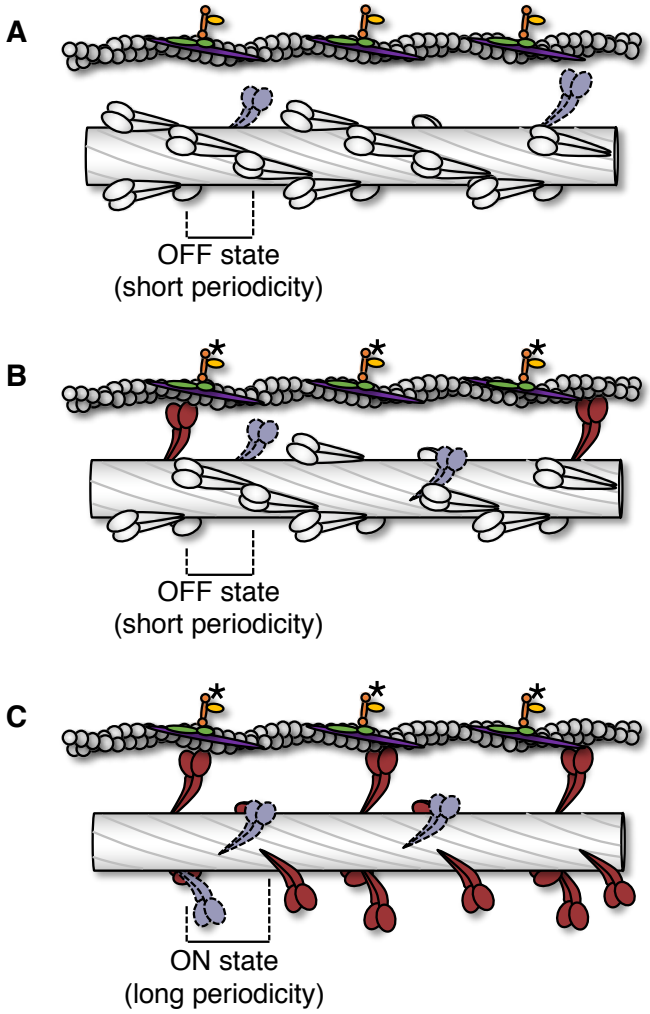

Figure 1.3. Dual-filament regulation in skeletal muscle.

When calcium is not present (**A**), both the thin filament and the thick filament are 'off,' characterizable in the thick filament by the short backbone periodicity (14.34 nm in the tibialis anterior from *Rana esculenta* (72)]. In the 'OFF' state, the majority of the myosin motors are in their resting conformation (grey motors) folded onto the thick filament backbone, while a few motors are constitutively 'ON' (purple motors). When calcium is present (denoted by the asterisks) the thin filament is activated, and the constitutively ON motors can immediately interact with actin forming strong cross-bridges (red motors), but the thick filament transiently remains under low load (**B**) with a short periodicity. (**C**) When constitutively ON motors interact with actin and generate force, stress in the thick filament backbone releases more motors from their resting conformation and the thick filament stretches to a longer periodicity [14.57 nm in in the tibialis

anterior from *Rana esculenta* (72)]. Filaments are not drawn to scale. [Modified from figure 4 of Linari *et al. Nature*, 2015; reference (72)].

An exciting experimental technique to capture similar thick filament structural dynamics without the need of synchrotron-based X-ray sources has recently been developed by Malcolm Irving and colleagues. This technology incorporates time-resolved polarized fluorescence from bifunctional rhodamine probes that report the average orientation of the regulatory light chain of myosin relative to the thick filament backbone with high temporal resolution. Fusi and colleagues have recently shown that this technique in permeabilized skeletal muscle preparations (24, 73, 74) can be used to investigate myosin motor orientation under different experimental conditions. They found that myosin motors in skeletal muscle are released from a resting conformation to an activated conformation via stress sensing after fast stretches in the absence of calcium. The authors conclude that passive force alone (likely mediated by titin) is sufficient to activate the thick filament through mechanosensing-based mechanisms that are independent of calcium (74).

A rapid, feed-forward, mechanosensing-based mechanism of thick filament activation likely plays a significant role in optimizing muscle energetics and efficiency in skeletal and cardiac muscle alike (75). In skeletal muscle, for example, the load-dependent structural dynamics of the thick filament has recently been implicated in regulating the number of myosin motors during unloaded shortening of a skeletal muscle fiber. During unloaded shortening of a tetanically stimulated intact skeletal muscle fiber, the structure of the thick filament adapts to reduce the number of activated myosin motors until only 1–4 motors are activated, thereby minimizing the rate of ATP utilization during extended unloaded shortening (76).

A similar mechanosensing-based regulatory mechanism involving myosin filament structural dynamics has recently been proposed in cardiac muscle (75, 77), and may play a critical role in sarcomere length-dependent activation and force augmentation, and thus the Frank-Starling law of the heart (42, 78, 79). Additionally, a mechanosensing-based mechanism of thick filament activation was recently implemented in a finite element model of a left ventricle, which enabled a semi-quantitative recapitulation of experimental data of the Frank-Starling response (43). However, the intrinsic disordered nature of cardiac muscle has caused great experimental challenges in attempting to achieve similar spatial resolution using traditional X-ray diffraction techniques as skeletal muscle. This has recently been at least partially circumvented, however, using a similar polarized fluorescent technique as described above to measure the dynamics of the orientation of myosin in permeabilized cardiac muscle preparations (80–82). Nevertheless, the question of whether the thick filament in intact cardiac muscle is activated during a twitch with similar load-dependent structural dynamics as skeletal muscle remained unknown. This unknown is what motivated the work highlighted in Chapter 4.

1.4.3. What factors control the structural basis of the regulatory state of the cardiac thick filament, and can it be actuated at rest to potentiate ensuing contractility?

The characterization of the rapid, feed-forward activation mechanism in the thick filament upon force development in skeletal muscle raises the question of whether there are mechanisms by which the sarcomere is actuated at rest, and whether this might aid initial contraction by increasing the population of motors that are 'primed' for actin-myosin interactions. In particular, understanding the factors that influence the structure of the resting sarcomere in cardiac muscle is of great interest in order to elucidate mechanisms during diastole that may affect systolic

contraction. These mechanisms may include structural dynamics of the myofilaments and/or sarcomere geometry dynamics due to resting sarcomere length changes, titin-induced thick filament stress, small molecule positive inotropes, and/or cardiomyopathy-related sarcomere protein mutations.

First, defining a structural basis for the Frank-Starling response that involves thick filament structural dynamics in resting cardiac muscle (*i.e.* during diastole) has been an onerous objective with tenuous results. Recent work by Ait-Mou *et al.* examined the effects of sarcomere length versus titin-mediated passive tension on myosin filament structure in intact cardiac muscle from rat hearts (42). The authors used X-ray diffraction methods to compare the resting thick filament structure at short (2.0 μm) and long (2.4 μm) sarcomere lengths in both wild-type cardiac muscle and in cardiac muscle from a transgenic rat harboring a mutation in the splicing factor RBM20 that causes the I-band region to be longer (and therefore more compliant). The RBM20-mutated cardiac muscle produced significantly less passive tension going from sarcomere length of 2.0 μm to 2.4 μm compared to wild-type. The authors report that wild-type cardiac muscle displays significant stretch-induced increases in the intensity of myosin-based X-ray reflections, as well as in the troponin-related reflection, indicating a stretch-induced increase in the periodic ordering of the thick and thin filaments. They also report a significant shift in the average mass of the myosin motors away from the thick filament backbone toward the actin filament. Interestingly, these results were diminished in the RBM20-mutated cardiac muscle. Thus, the authors conclude that titin-induced strain in the thick filament causes a perturbation in the resting state of the thick filament. They speculate that this may promote actin-myosin interaction upon activation and therefor may play a key role in the Frank-Starling response. However, one caveat of working with RBM20 splicing mutants is that they have also been shown to cause arrhythmogenic DCM related

to irregular calcium handling (83), as well as cardiac fibrosis (84). Consequently, the molecular mechanisms governing the potential actuation of the resting sarcomere upon stretch may be due to compensatory and/or unrelated contractile effects.

In addition to sarcomere length-dependent structural changes in resting cardiac myofilaments, there are a number of other factors that have been reported to disrupt the resting state of the thick filament in cardiac muscle—some physiological, some pharmacological, and others pathological. One physiological response that has been examined in terms of sarcomere structure is beta-adrenergic stimulation of the heart (the 'fight or flight' response), which triggers phosphorylation of numerous sarcomere proteins including titin, troponin I, MyBP-C, and the regulatory light chain of myosin, and increases cardiac contractility. Recent work by Rao and colleagues examined the effects of protein kinase A (PKA) phosphorylation of troponin I on sarcomere lattice spacing and myosin position (85). The authors found that both PKA-mediated phosphorylation of cardiac troponin I and substitution of native troponin I with a phosphomimic variant resulted in a significant shift in the myosin mass away from the thick filament backbone towards the actin filament. They concluded that this effect partially activates the thin filament at rest, which may draw myosin closer to actin in the resting sarcomere. Similarly, using a similar polarized fluorescence technique as described above that reports the orientation of cardiac myosin in permeabilized muscle preparations, Kampourakis and colleagues have shown that phosphorylation of the regulatory light chain of cardiac muscle is accompanied by structural changes in both the thick and thin filaments, and that these structural effects mediate the calcium-sensitivity of force (82).

In addition to physiological factors that may influence filament structure, various inotropic small molecules have also been investigated in the same context. Again using the polarized

fluorescent rhodamine probes in permeabilized cardiac preparations, Kampourakis and colleagues investigated the structural effects of the small molecule myosin activator omecamtiv mecarbil (OM) and deactivator blebbistatin (80). The authors report that with blebbistatin bound to myosin, the resting conformation of myosin is stabilized, inhibiting actin-myosin ATPase across a wide range of calcium concentrations. They report further that, at low levels of calcium, myosin bound to OM perturbs the regulatory state of the thick filament, causing myosin motors to be more perpendicular to the thick filament backbone. Interestingly, despite being in phase II human clinical trials (86), the authors report that OM inhibits force at higher levels of calcium by disrupting the actin-myosin ATPase cycle. A similar OM-mediated disruption of the cross-bridge cycle has also been suggested by other groups using solution biochemistry techniques (87).

Lastly, of great recent interest is determining the structural effects of various cardiomyopathy-related mutations on the resting conformation of myofilaments. In particular, focus has been on cardiomyopathy-related mutations in sarcomere proteins, as these may perturb the resting myofilament structure in such a way as to drive the pathological hypercontractility. Recent work by the Spudich group has proposed a conserved 'hotbed' location of myosin mutations associated with HCM weaken the interaction of myosin heads (the S1-S2 interaction) at rest and may cause myosin to prematurely be activated, in turn providing a structural model of the pathological hypercontractility associated with these mutations (88–90). Interestingly, recent work by Yuan and colleagues using X-ray diffraction techniques on permeabilized cardiac muscle from transgenic mouse hearts found that a DCM-associated myosin mutation had little effect on the radial position of myosin motors or interfilament lattice spacing in the absence of calcium (91).

Thus, it is clear that the structural basis of the regulatory state of the resting thick filament plays an important role in cardiac function, and likely serves as an important target for diastolic-

based intervention for contractile abnormalities and/or for novel therapies to address cardiomyopathies. Work we have done with regards to potentiating the cardiac myosin filament at rest is highlighted in Chapter 5.

1.4.4. How do the mechanical properties of the I-band region of titin influence active contractility?

Much of what we know about titin comes from *in vitro* experiments on deconstructed muscle preparations, such as fluorescently labeled titin in the I-band of isolated myofibrils (47, 48, 92), or atomic force microscopy on titin fragments (93, 94). However, very little is known about the role of titin in active muscle contraction, and whether the mechanical properties of the I-band region influence contractility. This is due to many intrinsic difficulties of studying titin in situ. For one, being mainly a passive elastic element in the sarcomere, it is very difficult to discern its mechanical contributions to the sarcomere from other molecular contributions, especially at short sarcomere lengths where it's slacked in the I-band (95). Secondly, modulating the stiffness of titin *in situ* is extremely difficult, and requires either precise control over post-translational modifications (*e.g.* PKA-mediated phosphorylation), or genetically engineered animal models with truncated or elongated titin isoforms that may display problematic secondary effects as a result of the mutated titin (96). Moreover, titin also may interact with calcium in the I-band to become stiffer upon activation (97, 98), but the role of such a mechanism has not yet been elucidated.

Recent work has approached this question through a number of different techniques. In particular, the development of a rat line harboring a heterozygous autosomal mutation (HM) that expresses a longer (and therefore more compliant) titin isoform has been exploited in a number of different studies (99, 100). In one such study the more compliant titin isoform in was shown to

reduce the tension generating capacity, the ATPase rate, and the calcium sensitivity of isometric tension in isolated myofibrils from tibialis anterior of the HM rats compared to controls (101).

In the same HM rat line, cardiac muscle was investigated to determine whether a more compliance titin isoform alters the Frank-Starling response (42). The authors found that the more compliance titin isoform in cardiac muscle imposes less stress on the thick filament upon stretch compared to controls, which caused a diminished stress-induced myofilament activation mechanism.

Outside of genetic modifications to study the role of titin in contracting muscle, significant progress has been made by studying isolated titin fragments *in vitro*. In recent work by Rivas-Pardo *et al.*, single-molecule force measurements were made with optical tweezers, which were coupled with measurements made from fluorescently labeled titin molecules in the I-band region of isolated myofibrils from rabbit psoas with time-resolved fluorescent microscopy, to quantify the structural dynamics of the I-band region of titin under physiologically relevant loads (48). They reported that serially linked immunoglobulin-like (Ig) domains in the I-band region that flank the spring-like PEVK segment unfold at much lower loads than the PEVK segment. The authors also report that, at about 4 pN per titin molecule, the Ig domains begin to unfold, and at about 8-10 pN per titin molecule, nearly all of the Ig domains are unfolded with a very low likelihood of re-folding. However, the authors claim that these load-dependent structural dynamics of the Ig domains in I-band titin provide appreciable mechanical work that can assist myosin motors in muscle contraction. While the refolding dynamics of unfolded Ig domains surely produce mechanical work, the kinetics of refolding events are orders-of-magnitude slower than that of the cross-bridge cycle. As such, the degree to which Ig domain refolding contributes to muscle contraction is unclear.

Nonetheless, the load-dependent structural dynamics of titin may provide a tunability to the I-band spring that may play a role in modulating the compliance of the sarcomere during contraction. Work we have done towards defining such a role in intact skeletal muscle fibers is highlighted in Chapter 3.

Finally, recent modeling efforts have gone towards elucidating a role of titin in modulating the mechanics of muscle contraction. Work by Nishikawa and colleagues has proposed a novel titin-based mechanism by which titin may be wound around the thin filament via myosin motors acting as rotors that twist the filaments relative to one another (102). In this way, titin may store large amounts of elastic potential energy during force development and active stretch that may contribute to force enhancement during stretch and force suppression during shortening. Work we have done with regards to computational modeling of the elastic properties of titin and their contributions to muscle mechanics and energetics is highlighted in Chapter 2.

Chapter 2

A spatially explicit model shows how titin stiffness modulates muscle mechanics and energetics

Abstract

In striated muscle, the giant protein titin spans the entire length of a half-sarcomere and extends from the backbone of the thick filament, reversibly attaches to the thin filaments, and anchors to the dense protein network of the z-disk capping the end of the half-sarcomere. However, little is known about the relationship between the basic mechanical properties of titin and muscle contractility. Here, we build upon our previous multifilament, spatial computational model of the half-sarcomere by incorporating the nonlinear mechanics of titin filaments in the I-band. We vary parameters of the nonlinearity to understand the effects of titin stiffness on contraction dynamics and efficiency. We do so by simulating isometric contraction for a range of sarcomere lengths (SL; 1.6–3.25 μm). Intermediate values of titin stiffness accurately reproduce the passive force–SL relation for skeletal muscle. The maximum force–SL relation is not affected by titin for SL ≤ 2.5 μm. However, as titin stiffness increases, maximum force for the four thick filament system at SL = 3.0 μm significantly decreases from 103.2 ± 2 pN to 58.8 ± 1 pN. Additionally, by monitoring ATP consumption, we measure contraction efficiency as a function of titin stiffness. We find that at SL = 3.0 μm, efficiency significantly decreases from 13.9 ± 0.4 pN/ATP to 7.0 ± 0.3 pN/ATP when increasing titin stiffness, with little or no effect below 2.5 μm. Taken together, our results suggest that, despite an increase in the fraction of motors bound to actin along the descending limb

when titin is stiffer, the force-generating capacity of the motors is reduced. These results suggest that titin stiffness has the potential to affect contractile efficiency.

2.1. Introduction

At the subcellular level, striated muscle contraction occurs through complex molecular interactions in dense, highly organized, repeating protein networks known as the sarcomere. The sarcomere is comprised of interdigitating thick (myosin) and thin (actin) myofilaments that are each decorated with various regulatory proteins. The giant protein titin is considered the third myofilament (37), as it spans the entire length of the half-sarcomere (from the Z-disk to the M-line). The A-band region of titin interacts primarily with the myosin filament, whereas the I-band region reversibly interacts with the actin filament and acts as an elastic link between the myosin filament and the Z-disk. Consequently, the I-band region of titin is responsible for the majority of the passive mechanical properties of muscle (46).

However, the elasticity of the I-band region of titin varies from muscle to muscle and can be modified *in vivo* to adjust the mechanical properties of the muscle. The I-band region of titin has multiple serially linked domains, each with unique elasticity (38, 47), giving the whole filament complex and nonlinear mechanical properties. Additionally, different striated muscle types express different titin isoforms and therefore have different mechanical properties (41). Human cardiac muscle, for example, expresses multiple titin isoforms, including a cardiac-specific isoform (the so-called N2B isoform), which has a molecular mass of ~3 MDa (41). This isoform is notably shorter (and therefore stiffer) than other isoforms expressed in human cardiac and skeletal muscle, which can be upwards of ~3.8 MDa, thereby contributing to the stiffer properties of cardiac muscle compared to skeletal muscle. Furthermore, various post-translational

modifications of the I-band region of titin can affect its mechanical properties, such as calcium-mediated stiffening (97) and phosphorylation of different spring elements in the I-band region (see (41) and references therein).

A current question in muscle physiology is: to what extent do the mechanical properties of titin influence the mechanics and energetics of active muscle contraction? This has been a central issue in a number of recent studies ((103) and references therein, (37, 104, 105)). Answering this question has remained elusive due to inherent difficulties of studying titin *in situ.* For one, it is difficult to discern titin-based contributions to the total sarcomere elasticity from other elastic elements within the sarcomere (*e.g.* cross-bridges, myosin binding protein C) or outside of the sarcomere (*e.g.* dystrophin, desmin). Secondly, modulating the stiffness of titin *in situ* is extremely difficult, and requires either precise control over post-translational modifications (*e.g.* PKA-mediated phosphorylation), or genetically engineered animal models with truncated or elongated titin isoforms that may display problematic secondary effects as a result of the mutated titin.

Early theoretical models of the sarcomere attempted to complement experimental analyses and uncover the effects of myofilament compliance on muscle contractility (106, 107). Historically, Huxley and colleagues used theoretical models to investigate the compliance of the contractile apparatus in relation to force generation and responses to rapid force transients (108–110), but did not consider titin as an elastic element in the sarcomere. Moreover, more recent computational models have shown that the kinetics and magnitude of muscle force generation depend on the mechanics of the myofilaments, cross-bridges, and the geometry of the myofilament lattice (58–60, 111–115), which was unaccounted for in early mathematical models of the sarcomere.

Here we modify previously developed, spatially explicit, multi-filament computational models of the half-sarcomere (113, 114, 116), to incorporate the mechanical influence of titin (117). Modeling titin as a nonlinear I-band spring, we are able to broadly investigate *in silico* the role titin stiffness in modulating the mechanics and energetics of contracting muscle.

2.2. Methods

2.2.1. Model description

Many aspects of the computational model used in this work have been described previously (113, 114, 116). Briefly, the model consists of four myosin filaments and eight actin filaments arranged in a double-hexagonal lattice in three dimensions (Figure 2.1 A & B). Periodic (toroidal) boundary conditions were employed to simulate a semi-infinite lattice. Each cross-bridge is modeled as a two-spring system consisting of a torsional and a linear element (113). Myosin and actin filaments consist of linear springs serially linked between each node of cross-bridge crowns (Figure 2.1 C). The stiffness of the springs for the myosin and actin filaments are 2020 pN/nm and 1743 pN/nm, respectively (60), and the lattice spacing (*i.e.* radial face-to-face distance between the myosin and actin filaments) is set to 14 nm.

The simulation is based on a three-state model for attachment, force generation and detachment of cross-bridges (60, 114). These state transitions determine not only the local forces borne by each cross-bridge, they also determine the ATP utilization rate associated with the number of times each cross-bridge detaches from the thin filament and hydrolyzes a subsequent ATP for subsequent binding and force generation. Thus the model provides predictions of both the mechanics and energetics of isometric contractions, and it is worth noting that all of the underlying

mechanical, geometric, and kinetic parameters can readily be modified to simulate various muscle types with different cross-bridge kinetics.

We build upon our previous spatially explicit model (114) by including nonlinear springs in the I-band to model titin. Six titin springs are added to each of the four myosin filaments, each of which span the length of the I-band and anchor to the Z-line at the actin filament-Z-line junction. Thus, each titin spring makes an angle, θ, with the myosin filament that is equal to the arctangent of the ratio of the filament lattice spacing (radial myosin-to-actin filament distance) and the length of the I-band.

Similar to other models (118, 119), the total force exerted by each titin spring (F_T) is modeled as an exponential dependence on length change of titin (ΔL):

$$F_T = a \cdot e^{(b \cdot \Delta L)} \qquad Eq.\ 2.1$$

where a and b are tunable parameters. For the "no titin" case, a was set to 0 pN, whereas for all other cases, a was arbitrarily fixed at 260 pN. The parameter b was varied across a range of 4-10 μm^{-1}. Using this value of a and range of b resulted in passive force-SL relations that span the range of published estimates for single titin molecules (47). The axial and radial components of F_T were taken as $F_T \cdot \cos(\theta)$ and $F_T \cdot \sin(\theta)$, respectively.

2.2.2. Simulation details

With the above geometric and mechanical properties established, the two key parameters we explore in this model are the influence of both sarcomere length (SL) and the titin stiffness parameter b. Each simulation trajectory represents a 15 ms isometric contraction (simulated time with 0.1 ms time-steps), which was sufficient time for isometric force to reach a steady state (Figure 2.1. D). For all parameter specifications, we average 50 independent trials.

As in previous iterations of the model (114), which followed from a long history of spatially explicit models of the sarcomere, beginning with Daniel et al. 1998, the simulation is initiated by defining a sarcomere length, lattice spacing, and titin stiffness, none of which change during contraction. As there is not any thin filament regulation in the current model (we do not consider Ca^{2+} regulation such as has been done by Tanner et al. 2012), the thin filament is completely activated upon initiation of the simulation. A stochastic perturbation is then given to the myosin motor positions and their state transition (*i.e.* unbound, weakly bound, or strongly bound) is then determined using Monte Carlo methods. After each time-step, we use an iterative optimization method to balance axial forces at all internal nodes (dots on the lattice proteins in Figure 2.1. C) of the spring system comprising the myofilaments (using an improvement over the optimization method in Williams et al. 2013) such that the net force is only experienced at the M-line of each myosin filament. (See the supplemental material in Williams et al. 2013 for more details.)

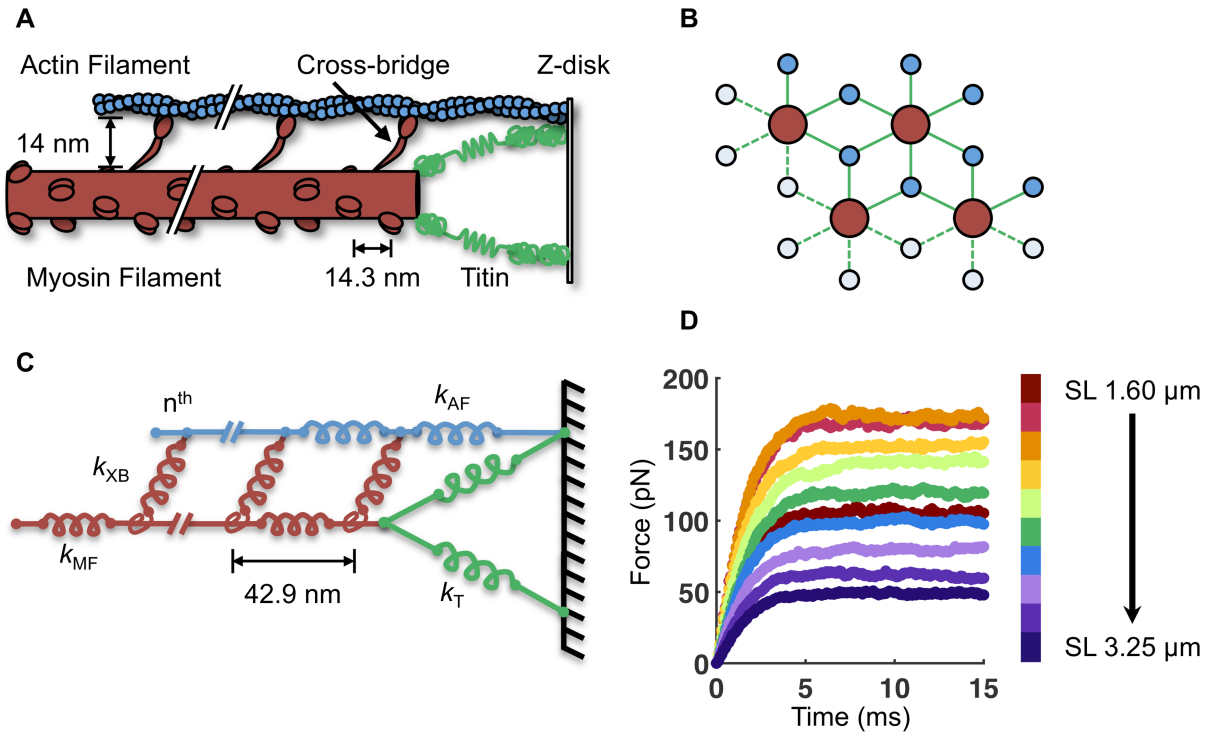

Figure 2.1. Description of the half-sarcomere model.

(**A**) A simplified schematic of the half-sarcomere, with the myosin filament shown in red, the actin filament in blue, and the I-band region of titin in green. (**B**) The myosin and actin filaments are arranged in 3D with double-hexagonal symmetry. Four myosin and eight actin filaments are modeled with periodic boundary conditions to simulate a semi-infinite lattice (**C**) The half-sarcomere is modeled as an array of springs of different stiffness (*k*) for the mysin filament (MF), actin filament (AF), titin (T) and *n* cross-bridges (XB). Each myosin filament contains 60 crowns of three myosin motors (180 cross-bridges per myosin filament). (**D**) By simulation 15 ms of isometric contraction, the steady-state force for each SL is measured. The average force of 50 independent runs with $b = 7.5\ \mu m^{-1}$ is shown here. *Figure from reference* (120).

2.3. Results

2.3.1. Effects of titin stiffness on the isometric force-SL relation

We investigated a range of sarcomere lengths (SL) from 1.5 µm to 3.25 µm for three different values of titin stiffness, and one case without titin. For the "no titin" case, the force of titin (F_T) was set to zero (by setting $a = 0$ in *Eq.* 1). For all other cases, a was set to 260 pN, and b was set to 4, 7.5, or 10 µm^{-1}. The relationship between predicted passive force and SL (Figure 2.2) shows that increasing values of b result in stiffer titin and therefore steeper passive force-SL relations (the force for the "no titin" case is necessarily 0 at all SL values). The passive force-SL relation for $b = 4$ µm^{-1} is in good quantitative agreement with previously published experimental data on isolated skeletal muscle myofibrils from rat psoas (47), shown in Figure 2.3.

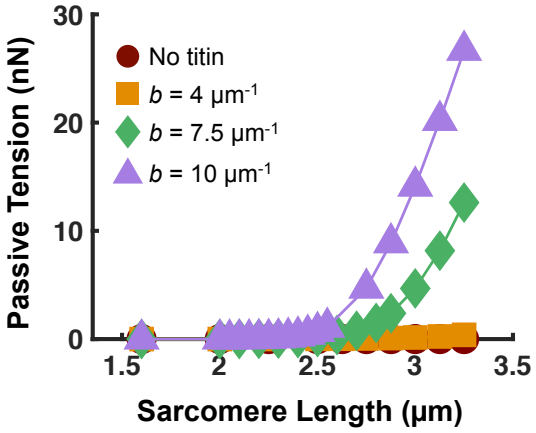

Figure 2.2. Passive tension versus SL for a range of titin stiffness.

The full passive tension-SL relation for the range of titin stiffness explored in the model. For clarity, a y-axis of only 0 to 1 nN is shown in Figure 2 of the main text. *Figure from reference* (120).

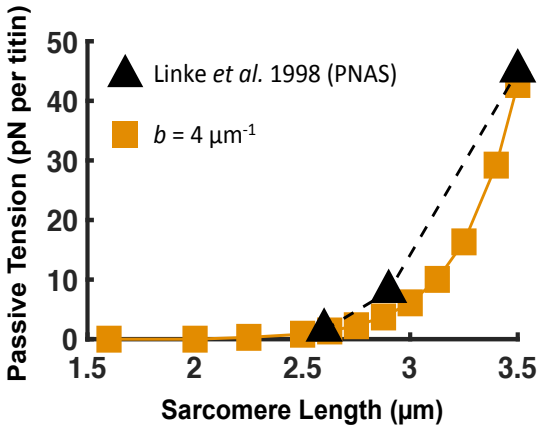

Figure 2.3. Experimental versus computational measures of the passive force-SL relation. Comparison of the passive steady-state stiffness of simulated titin (b = 4 μm^{-1}; gold squares) with demembranated myofibrils from rat psoas (black triangles; data from Linke *et al. 1998 PNAS* (47)). Passive tension per titin molecule was calculated in the model by dividing the total passive tension (Figure 2.2) by the number of titin springs (=24). *Figure from reference* (120).

We then investigated the effects of titin stiffness on the active force-SL relation by simulating isometric contraction and subtracting the passive force values (shown again with zoomed-in y-axis in Figure 2.4 A) from the steady-state force for each condition (Figure 2.4 B). The force-SL relation for the "no titin" condition (filled red circles) is nearly superimposed with the b = 4 μm^{-1} condition. However, for the b = 7.5 μm^{-1} and 10 μm^{-1} conditions (filled green diamonds and purple triangles, respectively), the descending limb of the active force-SL relation is significantly and progressively reduced compared to the "no titin" and b = 4 μm^{-1} cases. Since the descending limb of the force-SL relation of the "no titin" depends only on the extent of myofilament overlap (53), the similarity of the active force-SL relation between the "no titin" case and the b = 4 μm^{-1} case (Figure 2.4 B) suggests minimal effects of compliant realignment of binding sites upon introducing moderately stiff titin into the system.

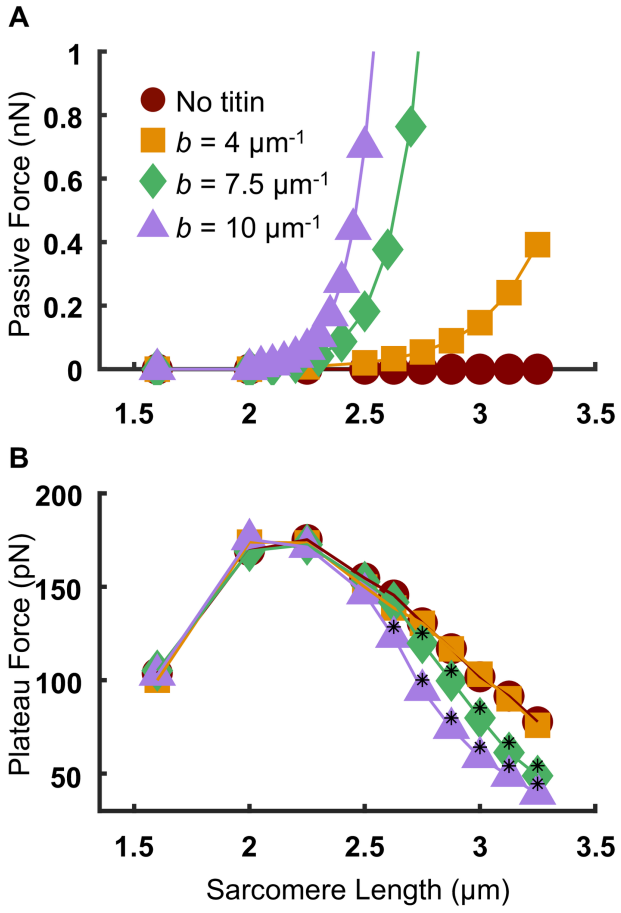

Figure 2.4. Effects of titin stiffness on the passive and active force-SL relations.

(**A**) Passive force-SL relation (average of 50 independent runs). (**B**) Active force-SL relation (with the passive component subtracted). Black asterisks indicate a statistically significant difference from the "no titin" case and the $b = 4\ \mu m^{-1}$ case ($P < 0.05$ using a one-way ANOVA with a Tukey's *post hoc* test of significance). *Figure from reference* (120).

2.3.2. Effects of titin stiffness on isometric contraction efficiency and energetics

To better understand the cause for the reduction of steady-state force along the descending limb with increasing titin stiffness, we investigated the effects of titin stiffness on the force-generating capacity of the cross-bridges. ATP utilization rates of the half-sarcomere were

calculated by monitoring the number of times any one cross-bridge in the system underwent a transition from a strongly bound state to an unbound state. This was monitored for each cross-bridge and summed over all cross-bridges in the half-sarcomere, for 5 ms of simulation time during the plateau region of isometric tetanic force, and averaged from 50 independent trajectories for each condition (SL and titin stiffness). Panel A of Figure 2.5 shows that the SL-dependence of ATP utilization rate is nearly identical for the "no titin" case (red circles) and the $b = 4$ μm^{-1} case (orange squares). However, for very stiff titin ($b = 7.5$ and 10 μm^{-1}), the ATP utilization rate during the plateau of isometric tetanus is significantly increased compared to the "no titin" case for SL > 2.7 μm.

Importantly, the fraction of strongly bound cross-bridges for the same 5 ms of the plateau region of contraction is not different when comparing the "no titin" case to the $b = 4$ and 7.5 μm^{-1} case over the SL range (Figure 2.5 B). However, for $b = 10$ μm^{-1} and SL ≥ 3.0 μm, there are significantly *more* motors in the strongly bound state compared to the "no titin" and the $b = 4$ μm^{-1} cases. This result was somewhat surprising given the significantly reduced force along the descending limb of the active force-SL relation for the $b = 10$ μm^{-1} case (Figure 2.4 B). We attribute this to potentially two factors: (*i*) titin-induced myosin filament strain bringing more motors overlapped with the actin filament at long SL in the stiff titin case compared to more compliant titin at the same SL (Figure 2.6), and (*ii*) more compliant realignment of binding sites (Daniel et al. 1998) at long SL with stiff titin compared to more compliant titin.

Finally, by relating the force generated to the amount of ATP used over 5 ms during the plateau of isometric tetanus, the contraction efficiency (as measured by the ratio of force to ATPase rate) in the half-sarcomere was determined for each case. Figure 2.5 C shows that, similar to the active force (Figure 2.4 B), the contraction efficiency significantly decreases for SL > ~ 2.7 μm

for stiff titin compared to the b = 4 μm^{-1} and "no titin" cases. Despite these changes in ATP consumption, we did not observe any significant SL-dependent or titin-dependent changes in the rate of force development (Figure 2.7).

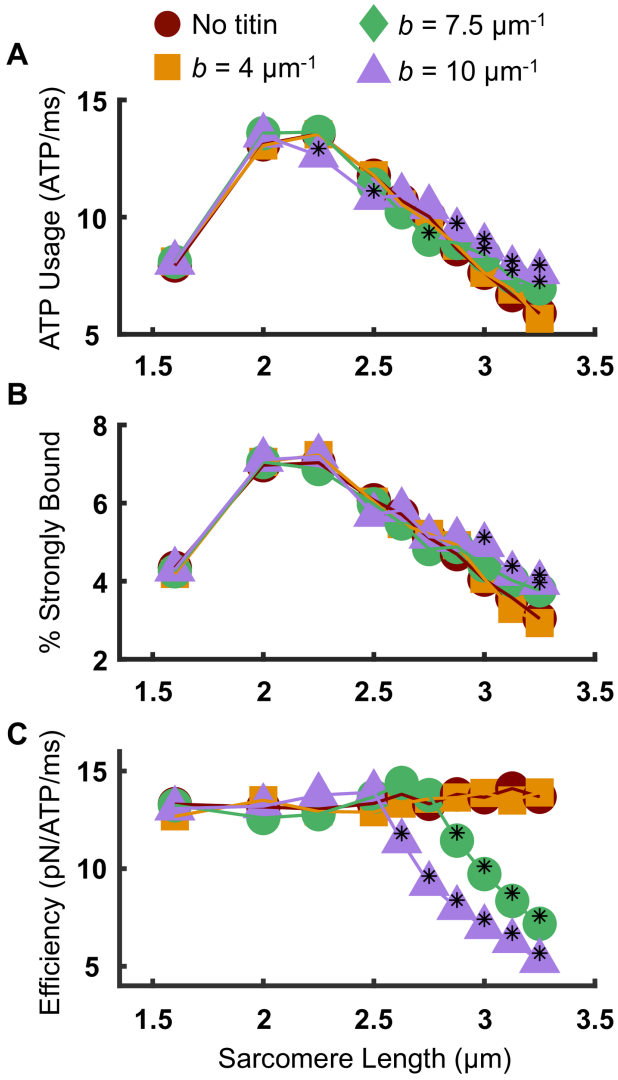

Figure 2.5. Effects of titin stiffness on cross-bridge mechanics and energetics.

(**A**) ATP usage was quantified by monitoring the number of transitions of each cross-bridge from a strongly bound state to an unbound state. Values reported here reflect the average of the entire cross-bridge ensemble during the plateau of isometric contraction. Stiff titin increases the amount of ATP at long SL compared with the "no titin" case. (**B**) Stiff titin does not affect the % of cross-bridges in the strongly bound state at the plateau of force generation, until SL = 3.0 μm, at which

point there are significantly more motors bound for $b = 10$ μm^{-1} compared with the "no titin" case and the $b = 4$ μm^{-1} case. (**C**) Despite the increase in strongly bound cross-bridges, there is a significant reduction in contraction efficiency as measured by the force per ATP during a period of the plateau of isometric contraction. Black asterisks indicate a statistically significant difference from both the "no titin" case and the $b = 4$ μm^{-1} case ($P < 0.05$ using a one-way ANOVA with a Tukey's post hoc test of significance). *Figure from reference* (120).

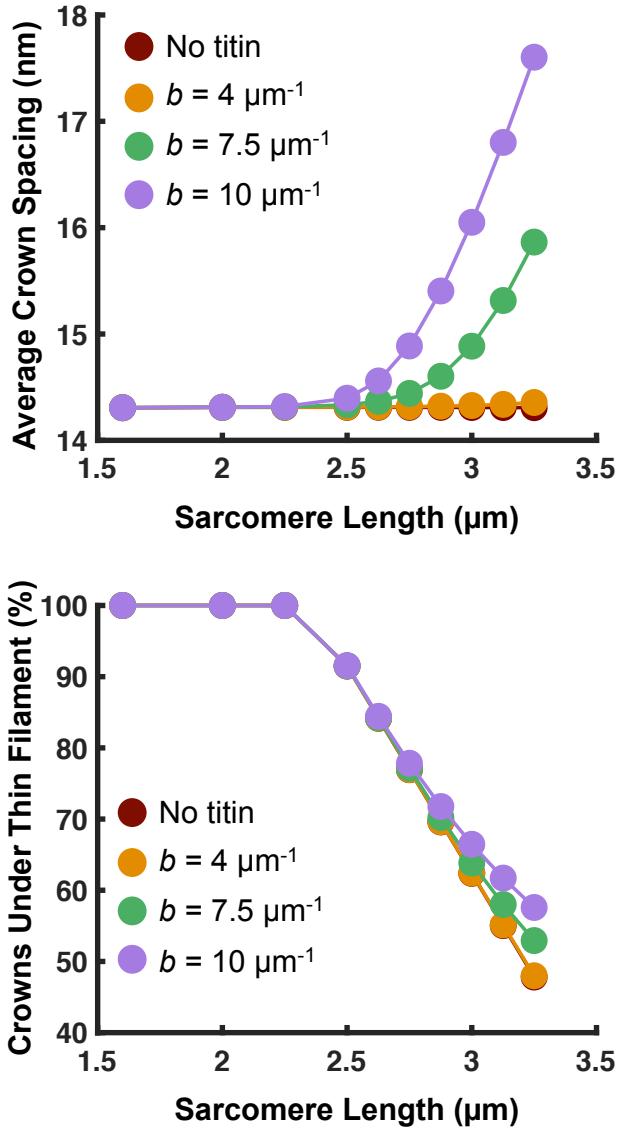

Figure 2.6. Effects of titin stiffness on myofilaments.

Thick filament strain translates to changes in the average crown spacing (axial distance between myosin crowns along each thick filament). As titin stiffness and SL increases, the average distance

between myosin crowns increases (top panel). This titin-induced thick filament strain causes more myosin crowns to be overlapped by the thin filament at long SL (> ~3.0 µm) for stiffer titin (b = 7.5 µm^{-1} & 10 µm^{-1}) compared to the "no titin" and b = 4 µm^{-1} case (bottom panel). This causes in increase in myosin binding and ATP usage in these cases (Figure 3 in the main text) despite a reduction in force (Figure 2 in the main text). *Figure from reference* (120).

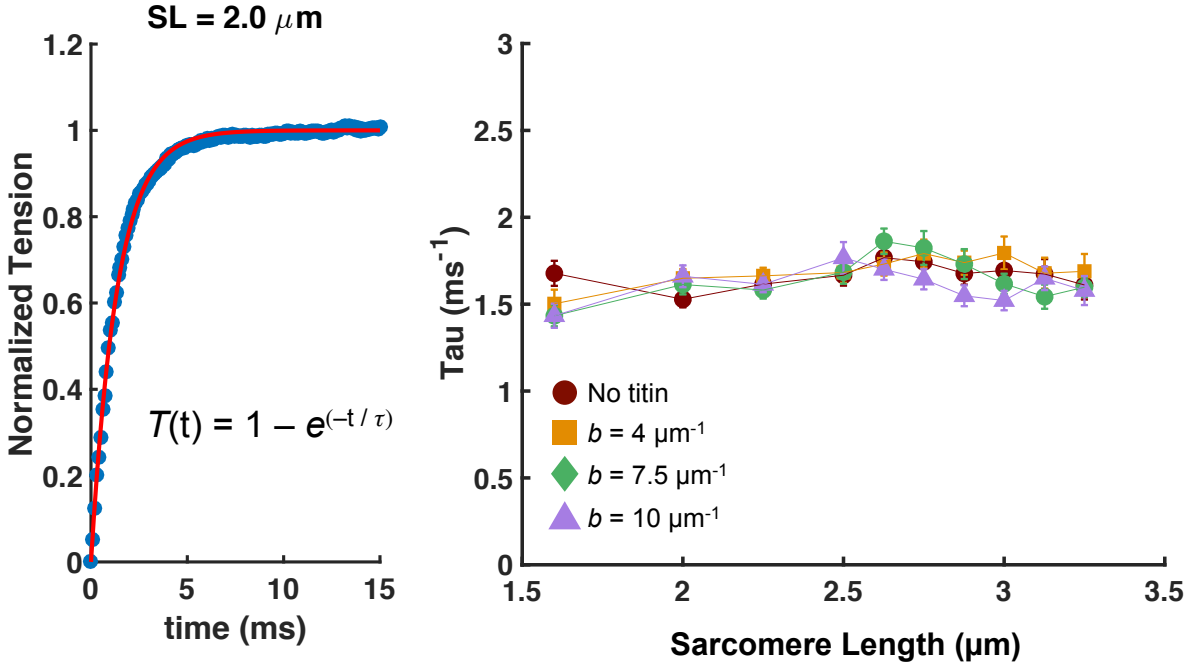

Figure 2.7. Effects of titin stiffness on rate of isometric force development.

The right panel shows a sample normalized tetanus trace for SL 2.0 µm without titin (blue circles) that has been fitted with the equation in the inset (red line). The value of tau was determined this way for each SL and titin stiffness investigated in the current work (left panel). Error bars reperesent standard error of the mean for 50 independent fits for each case. *Figure from reference* (120).

2.4. Discussion & Conclusions

The work presented in this chapter represents the first spatially explicit and multi-filament model of the half-sarcomere that relates the effects of increased titin stiffness to the mechanics and energetics of muscle contraction. We found that increased titin stiffness leads to reduced active force along the descending limb of the active force-SL relation (Figure 2.4 B). That force reduction corresponds with lower levels of contractile efficiencies in the SL range above about 2.7 μm (Figure 2.5 C). Moreover, both the reduced force and lower efficiency arose despite a significant increase in strongly bound cross-bridges for the same SL range (Figure 2.5 B).

Taken together, our results suggest that despite more motors bound to actin along the descending limb when titin is stiffer, the force-generating capacity of the motors is reduced as titin stiffness increases. We speculate that there is likely an elastic energy limit in the myosin filament above which cross-bridges become less efficient in producing force in the isometric condition. That is, our model predicts that increased titin stiffness limits the energy transfer from cross-bridges to the M-line by imposing significant strain in the myosin filament backbone. It is this titin-induced myosin filament strain that cross-bridges must have sufficient energy to deform in order to produce active force in the isometric condition.

Relying on the notion that energy (not force) is conserved, Figure 2.8 illustrates this point by depicting the elastic potential energy versus strain relation of the myosin filament. The elastic energy stored in each myosin filament was calculated using the effective stiffness of the entire myosin filament (k_{MF}) and the amount of strain (ΔL_{MF}) at the steady-state force for each SL. For compliant titin (b = 4 μm^{-1}), the amount of titin-based myosin filament strain (and therefore the amount of elastic energy stored in the myosin filament) at long SL (> 3 μm) is on the same order of magnitude as the collective energy delivered by the cross-bridges during tetanic contraction at

that SL (left inset of Figure 4). However, for very stiff titin (b = 10 μm^{-1}) at the same SL, the amount of titin-based strain imposed in the myosin filament results in orders-of-magnitude increases in elastic energy stored in the myosin filament backbone (right inset of Figure 2.8). Consequently, since the collective amount of cross-bridge energy able to be produced during contraction and transferred to the myosin filament is constant for a given SL, there is very little additional myosin filament strain (and therefore, force) delivered by the cross-bridges when titin has already delivered significant elastic potential energy to the myosin filament prior to activation at long SL. Thus, there is a point in our model (albeit outside the range of physiological titin stiffness and SL) where titin delivers enough elastic energy to the myosin filament backbone to render the added energy delivered by the cross-bridges insignificant.

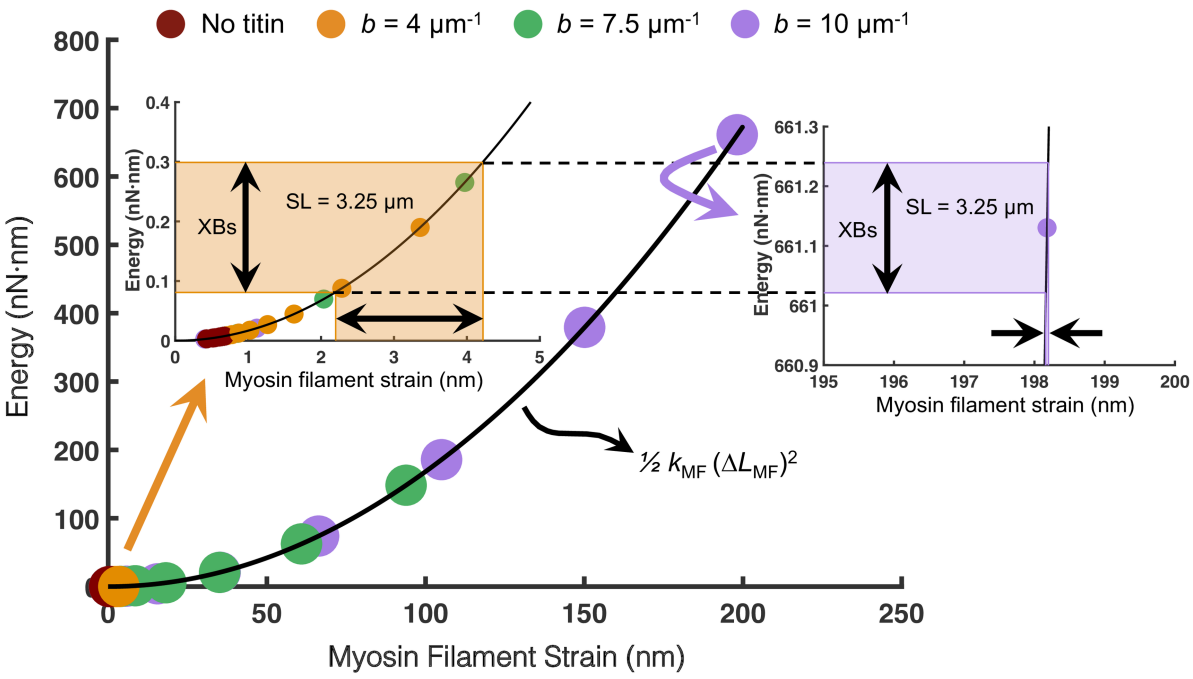

Figure 2.8. The predicted elastic potential energy versus strain relation of the myosin filament.

With stiffer titin and longer SL, cross-bridges produce less myosin filament strain thereby reducing force output and contraction efficiency. The elastic potential energy was calculated (using the

equation in the inset) for the myosin filament based on the amount of myosin filament strain imposed by the cross-bridges (XBs) under isometric maximum tension or by titin prior to activation. Each circle on the curve represents the amount of titin-based strain for each SL and titin stiffness. For more compliant titin (b = 4 μm^{-1}), the amount of titin-based strain at SL 3.25 μm is on the same order of magnitude as that delivered by the XBs (left inset). However, for very stiff titin (b = 10 μm^{-1}), the same amount of elastic energy delivered to the myosin filament from the XBs results in < 1 nm of strain. As titin delivers more strain to the myosin filament, the XBs become less effective in generating force. *Figure from reference* (120).

The inclusion of titin in this model provides a platform for many future investigations into the role of titin elasticity in regulating muscle function. Future iterations of the model will explore biophysical phenomena known to exist in the sarcomere. For example, it is known that there are significant geometrical dynamics (*e.g.* changes in SL and lattice spacing) during contraction, and these dynamics are not included in the current work. To investigate such lattice dynamics would require fairly extensive changes in the model architecture, but would represent an interesting avenue for future work, particularly given subtle lattice spacing changes that may arise during contraction (121). Additionally, recent experimental evidence has emerged demonstrating that both skeletal (72) and cardiac muscle (77) exhibit a mechanosensing-based (strain-dependent) mechanism of myosin filament activation in which titin may play a key role (42, 43, 74). It is also known that titin interacts in the I-band with actin, which may change where it is structurally anchored (122, 123). It has also been suggested that the I-band region of titin has calcium-dependent stiffness such that it may become stiffer upon activation ((124) and references therein), which can also be investigated with this model in the future.

Other models also predict that there may be appreciable and important torsional dynamics in the actin filaments during contraction that may influence the effective stiffness of titin if titin is

strongly interacting with actin in the I-band (102, 103). We suspect that interaction with axial tension and cross-bridge force generation would be similar to our results. That said, our current model lacks these types of molecular interactions, and therefore may miss interesting and important cooperative mechanisms occurring between titin, myosin, and actin.

Additionally, little is understood about how the mechanics of titin and the sarcomere determine whole muscle function, and a classic metric of whole muscle performance is the work done during cyclical length changes (a.k.a. work loop (125)). Our model is well-poised to study the effects of titin stiffness on the ability of sarcomeres to produce positive, zero, or negative work, and assess how titin influences a whole muscle's ability to behave as a motor, spring, brake, or strut (for a review, see (126)). Based on a recent experimental results (127), it is likely that increasing titin stiffness results in a reduction in negative work production, and we intend to investigate this via future iterations of the model presented here.

It is interesting to note the similarities between the "no titin" case and the $b = 4\ \mu m^{-1}$ case in the results we present here. We anticipate that this case will take on a more prominent role in future studies in which additional lattice dynamics and thick filament mechanosensing-based myosin activation are included.

Lastly, there is an emerging theme in the experimental literature in which titin is considered a major player in muscle function in general (105, 127) as well as in muscular disorders (128). With titin-truncating mutations being one of the leading causes of dilated cardiomyopathy (129), a deadly genetic cardiac disorder without current treatment options other than cardiac transplantation, there is a pressing need to understand how titin affects muscle contractility. In fact, recent work using a transgenic murine model with truncated (and stiffer) titin leads to reduced myosin filament lengths, and produces similar trends in decreased force along the descending limb

of the force-SL relation as presented here (105). The model we describe here presents an exciting new approach to specifically probe the mechanical properties of titin and examine the effects on contractility *in silico*. This ability represents a powerful new technique to predict how certain myopathy-associated titin mutations may drive pathological behavior *in vivo*.

Chapter 3

Titin is a dynamic I-band spring with a stiffness that is tuned to the length of the active muscle sarcomere

Abstract

Force in the sarcomere, the 2 μm long structural unit of skeletal and cardiac muscles, is generated by the action of two antiparallel arrays of myosin motors emerging from the thick filament and pulling the nearby actin filaments toward the center of the sarcomere. The ordered configuration on different hierarchical levels makes muscle output macroscopic by the summation of either the shortening by the serial arrangement of sarcomeres or the force by the packing of the myofilaments over the cell cross-section. The control and efficiency of this multiscale machine is attained by the co-assembly of contractile proteins with regulatory and cytoskeletal proteins. Among them, the gigantic protein titin connects the tip of thick filament with the sarcomere end, working as an I-band spring that accounts for the rise of passive force with sarcomere length (SL). Using nanometer-microsecond mechanics in single fibers from tibialis anterior muscle of *R. esculenta* contracting at SL ranging 2.15-3.1 μm (temperature 4°C), we find that the half-sarcomere compliance is influenced by an I-band spring with a stiffness that rises with SL and at SL > 2.7 μm attains a constant maximum value of ~6 pN/nm per thick filament, two orders of magnitude larger than that expected from passive force. We conclude that titin is a dynamic I-band spring made by an undamped elastic element in series with damped elastic elements (the immunoglobulin-like domains) that adapt titin length to SL with kinetics that enable titin to play a fundamental role against development of sarcomere length non-homogeneity.

Significance Statement

This paper gives a novel quantitative definition of the role of the various components of the half-sarcomere, the functional unit of skeletal and cardiac muscle in which force and movement are generated by an array of myosin motors on the thick filament during cyclical ATP- driven interactions with the nearby overlapping actin filaments. We find that, when the length of muscle sarcomere is increased above 2.5 μm, so that the length of the region of the actin filament not overlapping with the myosin filament (the I-band region) is larger than 0.45 μm, an I-band titin-based dynamic spring emerges that integrates with the myosin-based force generators in the A-band to damp the effects of different forces among sarcomeres in series.

3.1. Introduction

The force of striated muscle is generated at the level of its structural unit, the sarcomere, by ATP-driven cyclical interactions between myosin motors extending from the thick filament and their binding sites on the actin-containing thin filament (130, 131). In each half-sarcomere (hs) the myosin motors are mechanically coupled as parallel force generators via their filament attachment, and the collective motor formed by the array of myosin motors, the interdigitating actin filaments and the other cytoskeleton and regulatory proteins is the basic functional unit of muscle (Figure 3.1A). The emergent properties of the array of motors in the half-sarcomere allow the activated muscle to generate a steady isometric force (T_0) and, under a constant load lower than T_0 (isotonic contraction), to shorten at a constant velocity which increases as load decreases (132). The maximum power is delivered at ~1/3 T_0 with a limited increase (3-4 times) in the rates of both

ATP-driven detachment-attachment of the motors and energy (heat + work) liberation (133). Under a load above T_0 (eccentric contraction) the myosin motors and the meshwork of cytoskeleton proteins in the half-sarcomere act as a brake (134) that efficiently resists lengthening with reduced metabolic cost (133, 135). The braking response may also play a fundamental role in any sort of contraction in which it contributes to force equilibration among in-series sarcomeres, and, in this way, prevents the development of sarcomere length inhomogeneity. In this respect, it is likely that a role in preserving sarcomere structure during high-load contractions is played by the cytoskeletal protein titin (40, 136, 137). Titin spans the entire half-sarcomere, connecting the Z-line at the end of the sarcomere with the tip of the myosin filament and then running, bound to the surface of the thick filament, up to the M-line at the center of the sarcomere (Figure 3.1A). In a single muscle cell at rest, titin is the I-band spring responsible for the majority of force in response to lengthening of the sarcomeres, but its role in the active contraction remains controversial.

Fast sarcomere-level mechanics and X-ray diffraction in single fibers from frog muscle represent a powerful tool for *in situ* definition of the elastic properties and the active performance of the myosin motor (25, 138–140) and its regulation (72), but so far have not provided a similar quantitative description of titin function in active muscle. The presence of an additional elastic element in parallel with myosin motors in the half-sarcomere emerged from stiffness measurements with either large stretches (141, 142) or small length perturbations (143, 144) imposed early following the stimulation. This finding was confirmed in both intact (145) and skinned (146, 147) mammalian muscle preparations. All of these works, however, have not quantitatively defined titin function in active muscle, due to the limits of the protocols used. First of all, the response to large stretches may be complicated by both the rapid detachment and

reattachment of myosin motors (148) and the rise of sarcomere inhomogeneity with the consequent inter-sarcomere dynamics during recovery after the stretch end (119). Secondly, stiffness measurements by means of small length perturbations in the region of maximum filament overlap are limited to a sarcomere length (SL), ~2.15 μm, within which titin is slack and its mechanical contribution negligible, while the contribution of parallel elements in the A-band (Figure 3.1A), such as weakly bound myosin motors (149) or inter-filamentary links from the accessory protein myosin binding protein C (MyBP-C) (30, 150–152), may be more relevant.

Here, small 4 kHz length oscillations are used to measure the instantaneous half-sarcomere compliance (C_{hs}) during isometric force development in single fibers of *Rana esculenta* at 4°C in the SL range 2.15-3.1 μm. We find that early during force development, when the number of actin-attached motors is low and, consequently, C_{hs} is dominated by the parallel elastic element, the increase in SL causes a decrease in C_{hs}. This result can be explained only by an additional elastic element in the I-band, which does not scale its compliance with SL. Fitting the C_{hs}–T relations at each SL with a mathematical model of the half-sarcomere that integrates Ford *et al.* model (109) including a titin-like I-band spring (153), we provide quantitative estimates of the compliance of the I-band spring as a function of SL. We demonstrate that at SL >2.7 μm the I-band spring stiffness attains a constant maximum value of ~6 pN/nm per thick filament, which is two orders of magnitude larger than that estimated from passive force. We conclude that titin is a dynamic spring that adapts its length to the width of the I-band and gives a substantial force contribution against the development of sarcomere non-homogeneity during contraction.

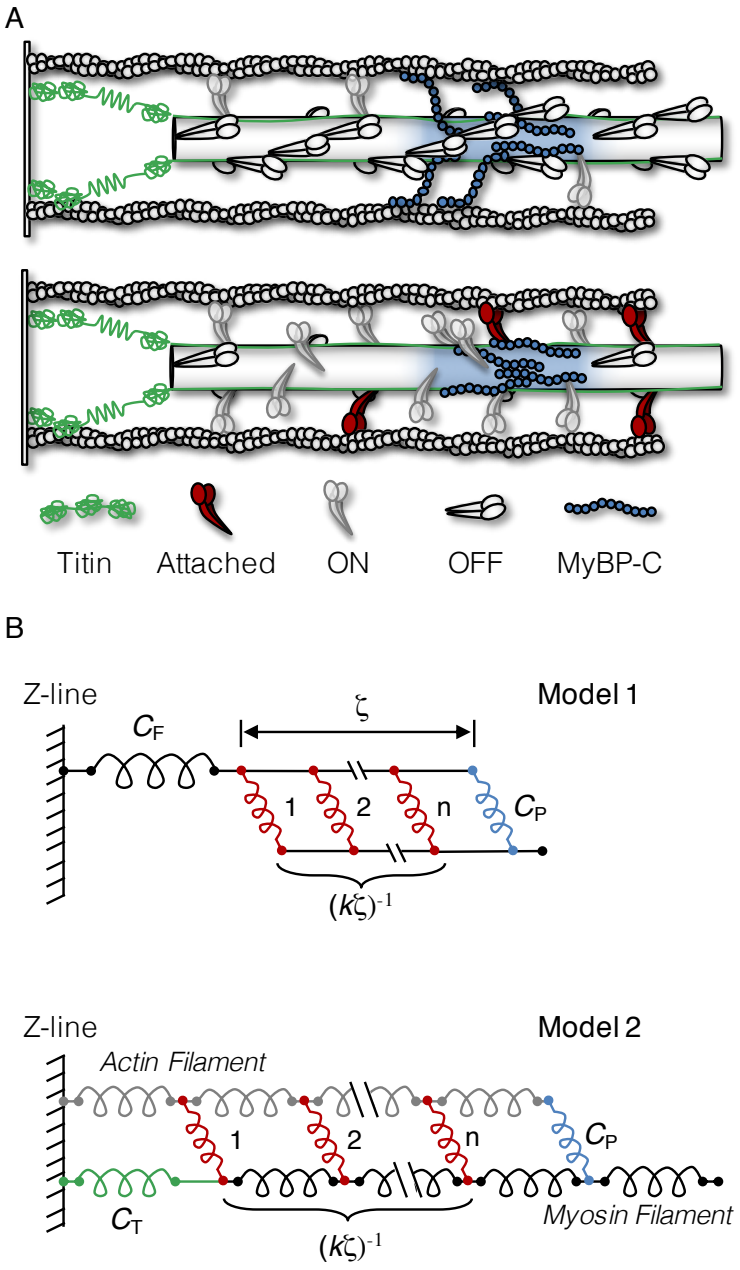

Figure 3.1. Schematic of various myofilament proteins that act as elastic elements in the half-sarcomere.

(**A**) Schematic of the half-sarcomere with the main constituent proteins. At rest (upper panel) the majority of the myosin motors lie on the surface of the thick filament backbone (light gray) and a few constitutively ON motors (gray) could be weakly bound. These motors, together with the Myosin Binding Protein-C (MyBP-C, blue) in the C-zone of the thick filament (blue shaded region) early during contraction and force development could represent an additional elastic

element in parallel to force generating attached myosin motors. During contraction (lower panel), the force-generating myosin motors (red) give the relevant contribution to the half-sarcomere stiffness in the A-band. Titin (green) constitutes an I-band spring that connects the Z-line to the tip of the thick filament. (**B**) Mechanical models of the half-sarcomere. In Model 1 the equivalent filament compliance (C_f) is in series with the A-band cross-links made by the parallel between the array of myosin motors (red) with compliance $(k\zeta)^{-1}$ and the additional element (blue) with compliance C_P. In Model 2 the compliances of myosin (black) and actin (gray) filaments are separated and distributed and another additional element with compliance C_T (green) connects the Z-line to thick filament at the node with the last attached motor.

3.2. Methods

3.2.1. Single intact skeletal muscle fiber preparation

Single intact skeletal muscle fibers were dissected from the lateral head of the tibialis anterior muscle of frogs (*Rana esculenta*) at room temperature. Frogs were sacrificed via decapitation followed by immediate destruction of the brain and spinal chord in agreement with the Italian regulation on animal experimentation (Authorization 956/2015-PR in compliance with Decreto Legislativo 26/2014 and with EU directive 2010/63). Upon isolation of a single intact fiber, custom aluminum T-clips were attached to the tendon as close as possible to the fiber end to minimize the contribution of tendon compliance in series with the fiber. As depicted in Figure 3.2, the fiber was mounted between a capacitance-based force transducer (resonance frequency of ~50 kHz) and a length-controlling loudspeaker motor; the hs length change (L) in a fibre segment 700–1000 μm long, selected near the force transducer end, was measured by a striation follower (Lombardi & Piazzesi, 1990, and references therein). The composition of the physiological solution bathing the fiber was (mM): 1.8 $CaCl_2$, 115 NaCl, 2.5 KCl, and 3 phosphate buffer (pH

~7.0). Experiments were conducted at 4°C with a total of 8 fibers with cross-sectional area of 9300 ± 2300 μm^2 (mean ± SD). Mean isometric force was 141.7 ± 6.6 kPa (mean ± SEM) at SL = 2.15 μm.

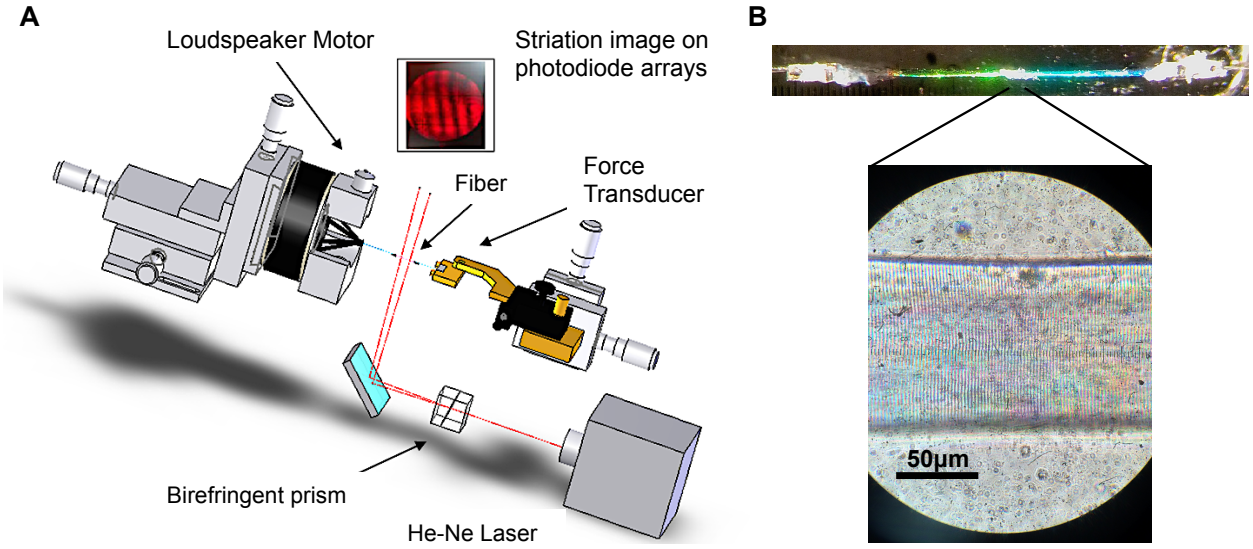

Figure 3.2. Apparatus used to measure the half-sarcomere elasticity during isometric contraction.

(**A**) The loudspeaker motor and force transducers are custom built in-house at the University of Florence (154), as is the striation follower, which uses a split laser to image two separate locations in the muscle fiber simultaneously (155). The images of the striations are shown on two independent photodiode arrays that monitor the change in luminescence to count the number of sarcomeres passing through the region between the two laser spots. Knowing the average sarcomere length in the fiber and the distance between the two laser spots gives a real-time measurement of the change in sarcomere length with microsecond and nanometer resolution. (**B**) A representative image of a single intact skeletal muscle fiber mounted between the force transducer and length-controller with custom aluminum T-clips. The sarcomere length was measured directly using a 40X wet objective lens on a stereomicroscope with a calibrated reticle in the 25X eyepiece. The magnified image in panel B (taken with a 10X eyepiece) clearly shows the striations in the intact fiber.

3.2.2. Experimental protocol & stiffness measurements

The fibre length at rest (l_0) was set at a sarcomere length of 2.15 μm, as measured with a 40x water immersion objective and a 25x eyepiece. Different sarcomere lengths in the range 2.15-3.1 μm were set by increasing the fibre length with the micromanipulator of the motor until the desired SL was reached. Half-sarcomere (hs) stiffness was measured during the rise of isometric tetanus (25, 144, 156) at different SL set in a random sequence (with the exception of SL 3.1, which was saved for the end of the experiment due to higher risk of fiber damage). Between each SL change, the protocol was repeated at SL 2.15 μm to ensure there was no rundown in force during the experiment and to check reproducibility of the data at that SL. Fibers were field-stimulated with pulses of alternating polarity and 1.5-fold the threshold voltage at the frequency (20-25 Hz) necessary to obtain a fused tetanus. Duration of tetanic stimulation was 350 ms and tetani were separated by 4-minute intervals. When going from long to short SL, fibers were stimulated with two twitches to quickly "reset" the sarcomere length before the next tetanus. 4 kHz length oscillations were imposed on the stimulated fiber (amplitude of ~2 nm/hs peak to peak) during isometric force development for the range of sarcomere lengths between 2.15 and 3.1 μm (Figure 3.1). The stiffness was estimated by calculating the Fourier transform of the oscillations to extract the in-phase and out-of-phase components and using the in-phase component to determine the ratio of the change in hs length to the corresponding change in force. Previous work (Fig. 2 in Ref. (144)) demonstrated that in the region of sarcomeres sampled by the striation follower, for forces >0.05 T_0, the 4 kHz oscillation probes an almost purely elastic response as the out-of phase component is negligible.

3.2.3. Mathematical modeling & analysis

As previously described (Fusi *et al.* 2014), the compliance of the half-sarcomere (C_{hs}) during tetanic contraction can be described by a simple 'linear' mechanical model (Model S1, depicted in Fig. 3.3 A). The dependence of C_{hs} on force (T) is a product of the relationship shown in Eq. 3.1 below.

$$C_{hs} = C_F + 1/(k\zeta) \quad \text{(Eq. 3.1)}$$

where $k\zeta$ is the stiffness of the array of myosin motors and is proportional to T, with a constant strain (s) in the array of myosin motors (that is, $k\zeta = T/s$). As shown in Fig 3.3 B, Model S1 fails to fit the experimental data at low forces ($T < \sim 0.3T_0$).

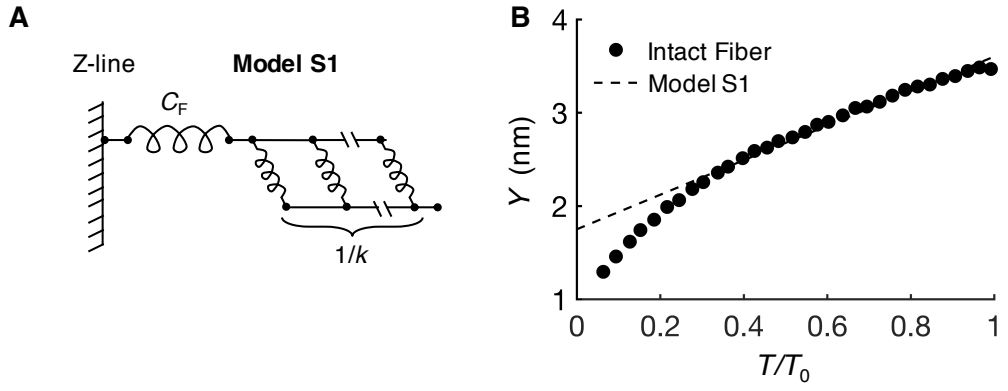

Figure 3.3. Simple mechanical model of the half-sarcomere compliance.

(**A**) Schematic of the simple 'linear' model (Model S1), the half-sarcomere is described as a parallel array of cross-bridges with a collective compliance of $(k\zeta)^{-1}$ in series with the total effective filament compliance (C_F). (**B**) Filled circles represent the measured half-sarcomere strain (Y) as a function of force (T expressed in units of maximum tetanic force, T_0) calculated from the C_{hs} values of Figure 3.5C in the main text. The dashed line represents the fit of the linear portion of the data ($T > 0.3\ T_0$) with the Eq. S1. (Figure modified from Fusi *et al.* 2014.)

To integrate the presence of the elastic element in parallel with the cross-bridges in the formalism developed in Pertici *et al*. 2018 (153) to also account for the I-band spring, it is convenient to convert the compliance C_p of this parallel element in terms of its stiffness per unit length $k_p=1/(C_p\zeta)$, where ζ is the length of the overlap between actin filament and the cross-bridges array. This relation is valid if the parallel elasticity expressed by C_p or k_p is uniformly distributed along the cross-bridge array, as it should be if it is attributed to weakly bound cross-bridges (see main text). In this case, the overall stiffness per unit length of the region covered by the cross-bridge array is expressed by k_0T+k_p, where k_0 is the stiffness per unit length of the force-generating cross-bridges at the plateau of the isometric tetanus, where their number is maximal, and T is the force in units of the maximal isometric force at a given SL and ζ, that scales in parallel with the number of attached force-generating cross-bridges. Substituting k_0T+k_p for k_c in Eq. 23 of Pertici *et al*. 2018 we obtain Eq. 3.2 shown below that accounts for both the elastic element parallel to the force-generating cross-bridges and the I-band spring. Eq. 3.2 expresses the half-sarcomere compliance as represented in Model 2, depicted in Figure 3.1B of the main text. See Pertici *et al.* 2018 for a detailed derivation and numerical analysis of the equation.

$$C_{\mathrm{hs}} = c_{\mathrm{M}}(l_{\mathrm{M}} - \zeta) + \frac{c_{\mathrm{A}}c_{\mathrm{T}}}{c_{\mathrm{A}} + c_{\mathrm{T}}}(l_{\mathrm{A}} - \zeta) + \frac{c_{\mathrm{A}}c_{\mathrm{M}}}{c_{\mathrm{A}} + c_{\mathrm{M}}}\zeta + \frac{\frac{{c_{\mathrm{T}}}^2}{c_{\mathrm{A}} + c_{\mathrm{T}}}(l_{\mathrm{A}} - \zeta) + \frac{{c_{\mathrm{M}}}^2}{c_{\mathrm{A}} + c_{\mathrm{M}}}\zeta + \frac{(k_0\ T + k_{\mathrm{P}})\zeta^2(l_{\mathrm{A}} - \zeta)}{12(c_{\mathrm{A}} + c_{\mathrm{T}})}\left\{{c_{\mathrm{T}}}^2(c_{\mathrm{M}} + c_{\mathrm{A}}) + \frac{3[c_{\mathrm{T}}(c_{\mathrm{M}} - c_{\mathrm{A}}) + 2c_{\mathrm{A}}c_{\mathrm{M}}]^2}{c_{\mathrm{M}} + c_{\mathrm{A}}}\right\}}{1 + \frac{(k_0\ T + k_{\mathrm{P}})\zeta}{3}[\zeta(c_{\mathrm{A}} + c_{\mathrm{M}}) + 3(l_{\mathrm{A}} - \zeta)(c_{\mathrm{A}} + c_{\mathrm{T}})]}$$

Eq. 3.2.

Abbreviations

T = Force during tetanic contraction (expressed in units of maximum isometric force, T_0)

C_{hs} = Compliance of the half-sarcomere (nm·T_0^{-1})

c_{M} = Compliance of the myosin filament per unit length (nm·T_0^{-1}·µm^{-1})

c_{A} = Compliance of the actin filament per unit length (nm·T_0^{-1}·µm^{-1})

c_{T} = Compliance of the titin filament per unit length (nm·T_0^{-1}·µm^{-1})

l_{M} = Length of the myosin filament (µm)

l_{A} = Length of the actin filament (µm)

ζ = Length of the filament overlap region (µm)

k_0 = Stiffness of the array of cross-bridges at the maximal isometric force (T_0·nm^{-1}·µm^{-1})

k_{P} = Stiffness of the additional parallel elastic element (T_0·nm^{-1}·µm^{-1})

Upon fitting this equation to the C_{hs}-T relations at SL 2.15 µm, the scaled value of C_{CB} (= $1/k_{\mathrm{CB}}$) determined at SL 2.15 µm was used to fit the equation shown above at all other SL. We used values of 14.3 nm/MPa/µm and 17.5 nm/MPa/µm the compliance of the actin and myosin filaments, respectively (157), and initial values of 0.8 µm and 1 µm for l_{M} and l_{A}, respectively (109). Thus, the only free parameter of Model 2 for SL > 2.15 µm was the compliance of the I-band spring, C_{T}.

3.2.4. Data analysis and statistics

The C_{hs}–T relations at each SL were fit using either Model 1 (Eq. 3.3) or Model 2 (Eq. 3.2) (see the main text for details). Fitting the model to the experimental C_{hs}–T relations was done using the 'fit' package in MATLAB software (2018a version, The MathWorks, Inc., Natick, MA). Errors for fit parameters were determined by 95% confidence intervals around each parameter from the fitting. Experimental stiffness data were binned into force groups of $0.03T_0$ for each SL and averaged, and errors were calculated as the standard error of the mean for each force group.

3.2.5. Spatially explicit computational model

The main components of the computational model used in this work were developed and used extensively by our group previously (114), and was recently modified to include an adjustable I-band spring (120). Briefly, the model consists of four myosin filaments and eight actin filaments arranged in a double-hexagonal lattice in three dimensions. Each cross-bridge is modeled as a two-spring system consisting of a torsional and a linear element (113). Myosin and actin filaments consist of linear springs serially linked between each node of cross-bridge crowns. The stiffness of the springs for the myosin and actin filaments were set to be the same as the experimental values described above (157), and the lattice spacing (*i.e.* radial face-to-face distance between the myosin and actin filaments) was fixed at 14 nm. Force is generated in the half-sarcomere using Monte Carlo methods to probabilistically determine the cross-bridge binging rates and kinetics (113, 114, 116).

Six titin springs attach to each of the four myosin filaments, each of which span the length of the I-band and anchor to the Z-line at the actin filament-Z-line junction. Thus, each titin spring makes an angle, θ, with the myosin filament that is equal to the arctangent of the ratio of the

filament lattice spacing (radial myosin-to-actin filament distance) and the length of the I-band. Similar to other models (118, 119), the total force exerted by each titin spring (F_T) is modeled as an exponential dependence on length change of titin (ΔL), as $F_T = a \cdot \exp(b \cdot \Delta L)$, where a and b are tunable parameters. For the "no titin" case, a was set to 0 pN, whereas for all other cases, a was arbitrarily fixed at 260 pN. The parameter b was varied across a range of 4-10 μm^{-1}. Using this value of a and range of b resulted in passive force-SL relations that span the range of published estimates for single titin molecules (47). The axial and radial components of F_T were taken as $F_T \cdot \cos(\theta)$ and $F_T \cdot \sin(\theta)$, respectively.

The half-sarcomere compliance (C_{hs}) was determined in the simulation by making a series of 10 small sarcomere length increases, each of 0.2 nm, and determining the resulting change in force. This was done after each timestep in the simulated isometric tetanus, which was fixed at 0.1 ms for a 15 ms contraction. This was repeated for SL = 2.15 μm and SL 2.9 μm (with the same lattice spacing for each SL). Thus, this measurement provides an *in-silico* analogue of the C_{hs}-T relation measurement made experimentally.

3.3. Results

3.3.1. An elastic element in parallel to myosin motors adds to active half-sarcomere elasticity.

During an isometric tetanus the force (T) rises to the isometric plateau force in proportion to the number of actin-attached motors in each half-sarcomere (hs) (158). The half-sarcomere stiffness, however, does not rise in proportion to force (and number of attached motors), due to the substantial contribution (about 50%) of the myofilament compliance to the half-sarcomere compliance (157, 159–161). A simple mechanical model of the half-sarcomere (Model S1, Figure

3.3A) assumes that the total half-sarcomere strain (Y) depends on T (Figure 3.3B) according to the equation $Y = T \cdot C_F + s$, where s, the ordinate intercept, is the strain in the array of myosin motors and C_F, the slope of the relation, is the combined equivalent compliance of the myosin and actin filaments (141, 142, 144, 158). Accordingly, the half-sarcomere compliance (C_{hs}) can be calculated as the sum of the equivalent compliances of the filaments and that of the array of myosin motors [$(k\zeta)^{-1} = s/T$], where k is the stiffness per unit length of the array of the attached motors and ζ is the extent of overlap of thin filament with the motor array (see Eq. 3.1). The presence of an additional elastic element functionally in parallel with myosin motors (Model 1 in Figure 3.1B, blue spring) causes the downward shift in the observed Y-T relation at low forces (Figure 3.3B; see also Ref. (144)). According to Model 1, C_{hs} can be interpreted as the sum of the filament compliance, C_F, and the compliance resulting from the parallel arrangement of the array of force-generating motors and the additional elastic element with compliance C_P:

$$C_{hs} = C_F + \frac{C_P}{1 + C_P \cdot k \cdot \zeta} = C_F + \frac{C_P \cdot s}{s + C_P \cdot T} \qquad (Eq.\ 3.3)$$

Small 4 kHz oscillations are superimposed on the fiber throughout the development of the isometric tetanus to determine the C_{hs}–T relations at SL 2.15 μm, at which there is full filament overlap ζ_0 (= 0.7 μm) and at different longer SL (2.15 + x μm), at which the overlap decreases according to the expression $\zeta = \zeta_0 - x/2$. The corresponding tetanic plateau force ($T_{0,x}$) decreases with respect to that developed at 2.15 μm (T_0) in proportion to the reduction of ζ (that is, $T_{0,x} = T_0 \cdot \zeta/\zeta_0$). In Figure 3.4 A and B, sample records from one of the 8 fibers used in these experiments are shown at SL 2.15 (black traces) and 2.7 μm (grey traces). The average C_{hs}–T relations at SL 2.15 μm, 2.5 μm, 2.7 μm and 2.9 μm are shown by filled circles in Figure 3.4 C, D, E, and F, respectively. The relevant effect of the increase in SL on the C_{hs}–T relation occurs at

the initial low forces. In fact, when C_{hs} determined at 0.1 T_0 (~15 kPa) ($C_{hs,0.1}$) is plotted versus SL (Figure 3.5 A, filled circles), it shows first a small increase with the increase of SL from 2.15 to 2.3 and then, for SL >2.3 μm, a sharp decrease from 115 nm/MPa to a value of ~95 nm/MPa, which remains almost constant as SL increases further.

The C_{hs}–T relation at 2.15 μm is fitted with Eq. 1 (Figure 3.4 C, dashed line superimposed on data points) under the constraint that C_F, the cumulative equivalent filament compliance, is 13 nm/MPa. This value was calculated from X-ray diffraction measurements of the compliances per unit length of the actin filament (c_A, 14.3 nm·MPa^{-1}·μm^{-1}) and the myosin filament (c_M, 17.5 nm·MPa^{-1}·μm^{-1}) (157). The free parameters of the fit are therefore the compliances of the parallel element, C_P, and of the array of motors $(k\zeta)^{-1}$. Under the condition that the force T is proportional to the number of attached motors during the tetanus rise, k varies with T according to the equation $k = k_0T/T_0$, where k_0 is the stiffness of the motor array per unit length at T_0. The fit gives estimates for C_P and $(k_0\zeta)^{-1}$ of 335 ± 21 nm/MPa and 13.2 ± 0.3 nm/MPa respectively, in agreement with previous work (144). Using the values of C_P and $(k\zeta)^{-1}$ from the fit at SL 2.15 μm, the C_{hs}–T relations can be calculated for SL > 2.15 μm by assuming that the stiffnesses of both elements in parallel in the A-band scale in proportion with the degree of filament overlap at each SL (SI). The predicted C_{hs}–T relations (Figure 3.4 D-F, dashed lines) at low forces are progressively shifted upward with respect to the experimental relations, demonstrating that the additional elastic element cannot simply be in parallel with myosin motors in the A-band. This conclusion is even more evident from the plot of $C_{hs,0.1}$ versus SL (Figure 3.5A). Model 1 predicts a monotonic increase in $C_{hs,0.1}$ (open circles) with SL, due to the increase in both $(k\zeta)^{-1}$ and C_P (Figure 3.5 B, open circles) with the reduction of overlap, while the experimental $C_{hs,0.1}$ (Figure 3.5A, filled circles) decreases for SL >2.3 μm.

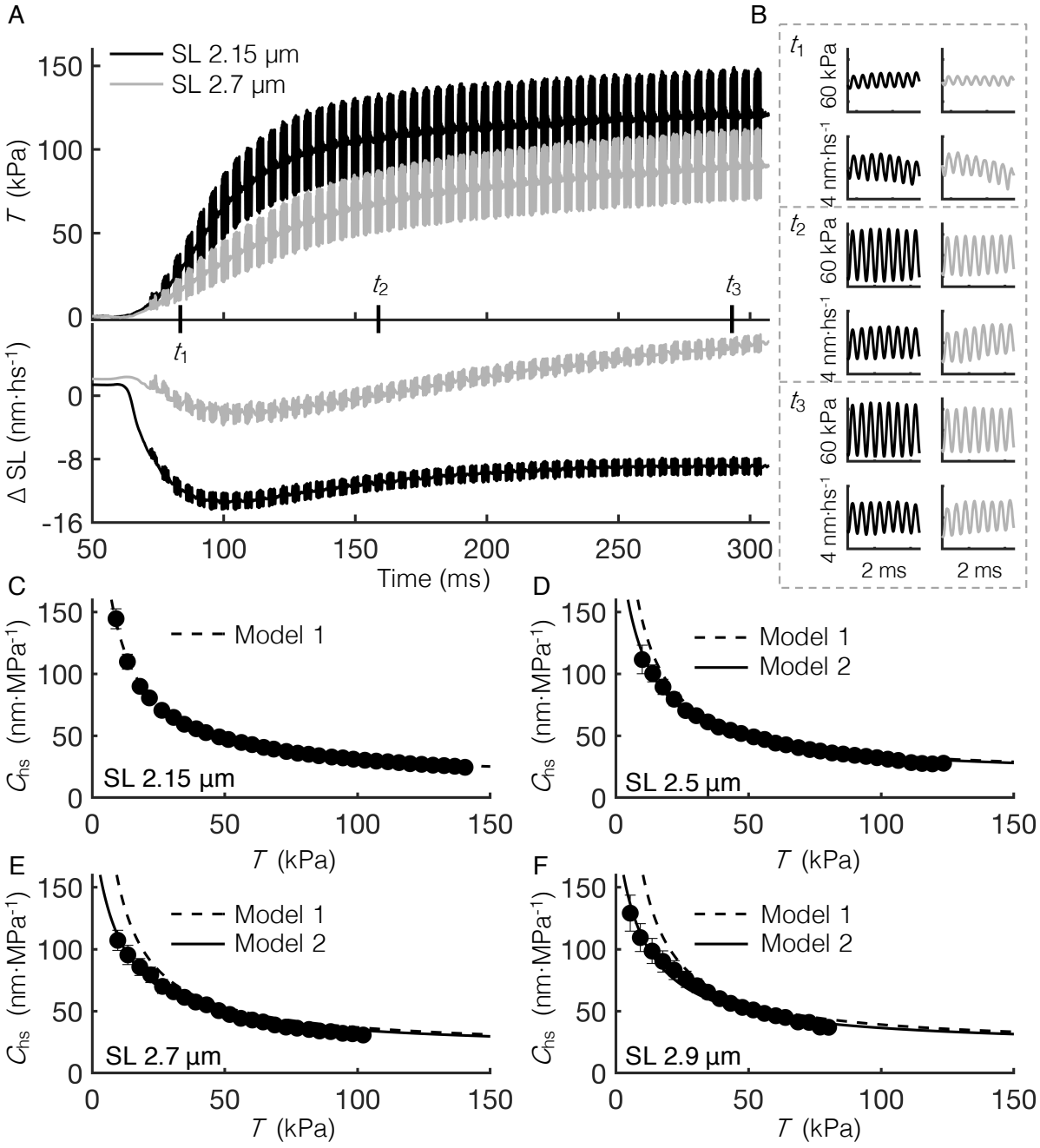

Figure 3.4. Measuring the half-sarcomere compliance (C_{hs}) during isometric force development at different SL.

(**A**) Sample records of force (*T*, upper panel) and half-sarcomere length changes (*L*, lower panel) in response to 4 kHz length oscillations imposed during force development following tetanic stimulation at SL 2.15 µm (black) and 2.7 µm (gray). (**B**) Expanded records (2 ms duration) of *T* and *L* at three times during force development (t_1, t_2, and t_3), as indicated in A. (**C–F**) C_{hs}-*T*

relations (filled circles) determined at SL 2.15 μm (**C**), 2.5 μm (**D**), 2.7 μm (**E**), 2.9 μm (**F**). Dashed lines are the relations calculated using Model 1; continuous lines are the fits of model 2.

3.3.2. The additional elastic element is explained with a titin-like I-band spring

The elastic element that causes $C_{hs,0.1}$ to decrease with SL is putatively titin acting as an I-band spring that comes into play at SL >2.5 μm, which, in the intact frog fiber, is large enough for titin to become taut and exhibit its elasticity as suggested by the passive force–SL relation (see open circles in Figure 3.5 D). To interpret the data under this condition, we use an explicit mathematical model of the half-sarcomere compliance based on the model originally proposed by Ford *et al.* (109) and modified to include an I-band spring (153). To account for the parallel elasticity shown at SL <2.5 μm, where putatively there are no appreciable contributions from titin, the model in reference (153) was further refined with an elastic element in parallel with the array of motors in the A band (Model 2 in Figure 3.1 B, and Eq. 3.2). Thus, the term k (the stiffness per unit length of the array of motors) in Eq. 23 of Ref. (153) is substituted in Eq. S2 by $k + k_P$, where k_P is the stiffness per unit length of the additional A-band spring. k and k_P are obtained from Model 1 estimates at 2.15 μm: in particular k_P at 2.15 μm is related to C_P by the expression $k_P = 1/(C_P \cdot 0.7\ \mu m)$. Note that a more precise definition of k ($= k_0 T \cdot \zeta_0/\zeta$) is given in Eq. S2 to account for its dependence on both SL and force during tetanus rise. Moreover, In Model 2, the compliances of the actin and myosin filaments can no longer be expressed as equivalent compliances (C_A and C_M) and cumulated in an equivalent filament compliance C_F (Figure 3.1 B and Eq. 3.2). Using the same c_A and c_M values from X-ray diffraction measurements as in Model 1 (157), the only free parameter remained to fit the experimental C_{hs}–T relations with Eq. S2 is C_T (the compliance of the I-band spring). The model 2 fit of C_{hs}-T relations is limited to SL ≥2.5 μm, for which there is a significant

contribution of the I-band spring, as shown in Figure 3.4 D-F (continuous line superimposed on data points). The compliance of the titin-like I band spring, C_T, drops from 463 ± 59 nm·MPa^{-1} at SL 2.5 μm to an almost constant value of ~270 nm/MPa at SL >2.7 μm (Figure 3.5 B, filled circles). The corresponding compliance per unit length, c_T (Figure 3.5 C, filled circles) is related to C_T through the expression: $C_T = c_T \cdot l_I$, where l_I is the length of the I-band spring and is given by the difference between the length of the actin filament (l_A, 0.975 μm in frog skeletal muscle (5)) and the length of the overlap region (ζ). c_T decreases with SL from 1213 nm·MPa^{-1}·μm^{-1} at 2.5 μm down to 350 nm·MPa^{-1}·μm^{-1} at 3.1 μm. If this decrease were to depend only on the hyperbolic relation expected for the increase width of the I-band, it would be accompanied by a constant value of C_T. However, as shown in Figure 3.5 B, there is a quite marked decrease in C_T with increasing SL between 2.5 and 2.7 μm, underlying a decrease in c_T much larger than that expected from the hyperbolic c_T–SL relation (Figure 3.5 C, dashed line). This result supports the view that the impact of the I-band spring on the hs elasticity takes a few hundred nm (from 2.5 to 2.7 μm) to establish its role as an elastic element with stiffness that becomes constant independent of SL.

The fit by Model 2 to the C_{hs}–T relation at low forces in the range 2.5-2.7 μm is better appreciated plotting $C_{hs,0.1}$ versus SL (grey circles in Figure 3.5 A, almost superimposed with the filled circles).

It emerges that the decrease in $C_{hs,0.1}$ at SL >2.3 μm is explained by the fall of the I-band spring compliance (C_T, Figure 3.5 B, filled circles) that overcomes the effects of the SL-dependent increase in the compliances of the elastic elements in the A-band, $(k\zeta)^{-1}$ and C_P. $C_{hs,0.1}$ shows a slight rise for SL >2.7 μm because C_T becomes almost constant (filled circles in Figure 3.5 B) and the effects of increase in $(k\zeta)^{-1}$ and C_P with SL emerge again.

The results of the analysis for C_T reported above can be translated into terms of stiffness of the I-band spring per thick filament (e_T) by simple lattice geometry considerations. Given a density of thick filament of $5.87 \cdot 10^{14}$ m^{-2} in frog muscle (162), the relation between e_T and SL can be calculated from filled circles in Figure 3.5 B and is reported in Figure 3.5 D (filled circles). e_T increases with SL in the range 2.5-3.1 μm from 3.7 ± 0.5 to an almost constant value of 6.3 pN/nm per thick filament. No reliable estimate of e_T can be made at SL <2.5 μm because C_P is much smaller than C_T (Figure 3.5 B) and accounts by itself for the additional elasticity. It is worth noting once again that in the single muscle fiber of the frog at rest, SL 2.5-2.6 μm represents the threshold for the rise of titin-based passive force, as shown by open circles in Figure 3.5 D.

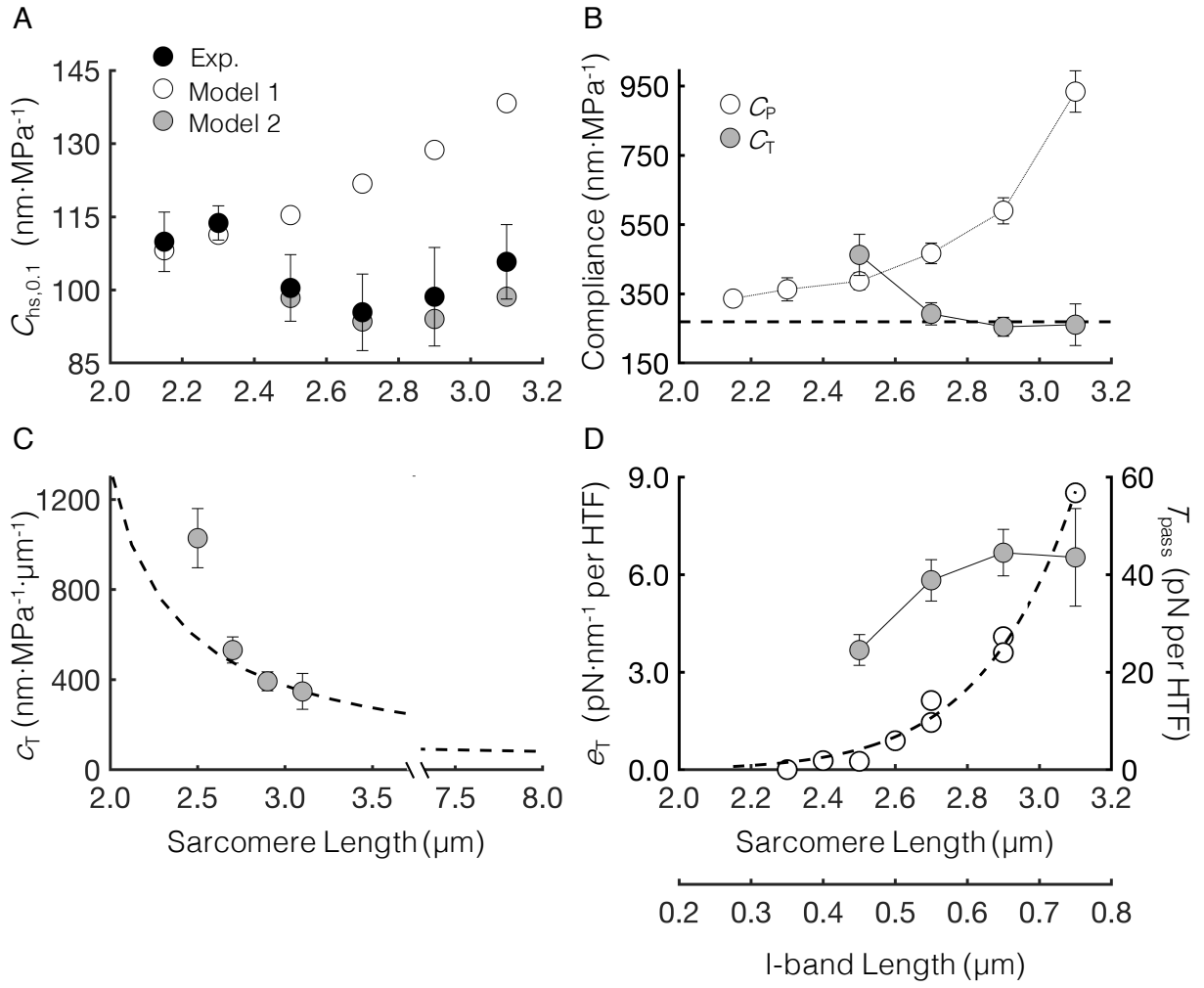

Figure 3.5. SL dependence of the elasticity of the half-sarcomere at low force and of the additional spring elements.

(**A**) Compliance of the hs at 0.1 T_0 ($C_{hs,0.1}$, 15 kPa). Filled circles, experimental values; open circles, values calculated with model 1; gray circles, values from Model 2 fit of the C_{hs}-T relations. Error bars represent the SEM for 8 fibers. (**B**) Compliance of the additional elastic elements: open circles, C_P–SL relation calculated with Model 1; gray circles, C_T-SL relation estimated with Model 2 fits. The continuous lines are drawn to connect the points; the dashed horizontal line is drawn passing through the C_T value estimated at SL 3.1 µm. (**C**) Compliance of the I-band spring per unit length (c_T) estimated with Model 2. The dashed line is the hyperbolic relation predicted by assuming C_T constant and equal to the value estimated at SL 3.1 µm. (**D**) Gray circles and continuous line (left ordinate): stiffness of the I-band spring per half- thick filament (HTF), e_T, calculated as detailed in the text. Open circles and dashed line (right ordinate): passive force (T_{pass});

data pooled from the present experiments and those in ref. (39). The I-band width at each SL is reported in the lower abscissa. For B–C, the error bars represent 95% confidence intervals around the fit parameters.

Table 3.1. Compliance of the parameters of the half-sarcomere elasticity in the SL range 2.15-3.1 µm.

Compliance ($nm \cdot MPa^{-1}$)	SL 2.15 µm	SL 2.3 µm	SL 2.5 µm	SL 2.7 µm	SL 2.9 µm	SL 3.1 µm
$C_{hs,0.1}$	110 ± 6	114 ± 3	100 ± 7	95 ± 8	99 ± 10	106 ± 8
$(k\zeta)^{-1}$	132 ± 3	148 ± 4	177 ± 4	218 ± 5	285 ± 7	412 ± 9
C_P	336 ± 21	363 ± 33	387 ± 25	467 ± 30	590 ± 38	934 ± 60
C_T	--	--	463 ± 59	293 ± 32	255 ± 27	261 ± 60

$C_{hs,0.1}$ and $(k\zeta)^{-1}$ refer to the estimates at force 0.1 T_0. Errors for $C_{hs,0.1}$ are SEM and all other errors are 95% confidence intervals around fit parameter.

3.3.3. Increasing titin stiffness in a spatially explicit computational model of the half-sarcomere predicts experimental measurements of C_{hs}

Our unexpected finding that the dynamic stiffness of titin is independent of SL > 2.7 µm (Figure 3.5D) warranted further investigation. We turned to our spatially explicit computational model of the half-sarcomere that includes an adjustable I-band spring (120). The motivation for employing the model here arose from its ability to vary the elasticity of specific elements in the sarcomere individually and assess the effects on contraction and overall sarcomere mechanics, making it an ideal tool to help interpret our experimental findings and further validate the results of the mathematical model used to fit the data.

At SL 2.9 μm, the sarcomere geometry of an intact fiber is such that MyBP-C is outside the range of overlapped myofilaments (163), rendering it's putative contribution to C_{hs} negligible. This lends a convenient comparison to our computational model of the half-sarcomere, in which only myosin, actin, and titin are the only elastic elements. Thus, we performed an analogous measurement *in-silico* of the dynamic half-sarcomere compliance at SL 2.9 μm with and without the presence of titin springs to further examine the dependence of the C_{hs}–T relation on titin stiffness. Isometric tetanus was simulated for 15 ms, and, after each time-step (0.1 ms), the SL was shortened by a total of 2 nm in 10 sequential length steps (of 0.2 nm each). The force responses to each of the 10 length steps were averaged after each time-step, the SL was returned to 2.9 μm, and the isometric contraction simulation proceeded to the next time-step. This measurement was repeated with and without the titin I-band spring and averaged over 50 independent tetani, giving a measurement of C_{hs} as a function of isometric force development and titin stiffness. (More details outlining the model are in the Methods section.)

Figure 3.6 shows the C_{hs}–T relations of intact fibers and the simulated analog at SL 2.9 μm. For a more direct comparison between experimental and computational measurements, C_{hs} was normalized to the maximum force generated at SL 2.15 μm (T_0). Figure 3.6 A shows the same data and predicted relation as in Figure 3.4 D, now with units of nm/T_0. Figure 3.6 B shows the analogous measurement made *in-silico* at SL 2.9 μm for the case without titin (open squares) and with stiff titin (filled squares). Because the only elastic elements in the computational model are the myofilaments and myosin motors, the 'no titin' case represents a physiologically similar condition to that of the predicted relation in Figure 3.6 A, in which MyBP-C is outside the range of filament overlap and titin was assumed to have negligible contributions. With the addition of a stiff titin I-band spring, the C_{hs}–T relation is decreased at low forces relative to the 'no titin' case,

in very good agreement with the measured relation in intact fibers at the same SL. Thus, making no other *a priori* assumptions, and by *only* increasing the stiffness of the I-band spring at SL 2.9 µm, the computational model qualitatively and quantitatively predicts similar behavior to what is observed experimentally in intact fibers at the same SL. This finding not only demonstrates the ability of the model to make accurate and insightful physiological predictions, but it also helps to confirm our interpretation of tunable titin stiffness as a primary molecular origin of the increased half-sarcomere stiffness at long SL.

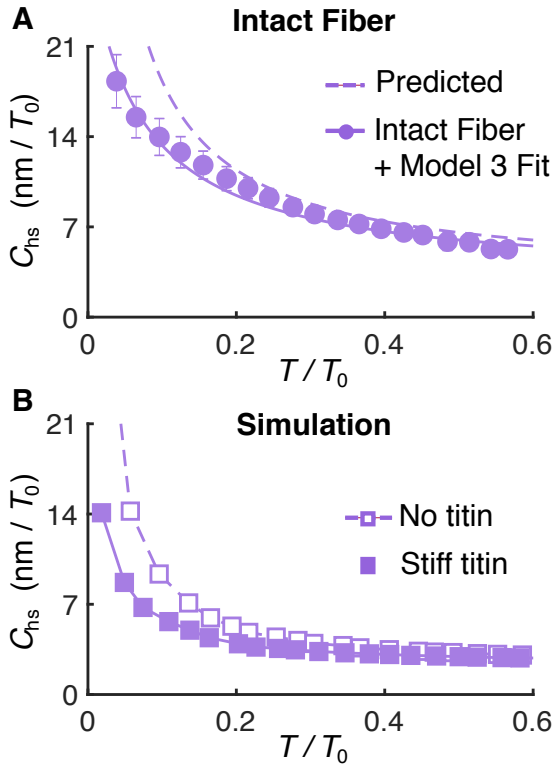

Figure 3.6. *In-silico* measurements of C_{hs} at SL 2.9 µm with and without an I-band spring. **(A)** The predicted (dashed line) and measured (filled circles) C_{hs}-T relations for SL 2.9 µm in intact fibers are the same as what is shown in Figure 3C, now with units that are normalized to the maximum isometric force at SL 2.15 µm (T_0) in order to make comparisons to measurements made *in silico*. **(B)** Analogous C_{hs}–T relations from the simulated half-sarcomere with and without a titin

I-band spring. Data points represent averages of 50 independent simulated isometric tetani and C_{hs} measurements.

3.4. Discussion

3.4.1. Origin of the additional elastic elements in the active sarcomere

We have investigated the molecular basis of additional elastic element responsible for the nonlinear relationship between half-sarcomere compliance (C_{hs}) and force (T) (144), by exploiting fast sarcomere-level mechanics on active single fibers from frog muscle at different sarcomere lengths. We find that at a force, 0.1 T_0, at which the compliances from the attached motors and from the additional elastic element are comparable (Table 1), the half-sarcomere compliance ($C_{hs,0.1}$) decreases at SL >2.3 μm and attains a roughly constant value at SL >2.7 μm. The reduction of $C_{hs,0.1}$ with the increase in SL would be unexpected if the additional elasticity resided in an element in parallel with myosin motors in the A-band (*e.g.*, weakly bound myosin motors or MyBP-C links), because in this case the reduction of the periodic cross-links between actin and myosin filaments with the reduction of overlap would increase $C_{hs,0.1}$ (dashed lines in Figure 3.4 D-F and open circles in Figure 3.5 A).

The marked reduction of $C_{hs,0.1}$ with increase in SL above 2.3 μm can be accounted for only by a mechanical model (Model 2) in which a titin-like I-band spring contributes to the hs compliance. The finding that the reduction of $C_{hs,0.1}$ occurs mainly around 2.5 μm suggests that this is the threshold at which titin-based elastic contribution comes into play. Accordingly, the passive, titin-dependent force of an intact single fiber starts to rise at SL 2.5-2.6 μm (open circles in Figure 3.5 D). If the compliance of the titin spring (C_T) is constant independent of SL, its compliance per unit length (c_T) is expected to increase with the reduction of SL (and I-band width)

in a hyperbolic manner (dashed line in Figure 3.5 C). The upward shift of c_T at 2.5 μm relative to the hyperbolic relation demonstrates that titin elasticity vanishes abruptly for SL <2.5 μm, the only remaining additional elasticity being the A-band element (144). Furthermore, the finding that, within the limits of the experimental error, $C_{hs,0.1}$ increases with the increase in SL from 2.15 to 2.3 μm (filled circles in Figure 3.5 A) suggests that the compliance of the additional A-band elastic element increases between 2.15 and 2.3 μm for the reduction of ζ, as predicted for C_P by Model 1 (open circles in Figure 3.5 B). This conclusion suggests that the A-band spring, as implicitly assumed in Model 1, is due to weakly bound motors (144, 156). In fact, if the additional A-band elastic element were due to MyBP-C links, C_P would have started to increase only for SL >2.5 μm when the C-zone starts to reduce its overlap with the actin filament (152, 163).

3.4.2. Molecular basis of the I-band spring tunability

The finding that the compliance of the I-band spring (C_T) remains approximately constant as SL increases beyond 2.7 μm strongly suggests that titin, the elastic element in the I-band, is able to adapt its compliance per unit length in response to changes in SL and thus in the I-band width. This property must be intrinsic to the structure of titin in the I-band, which, in a sufficiently slow time scale, absorbs large changes in length by adapting its conformation so that the elastic component maintains a constant length, responding with the same stress to a given length perturbation. This conclusion is further supported and validated by the results of the computational model (Figure 3.6), in which only myosin, actin, and titin filaments are present, yet a similar qualitative drop in C_{hs} at low forces is seen with stiff titin compared to no titin.

The I-band region of titin is comprised of the entropic spring-like domain with unique sequences rich of proline (P), glutamate (E), valine (V), and lysine (K) (PEVK region) flanked by

many immunoglobulin (Ig)-like domains (proximal and distal tandem Ig region) (164). Single-molecule force spectroscopy on genetically engineered titin segments demonstrated that the PEVK region is responsible for titin's elastic response to ramp-shaped stretches that induce force increases in the range of 1-30 pN (94, 165). Assuming 6 titin molecules per half-thick filament (47), the lower part of this force range corresponds to the passive force that a muscle fiber develops near the upper limit of the SL working range (15 pN per thick filament at SL 2.8 μm, see Figure 3.5 D, open circles). For SL shorter than 2.5 μm, at which passive force starts to develop, small increases in length imply only straightening of very extensible, randomly bent elements without any significant rise in force (166). This mechanism is depicted in the upper (SL 2.15 μm) and middle (SL 2. 5 μm) panels of Figure 3.7. Single-molecule force spectroscopy showed that, when the ramp-shaped stretch is large enough to elicit forces of several tens of piconewtons (≥ 40 pN), the force response becomes sawtooth-shaped, with peaks followed by abrupt drops in force (167). The force drops are the manifestation of Ig domain unfolding events that cause a sudden 20-30 nm increase in the length of the molecule. Under these conditions, the following release is characterized by hysteresis that is larger the longer the time the molecule is maintained in the stretched state. In force clamp, both the whole titin molecule from rabbit muscle (93) and titin constructs made only by 8 Ig domains (48) show stepwise changes in length (ΔL) of 11-25 nm in response to a drop/rise in force, which are the mechanical manifestation of Ig folding/unfolding events. In the Ig construct nearly 100% of the Ig domains are unfolded under a steady force > 10 pN. Notably, 10 pN per titin (or 60 pN the thick filament) is just beyond the upper limit of the passive force in the present experiments (Figure 3.5 D, open circles). Thus, unfolding and refolding of Ig domains occurs in the physiological range of passive forces, with a two-state load-dependent kinetics that predicts that at 6-7 pN (~40 pN per thick filament) an Ig domain has ~50% probability

of being unfolded with a transition rate constant of <0.2 s^{-1} (Fig. 4 in Ref. (48)). A similar rate constant had been previously found for the whole titin molecule under a force of 7 pN (Fig. 3C in Ref. (93), ignoring for simplicity the presence of a slower component). In that case, however, the contribution of non-Ig domain elements could not be excluded, until the experiment in Ref. (48) had demonstrated that Ig domains by themselves account for the kinetics.

The structural dynamics of Ig domain folding-unfolding determined with single-molecule force spectroscopy offer a mechanism able to explain the behavior of the titin-like I-band spring described in this work. In the range of SL 2.5-3.1 μm, in which the width of the I-band increases by (750-450 =) 300 nm, the passive force (T_{pass}) rises up to 56 pN per thick filament (Figure 3.5 D, open circles), that is ~9 pN per titin molecule. With a ΔL (the increase in length of titin per Ig-unfolding) of 15-20 nm, the 300 nm increase in the I-band width is accounted for by the unfolding of 15-20 Ig domains. Taking the number of Ig domains present in the I-band titin (N) =80, the unfolded fraction is smaller than that predicted for 9 pN force from the load-dependent kinetics of the Ig construct (48), but in rough agreement with the three times larger force (22 pN), necessary for 50% unfolding shown by the whole molecule (Fig 3B in Ref. (93)). The difference of the force for half-unfolding between the 8 Ig construct (48) and the whole molecule (167) is likely an indication of the presence of a hierarchy in the load dependence of Ig unfolding, suggesting in turn that the whole molecule kinetics is more representative of the *in-situ* kinetics. Under these conditions, Ig unfolding *in situ* can account for the tuning of titin length to I-band width in the range of SL explored in the present experiments, by exploiting the negative feedback between the increase in titin length produced by Ig unfolding and the force that sustains the unfolding process. The slow rate constant of the transition (<0.2 s^{-1} at ~6 pN) is adequate for this task.

In conclusion, in the slow time scale of SL changes of our protocol, I-band titin absorbs large changes in length by exploiting its load-dependent structural dynamics of the serially linked Ig domains. This action allows for the number of unfolded Ig domains to adapt to the increase in length so that the elastic component, putatively constituted by the PEVK region, maintains a constant length, responding with the same stress to a given length perturbation. This mechanism, depicted in Figure 3.7 by the middle (SL 2.5 μm) and lower (SL 2.9 μm) panels, implies that, in the 4 kHz regime used here (which probes purely elastic components), the dominant elastic element is the PEVK region, while the tandem Ig regions are effectively infinitely stiff (*i.e.*, highly viscoelastic in the 4 kHz regime). This assumption is supported by the structural features of the two components: the PEVK domain has a random-coil structure that maximizes its conformational entropy in the compact configuration and responds to force with increase in its extension, while the Ig domains have a well-defined β-barrel structure and are connected in series by linkers made by 2-4 amino acids (168). At SL > 2.5 μm (just prior to passive force development, Figure 3.5 D, open circles), the Ig domains are taut and change their length only when, under stress, one Ig pops with a transition from its β-barrel structure to a fully unfolded peptide chain. In this way, either before or after the unfolding event, the Ig domain manifests in our measurements as infinitely stiff relative to the PEVK element in series.

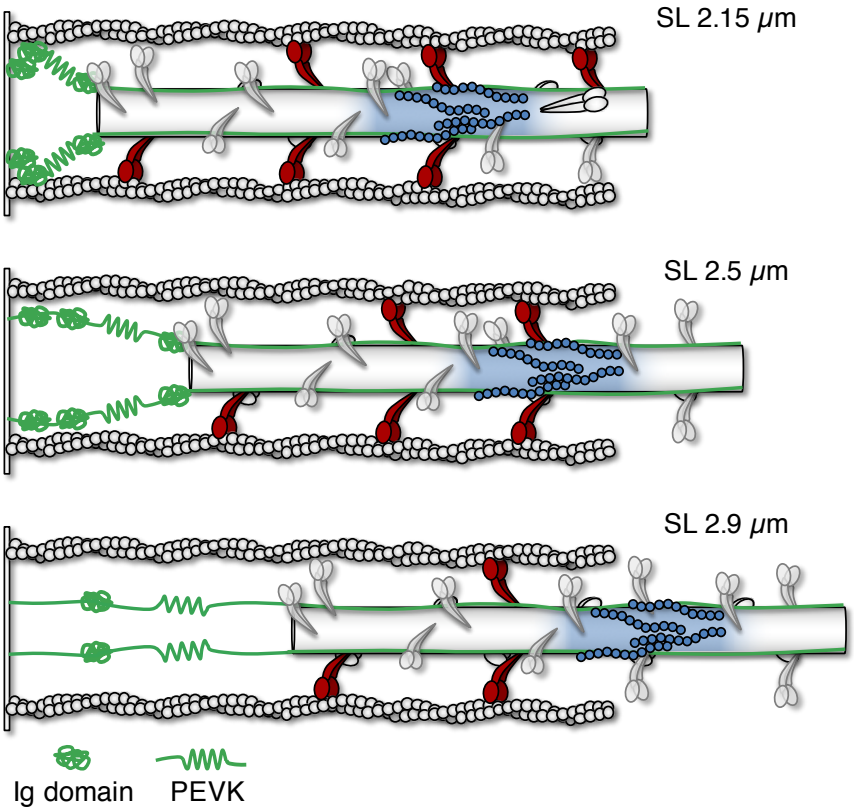

Figure 3.7. Illustration of the proposed mechanism for the tuning of the I-band spring stiffness to SL.

For SL 2.15 μm (top figure), the PEVK region and the distal and proximal immunoglobulin (Ig) domains are slacked and in their native folded state. This manifests in the 4 kHz regime as two springs in series with a high overall compliance (~330 nm/MPa; Figure 3.5 C). When the SL increases to ~2.5 μm (middle figure) the PEVK region and Ig domains become taut, just before passive tension (T_{pass}) begins to develop in the T_{pass}–SL relation (Figure 3.5 D). This situation again manifests as a two-spring system, with a slightly lower overall compliance. When SL is increased to 2.9 μm (bottom figure) significant passive tension has developed in the fiber, and therefore in each titin molecule. Under physiological tension, the distal and proximal Ig domains unfold with a very low probability of refolding (48). In the 4 kHz regime, the unfolded Ig domains manifest as an elastic element with very high effective stiffness that is in series with the preserved PEVK region. Therefore, the dynamic stiffness of the I-band spring measured for this SL (~12 pN/nm per thick filament; Figure 3.7 D) is likely the *in-situ* stiffness of the PEVK region.

3.4.3. Physiological relevance of an I-band tunable spring with dynamic characteristics.

The integration of our results with those from single-molecule force spectroscopy provides a picture of the structural and kinetic characteristics of titin which allows for a precise quantitative definition of its role in the active sarcomere *in vivo*.

Titin could play a direct role in the stress-sensing mechanism that is responsible for switching ON myosin motors from the OFF state, in which they lie along the surface of the thick filament in a conformation unable to attach to actin and split ATP (17, 72, 169). However, the effectiveness of titin in producing a stress-dependent structural change in the head conformation of the relaxed fiber from mammalian skeletal muscle has been demonstrated only at SL above 2.8 μm (74), which is beyond the upper limit of the physiological working range of SL for mammalian muscle. In the frog muscle fibers used in this work the physiological SL range (2.0-2.3 μm) is much lower than that (≥2.5 μm) at which the stiffness of the I-band spring emerges. This result further contests a direct role of titin as a stress sensor in the contraction occurring under physiological conditions. The difference in SL at which titin manifests its mechanical effects, ≥ 2.5 μm in frog fibers (this work) and ≥ 2.8 μm in mammalian fibers (74), strengthens and generalizes the conclusion that there is no direct effect of titin on the stress-sensing mechanism that switches ON the myosin motors in the physiological working range of SL.

Titin effects *in-situ* must be based on the two fundamental characteristics of the molecule that emerge from this work and previous single-molecule force spectroscopy data, namely the findings that: (*i*), at SL>2.7 μm, titin mechanical relevance appears with a stiffness of the I-band spring (~6 pN/nm) that remains constant, independent of SL, and (*ii*) the *in vitro* Ig domain folding/unfolding kinetics and the *in vivo* steady passive force are related by the negative feedback between force and unfolding reaction. This negative feedback ensures, at any I-band width above

0.5 μm (passive force >0, open circles in Figure 3.5 D), a dynamic equilibrium between unfolding events that lengthen the molecule and drop the force and refolding events that shorten the molecule and raise the force.

The above characteristics are exploited *in vivo* to limit the development of SL non-homogeneity. This condition occurs during eccentric, isometric or high load contractions whenever there is a given degree of non-homogeneity in force-generating capacity among half-sarcomeres, sarcomeres, or sarcomere populations in series along the muscle fiber. First of all, it must be considered that under dynamic conditions, for instance during steady lengthening, the force exerted by titin at a given SL > 2.5 μm can be several times larger than the static force at that SL (which underlies the passive force-SL relation). The size of this additional force can be calculated using the kinetic information from single-molecule force spectroscopy experiments. According to ref. (167) (Fig. 3B), at a force of 22 pN on titin, corresponding to (22 · 6 =) 132 pN per thick filament, the rate constants for folding (k_f) and unfolding (k_u) are equal and 50% of Ig are unfolded at the equilibrium. Ignoring for simplicity the different temperature and animal species, 132 pN of force per thick filament is about 0.5 the tetanic force at full filament overlap in frog muscle fibers at 4 °C. With ΔL (the increase in length of titin per Ig-unfolding) = 20 nm, and N (the number of Ig domains in the I-band) = 80, the equilibrium I-band lengthening would be (20 nm · 80/2 =) 800 nm and thus the SL would increase from 2.5 to 4.1 μm. However, accounting for the dynamic properties of titin, the actual lengthening of the I-band and thus of the sarcomere is quite smaller: given the rate constant for Ig folding/unfolding reaction at 22 pN equal to 0.3 s^{-1} (Fig 3C in ref. (167)), the initial rate of Ig unfolding is ($N \cdot k_u = 80 \cdot 0.15\ s^{-1}$ =) 12 s^{-1} and the corresponding initial I-band lengthening velocity (20 nm · 12 s^{-1} =) 240 nm s^{-1}. For a hypothetical sarcomere isometrically contracting at SL 2.5 μm this calculation implies that, based just on the dynamic

response of titin, it would be able to respond to a supplementary stress of 0.5 T_0 by undergoing a lengthening that, during 1 s of contraction, would bring the SL to (2.5 + 1.6 · 0.26 =) 2.9 μm. This example illustrates the power of titin in buffering the lengthening that a weaker sarcomere would undergo in response to the higher force exerted by the stronger sarcomeres in series. Note that this example represents an unlikely upper limit for rise in SL non-homogeneity because in vivo the difference in force between sarcomeres in series is much smaller than 0.5 T_0 (with a correspondingly smaller lengthening of the weak sarcomere) and 1 s is an unusually long duration for a tetanic contraction.

The above analysis ignores for simplicity the braking action of myosin motors based on the strain-dependent rapid recruitment of new actin-attached motors occurring in response to a stretch (170, 171). Notably, in those studies the possibility to develop sarcomere non-homogeneity was minimized by using stretches smaller than 4 nm per hs on fibers contracting at SL 2.15 μm. Here we demonstrate that, apart from the stretch potentiation accounted for by the myosin-based rapid recruitment of motors in the A-band (170, 171), there is a supplementary mechanism in the I-band, based on the dynamic stiffness of titin, that equilibrates the force difference among sarcomeres in series, adding its force contribution to the weaker sarcomeres so as to prevent the development of large sarcomere length non-homogeneity.

Chapter 4

Structural dynamics of the myosin filament in intact cardiac muscle and molecular determinants of contractile force

4.1. Introduction

4.1.1. X-ray diffraction-based measurements of cardiac myofilament structure

Over the past couple of decades, remarkable advancements have been made in developing approaches to harness synchrotron light to probe molecular-level structural dynamics of muscle with X-ray diffraction analyses. Early seminal work focused on vertebrate skeletal muscle to exploit its high degree of subcellular structural order (67, 159, 172), but, more recently, we (and others) have been able to reach similar resolution in cardiac muscle (42, 173). This has led to a richer understanding of the differences in regulation between skeletal and cardiac muscle from a structural basis, which can now be applied to understanding structural implications of mutation-based cardiomyopathies and inotropic interventions (75, 88). In this chapter, a series of experiments are discussed in which the resting and active structure of myofilaments in intact cardiac muscle was investigated under various inotropic intervention using X-ray diffraction techniques, focusing on the regulatory state of the thick filament and sarcomere lattice geometry.

4.1.2. Structural responses to physiological inotropic interventions in the myosin filament of cardiac muscle

Although inotropes are broadly classified as agents that increase muscle contractility, they are often associated with drugs or small molecules. However, positive inotropes may also refer to

physiological or pathophysiological conditions of the muscle that cause hypercontractility. For example, in cardiac muscle, physiological positive inotropes include increased sarcomere length, or phosphorylation of various sarcomere proteins may enhance contractility, whereas pathological inotropes may be an HCM-associated sarcomere protein mutation that cause hypercontractility. A recent study has suggested that phosphorylation of myosin binding protein-C (MyBP-C) and mutations that are associated with hypercontractility and HCM cause cardiac myosin to be perturbed from its resting conformation, which may underlie the hypercontractility of HCM (88). Similarly, phosphorylation of the regulatory light chain has been shown to alter the position of myosin motors in resting cardiac muscle, bringing them closer to actin (174). Therefore, there are important structural dynamics in the thick filament in response to phosphorylation of sarcomere proteins that may be a structural basis for enhanced contractility.

The effects of increasing sarcomere length on the structure of the thick filament in cardiac muscle have been elusive to uncover. A recent study used X-ray diffraction techniques to investigate titin-mediated thick filament stress as a mechanism for releasing myosin motors from their resting conformation in intact cardiac muscle (42). A transgenic rat was used which harbors a longer isoform of titin (and therefore more compliant) causing a reduction in SL-dependent passive tension. The authors found that stretching resting trabeculae resulted in an increase in the spacing and intensities of the Tn3 reflection (troponin-based periodicity), the M2 reflection (associated with myosin and myosin-binding protein-C, MyBP-C), and the M6 reflection (associated with the periodicity of the thick filament backbone). The authors concluded that, upon stretch in intact cardiac muscle, titin delivers strain to the thick filament backbone that may alter the MyBP-C interaction with the thin filament, thereby priming both the thick and thin filament for contraction. However, the authors did not see any appreciable movement of the myosin motors,

either axially (spacing or intensity of the M3) or radially (changes in the $I_{1,1}/I_{1,0}$ ratio). Thus, it is somewhat unclear if the structural arrangement of myosin motors is sensitive to sarcomere length.

In addition to sarcomere length-dependent force augmentation, myosin-binding protein-C (MyBP-C) is emerging as a key modulator of force in cardiac muscle (28). It has recently been proposed that the N-terminal domains of MyBP-C can bind to and activate of inhibit the thin filament by displacing tropomyosin and to the "open" structural state, thereby increasing the likelihood of strong cross-bridge attachment (30). Interestingly, high ratios of N-terminal MyBP-C–actin interactions result in inhibition of actin-myosin binding due to direct competition of binding sites on actin. Indeed, other studies have shown that the thin filament is activated by MyBP-C, and may also be controlled by the degree to which MyBP-C is phosphorylated by PKA-mediated signaling cascades (174–177). It was also found that dephosphorylation of MyBP-C preferentially binds myosin, reducing the probability of myosin to bind to actin, while this affect is diminished with either MyBP-C phosphorylation or elimination (178). Lastly, the structural correlate of these effects on a single myosin filament were confirmed using electron microscopy to show that phosphorylation of MyBP-C causes a shift in the average position of myosin motors away from the thick filament backbone (179). However, the structural response of the myosin filament in intact cardiac muscle, and how it might differ from that of sarcomere length-dependent structural responses has yet to be determined.

The work presented here is aimed at elucidating the structural basis for the potentiation of cardiac contraction (the positive inotropic effect) by both increased sarcomere length and increased degree of MyBP-C phosphorylation in the diastole preceding contraction. In particular, we investigate using X-ray diffraction methods the structure of intact cardiac sarcomeres after phosphorylation of sarcomere proteins, increases in sarcomere length, and increases in load during

contraction (afterload) to determine if there are unique structural bases for the force augmentation with each type of treatment. We find that at rest, changing sarcomere length alone has little effect on the position of the myosin motors. Moreover, after treating intact cardiac muscle with the beta-adrenergic agonist isoprenaline, we find the largest structural changes in the thin filament, based on increases in the M1 and M2 X-ray reflections, while isoprenaline has little effect on the myosin-based reflections (M3 and M6). Lastly, we find that the load during contraction has the most significant effect on the myosin filament structure. We conclude that force augmentation in cardiac muscle involves a rapid, feed-forward mechanosensing mechanism of the thick filament that is adjusted based on the contractile demands during systole.

4.2. Methods

4.2.1. Animal use and ethics

Male *Rattus norvegicus* (Wistar Han weighing 250–350 g, Charles River - Research Models and Services, Italy) were housed at the Bio-Medical Facility (ID17) of European Synchrotron Radiation Facility (ESRF), under controlled temperature (20 ± 1°C), humidity (55 ± 10%), and illumination (light on for 12 h daily, from 7 AM to 7 PM). Rats were chosen at random for each experiment from the available batch and euthanized in agreement with Italian regulation on animal experimentation (Authorization 956/2015-PR, in compliance with Decreto Legislativo 26/2014). Rats were anesthetized with isoflurane [5% (vol/vol)] and the heart was rapidly excised.

4.2.2. Heart excision and trabeculae preparation

Excised rat hearts were placed in a dissection dish and perfused via retrograde flow with a modified Krebs–Henseleit (KH) buffer (in mM: NaCl, 115; KCl, 4.7; $MgSO_4$, 1.2; KH_2PO_4, 1.2;

$NaHCO_3$, 25; $CaCl_2$, 0.5; glucose, 10), containing 20 mM 2,3-butanedione monoxime (BDM), and oxygenated with 95% O_2 and 5% CO_2 (pH 7.4). Thin, unbranched, and uniform trabeculae were dissected from the right ventricle under a stereomicroscope. The trabecula was placed in a custom dish that allowed for measurements of the length, width, and thickness using a stereomicroscope and the cross-sectional area (CSA) was calculated as (thickness*width)•π/4. The trabecula was then transferred into a thermoregulated trough perfused (1.2 ml/min) with oxygenated KH solution (27°C) and mounted between the force transducer and length-controlling motor via custom titanium double hooks. These hooks allowed for the trabecula to be mounted rotated by 90° such that its wider transverse axis was orthogonal to the X-ray beam. This maximized the surface area for X-ray exposure. Sarcomere length (SL) was measured with a 40x dry objective and a 25x eyepiece. SL was set at ~2.2 μm at rest; the corresponding trabecula length (L_0) was measured again and the CSA corrected for the change in length (L_0-L_t) assuming constant volume behavior. A pair of mylar windows was positioned close to the trabecula, about 1 mm apart, to minimize the X-ray path in the solution. The trough was sealed to prevent solution leakage and the trabecula was mounted vertically at the ID02 beamline of the ESRF. The KH solution perfusing the trabecula was exchanged with a KH solution without BDM and containing 2.5 mM $CaCl_2$. Trabeculae were electrically stimulated at 0.5 Hz to produce twitches, and the force, motor lever position, and stimulus signals were recorded with a multifunction I/O board (National Instruments, PXIE-6358).

4.2.3. X-ray diffraction data collection

Figure 4.1 shows a representative 2-D X-ray pattern of an intact, resting trabecula (Figure 4.1A) with schematics describing various components of the meridional reflections (Figure 4.1B) and the equatorial reflections (Figure 4.1C).

The beamline ID02 of the ESRF provides up to 2 x10^{13} photons per second with 0.1 nm wavelength in a beam of size ~300 μm [horizontal, full width at half-maximum (FWHM)] and ~50 μm [vertical; (180)]. The beam was attenuated for trabecula alignment. To minimize radiation damage, X-ray exposure was limited to the data collection period using a fast, electromagnetic shutter (model LS500, nmLaser Products, Inc.) and the trabecula was shifted along its axis by 100–200 μm between twitches. X-ray diffraction patterns were recorded using the FReLoN charge-coupled device (CCD)-based detector with 2,048 x 2,048 pixels (50x50 mm^2 active area). Pixels were binned by 8 in the equatorial direction (perpendicular to the fiber axis) before the readout to increase the signal-to-noise ratio. Twitches were preliminarily elicited with the X-ray detector at 31 m from the preparation in fixed-end conditions (FE), in which case the sarcomeres shorten during force development against the end compliance. SL during diastole and at the peak of the twitch (force T_p) was measured by using the second order sarcomeric reflection (Dia and FE respectively in Fig. 4.2 A). In the next series of twitches shortening was prevented (sarcomere length clamp condition, LC) by feeding the motor-servo system with a signal based on the changes in SL recorded at the peak of the preceding FE twitch (181), and the actual SL at the peak of the twitch was again recorded using the second order sarcomeric reflection (LC in Fig. 4.2 A). Due to limits in the range of movement allowed by the motor used at the beamline, the maneuver did not always succeed in completely avoiding sarcomere shortening that anyway was drastically reduced.

Then the detector was moved to 1.6 m from the preparation and patterns were recorded in diastole and at the peak of FE and LC twitches in a random sequence, with 5 ms exposure times. In the four trabeculae selected for the analysis (each from a different rat) X-rays were collected from at least 10 twitches in each trabecula with no detectable sign of radiation damage.

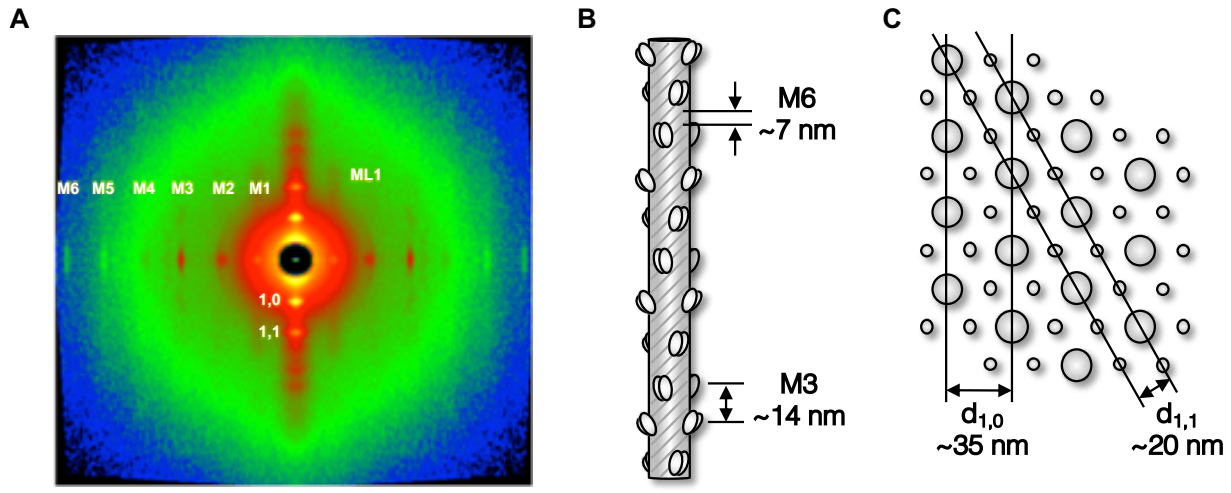

Figure 4.1. X-ray diffraction patterns reveal myofilament structure and lattice geometry in intact cardiac muscle.

(**A**) Example of a 2D X-ray diffraction pattern of an intact cardiac trabeculae with 15 ms exposure time (image courtesy of Gabriella Piazzesi; PhysioLab, Unifi). Peaks in the image are a result of the average electron density of the proteins comprising periodic strictures in the sarcomeres. The reflections along the horizonal axis define the 'meridional' axis, which correspond to the periodic elements along the long axis of the myofilaments. For example, the M3 reflection corresponds to the adjacent myosin crowns along the thick filament that are separated by ~14 nm, and the M6 reflection corresponds to the ~7 nm periodic repeats of the helical backbone of the thick filaments (**B**). The vertical reflections in panel A define the 'equatorial' axis, which correspond to the interfilament geometry (at small diffraction angles). (**C**) Schematic of the cross-section of a sarcomere, showing thick filaments (large circles) and thin filaments (small circles) arranged in a lattice with double hexagonal symmetry. The 1,0 reflection is a result of the plane of symmetry of adjacent thick filaments (large circles), and the 1,1 reflection corresponds to the plane of symmetry between thick and thin filaments (small circles).

4.2.4. Intact trabecula mechanics

To monitor the structural dynamics of the myosin filament during a cardiac twitch, trabeculae were stimulated at 0.5 Hz via field stimulation. Trabeculae were exposed to 1-ms X-ray pulses in one of three different conditions: (*i*) at rest, or diastole (Dia), (*ii*) at the peak of a twitch under fixed-end (FE) length control (*i.e.*, fiber isometric), and (*iii*) at the peak of a twitch under sarcomere length-clamp (LC) control. Figure 4.2A shows representative traces of the FE and LC protocol. In the FE protocol, the sarcomere length (SL) was set to 2.2 μm and, when the trabeculae underwent a twitch, the ends of the trabeculae were held fixed by the length controlling motor and the SL was allowed to shorten against the compliance in the attachments of the preparation. During an LC twitch, a positive-feedback stretch from the motor was imposed on the trabecula to prevent the SL from changing. This allowed the SL to remain precisely at 2.2 μm throughout the duration of the twitch, which resulted in a stronger contraction (181).

Figure 4.2B shows the twitch force-SL relation for intact trabeculae, with the active force shown as circles and the passive tension shown as triangles. The average peak of an FE twitch is shown by the red circle and the average peak of a twitch is shown in purple. Despite both twitch types starting from the same SL (2.2 μm, shown in Figure 4.2B by the blue triangle) the FE twitch produced nearly half of the twitch force as the LC twitch. This is due to significant sarcomere length shortening in the FE twitch, from 2.2 μm to about 1.9 μm (red trace in Figure 4.2C), compared to shortening of only ~0.1 μm in the LC condition (purple trace in Figure 4.2C). However, it is important to note that the FE and LC twitches both fall on the same unique force-SL relation.

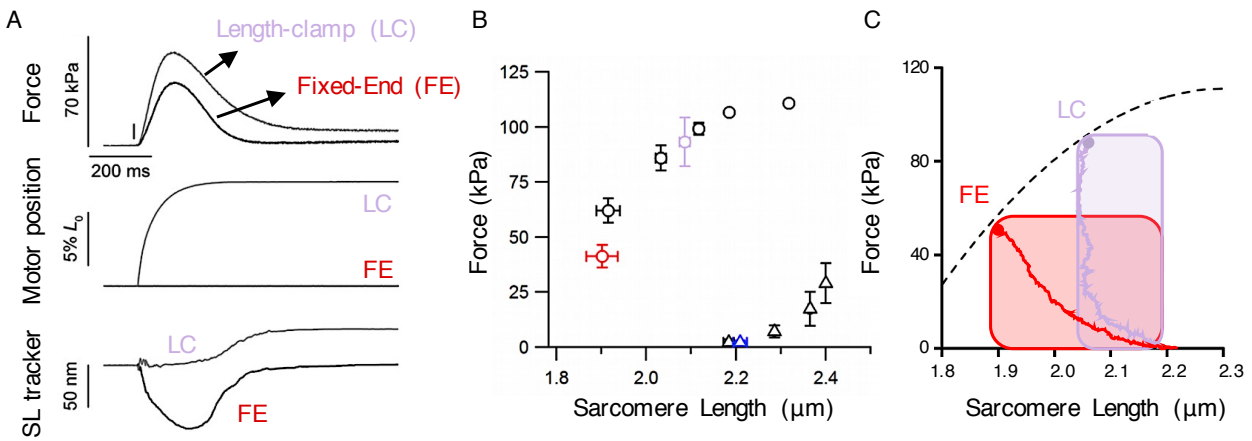

Figure 4.2. Different twitch conditions used to investigate the load-dependent structural dynamics of the cardiac thick filament.

(**A**) Sample traces of the different twitch protocols with real-time sarcomere length tracking using a striation follower (bottom trace). During a twitch in fixed-end (FE) conditions, the sarcomere length (SL) was set to 2.2 µm and the ends of the trabeculae were held fixed by the length controlling motor (middle trace). The SL was allowed to shorten against the compliance in the attachments of the preparation (bottom trace). During an LC twitch, a double-exponential, feedforward stretch from the motor was imposed on the trabecula to prevent the SL from changing. (**B**) Twitch force-SL values (circles), including FE condition (red), LC conditions (purple). Passive force-SL values are shown by the triangle symbols, including the diastolic (Dia) condition of SL 2.2 µm (shown in blue). (**C**) The striation follower allowed visualization of the change in SL during a twitch in each condition. In FE conditions (red), the SL shortened from 2.2 µm to ~1.9 µm, whereas the SL during a LC twitch shortened from 2.2 µm to ~2.1 µm. This protocol allowed us to simulate contraction against different afterloads, mimicking a pressure-volume loop of the cardiac cycle (shown by the loops in panel C) beginning from the same end-diastolic volume (*i.e.*, SL). (Figure modified from Caremani *et al.*, 2016 and Reconditi *et al.*, 2017.)

Sarcomere length was measured at the ID-02 beamline at ESRF using the moveable detector system. This system allows the photon detector to be placed 31 meters away from the sample, which yields resolution of ultra-small-angle X-ray diffraction patterns, including sarcomere-based meridional reflections. Figure 4.3A shows sample sarcomere-based reflections

of the diastolic (Dia) condition and the peak of a twitch in fixed-end (FE) and length-clamp (LC) conditions. Using the spacing of the second-order sarcomere reflection (Figure 4.2B), the sarcomere length was measured for each condition.

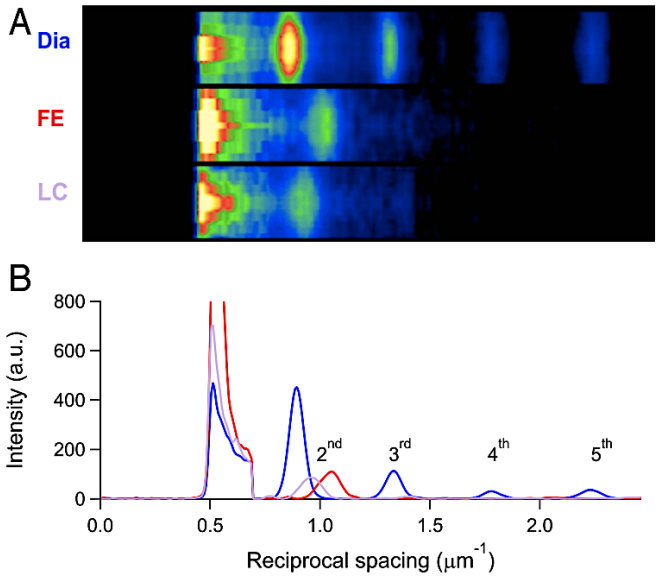

Figure 4.3. Sarcomere-based X-ray reflections.

(**A**) With the detector 31 meters from the sample, the 2nd order sarcomere-based X-ray reflection was determined at the rest (diastole; Dia), or at the peak of either a fixed-end twitch (FE) or a length-clamp twitch (LC). (**B**) Using a line-scan of the intensity profile, the sarcomere length of the intact trabecula was measured under each condition using the X-ray reflections [figure from reference (77)].

4.2.5. X-ray data analysis and statistics

X-ray diffraction data were analyzed using Fit2D (A. Hammersley, ESRF), PeakFit (SYSTAT Software, Inc.) and IgorPro (WaveMetrix, Inc.). Patterns were centered and aligned using the equatorial 1,0 reflections, then mirrored horizontally and vertically (quadrant-folded).

The patterns were analyzed individually, except for the measurements on the weaker reflection M6 that required to add the patterns collected at 1.6 m to improve the signal-to-noise ratio. The number of trabeculae was chosen in order to measure changes in relative intensities and spacings of the relevant X-ray reflections with adequate signal-to-noise ratio and minimize the number of animals to be sacrificed. This could be achieved with a small number of trabeculae because the X-ray signals can be measured with extremely high precision and low biological variability. The distribution of diffracted intensity along the meridional axis of the X-ray pattern (parallel to the trabecula axis) was obtained by integrating the 2D pattern from 0.021 nm^{-1} on either side of the meridian. Given the arcing of the reflections (Figure 4.1A), these integration limits were not appropriate to accurately determine their spacing, thus, for the spacing, a narrower integration, 0.006 nm^{-1} on either side of the meridian, was used. The first myosin layer line (ML1) intensity distribution was obtained by integrating the region between 0.064 and 0.037 nm^{-1} from the meridional axis. The small residual background was removed using the intensity from a nearby region of the X-ray pattern containing no reflections. The total intensities of the reflections were then obtained by integrating the axial distribution in the corresponding regions: M3, 0.066–0.073 nm^{-1}, M6, 0.133–0.144 nm^{-1}, and ML1, 0.019–0.023 nm^{-1}. The limits for the ML1 integration were chosen to exclude the contribution of the partially overlapping first order actin layer line. The intensities were then corrected to account for the different mass of the trabecula crossed by the X-ray beam at the different SL. M3 and M6 reflections were further corrected for the different cross-meridional widths, determined from the radial (parallel to the equatorial axis) intensity distribution in the axial regions specified above, using a Gaussian fit in the region ±0.04 nm^{-1} across the meridian. The combined point spread function was negligible compared with the radial width of the M3 reflection. The interference components of the M3 reflection were determined by fitting

multiple Gaussian peaks with the same axial width to the meridional intensity distribution, and the total intensity of the reflection was calculated as the sum of the component peaks. The spacing of the reflection was determined from the weighted mean of the component peaks and calibrated using an M3 spacing of 14.34 nm in the resting frog skeletal muscle fiber mounted in the same experimental set up at 1.6 m camera length.

4.3. Results

4.3.1. Physiological positive inotropes do not change the resting state of myosin motors during cardiac diastole

There are several physiological factors that augment contractility in cardiac muscle, including increased phosphorylation of sarcomere proteins and increased sarcomere length. We hypothesized that there are different structural responses in the diastolic thick filament unique to two inotropic interventions that equally potentiate contractility: (*i*) increasing sarcomere length (SL), and (*ii*) treatment with the beta-adrenergic agonist isoprenaline. We tested this hypothesis using X-ray diffraction-based analysis of the structure of resting, intact cardiac trabeculae from rat hearts at different SL and before and after isoprenaline treatment.

Figure 4.4 shows the effects of 0.1 μM isoprenaline on a twitch of an intact cardiac trabecula for a range of SL. Similar to increasing the outer (extracellular) calcium concentration ($[Ca^{2+}]_o$) from 1 mM to 2.5 mM at SL 2.1 μm (diamonds versus circles, respectively, in Figure 4.4A), addition of isoprenaline increases the peak twitch force (T_p) by approximately 70% (Figure 4.4B). Given that either increasing SL or a 2.5-fold increase in $[Ca^{2+}]_o$ causes a similar increase in T_p, we chose to only increase SL in control conditions as to not interfere with other regulatory

mechanisms operating within the cardiomyocyte. Nevertheless, we show that adding 0.1 μM isoprenaline and increasing SL have similar force augmentation effects on T_P (Figure 4.4).

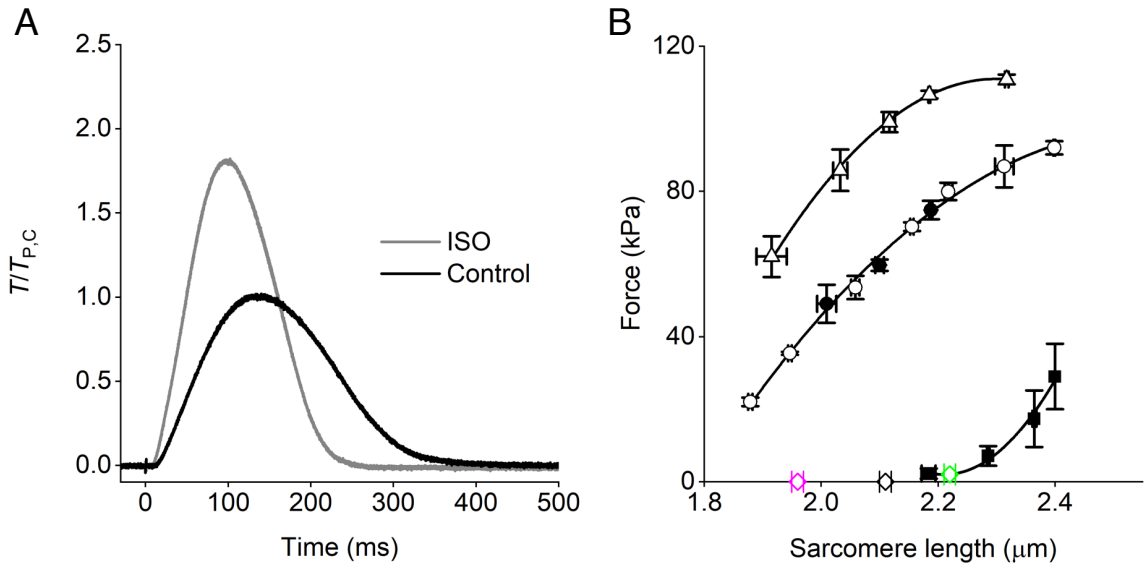

Figure 4.4. Mechanical responses of intact cardiac trabeculae under two inotropic protocols. (**A**) Time course of the twitch force with $[Ca^{2+}]_o$ 1 mM and SL 2.1 μm either in control (black trace) or in the presence of 10^{-7} M ISO (gray trace). Force is relative to T_P in control. The artefact on the force trace (at 0 ms) marks the stimulus start. (**B)** Relations between twitch peak force (T_P) and sarcomere length at 1 mM $[Ca^{2+}]_o$ (circles) and 2.5 mM $[Ca^{2+}]_o$ (triangles). Passive force shown by squares. The lines are polynomial fits to points. Data from Caremani *et al*. (2016). The force–sarcomere length relation is unique independent of fixed-end (filled circles) or sarcomere-length clamp condition (open circles). Open diamonds indicate the three sarcomere lengths used for the X-ray study of the effect of sarcomere length with $[Ca^{2+}]_o$ 1 mM. Error bars are SEM for four trabeculae. (Image courtesy of Vincenzo Lombardi from Caremani *et al.*, *in revision*.)

Next, given that either increasing SL or adding isoprenaline causes nearly a twofold increase in twitch force, we investigated whether either inotropic treatment has appreciable structural effects on the myofilaments prior to the twitch (during 'diastole') that may potentiate

the ensuing contraction. To do so, we investigated the spacing and intensity of the meridional and equatorial X-ray reflections in intact resting cardiac muscle for a range of SL before and after treatment with 0.1 μM isoprenaline. The top column of Figure 4.5 shows the quantification of the equatorial X-ray reflections in control condition ($[Ca^{2+}]_o$ = 1 mM; black circles) and after treatment with isoprenaline (white circles) for a range of SL. As expected from previous work, the spacing of the 1,0 reflection ($d_{1,0}$), which corresponds to the thick-to-thick filament lattice spacing (Figure 4.1C) decreases linearly as SL increases (Figure 4.5A, black circles). The spacing of the 1,1 reflection ($d_{1,1}$), corresponding to the distance between thick and thin filaments (Figure 4.1C) has a similar decrease as SL increases (Figure 4.5B, black circles). However, treatment with isoprenaline has no discernable effect on either reflection, and therefore does not significantly alter lattice spacing independent of SL (Figure 4.5A & B, white circles).

Figure 4.5C-H show the effects of SL and isoprenaline on the spacing of the meridional reflections. Interestingly, the spacing of each of the myosin-based reflections (M1-M6; Figure 4.5C-G, filled circles) are not affected by increases in SL. However, with treatment of 0.1 μM isoprenaline, the spacing of the M1 reflection, which is associated with the perturbation in the axial repeat of three consecutive myosin crowns within each 43 nm repeat in the C-zone (Figure 4.5C, white circles). This suggests that, in agreement with previous studies (176, 177), MyBP-C phosphorylation has appreciable structural effects on the myosin filament, at least in the C-zone where MyBP-C is localized.

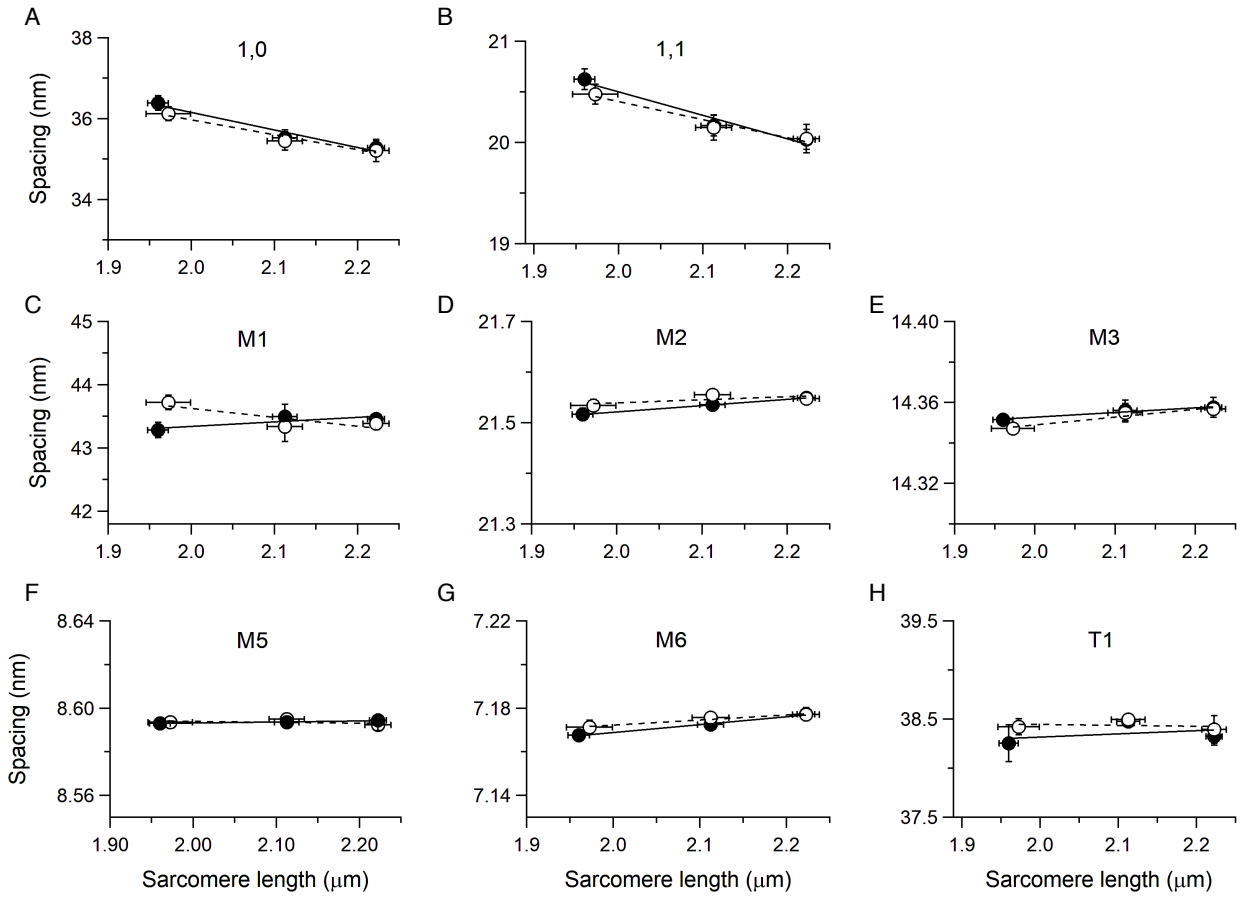

Figure 4.5. SL dependence of the spacing of the X-ray reflections in resting intact cardiac trabeculae under two different inotropic protocols.

Equatorial 1,0 and 1,1 reflections, the myosin-based M1-M6 meridional reflections, and the troponin-based T1 reflection. Filled circles, control; open circles, 10^{-7} M isoprenaline (ISO). Continuous and dashed lines are the linear fit to filled and open circles respectively. Mean ± SEM, four trabeculae. (Image courtesy of Vincenzo Lombardi from Caremani *et al.*, *in revision*.)

The intensities of each X-ray reflections are shown in Figure 4.6 for each condition, normalized to the intensity of the same reflection in control conditions at SL 2.1 μm ($I_{2.1,c}$). The intensity of the 1,0 increases as SL is increased in both control and ISO condition (Figure 4.6A, black and white circles, respectively), while the intensity of the 1,1 reflection is unaffected by SL (Figure 4.6B).

Interestingly, the relations versus SL of the intensity of the various reflections (Figure 4.6) in preparations treated with ISO (open circles) are quite similar to those determined in control (filled circles), with the only exceptions of I_{M1} (Figure 4.6D) and I_{T1} (Figure 4.6E), which exhibit a small but systematic reduction (~20%) so that, as shown by the vertical shift of the respective linear fits, the ISO relations (dashed lines) lie below those in control (continuous line).

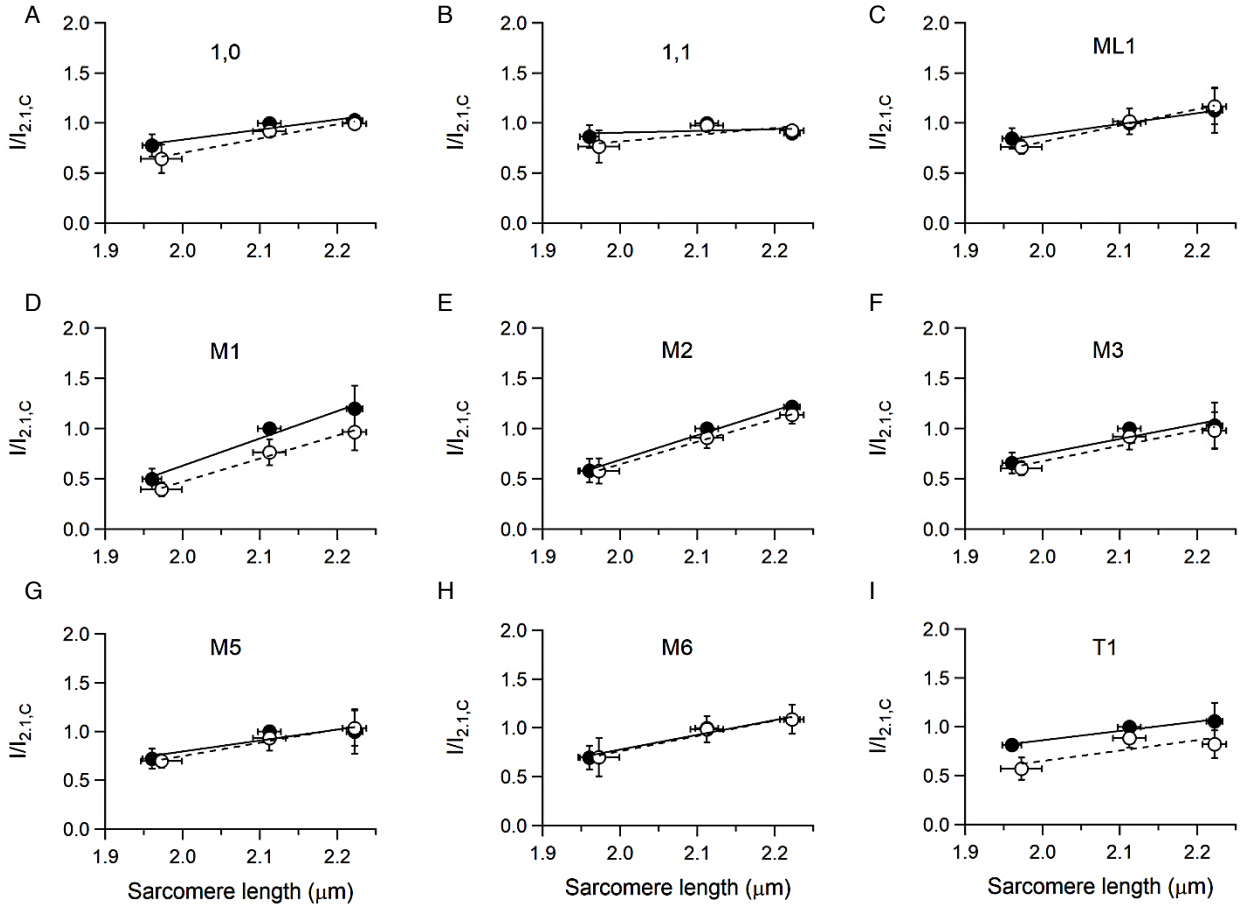

Figure 4.6. SL dependence of the periodicity of the myofilaments and sarcomere lattice geometry in resting intact cardiac trabeculae under two different inotropic protocols.

Sarcomere length dependence of the intensities of the equatorial 1,0 and 1,1 reflections (**A** & **B**) for control conditions and treatment with 0.1 μM isoprenaline (black and white circles, respectively). The myosin-based ML1 layer line (**C**) and M1-M6 meridional reflections, and the troponin-based T1 reflection. Intensities are relative to the intensity in control at SL 2.11 μm. Data,

symbols and lines as explained in Fig 4.5. (Image courtesy of Vincenzo Lombardi from Caremani *et al.*, *in revision*.)

As observed in control, the $I_{1,0}$ after treatment with isoprenaline (ISO) increases with SL (+55% from SL 1.98 to 2.22 μm) more than the $I_{1,1}$ (+21%) (first two panels in Figure 4.6, open circles), so that for the same SL, as shown at SL 2.11 μm in Fig. 4.7, the ratio $I_{1,1}/I_{1,0}$ in ISO (dashed) is not significantly different to that in control (gray).

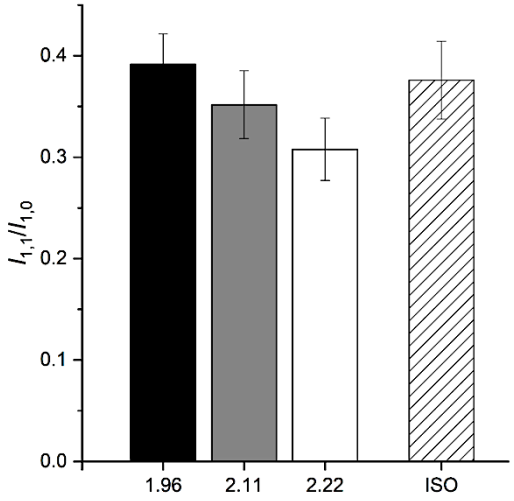

Figure 4.7. Intensity ratio of resting intact trabeculae under different inotropic conditions.
The intensity ratio of the 1,1 over the 1,0 equatorial reflections ($I_{1,1}/I_{1,0}$) during the diastole at different sarcomere lengths (black, 1.96 μm; gray, 2.11 μm; white, 2.22 μm) and with 10^{-7} M ISO at 2.11 μm sarcomere length (dashed). Means ± SEM, four trabeculae. (Image courtesy of Vincenzo Lombardi from Caremani *et al.*, *in revision*.)

4.3.2. Changes in the myosin-based reflections with force development

Based on the lack of a structural effect on the resting myosin filament with treatment of isoprenaline or increase in SL, we hypothesized that a key structural component of force augmentation in cardiac muscle is a mechanism based on thick filament activation that occurs downstream of the canonical, calcium-mediated thin filament activation. It was recently demonstrated that skeletal muscle exhibits a thick filament mechanosensing-based mechanism of activation, whereby myosin motors are released from their resting conformation in a stress dependent manner. That is, as more myosin motors bind to actin to form strong, force-generating cross-bridges, the tension borne by the thick filament backbone causes a disturbance in the resting regulatory state of the thick filament and releases more myosin motors, acting as a rapid, feed-forward mechanism of activation. We tested the hypothesis that a similar mechanism exists in intact cardiac muscle, regardless of the possible potentiation mechanisms occurring at rest, by examining the myofilament structure and lattice geometry at the peak of a twitch and compared it with that of resting muscle. As discussed in the Methods section (section 4.2), trabeculae were exposed to X-ray in one of three states: (*i*) at rest, (Diastole; Dia), (*ii*) at the peak of a twitch in fixed-end (FE) controlled conditions, or (*iii*) at the peak of a twitch in sarcomere length-clamp (LC) control conditions.

Figure 4.8 shows the results of the meridional reflection analysis in the three conditions, Dia, FE, and LC (panel A), with the corresponding sample intensity profiles (panel B; Dia in blue, FE in red, and LC in purple). The myosin-based reflections (M1-M6; Figure 4.8B) were visible in all three conditions, as well as the thin filament, troponin-based reflections (T1 and T3; Figure 4.8B). The spacing of the X-ray reflection were measured by fitting the intensity profiles to a Gaussian and determining where the center of the curve is in relation to the center of the image.

Figure 4.8C shows the intensity profiles of the M3 reflections for each condition which corresponds to the axial repeat of the myosin motor crowns along the thick filament, and Figure 4.8D shows the quantification of the spacing of the M3 reflection for each condition. While the intensity of the M3 profile is strongest in diastole (Dia) and not different between FE and LC twitches (Figure 4.8C), it is clear that the spacing of the M3 reflection increases dramatically for the LC twitch and is not different between the peak of a twitch in FE conditions and diastole (Figure 4.8D). Finally, the intensity and spacing of the M6 reflection, which are associated with the helical periodicity of the thick filament backbone, are shown in Figure 4.8 E & F, respectively. Interestingly, the intensity of the M6 reflection is not different between the three conditions (Figure 4.8E), while the spacing significantly increases between diastole and the peak of either the FE or LC condition (Figure 4.8F).

To further elucidate the precise mechanisms that are contributing to thick filament activation in cardiac muscle, we examined whether there is a structural difference between a resting myosin filament that is between twitches (diastole) and a resting myosin filament that has not been activated in 20 minutes (quiescent). Interestingly, there are not any structural differences in myosin filaments from trabeculae that have been quiescent for 20 minutes, or in diastole after the 10^{th} twitch, or in diastole after the 20^{th} twitch (black, blue, and yellow lines in Figure 4.9, respectively). This suggests that there are not history-dependent structural dynamics in intact cardiac muscle.

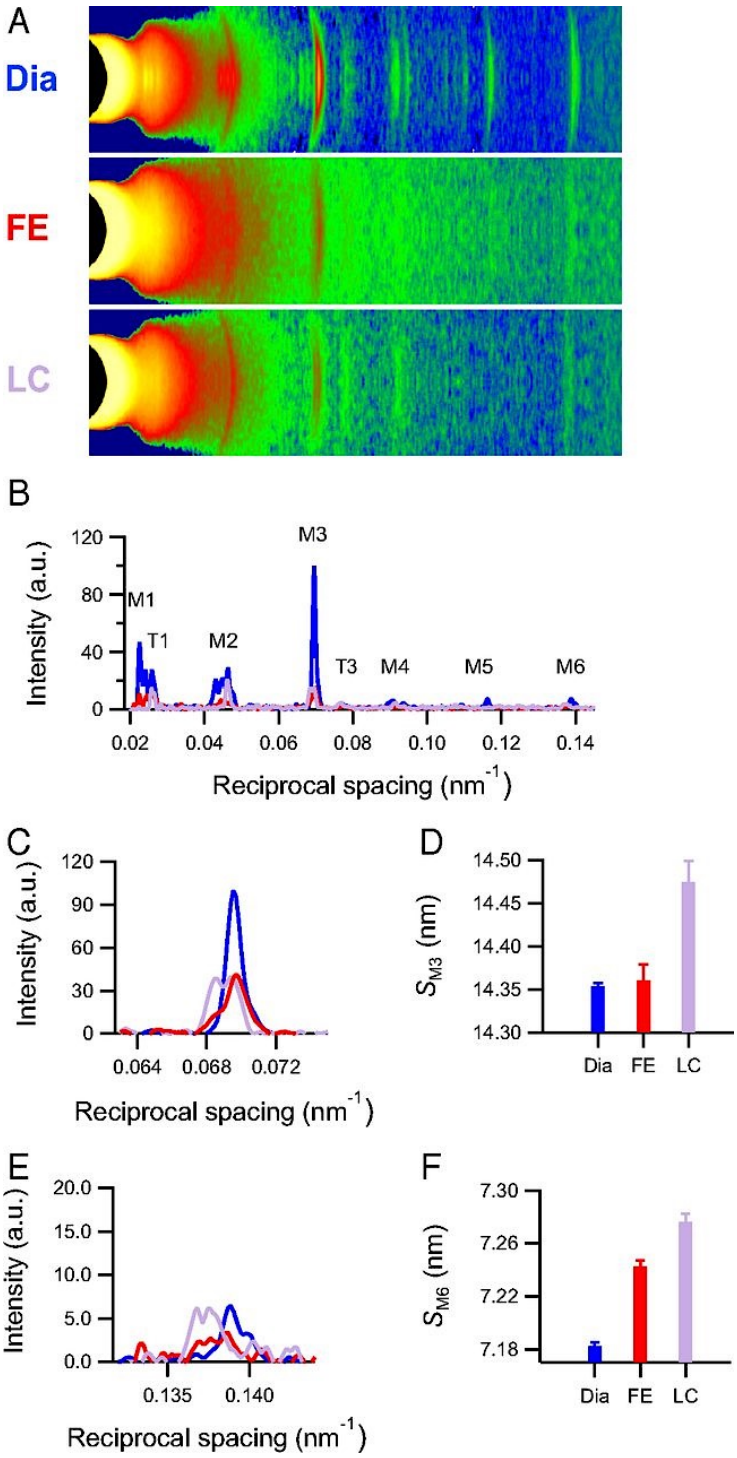

Figure 4.8. Sample meridional reflections during diastole and twitches of different loading conditions.

(**A**) With the photon detector at a 1.6-meter distance from the intact trabecula, the meridional X-ray reflections could be captured in diastole (Dia; blue), at the peak of a fixed-end (FE; red) twitch,

or at the peak of a length-clamp (LC; purple) twitch. (**B**) Sample intensity profile outlining the significant peaks of the X-ray reflection intensity, including the myosin-based reflections (M1-M6) and the thin filament, troponin-based reflections (T1 and T3). The intensity (**C**) and spacing (**D**) of the M3, and the intensity (**E**) and spacing of the M6 (**F**) reflection for each load condition (Image from Reconditi *et al. PNAS* 2017).

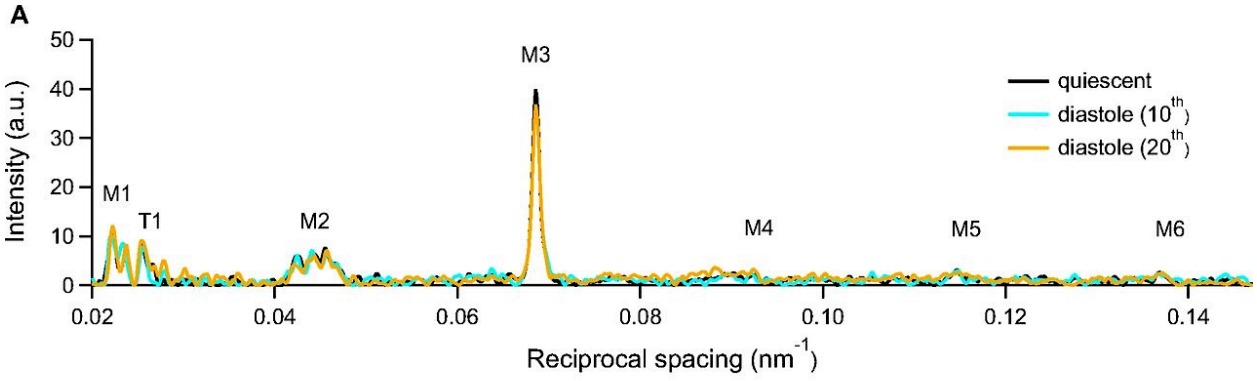

Figure 4.9. Myosin-based reflections are not different between quiescent trabeculae and trabeculae in diastole between twitches.

Quiescent trabeculae (black) are defined as not having been stimulated since dissection from the right ventricle, while the diastole reflections are taken after the first 10 twitches (blue) and 20 twitches (yellow). There are not any discernable differences in the spacing or intensity of each reflection in each case. (Image from Reconditi *et al. PNAS* 2017).

Next, we investigated the effects of the varying loading conditions on an intact fiber on the myofilament lattice geometry and the radial distribution of the myosin motors along the thick filament. Figure 4.10A shows the lattice spacing ($d_{1,0}$) for the intact trabecula for the three conditions (Dia, FE, and LC, shown as blue, red, and purple curves, respectively). The lattice spacing decreases as SL increases, as expected from previous studies (182, 183), as well as the

data shown in Figure 4.5 A & B. Interestingly, this relation occurred despite the fact that the trabecula was at the peak of a twitch at shorter SL (red and purple points on Figure 4.10A).

Interestingly, the intensity of the off-meridional reflection, the myosin layer line 1 (ML1), which corresponds to the radial position of the myosin head mass (relative to the thick filament backbone), decreases progressively going from Dia, to FE to LC (Figure 4.10D). This strongly suggests that the thick filament is in a more active state with more of its myosin motors in the ON position for the stronger, LC twitch compared to the weaker FE twitch.

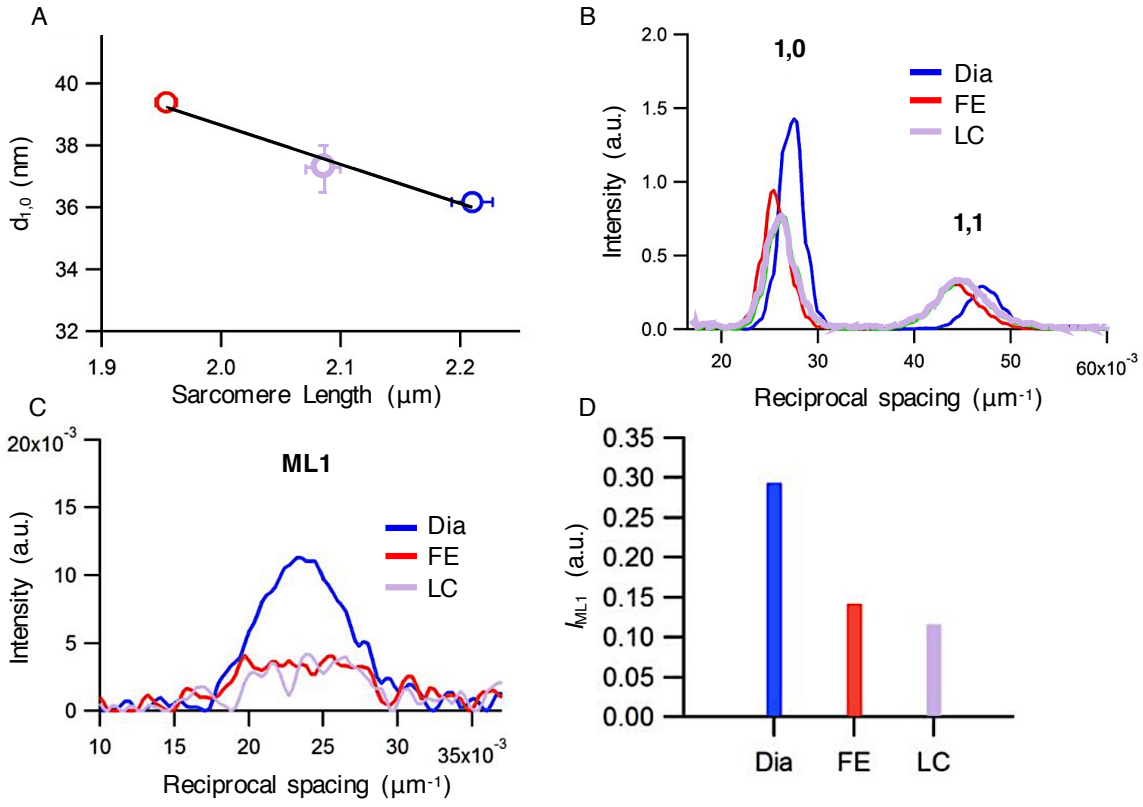

Figure 4.10. Structural dynamics of the cardiac sarcomere during diastole and twitches of different loads.

The lattice spacing ($d_{1,0}$; **A**), the intensity profiles of the equatorial reflections (1,0 and 1,1; **B**), and the intensity of the myosin layer line (ML1; **C** & **D**) of intact trabeculae under load control. Dia

(blue) is diastole, FE is fixed-end (red), and LC is length-clamp (purple) (Image from Reconditi *et al. PNAS* 2017).

4.3.3. Changes in the state of myosin motors during systole calculated by simulation of the M3 intensity profile with a structural model of the sarcomere

Lastly, the meridional X-ray reflections were used to calculate the fraction of motors in the OFF state (*i.e.*, resting on the thick filament backbone, with their heads folded towards the M-line) using a previously described structural model (68). This model calculates an intensity profile for the average position of myosin heads relative to a resting conformation based on the spacing and intensity of the M3 meridional X-ray reflection. In diastole, the motors are on the surface of the thick filament folded back toward the center of the sarcomere (blue motors in Figure 4.11A).The model assumes a an axial periodicity of 14.35 nm and separated by a bare zone of 161 nm for the resting thick filament, and the axial mass density profile of the OFF motors is represented by a Gaussian centered at −7.97 nm from the head–rod junction and σ = 3.5 nm (Figure 4.11B). At the peak of the twitch force (T_p), the bare zone is assumed to extend according to the compliance of the thick filament [17.5 nm/MPa/μm (184)], and the axial periodicity of the motors along the filament is adjusted to the observed spacing of the M3 reflection. In the LC twitch (Figure 4.11C & F), the free parameters for fitting the M3 intensity profile are the fraction of attached force-generating motors (f_A) and the rotation of the myosin head with respect to the filament axis, with a uniform angular dispersion of ± 17° starting from the nucleotide-free (rigor) crystallographic structure of the myosin motor in its actin-attached orientation [(185); see Supplemental information from Reconditi *et al., PNAS* 2017]. In the FE twitch, the tilting of attached motors is constrained by the value obtained from the LC twitch simulation, and f_A is constrained by the direct

proportionality between T_p and the number of attached motors (13), so that the only free parameter is the fraction of motors in the off state (f_{OFF}).

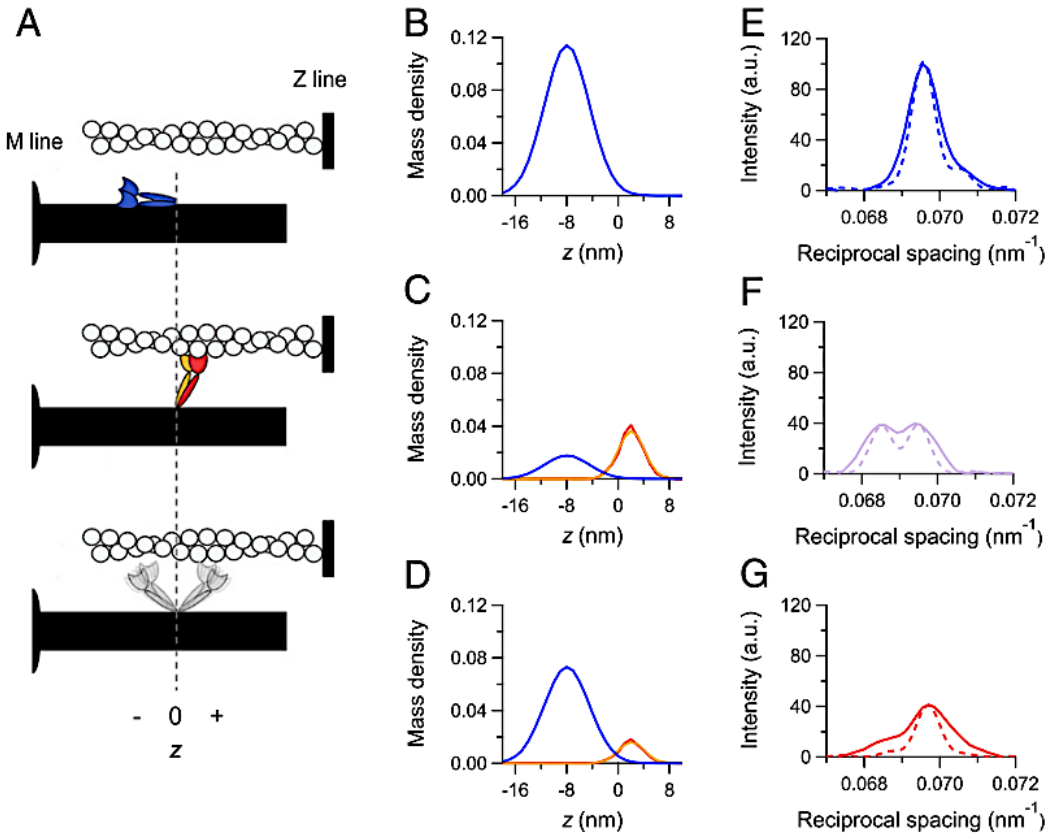

Figure 4.11. Structural model of the mass distribution of the myosin filament reveals load-dependent regulation of myosin motors.

Mass intensity predictions based on a structural model of the average position of the myosin heads. (Image from Reconditi *et al. PNAS* 2017).

The results of the simulation of the myosin mass position corroborate the prediction based on the reduction of the ML1 reflection intensity and increased spacing of the M3 and M6 reflections that the LC twitch increases the fraction of motors in an ON conformation compared with twitches in the FE condition. Based on the simulation, the fraction of OFF motors (f_{OFF}) at the peak of a twitch in LC conditions 0.15 ± 0.10, whereas f_{OFF} at the peak of a twitch in FE

conditions is 0.64 ± 0.08. Interestingly, the fold-change in the f_{OFF} is directly proportional to the change in T_p. That is, the fraction of motors leaving the resting conformation is directly proportional to the amount of force produced during the twitch. This suggests that the degree to which the thick filament is activated strongly depends on the load against which the sarcomeres are contracting.

4.4. Discussion

4.4.1. The structural basis of positive inotropes in cardiac muscle

This work reports multiple X-ray diffraction studies on intact cardiac trabeculae to investigate the effects on the regulatory state of the thick filament in systole and diastole with two positively inotropic interventions that almost double the twitch peak force. The first intervention is to increase sarcomere length in the range 1.95-2.22 μm, to exploit the length-dependent activation that is the cellular basis of the Frank-Starling response (186). We provide an integrated view of the Frank-Starling law that combines mechanical, structural, and energetic aspects of cardiac performance. We show that mechanosensing in the thick filament adjusts the number of myosin motors that are recruited from their resting conformation, making them available for strong cross-bridge formation and ATP hydrolysis. The second inotropic intervention is the addition to the perfusion solution of the β-adrenergic effector isoprenaline 0.1 μM that promotes the PKA-dependent increase in the degree of phosphorylation of many sarcomeric proteins, among which is MyBP-C. This thick filament accessory protein in demembranated preparations is thought to potentiate the contraction, in relation to its degree of phosphorylation, via the disruption of the interacting head motif (IHM) and mobilization of the myosin heads from their OFF state even at

low [Ca^{2+}] (176, 179). Interestingly, we find that the results of the inotropic agents studied here do not act through the mobilization of myosin heads prior to and independently of the Ca^{2+}-dependent thin filament activation. This is evident by the fact that all of the X-ray signals marking the OFF state of the thick filament are preserved independent of the increase in SL or addition of isoprenaline (Figures 4.5 and 4.6). In particular, mobilization of myosin heads from their OFF state is contradicted by the behavior of the following parameters: (*i*) the intensity of ML1, which depends on the ordered disposition of the myosin heads along three-stranded helical tracks on the surface of the thick filament, (*ii*) the intensity and fine structure of M3, which depends on the OFF state of the myosin heads lying on the surface of the thick filament folded back towards the center of the sarcomere, (*iii*) the intensity of the forbidden reflections (M2, M5), which depends on the perturbation in triplets of the axial repeat of myosin heads in the C-zone, (*iv*) the intensity ratio $I_{1,1}/I_{1,0}$, which depends on the proximity of myosin head mass to the thick filament.

In contrast to these results, myosin head mobilization away from their resting state has been consistently found in demembranated cardiac myocytes at low [Ca^{2+}] following whatever inotropic intervention, either increase in SL (81, 82) or increase in MyBP-C phosphorylation (176), or an increase in RLC phosphorylation (82, 174). Moreover, the head mobilization by MyBP-C phosphorylation has been recently confirmed by electron microscopy on isolated thick filaments (179). Under these conditions, the only explanation for the different sensitivity to inotropic interventions should be related to the preparation itself. It is possible that in permeabilized myocytes (and in isolated thick filaments) the IHM interactions that are putatively responsible for maintaining the resting conformation of myosin motors may be weakened by the permeabilization of the muscle preparations such that any inotropic intervention that implies further weakening of the intra- and intermolecular interactions responsible to the IHM state is sufficient to disrupt the

state and release the heads away from the proximity of the thick filament backbone. Moreover, in permeabilized myocytes at pCa 9, myosin heads can already be substantially away from their OFF state, as demonstrated with the fluorescent probe in the RLC (82). In this respect, it is worth noting that in skinned fibers from mammalian skeletal muscle X-ray meridional reflections are weaker and the fine structure of M3 reflection is different from that in the intact preparation and that the whole X-ray pattern partially recovers that of the resting intact muscle with the osmotic recovery of the lattice dimension (187).

4.4.2. An explanation for the SL-dependent increase of the intensity of all the reflections.

A general effect of the increase in SL from 1.96 to 2.22 μm is the increase in the intensity of all the reflections mentioned above, as well as the actin-based meridional T1 reflection (Fig. 4.6). This finding was unexpected based on similar measurements done in resting fibers from frog skeletal muscle (163), and likely depends on some basic structural differences between the two striated muscle types. As reported in the literature: (*i*) the length of the thin filament (L_A) is 0.1 μm longer in cardiac muscle (1.04 μm) than in frog skeletal muscle (0.94 μm) (5), and (*ii*) the width of the Z line (Z_w) is ~50 nm larger in the cardiac muscle (100 nm) than in the frog skeletal muscle (188). The minimum SL at which there is no double overlap of the thin filament at the center of the sarcomere (SL_{min}) for either muscle can be calculated with the equation $SL_{min} = Z_w + 2 \times L_A$ and is 2.18 μm for the cardiac muscle and 1.93 μm for the skeletal muscle. It is evident, from these structural considerations, that in the trabecula for SL's < 2.18 μm, and thus for a large portion of the SL range explored by X-rays in this study (1.96-2.22 μm), there is a small but increasing portion of thin filament undergoing double overlap as SL decreases. This is likely the structural

basis for the perturbation of the ordered three-dimensional disposition of the filaments in a progressive way with the reduction of SL below 2.18 μm.

Another result that is likely related to thin filament structure is the decrease of the intensity ratio of equatorial reflections ($I_{1,1}/I_{1,0}$) with the increase in SL. As shown by Figure 4.6 A & B, the reduction is mainly related to the smaller SL-dependent increase of $I_{1,1}$ with respect to $I_{1,0}$. Noteworthy a reduction of $I_{1,1}$ with increase in SL, without reduction in $I_{1,0}$, has been reported for relaxed skeletal muscle [(182) and references therein] and attributed to the increase of lateral thin filament disorder with the increase in SL and the corresponding decrease of the length of the thin filament overlapping the thick filament, and thus constrained within the double hexagonal lattice. In the heart muscle, due to the larger thin filament length, the increase in SL in the range explored by X-ray (1.95-2.22 μm) has the combined effect of reducing the double thin filament overlap at the sarcomere center and increasing the not overlapped portion of thin filament in the I-band, in this way explaining the reduced increase of $I_{1,1}$ and consequently the reduction in the ratio $I_{1,1}/I_{1,0}$. This analysis demonstrates that, even if the change in the ratio (42) with SL is in the opposite direction of that expected by a radial shift of the mass of the myosin heads moving away from the helical track, there are other structural reasons against the usual interpretation of the length-dependent changes in $I_{1,1}/I_{1,0}$ in terms of radial movement of the mass.

The OFF state of the thick filament is characterized also by short backbone periodicity, as measured by the spacing of the myosin-based meridional reflections, in particular the M6 reflection (S_{M6} = 7.17 nm), which is the second order of a periodic structure with the same periodicity of the myosin heads at rest [14.35 nm; (173)], but mainly originating from the backbone of the thick filament. M6, with respect to M3, is much less sensitive to head movements that may influence its spacing, and thus is a better measure of the change in extension of the filament [either

elastic or structural; (140, 157)]. Actually, as shown in the second and third row of Fig. 4.6, the spacing of all the myosin-based meridional reflections slightly increases with SL. In particular, the increase of S_{M6} at SL 2.22 μm (+ 0.13%) is more than twice larger than that of S_{M3}. Noteworthy, 2.22 μm is the SL at which the passive tension starts to rise (green diamond in Fig. 4.4B). In this respect the behavior of the spacing of M6 and M3 reflections is quite similar to that in frog skeletal muscle fibers at SL ~2.7 μm, which in this preparation is the sarcomere length at which the passive force starts to rise. This common behavior at the threshold of the structural response of the thick filament to the passive force indicates that the stress sensitivity shown through changes in S_{M6} cannot be exclusively related to LDA in the trabecula but is a common feature of striated muscle.

Thus, based on the response to SL increase of equatorial and myosin-based meridional and layer line reflections, the SL-dependent inotropic effect at the basis of LDA does not imply any disruption of the IHM characterizing the OFF state of the myosin motors at low calcium.

4.4.3. The effects of isoprenaline on MyBP-C and troponin-based X-ray reflections.

Isoprenaline exerts its positive inotropic action through the PKA-induced phosphorylation of several sarcomeric proteins, that is: (*i*) proteins involved in the handling of Ca^{2+} (L-type Ca-channels, ryanodine receptors and phospholamban), (*ii*) troponin I, the phosphorylation of which induces a faster Ca^{2+} dissociation from troponin C and (*iii*) MyBP-C, which is believed to exert, also at low Ca^{2+}, a phosphorylation-dependent disruption of the IHM state and mobilization of the myosin heads. This multiple action of isoprenaline accounts for its positive inotropic effect on the twitch of the intact trabecula, which is accompanied by a faster rate of force rise and relaxation (Fig. 4.4A).

In this study we find that in the diastole of an electrically paced intact trabecula the intensity, fine structure and spacing of the X-ray reflections and their SL dependence are in general not affected by the addition of isoprenaline 10^{-7} M, which induces a 71% increase in T_P.

Two exceptions concern the intensity of the cluster around the M1 reflection, which includes the contribution of the MyBP-C present in the C zone of the thick filament, and the intensity of the T1 reflection which arises from the troponin periodicity along the thin filament. In ISO (open circles in Fig. 4.6) both reflections are ~20% lower than in control (filled circles). The paired t-test indicates that the differences are significant ($P<0.03$).

To interpret these changes in term of the regulatory state of the filaments, it must be considered that (*i*) the effect on these two reflections is not present using as inotropic intervention the increase in SL, (*ii*) the structural change induced by isoprenaline is strictly limited to M1 and T1 and thus, very likely, to MyBP-C on the thick filament and troponin on the thin filament, which are the filament proteins that represent the target of PKA-dependent phosphorylation induced by isoprenaline. However, not necessarily T1 changes have to be attributed to a direct effect of troponin I phosphorylation. The coupled effect of isoprenaline on M1 and T1 reflections could be explained by the dynamic interactions of MyBP-C with the thin filament, which are strengthened by phosphorylation (30, 33, 151).

4.4.4. The role of inotropic interventions in thick filament activation

None of the signals marking the OFF state of the myosin motors during diastole are affected by inotropic interventions that can double the systolic force, such as increased degree of phosphorylation of MyBP-C or increased SL. Thus, inotropic effectors present during diastole in relation to either neuro-humoral control of the heart or ventricle filling exert their effect on the

thick filament activation only once the Ca^{2+}-dependent thin filament activation is ON. The idea that thick filament activation is based on a mechanism downstream with respect to thin filament activation is also supported by the finding that switching ON of the myosin heads is independent of the diastolic SL and depends on the systolic SL (Fig. 4.8 & 4.11). All these data converge toward a unique explanation based on the role of thick filament mechano-sensing in striated muscle: recruitment of myosin motors from their energetically convenient OFF state depends on the stress on the thick filament (72, 75, 173). How do inotropic interventions operate in this scenario? The evidence that in relaxed skinned myocytes inotropic interventions promote the release of the heads away from the backbone of the thick filament by weakening the interactions responsible for the IHM state of the myosin molecule strongly sustains the idea that both LDA and MyBP-C phosphorylation set the gain of the positive feedback that relates motor recruitment to the stress on the thick filament (Fig. 9). It must be noted that this mechanism, if it is confirmed by direct investigation, is independent of and complementary to that operating on thin filament-based regulation through protein phosphorylation and sarcomere length-dependent force augmentation.

Mutations in cardiac MyBP-C and in the domains of cardiac myosin which interact with MyBP-C are responsible for 80% of cases of hypertrophic cardiomyopathy (HCM), an inherited heart disease characterized by thickening of the ventricular wall that diminishes the relaxation capacity and ventricular filling. These HCM-causing mutations are thought to disrupt the intermolecular interactions controlling the formation of the IHM and produce the hyper-contractility that leads to HCM (89, 189). The conclusion that the stress-sensing mechanism that switches ON myosin motors is modulated by the inotropic interventions opens a new scenario in which the HCM-causing mutations would operate by lowering the force threshold of the switch that controls the thick filament activation.

4.4.5. Downstream rapid regulation of myosin activation

Lastly, we investigated the structural effects on the thick filament at the peak of load-controlled twitches in intact cardiac muscle. To do so, we exploited the compliance in the attachments of the intact trabecula preparation to allow the sarcomeres to shorten against this relatively light load during the twitch [fixed-end (FE) conditions], and compared the results to the case where we apply a rapid (feed-forward) stretch to the trabecula during the twitch to prevent sarcomere shortening (181) and maintain contraction against a high load [length-clamp (LC) conditions (77)].

Length dependent activation (LDA) is often attributed to SL modulation of the sensitivity of the thin filament to cytosolic calcium concentration (186, 190), and many of the mechanisms governing this modulation are still unclear. Although, several factors have been shown to affect LDA and the Frank-Starling response, including phosphorylation of troponin (85), protein isoform expression (84, 191), and sarcomere protein mutations associated with hypertrophic cardiomyopathy (64, 192). Many of these studies focused on the resting sarcomere length prior to force production, in the context of cooperative mechanisms of activation that are enhanced at longer SL. However, the work we present here describes a new mechanism that occurs in wild-type cardiac muscle, in which thick filament mechanosensing can augment force production during systole based on the load against which the sarcomeres are contracting. This novel component of force modulation in cardiac muscle arises from our structural simulation which indicates that only a fraction of myosin motors leaves the resting conformation during a twitch, and this fraction depends on the level of force generated. Importantly, this occurs independently of the initial (end-diastolic) sarcomere length. Thus, it is not only the resting sarcomere length prior to a cardiac twitch that modulates contractility, but likely also a rapid, feed-forward mechanism involving thick

filament mechanosensing that releases myosin motors from their resting conformation depending on the degree of afterload during a twitch. Moreover, given that the structure of the myosin filament in intact cardiac muscle is relatively insensitive to treatment with isoprenaline, it is likely that the force augmentation accompanied by PKA-mediated phosphorylation of sarcomere proteins is acting through thin filament-based mechanisms of activation that work in concert with the thick filament mechanosensing upon calcium release during a twitch.

Chapter 5

Altered myosin allostery and electrostatics provide the structural basis of force augmentation by 2-deoxy-ATP in cardiac muscle

Abstract

We have demonstrated that 2-deoxy-ATP (dATP) enhances muscle contraction by increasing cross-bridge binding and cycling rates. Our recent molecular dynamics study (193) suggested that dATP increases the positive charge of the actin binding surface of myosin, thus enhanced binding may result from increased electrostatic interactions with actin in resting heart muscle. To test this hypothesis, we employed multiple biophysical approaches. X-ray diffraction analysis comparing dATP vs. ATP was performed on rat cardiac muscle in physiological (170 mM) and low (100 mM) ionic strength (μ) solutions at two sarcomere lengths (SL). In μ = 170 mM relaxing solution (pCa 9.0) with dATP, cardiac muscle had a significantly higher $I_{1,1}/I_{1,0}$ ratio, larger M3 spacing (S_{M3}) and lattice spacing ($d_{1,0}$) at both SL. These results suggest that, compared with ATP, dATP in resting cardiac muscle causes myosin to move towards actin filaments, and the space between adjacent crowns is similar to the activated myosin conformation (pCa 5.2). These effects were reduced or eliminated at μ = 100 mM where surface charge is increased (with ATP). This suggests that increased positive charge on the actin binding surface of myosin with dATP may indeed be responsible for enhanced cross-bridge binding. Brownian Dynamics simulations predicted the myosin·dADP·Pi structure has a significantly higher association rate to actin (than myosin·ADP·Pi) over a wide range of reaction distances, and this results primarily via an increase in positive (myosin) and negative (actin) contact pairs. Consistent with this, as the μ of solutions

in the *in vitro* motility assay was increased, more actin filaments remained on cardiac myosin-coated surfaces with dATP compared with ATP. Combined these data suggest that dATP enhances electrostatic interactions that facilitate increased weak myosin-actin binding, leadings to increased cross-bridge binding and contraction in cardiac muscle.

Significance Statement

Heart failure is a progressive condition leading to systolic and diastolic dysfunction without a current effective treatment to restore cardiac muscle function. We have previously demonstrated that 2-deoxy-ATP (dATP) enhances contractility of failing and nonfailing hearts. Here, we combine computational and experimental approaches to investigate the structural basis of dATP-induced force augmentation in cardiac muscle. Simulation data show that, compared with ADP, dADP restructures the actin-binding surface of myosin, increasing actin-myosin electrostatic interaction and association rates. X-ray diffraction data reveal that dATP primes relaxed myofilaments, making the resting sarcomere contacting dATP structurally similar to submaximally activated sarcomeres containing ATP. Our study suggests that cardiac muscle force augmentation by dATP stems from altered myofilament structure via enhanced electrostatic actin-myosin interaction.

5.1. Introduction

Heart failure (HF) is a chronic progressive condition in which the heart is unable to pump enough blood to meet the body's need for oxygen and nutrients, and it is a significant and growing medical challenge. Current treatments only slow progression of HF and do not rescue cardiac

muscle function. Consequently, there is a pressing need for novel therapeutic interventions that enhance cardiac contractility in failing hearts.

Cardiac muscle contraction is generated at the molecular level by cyclical, ATP-driven actin-myosin interactions, making myosin an appealing therapeutic target for treating HF. As such, there are several myosin-specific small molecule compounds currently being developed and tested to treat HF. One is the naturally occurring ATP analogue 2-deoxy-ATP (denoted dATP). We have previously demonstrated that dATP can be used by cardiac myosin in place of ATP as the substrate that fuels actin-myosin cross-bridge cycling (194). Moreover, we have shown that dATP increases contractility in rat myocardium (194), improves left ventricular function in a porcine model of myocardial infarction (195), and increase contractility of ventricular muscle from patients in human end-stage heart failure (196).

Chemo-mechanical studies suggest that the dATP-mediated force augmentation occurs by increasing cross-bridge binding and cycling rates (57, 197–199), but a precise structural explanation for this is lacking. A recent computational study using molecular dynamics simulations suggests that dATP behaves as an allosteric effector of pre-powerstroke myosin, such that when dADP·Pi is in the nucleotide binding pocket, local structural changes lead to exposure of more positively charged residues on the actin binding surface of myosin compared with ADP·Pi (193). This led us to hypothesize that dATP increases electrostatic interactions between cardiac myosin and actin, and that this should cause: (*i*) a destabilization of the resting conformation of myosin in the cardiac sarcomere, and (*ii*) prime myosin for binding to actin to increase cross-bridge formation during activation.

To test these hypotheses, we used a combination of computational and experimental techniques. Brownian Dynamics simulations [using Browndye software (200)] of myosin binding

to actin were used to predict actin-myosin electrostatic contract pairs and binding kinetics. Next, F-actin filament binding on cardiac myosin-coated surfaces in solutions of varying ionic strength was used to confirm the role of surface charge on actin-myosin binding with ATP vs. dATP. Finally, small-angle X-ray diffraction was used to investigate myofilament structure in sarcomeres with dATP- versus ATP-containing solutions under relaxed and Ca^{2+}-activated conditions, at short and long sarcomere lengths (SL), and in physiological and low ionic strength relaxation solutions. Browndye simulations suggested an increased number of electrostatic binding interactions between opposite charges on myosin and actin and a predicted highly non-linearly increased rate of binding as the distance of myosin from actin is reduced. The results of the equatorial X-ray diffraction pattern studies suggest that dATP destabilizes the resting conformation of myosin, facilitating the movement of the S1 head away from the thick filament backbone and towards actin. Lowering ionic strength (where the surface charge of proteins is increased) reduced the advantage of dATP in facilitating myosin movement, supporting the hypothesis that dATP induced structural changes in myosin promote myosin-actin interaction via increased electrostatic contacts. Moreover, meridional X-ray diffraction patterns indicated that the resting (pCa 9.0) myofilament structure with dATP closely resembles a submaximal active state with ATP. Taken together, the structural, protein biomechanical, and computational approaches used in this study suggest a molecular mechanism for enhanced myosin-actin cross-bridge binding with dATP in cardiac muscle that can explain the observed increased contraction of myofibrils, myocytes and tissue and enhanced ventricular function.

5.2. Methods

5.2.1. Animal use and ethics

All animal experiments were done in compliance with protocols approved by both the University of Washington and the Illinois Institute of Technology Institutional Animal Care and Use Committees and followed the "Guide for the Care and Use of Laboratory Animals" (National Research Council, 2011). Fourteen Fischer 334 rats were used in the experiments. Adult rats were euthanized by carbon dioxide inhalation and exsanguination.

5.2.2. Heart excision and trabeculae preparation

Rat hearts were rapidly excised and perfused via retrograde flow through the aorta with room-temperature and oxygenated (95% O2 and 5% CO2) Kreb-Henseleit (KH) solutions containing (in mM) 118.5 NaCl, 5 KCl, 1.2 $MgSO_4$, 2 NaH_2PO_4, 25 $NaHCO_3$, 1.8 $CaCl_2$, 10 glucose, and 20 2,3-butanedione monoxime, (BDM; used to minimize damage during dissection). Papillary muscles and trabeculae were carefully dissected from the right ventricle and immediately placed in 'skinning' solution containing 100 mM KCl, 10 mM MOPS, 5 mM EGTA, 9 mM $MgCl_2$ and either 1 mM dATP or 4 mM ATP (adjusted to pH = 7 with KOH), 1% (by volume) Triton X-100 and 1% protease inhibitor (sigma P8340) at room temperature. The solution was replaced every 30-45 minutes and preparations were removed after 90-120 minutes of incubation in the skinning solution. Custom aluminum T-clips were placed on each end of the preparations to facilitate mounting them between a rigid post and a dual-action length/force transducer (Aurora Scientific 402A). Skinned muscle preparations were then washed 3 times with solution without TritonX-100 on ice. Skinned muscle bundles were transferred to 'resting solution' (pCa 9.0)

containing either 2mM dATP or ATP before X-ray experiments. Preparations were only ever in contact with ATP or dATP-containing solution once skinning had begun.

5.2.3. X-ray diffraction data collection

X-ray diffraction experiments used the small-angle instrument on the BioCAT beamline 18ID at the Advanced Photon Source, Argonne National Laboratory (201). X-ray focal spots were about 0.5 x 0.5 mm at the sample and 0.06 x 0.15 mm at the detector with a maximum incident flux of 10^{13} keV photons/s. To reduce radiation damage, the beam was attenuated (typically 100-fold) using aluminum attenuators. The sample-to-detector distance was 3 meters. Skinned muscle preparations were mounted in a custom mechanics rig allowing for simultaneous X-ray diffraction and mechanics measurements. Fibers were mounted on a 500 mV force transducer (Model 402A, Aurora Scientific Inc.) and force was monitored by an ASI 610A data acquisition and control system. Solutions were changed using a syringe pump equipped with a multiway valve (Hamilton model 500). Sarcomere length was adjusted to ~2.0 μm using laser diffraction (or by adjusting the length such that the trabeculae is taut) and stretched by 15% to reach a length of 2.3 μm. Simultaneous force and diffraction pattern measurements were performed in pCa 9.0 and pCa 5.2 solutions. Diffraction patterns were collected only at the plateau phase of force development in activation pCa 5.2 solution. Small-angle X-ray diffraction patterns were collected on a CCD-based X-ray detector (Mar 165, Rayonix Inc. Evanston, IL). The instrument was calibrated using the 58.380 d_{001} peak of a silver behanate standard.

5.2.4. X-ray data analysis and statistics

The data were analyzed using data analysis programs belonging to the MuscleX software package (Version 1.13) developed at BioCAT (Jiratrakanvong et al., 2018). The lattice spacing and intensity ratios were measured using the "Equator" routine in MuscleX. The spacing and intensity of the M3 layer were measured using the "Diffraction Centroids" routine in MuscleX. The M3 intensity has been normalized with the total intensity of the estimated diffuse background generated by the "Quadrant fold" routine.

5.2.5. Brownian Dynamics Simulation

Simulations were performed using Browndye software to determine the differences between ATP- and dATP-bound myosin in terms of actin association (200). A previous Molecular Dynamics study on pre-powerstroke myosin (PDB: 1VOM) yielded the starting structures for our myosin rigid bodies (193). PDB files for Run 1 of the MD simulations at the 50,000 ps timepoint with only protein present (no ligands) were used for both ADP-bound and dADP-bound myosin. An actin monomer (PDB: 2ZWH) with all ligands removed was used to represent the thin filament to avoid electrostatic interactions with other binding sites along the filament. The actin and myosin-ADP structures were manually aligned using Visual Molecular Dynamics (VMD) to ensure that the myosin binding cleft on actin was appropriately oriented with the binding domain on myosin. To ensure the accuracy of the bound conformation, the actin monomer was aligned with Chain B of PDB:5KG8 (rigor myosin X co-complexed with actin) and the myosin structures were aligned with chain A of the same PDB structure. The dADP-myosin and ADP-myosin structures were aligned to an identical structure using VMD to ensure that the simulations are fully comparable.

PQR files were generated for all structures using PDB2PQR (202). Electrostatic potential grids were generated using APBS version 1.4 by solving the Poisson-Boltzmann equation using the Amber force field at 300K (203). A relative permittivity of 4 was used for the solute, and 78.5 for the solvent, and a 0.15 mM concentration of KCl was assumed for the system. A list of polar complex pairs (defined as 'contact pairs') was generated by comparing the myosin and actin input coordinates and considering pairs of atoms within 3.5 Å of each other, and the complete list of contact pairs can be found in associated files. A total of 49 atom pairs met the criteria for the ADP case, and 66 atom pairs met the criteria for the dADP case. A simulation trajectory was considered successful when at least 3 polar contact pairs were within the prescribed 'reaction distance' criterion, and association rates were determined by taking the inverse of the time required to reach at least 3 contact pairs. The reaction distance criterion was varied to examine a large range of possible rates since experimental association rate data for this system are unavailable. One million trajectories were performed to calculate the average association rates for both the ADP and dADP case.

5.2.6. In vitro motility assay

In vitro motility (IVM) assays were performed as previously described (31). In brief, cardiac myosin was prepared from male Fisher rat ventricles by first adding extraction buffer (0.3mM KCl, 0.15mM Imidazole, 10mM $Na_2P_2O_7$, 1mM $MgCl_2$, 2mM DTT) to minced ventricle tissue and stirring for approximately 30 minutes in a small beaker. Excess protein and residual actin was then removed by centrifugation for 1 hour with the supernatant then diluted in 2 mM DTT on ice for 1 hour to allow for myosin precipitation. Heavy meromyosin (HMM) and Rhodamine-phalloidin– (RhPh; Molecular Probes, Eugene, OR) labeled F-actin was prepared

fromrabbit skeletal muscle as described by Kron and colleagues (204). Harvested HMM was stored in -80°C for up to a week with 1% sucrose and 1% protease inhibitor (Sigma-Aldritch, St. Louis, MO).

Flow cells were constructed from two glass cover slips separated by 2-mm foam adhesion strips with a total chamber volume of ~60 μL. The lower side surface was coated with 0.1% nitrocellulose in amyl-acetate (Sigma). Experimental procedure was similar to Gordon and colleagues (205). Briefly, isolated HMM (0.16 mM) in Buffer D solution (2mM $MgCl_2$, 5mM EGTA, 5mM DTT, 10mM Imidazole, 0.2mM PMSF) was added to the flow cell for 3 minutes followed by bovine serum albumin (0.5mg/mL BSA) in actin buffer (AB) (50mM Imidazole, 2mM EGTA, 8mM MgCl2, 50mM KCl) to block nonspecific protein binding to the surface. This was then followed by an AB wash, addition of non-labeled sheared F-actin (1 μM) for 1 min, followed by another AB wash, and finally the addition of 0.5 mM ATP in AB. This was followed by another AB wash and RhPh F-actin was then added for 1 minute, finally followed by the experimental motility buffer (MB) with varying ionic strength. Percent composition of MB was 50% AB, 0.04% 1 mM DTT, 0.06% Cocktail solution (0.3M Catalase, 1.66M Gl. Oxidase, 50M D- glucose) 2 mM ATP/dATP, and 2M KCL). Variation in ionic strength depended on volume percentage of 2M KCL, with 0% at IS 50 and linearly increasing by 0.005% per 10 mM of IS. The motility buffer was then heated to 30°C on the slide for approximately 3 to 4 minutes. Each experimental slide was analyzed in at least six different regions, with the recording set for 10 seconds, each at 10Hz with IVM Image Acquisition. Recordings were then analyzed digitally, using a custom software developed by our laboratory that allows for filament counting and tracking.

5.3. Results

5.3.1. Brownian Dynamics simulations predict a more rapid myosin-dADP·Pi interaction with actin.

Weak cross-bridge binding is difficult to assess experimentally, as the rates of association and dissociation are very rapid. Thus, we employed Brownian dynamics simulations to estimate the 2nd order bi-molecular association rates for actin-myosin complex with either dADP.Pi or ADP.Pi (represented as dADP or ADP hereafter) bound in the nucleotide binding pocket of myosin. The atomistic detail of the simulation allowed us to examine the effects of each nucleotide on the structure of the actin-binding surface of myosin. Figure 5.1A shows the electrostatic surface of an actin monomer (top), an ADP-bound myosin S1 unit (middle), and a dADP-bound myosin S1 unit (bottom). The myosin-binding region on the actin monomer is predominantly negatively charged (red residues) while the actin-binding region of myosin is mainly positively charged (blue residues). In agreement with our previous work (193), with dADP-bound myosin (myosin-dADP) there was a wider distribution of positively charged residues in the actin-binding region compared with ADP. By aligning the protein structures, we determined how dADP affects the actin-myosin interaction interface (see Methods section). Figure 5.1B depicts the various residue interactions for actin and the actin-binding surface of myosin-ADP (black lines) or myosin-dADP (blue lines), where the thickness of the lines corresponds to the number of atoms in 'contact' (defined as being < 3.5 Å apart) between the two residues. There was a significant increase in the number of residue contact pairs with myosin-dADP compared to myosin-ADP (66 pairs for dADP compared to 49 for the ADP case). Moreover, for myosin-dADP, more contact pairs are associated with Histidine, Lysine, and Serine. Because Lysine and Histidine are positively charged residues at pH 7, the actin-binding region of myosin·dADP contains significantly more positively charged residues than

the actin-binding region of myosin·ADP which likely enables a stronger electrostatic interaction with the predominantly negatively charged myosin-binding surface of actin.

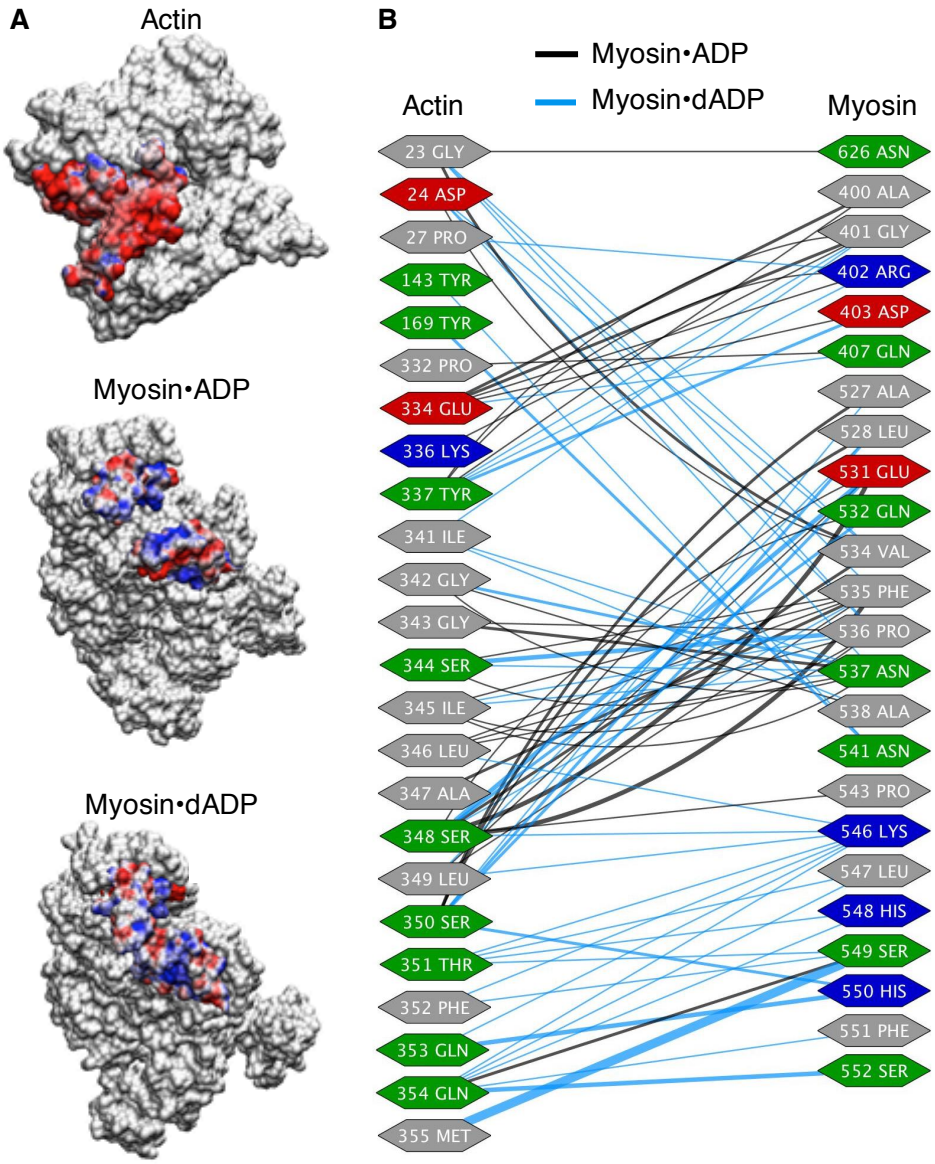

Figure 5.1. Computational structural model predicts a dATP-induced conformational change in myosin that increases actin-myosin interaction and association rates.

(**A**) An actin monomer (top) and either ADP-bound (middle) or dADP-bound (bottom) myosin S1 segments, where blue coloring indicates positively charged exposed residues and red indicates

negatively charged exposed residues. (**B**) Contact pairs of residues between actin and ADP-bound myosin (black lines) and dADP-bound myosin (blue lines) for an actin-myosin complex. The thickness of the line connecting the interacting residues corresponds to the number of atoms in contact between the residues, and the color of the residue indicates whether it is acidic (red) basic (blue) polar (green) or nonpolar (gray).

We then tested whether increased electrostatic interactions between actin and myosin-dADP would increase the actin-myosin association kinetics using Brownian dynamics simulation [Browndye software (200)]. We determined the association rates between actin and ADP-bound or dADP-bound myosin for a wide range of 'reaction distance' criteria (as defined in the Methods section). The association rates for each nucleotide are shown as a function of the reaction distance criteria and fold change in rates for ADP versus dADP are shown in Table 5.1. As expected, association rates increased with decreasing reaction distance for both nucleotides. However, as we hypothesized, myosin-dADP is predicted to have a higher association rate to actin than myosin-ADP, and this effect increases nonlinearly as the reaction distance decreases. The most likely explanation for this is that the more positively charged binding surface of myosin-dADP in the loop 2 region (as previously described) contributes to greater electrostatic affinity between actin and myosin (193).

Table 5.1. Second-order bi-molecular association rate constants for actin and either myosin·ADP or myosin·dADP.

Reaction Distance (Å)	Actin-myosin on-rates ($\mu M^{-1} \cdot s^{-1}$)		Fold Change
	Myosin·ADP	Myosin·dADP	
6	0.17	22.80	132.5
8	3.79	155.38	41.0
10	16.71	501.10	30.0
12	50.31	972.43	19.2
25	850.82	2842.94	3.2
50	4190.64	5005.47	1.2

Rate constants were determined by the Browndye simulations described in the main text. A reaction distance is defined as the separation distance required for the actin-myosin complex to reach before a reaction was considered to occur. As the reaction distance gets larger, the fold change in on-rate between ADP and dADP reduces nonlinearly, suggesting that dADP has a greater effect on the association rate of actin and myosin at short distances. This strongly supports the notion of an increased electrostatic affinity between actin and myosin induced by dADP.

5.3.2. dATP promotes electrostatic interaction of unregulated actin filaments and cardiac myosin

To determine if dATP promotes electrostatic actin-myosin association we used the *in vitro* motility (IVM) assay. This assay allows the study of actin-myosin interactions and how they are affected by changing conditions (ionic strength, temperature, pH, etc.). In many studies, the ionic strength of motility solutions is maintained between 40 to 100 mM since higher ionic strength conditions tend to disrupt electrostatic interactions, resulting in dissociation of actin from myosin coated surfaces and loss of movement (206, 207). Previous work using IVM assays with skeletal muscle myosin demonstrated that as ionic strength was increased (> ~100 mM), the fraction of

motile actin filaments decreased due to weakened electrostatic interactions with myosin, but the fraction was greater with dATP (versus ATP) at each ionic strength (193). Therefore, we hypothesized that cardiac myosin would also maintain a higher degree of actin filament interaction with dATP as ionic strength increases. Figure 5.2A demonstrates this, showing a greater fraction of F-actin interaction (sliding) as ionic strength is increased up to 130 mM. Greater consistency of electrostatic interactions resulted in significantly F-actin filament sliding velocity across a wide range of ionic strength (Figure 5.2B). Increased sliding velocity and NTPase rate with dATP has been reported in previous work (194), but Figure 5.2 demonstrates that dATP significantly increases the interaction between actin and cardiac myosin across a wide range of ionic strength compared to ATP. This further supports the notion that dATP enhances the electrostatic interaction between actin and cardiac myosin relative to ATP.

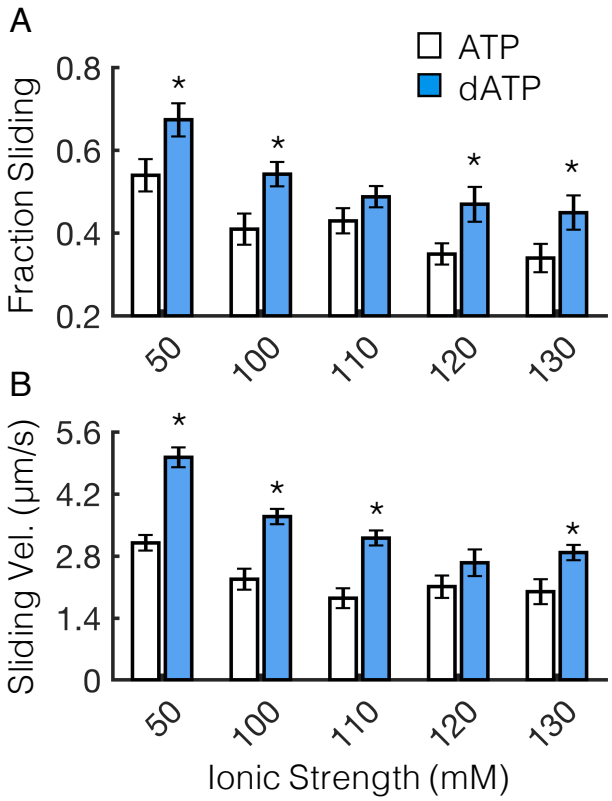

Figure 5.2. dATP promotes motility of unregulated F-actin across a range of ionic strengths. (**A**) The fraction of sliding actin filaments is significantly greater across a range of ionic strengths for ATP-bound myosin (white bars) compared to dATP-bound myosin (blue bars). (**B**) The (non-erratic) filament sliding velocity is also significantly increased across a wide range of ionic strengths for dATP compared with ATP, likely owing to a combination of increased ATPase rates and increased actin affinity of dATP-bound myosin compared with ATP. *$p < 0.05$ with an unpaired student's t-test. Error bars represent S.E.M. for n ≥ 12 slides.

5.3.3. *dATP destabilizes the resting state of myosin*

To determine how dATP affects myosin structure and proximity to actin within myofilaments and the sarcomere lattice geometry, we used small-angle X-ray diffraction analysis of chemically demembranated (skinned) rat cardiac muscle preparations. Trabeculae or papillary

muscles were skinned in relaxing solutions containing either dATP or ATP (see Methods) and maintained in the same nucleotide species throughout the entire experiment. Measurements were made in physiological (170 mM) and low (100 mM) ionic strength solutions at sarcomere length (SL) 2.0 µm and 2.3 µm. Figure 5.3 shows sample 2D X-ray diffraction patterns of resting (pCa 9.0) permeabilized cardiac preparations in ATP or dATP solutions (ionic strength 107 mM). From these images, we quantify: (*i*) the intensity and spacing of the myosin-based meridional reflection (I_{M3} and S_{M3}, respectively), which correspond to the periodicity and axial separation distance (respectively) of myosin heads along the thick filament, (*ii*) the filament lattice spacing by measuring the spacing of the 1,0 reflection ($d_{1,0}$) in the equatorial axis, and (*iii*) the intensity ratio of the equatorial reflections ($I_{1,1}/I_{1,0}$) as a proxy for the radial distribution of myosin mass relative to the thin and thick filaments.

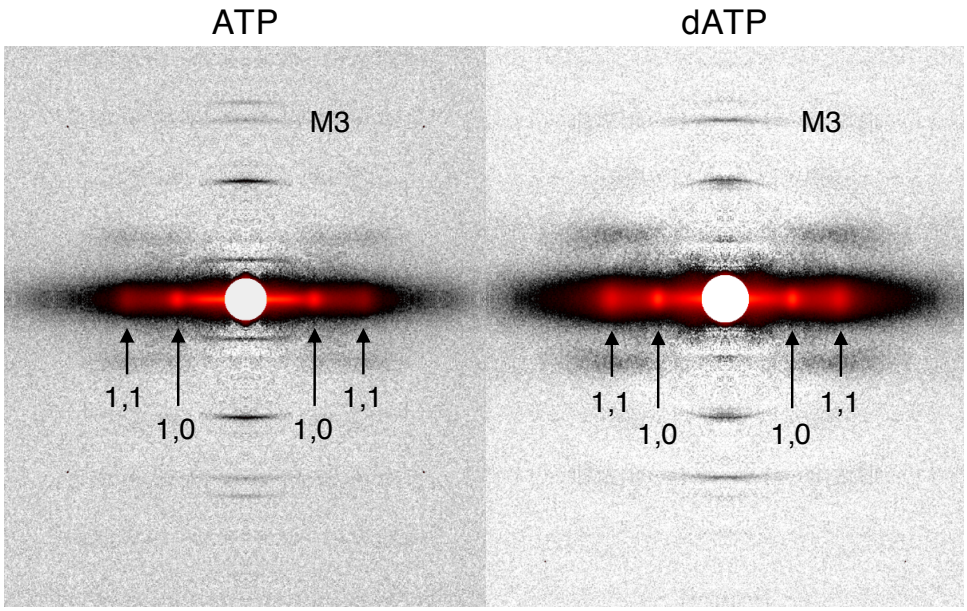

Figure 5.3. Sample 2D X-ray diffraction images of resting cardiac muscle.

Demembranated cardiac trabeculae or papillary muscles from rat right ventricles were exposed to X-ray beam while bathed in solutions containing ATP (left image) or dATP (right image; pCa 9.0; ionic strength 170 mM, SL 2.3 µm). In each diffraction pattern, the reflections of interest are

labeled. M3: Myosin-based meridional reflection due to the axial repeat of myosin crowns; 1,1 and 1,0: Equatorial reflections due to the planes of symmetry in the cross-section of the myofilament lattice.

Under physiological ionic strength conditions, in the absence of calcium (pCa 9.0), cardiac muscle with dATP had significantly increased inter-filament lattice spacing ($d_{1,0}$) compared to ATP at both SL (Figure 5.4A). Interestingly, the $I_{1,1}/I_{1,0}$ intensity ratio, was also significantly increased at both SL (Figure 5.4B). This suggests that dATP causes a shift in the average myosin mass distribution away from the thick filament backbone and toward the thin filament.

We then investigated the effects of nucleotide on myosin filament structure by examining the myosin-based meridional X-ray reflections. Cardiac muscle with dATP had a significantly increased S_{M3} compared with ATP-treated muscle at both SL and μ = 170 mM (Figure 5.4C), while the I_{M3} did not significantly differ with nucleotide species at either SL (Figure 5.4D). This suggests that the average axial separation (*i.e.*, distance along the thick filament backbone) of the myosin heads is increased with dATP compared to ATP, but the degree of axial ordering of the myosin heads was not affected by the different nucleotides.

Next, we hypothesized that if the effects of dATP observed at physiological ionic strength on myofilament structure are electrostatic in nature (as suggested by our simulation and IVM data), then lowering the ionic strength would diminish these effects such that sarcomere structure would be similar to that with ATP. Indeed, there were no significant differences between cardiac muscle with dATP versus ATP in any of the X-ray reflections investigated at low ionic strength (100 mM), at either SL (Figure 5.4E–H). Moreover, these parameters are insensitive to changes in SL in either ionic strength. (See Table 5.2 for numerical values of the X-ray reflections in each experimental condition.)

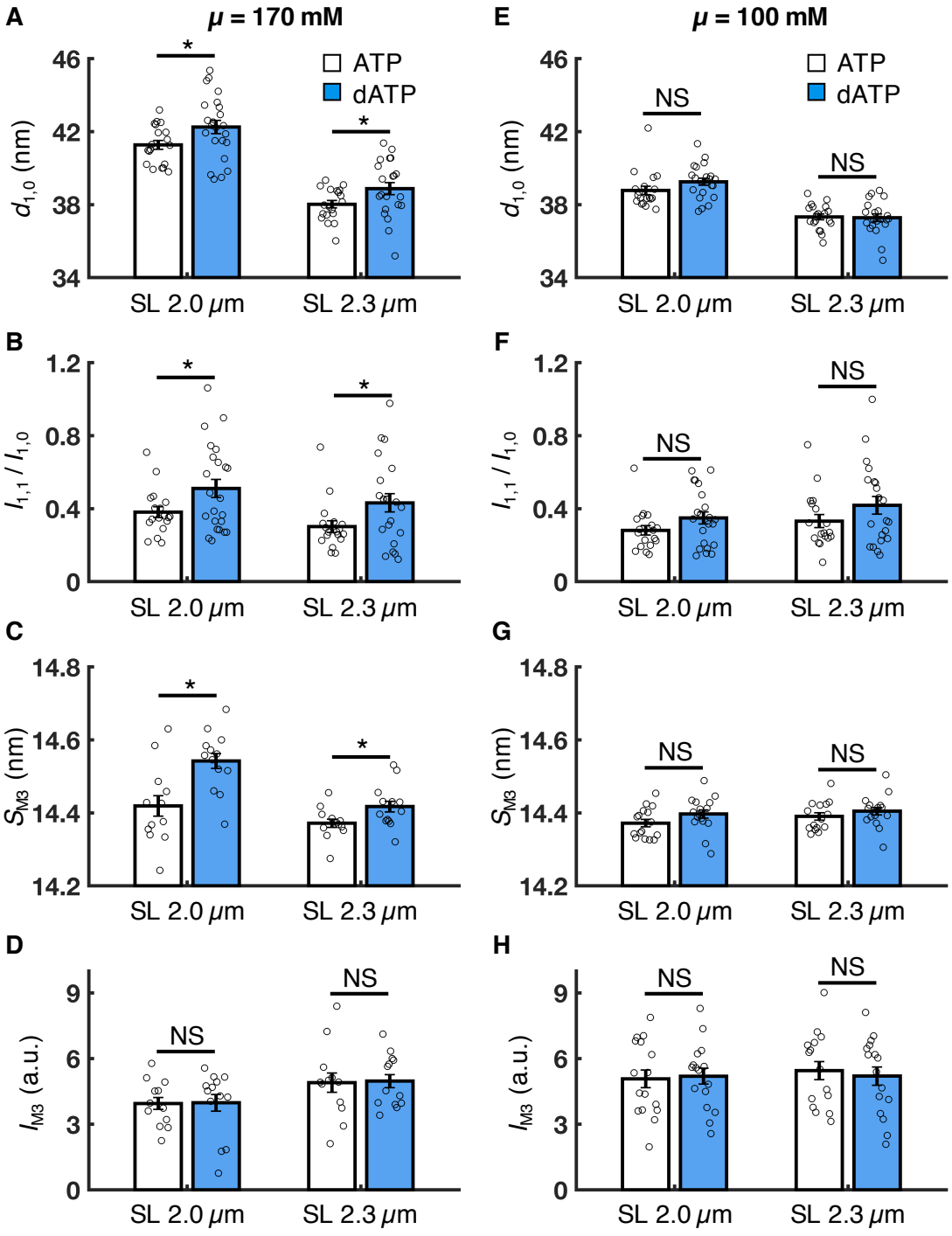

Figure 5.4. The effects of dATP on lattice geometry and myofilament structure in resting cardiac muscle (pCa 9.0).

At physiological ionic strength (μ = 170 Mm), dATP (blue bars) significantly increases the lattice spacing ($d_{1,0}$; **A**), the intensity ratio of the primary equatorial reflections ($I_{1,1}/I_{1,0}$; **B**) and the spacing

of the M3 reflection (S_{M3}; **C**) at both short and long SL compared with ATP (white bars), but does not affect the intensity of the M3 reflection (I_{M3}; **D**) at either SL. However, at low ionic strength (μ = 100 mM) these effects are diminished at both short and long SL (**E-G**) and the I_{M3} remains unaffected by dATP (**H**). Error bars represent S.E.M. for n ≥ 14 preparations. *$p < 0.05$; NS = Not Significant.

Table 5.2. Numerical values of X-ray diffraction reflections in each condition.

	SL = 2.0 μm			
	μ = 170 mM		**μ = 100 mM**	
X-ray Reflection	**ATP**	**dATP**	**ATP**	**dATP**
$d_{1,0}$ (nm)	42.25 ± 0.36	41.29 ± 0.24*	38.77 ± 0.23	39.26 ± 0.20
$I_{1,1}/I_{1,0}$	0.38 ± 0.03	0.51 ± 0.05*	0.28 ± 0.03	0.35 ± 0.03
S_{M3} (nm)	14.42 ± 0.03	14.54 ± 0.02*	14.37 ± 0.01	14.40 ± 0.01
I_{M3} (a.u.)	3.95 ± 0.30	3.98 ± 0.42	5.07 ± 0.43	5.19 ± 0.38

	SL 2.3 μm			
	μ = 170 mM		**μ = 100 mM**	
X-ray Reflection	**ATP**	**dATP**	**ATP**	**dATP**
$d_{1,0}$ (nm)	38.02 ± 0.21	38.88 ± 0.34*	37.33 ± 0.69	37.28 ± 0.93
$I_{1,1}/I_{1,0}$	0.30 ± 0.03	0.43 ± 0.05*	0.33 ± 0.04	0.42 ± 0.05
S_{M3} (nm)	14.37 ± 0.01	14.42 ± 0.02*	14.39 ± 0.04	14.40 ± 0.04
I_{M3} (a.u.)	4.90 ± 0.49	4.97 ± 0.33	5.45 ± 0.45	5.20 ± 0.44

Values represent mean ± S.E.M. for N > 14 preparations. *p<0.05 using an unpaired student t-test.

Thus, our structural data collected in relaxed (pCa 9.0) cardiac muscle preparations demonstrate that, compared to ATP, dATP destabilizes the resting conformation of myosin heads on the thick filament backbone, repositions them closer to thin filaments, and increases their separation distance along the thick filament backbone. Furthermore, the loss of this effect at low ionic strength strongly suggests that the dATP-induced alterations of myofilament structure involve the electrostatic restructuring of myosin predicted by our Brownian dynamics simulations. This conclusion is strengthened by the finding that the effects of dATP on sarcomere and myofilament structure at are unaffected by changes in SL in either ionic strength condition.

5.3.4. *dATP induces a structural change similar to calcium-mediated activation of thick filaments*

Because dATP affects the resting conformation of the of myosin heads in the absence of calcium, it is also possible that the nucleotide may also affect myofilament structure and lattice geometry during activation. As such, we compared the myofilament structure between relaxed (pCa 9.0) and sub-maximally activated (pCa 5.2) cardiac muscle with dATP versus ATP at SL = 2.3 μm and ionic strength = 170 mM. With ATP cardiac muscle had a significantly increased lattice spacing during Ca^{2+} activation, while there were no differences in lattice spacing between resting and Ca^{2+} activated cardiac muscle with dATP (Figure 5.5A). However, the $I_{1,1}/I_{1,0}$ ratio increased significantly for both groups during Ca^{2+} activation (Figure 5.5B), indicating that myosin heads move toward actin filaments to a similar degree during isometric contraction. Interestingly, S_{M3} appeared to be moderately increased for both nucleotides during activation at pCa 5.2, but this change was not statistically significant (Figure 5.5C). Finally, the I_{M3} was significantly reduced upon cardiac muscle activation with ATP, but not dATP (Figure 5.5D), indicating that the periodicity of thick filaments is less affected during activation with dATP. (See Table 5.3 for

numerical values.) Thus, dATP has a greater structural effect on cardiac myofilaments at rest than in (submaximally) Ca^{2+} activated muscle.

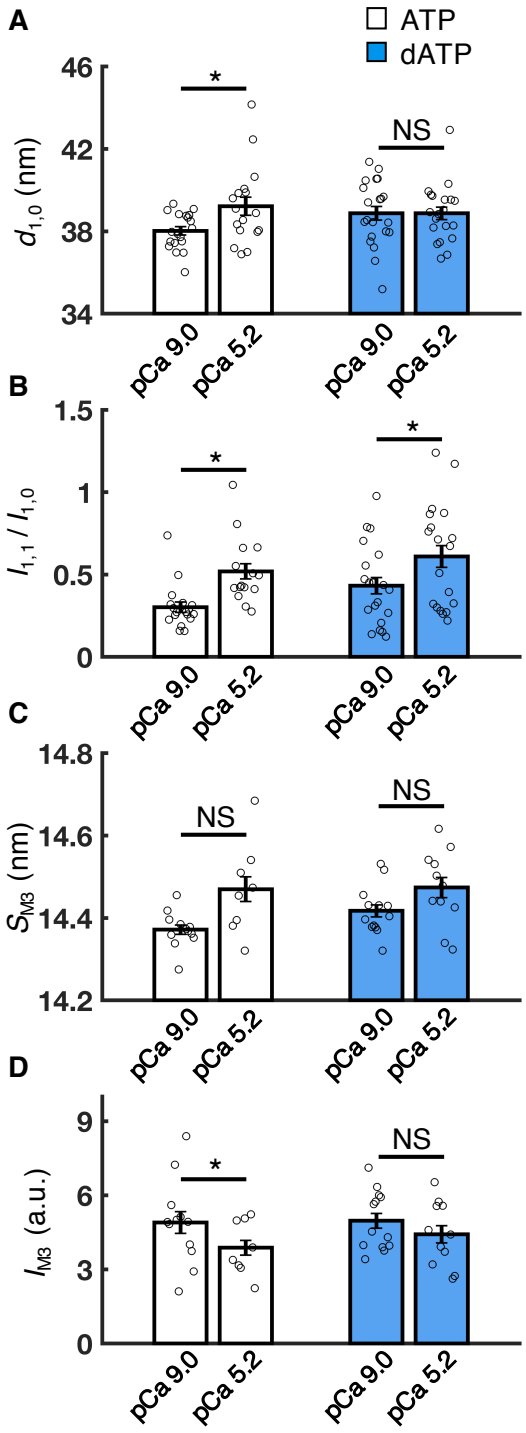

Figure 5.5. The effects of dATP on lattice geometry and myosin filament structure in activated muscle (SL = 2.3 µm; µ = 170 mM).

Upon activation (pCa 5.2), cardiac muscle with ATP (white bars) has an increased lattice spacing ($d_{1,0}$; **A**), an increased $I_{1,0}/I_{1,1}$ ratio (**B**), no change in the spacing of the M3 reflection (S_{M3}; **C**), and

a significantly reduced intensity of the M3 reflection (I_{M3}; **D**) compared to resting muscle (pCa 9.0). However, in preparations containing dATP (blue bars), the $I_{1,0}/I_{1,1}$ is significantly increased upon activation, while all other parameters are not significantly different between relaxed (pCa 9.0) and activated (pCa 5.2). Error bars represent S.E.M. for n ≥ 8 preparations. *$p < 0.05$ using a paired student t-test; NS = Not Significant.

Table 5.3. Quantification of X-ray diffraction reflections in resting and activated cardiac muscle with ATP or dATP.

	ATP		dATP	
X-ray Reflection	**pCa 9.0**	**pCa 5.2**	**pCa 9.0**	**pCa 5.2**
$d_{1,0}$ (nm)	38.02 ± 0.20	39.22 ± 0.46*	38.86 ± 0.33	39.04 ± 0.32
$I_{1,1}/I_{1,0}$	0.30 ± 0.03	0.52 ± 0.05*	0.43 ± 0.05	0.61 ± 0.07*
S_{M3} (nm)	14.37 ± 0.01	14.47 ± 0.04	14.42 ± 0.02	14.47 ± 0.03
I_{M3} (a.u.)	4.90 ± 0.49	3.88 ± 0.39*	4.97 ± 0.33	4.42 ± 0.40

SL = 2.3 μm; μ = 170 mM; Values represent mean ± S.E.M. for n > 8 preparations; *p < 0.05 using a paired t-test within nucleotide groups across pCa.

5.4. Discussion

5.4.1. A structural basis of dATP-mediated force augmentation—from a single molecule to the sarcomere

Previous work by our group and others has demonstrated that the naturally occurring nucleotide 2-deoxy-ATP (dATP) can serve as an alternative energy substrate by cardiac myosin, that promotes cross-bridge formation and increases cycling rates (57, 194, 208). Our goal in this study was to understand the structural basis of dATP effects on myosin molecules and myofilament ultrastructure in resting and activated cardiac muscle that underlie changes in actin-myosin cycling

and cardiac function. We used a multifaceted approach, combining computational and experimental techniques that melds single-molecule and protein biochemistry with angstrom-level structural assessments of myofilaments and sarcomere lattice geometry in cardiac muscle.

Brownian dynamics simulations of the bi-molecular association of an actin monomer with either ADP- or dADP-bound myosin predict that dADP significantly increases the association rate compared with ADP. We attribute this to a dADP-induced conformational change of the actin-binding surface of myosin that exposes more positively charged residues (Figure 5.1), effectively increasing its electrostatic affinity for actin. We then verified that dATP induces an electrostatic-based enhancement of the actin-myosin interaction by demonstrating an increased fraction of F-actin sliding and increased sliding velocity in the IVM assay with dATP across a wide range of ionic strengths. This, together with the results from dynamics computational simulations, supports the idea that dATP causes a conformational change of the actin-binding surface of cardiac myosin that enhances its electrostatic interaction with actin. Lastly, we used X-ray diffraction analysis to demonstrate that the dATP-induced effects on myosin structure translate into changes in myofilament structure and sarcomere lattice geometry, primarily in resting cardiac muscle. Figure 5.6 summarizes the X-ray results, showing that dATP increases the fraction of myosin motors that are destabilized from the resting conformation compared with ATP, resulting in myosin S1 heads moving closer to actin filaments on average. These changes in resting myosin structure may prime the sarcomere prior to Ca^{2+}-mediated activation, thereby increasing the probability of strong cross-bridge formation and cycling.

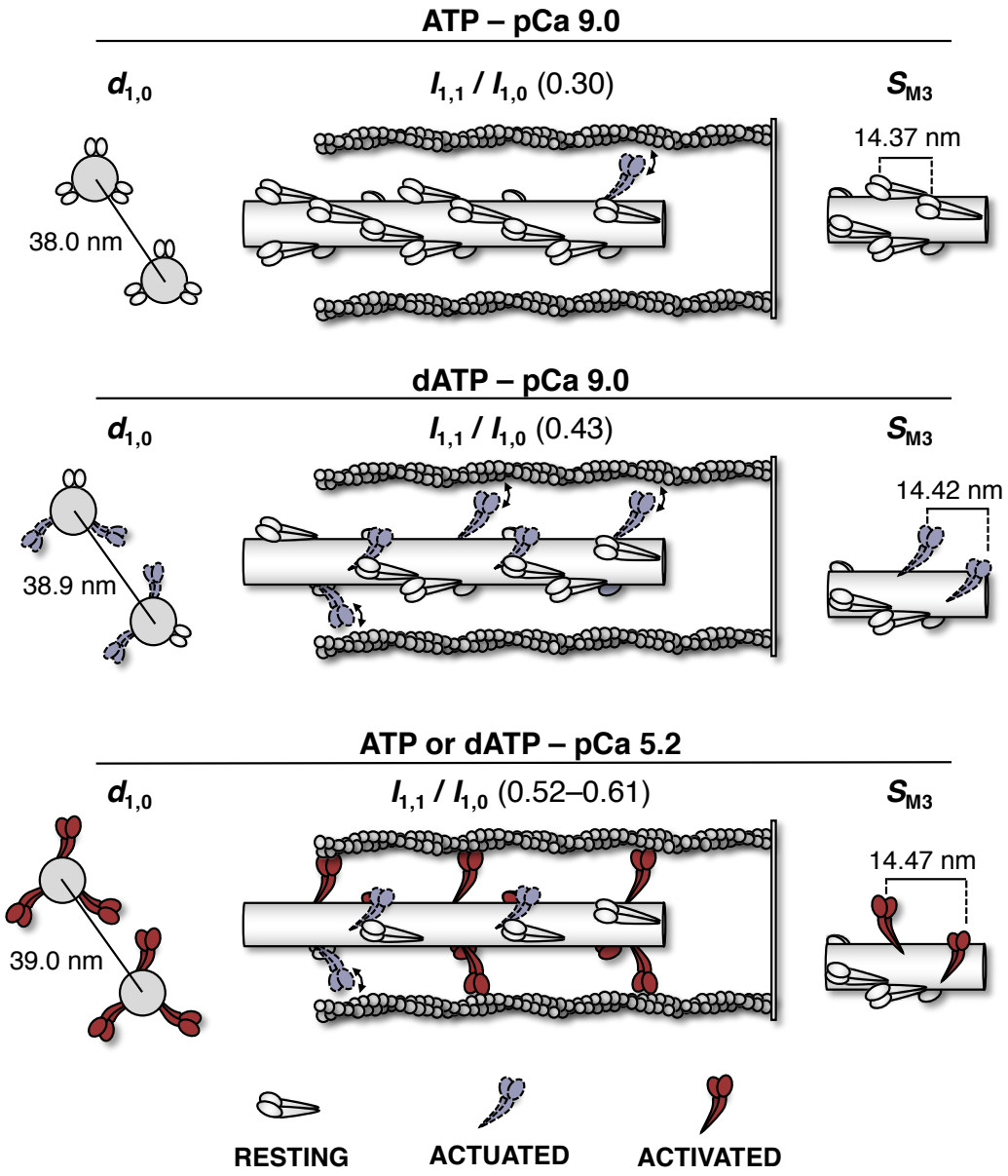

Figure 5.6. Illustration of the combined effects of dATP on the cardiac myosin filament structure and lattice geometry.

Based on the results of the x-ray diffraction experiments, we posit that dATP increases the fraction of actuated myosin motors (i.e. perturbed from their resting conformation and weakly interacting with actin) in resting cardiac muscle. This is evident by the increase in lattice spacing ($d_{1,0}$), the increase of mass shifted away from the thick filament backbone toward actin ($I_{1,1}/I_{1,0}$) and the increase in the axial spacing between myosin crowns on the thick filament (S_{M3}) observed in permeabilized cardiac preparations containing dATP compared with preparations containing ATP. (Numerical values correspond to SL = 2.3 μm and μ = 170 mM in Table 5.2.) During activation

(pCa 5.2), the myosin filament structure and lattice geometry are not different between ATP and dATP. Thus, the structure and lattice geometry of resting muscle with dATP is more similar to the active state with either nucleotide than it is to the resting state with ATP.

5.4.2. Electrostatic restructuring of myosin by dATP actuates sarcomeres in resting cardiac muscle

Our combined structural data suggest that dATP induces a conformational change in myosin that results in increased exposure of polar and charged amino acid side chains on its actin-binding surface and this, in turn, promotes actin binding when myosin is in the post-hydrolysis, pre-powerstroke state. If the mechanism for the altered resting myofilament structure is mainly an increased electrostatic affinity of myosin for actin, then we would expect that compressing the myofilament lattice would enhance these effects by physically bringing actin closer to myosin. This can be done in demembranated muscle either by increasing osmotic compression with dextran or by increasing SL (183, 209). Indeed, for pCa 9.0 and μ = 170 mM, the $I_{1,1}/I_{1,0}$ increased by 43% at SL 2.3 μm (compressed lattice) for dATP compared with ATP, whereas at SL 2.0 μm (expanded lattice) $I_{1,1}/I_{1,0}$ increased by only 34% (Figure 5.4 and Table 5.2).

However, a number of other mechanisms may also contribute to destabilization of resting state of myosin motors caused by dATP. First, it is possible that the dATP-induced changes in charge distribution of the actin-binding domain may allosterically affect head-head and/or head-tail interactions (the interacting head motif) of resting myosin motors (210). This could be due to a disruption of either the essential light chain-free motor domain interaction, or the blocked motor domain-S2 interaction that has been described in resting skeletal muscle (17). Secondly, it has recently been shown that multiple phosphorylation pathways that target thick filament proteins

also affect the resting structure. For example, phosphorylation of myosin-binding protein C (MyBP-C) repositions myosin heads closer to the actin filaments in demembranated cardiac muscle in the absence of calcium (176, 177), while under normal conditions interacts with the S2 domain of myosin and/or the thick filament backbone to stabilize the resting state of thick filaments (69, 175). These findings suggest that MyBP-C plays a significant role in modulating the resting myosin filament structure. It is possible that the change in myosin structure with dATP may alter regulation of the MyBP-C-myosin system in the absence of Ca^{2+}. Furthermore, phosphorylation of the regulatory light chain (RLC) of myosin via myosin light chain kinase (MLCK) also repositions myosin motors closer to actin in resting cardiac muscle (174). This is likely the structural basis of the phosphorylation-dependent increased rate of force development, Ca^{2+} sensitivity of force, and maximum force production in skinned cardiac muscle after treatment with MLCK (174). It is possible that the structural effects of dATP on myosin we present here underpin a similar structural basis of augmented cardiac contractility as these physiological responses.

In addition to phosphorylation pathways, it has been known for decades that decreasing ionic strength causes an increase in the affinity of myosin for actin and shifts the average position of myosin closer to actin in resting, demembranated rabbit psoas (211) and cardiac muscle (212), and others have exploited this in previous studies. Additionally, in a study with permeabilized rabbit psoas muscle fibers treated with polyethylene glycol (PEG), changes in sarcomere structure were investigated with X-ray diffraction in low and high ionic strength solutions (213). Muscle fibers treated with PEG promoted the weakly bound A·M·ADP·Pi state of the cross-bridge cycle, suggesting an increased affinity of myosin for actin. Compared to untreated conditions, PEG-treated resting fibers had a significant increase in the $I_{1,0}/I_{1,1}$ ratio, indicating a shift in the radial position of myosin heads towards the actin filament. Consistent with our findings, the authors

showed that these effects were diminished in low ionic strength solutions, suggesting that the increase in electrostatic affinity of myosin for actin in the presence of PEG is sufficient to bring myosin motors closer to actin filaments in resting muscle.

Finally, it has recently been suggested that systolic force development is regulated by a mechanosensing-based mechanism in the thick filament that occurs downstream from calcium-mediated thin filament activation and involves a rapid, feed-forward and load-dependent recruitment of resting myosin motors for strong cross-bridge binding [(77) Caremani *et al., JGP, in press*]. In the absence of Ca^{2+} how might the dATP-induced 'primed' state of the myosin filament affect such a feed-forward mechanism? The combination of the perturbed resting state of myosin motors and increased electrostatic affinity of actin caused by dATP may work in concert to potentiate cardiac force production both upstream and downstream of Ca^{2+}-mediated thin filament activation by (*i*) increasing the fraction of 'actuated' motors (*i.e.*, motors that are positioned closer to actin and primed for strong cross-bridge formation) in the absence of Ca^{2+}, and (*ii*) increasing the probability of strong cross-bridge formation and force development upon Ca^{2+}-mediated thin filament activation.

5.4.3. Clinical perspectives on targeting the cardiac thick filament

Advances in X-ray diffraction and electron microscopy techniques have allowed a greater understanding of cardiac myosin thick filament structural changes in various forms of heart failure. Recent studies toward that end have primarily investigated the structural consequences of myosin-based mutations associated with cardiomyopathy, as well as small molecule myosin effectors. A number of small molecule-based inotropes that target cardiac myosin are currently being

developed to treat heart failure. One inotrope, omecamtiv mecarbil (OM; formally known as CK-1827452 and AMG 423) is currently in phase III clinical trials for treatment of systolic heart failure. OM selectively binds to myosin and increases fraction of myosin motors that strongly bound to actin (86, 214) and may increase the transition from weak-to-strong actin-myosin interactions without affecting intracellular Ca^{2+} handling (215). Additionally, similar to what we report here with dATP, OM perturbs the regulatory state of the cardiac thick filament and causes myosin motors to switch to a more activated state at low levels of Ca^{2+} where they are more perpendicular to the thick filament backbone (80). Interestingly, despite mobilizing myosin motors in the absence of Ca^{2+}, OM reduces force production at higher Ca^{2+} concentrations in demembranated cardiac muscle (80, 216), while dATP increases force at all levels of Ca^{2+} (57). A recent study by Liu *et al*. used harmonic force spectroscopy with single myosin molecules to determine the effects of various small molecules, including OM and dATP, on the load-dependent binding kinetics of β-cardiac myosin to actin (217). The authors report that dATP significantly accelerates the detachment rate of myosin from actin (likely by increasing the release of dADP from the nucleotide-binding site on myosin), which increases the overall cross-bridge cycling rate. Their results show that dATP increases the average power of a single β-cardiac myosin without affecting the load dependence of force per cross-bridge. Conversely, the authors report that OM causes a significant reduction in the detachment rate of myosin from actin, causing a prolonged powerstroke and increased fraction of time spent in the actin-bound state of the cross-bridge cycle. The authors point out that this is consistent with the prolonged systole others have reported for high doses of OM (218). Therefore, dATP has similar beneficial effects on augmenting systolic pressure development as OM but, in contrast to OM, systole is not prolonged, and the rate of pressure decline at the end of systole is enhanced (195, 219).

Another myosin-targeted small molecule that is currently in clinical trials is the ATPase inhibitor mavacamten, which has recently been shown to stabilize the resting confirmation of cardiac myosin in thick filaments (220). This makes it appealing as a potential therapeutic for hypertrophic cardiomyopathy-associated sarcomere mutations that destabilize the resting state of the myosin filament (88, 221). In a similar context, we recently reported that dATP may be a promising therapeutic to target sarcomere protein mutations associated with dilated cardiomyopathy, by improving myosin recruitment to restore ventricular contractile capacity (222).

Chapter 6

Targeting sarcomere dysfunction in dilated cardiomyopathy by genetically engineering filament-specific intervention

Abstract

In hearts with dilated cardiomyopathy (DCM), the ventricular walls become thin and weak, causing systolic dysfunction, and interventions to prevent the DCM phenotype are lacking. However, we recently introduced a metric capable of predicting the type and severity of myocardial remodeling in progressive cardiomyopathies (Davis *et al. Cell*, 2016), which hinges on relating force-time integrals of computationally derived twitches of diseased cardiomyocytes to wild-type. Negative values of this metric (the 'tension index') correlate with eccentric hypertrophy associated with DCM, and the magnitude correlates with the severity of phenotype. Here, we test the hypothesis that an experimental analogue of the tension index can be generated from twitches of intact cardiac trabeculae from genetically engineered murine models of DCM, and that it will predict the degree of myocardial remodeling. Intact trabeculae from a DCM model—a calcium-desensitizing tropomyosin mutation (D230N)—have significantly decreased twitch force compared to wild-type trabeculae (16 ± 2 versus 31 ± 3 kPa, respectively). The corresponding tension index for D230N trabeculae is -6.62×10^3 (normalized force·ms), predicting significant eccentric hypertrophy. Indeed, our predictions are verified by echocardiographic measurements of ventricular diameters *in vivo*. In D230N hearts, the left-ventricular systolic and diastolic diameters are significantly greater than wild-type (3.1 and 4.3mm, versus 2.4 and 3.8mm, respectively). Furthermore, intact trabeculae from a double-transgenic (DTG) murine model,

(D230N plus the calcium-sensitizing troponin mutation, L48Q), produce twitch forces similar to wild-type (32 ± 3 kPa). The tension index for DTG trabeculae is -1.48×10^3 (normalized force·ms), predicting less remodeling than D230N alone. Consistently, systolic and diastolic diameters of DTG hearts are not different from wild-type (2.5 and 3.9 mm, respectively). Our work demonstrates the ability of a trabecula-based tension index to predict organ-level morphology in DCM hearts and to use these predictions to develop interventions that prevent pathological remodeling.

6.1. Introduction

Dilated cardiomyopathy (DCM) is a common and deadly genetic cardiac disorder that affects >1/3,000 individuals (61) and is often caused by mutations in genes encoding proteins that comprise the sarcomere (61, 223). DCM is typically characterized by enlargement and thinning of the ventricular walls and systolic dysfunction with an ejection fraction of < 45–50% (224, 225). Treatment options for patients with DCM are currently limited to cardiac transplantation, and the development of new pharmacological therapeutic options (e.g. positive inotropes) has been largely unsuccessful to date. This hampered ability to restore function (or prevent dysfunction) of DCM failing hearts is likely due to the complexity of the fundamental regulatory mechanisms operating within the sarcomere that may be disrupted by the mutation underpinning the DCM phenotype.

The processes by which healthy cardiac muscle contraction is regulated involve highly coordinated molecular interactions between the interdigitating thick and thin filaments comprising the sarcomere. Upon calcium release into the sarcoplasm, the canonical force production pathway begins with calcium binding to troponin on the thin filament which leads to azimuthal displacement of tropomyosin that exposes myosin binding sites on actin ((3) and references

therein). Myosin is then able to interact with actin to form strong, force-generating cross-bridges that drive sarcomeric shortening and overall cardiac contractility. It is, perhaps, unsurprising that with such finely tuned regulatory mechanisms operating within the sarcomere, small perturbations (in the form of point mutations) can have major effects on muscle function and contractility. Indeed, the importance of the various regulatory proteins of the sarcomere is highlighted by the mutations in them that cause cardiomyopathies. Mutations in many sarcomere proteins have already been linked to cardiomyopathy.

The vast diversity of sarcomere mutations that have already been linked to DCM (223, 226, 227) emphasizes the need for a precision medicine model for treating and preventing DCM. The most effective form of treatment for patients with DCM likely varies from patient to patient depending on the underlying mutation. As such, there is a pressing need to elucidate the mechanisms by which specific DCM-linked mutations in the sarcomere drive disease progression, and how to rescue mutation-specific failing hearts with targeted and rational approaches. Towards that end, recent work by Davis *et al.* (2016) has demonstrated the ability to use computationally generated myofilament tension-time integrals to accurately predict the degree of myocardial remodeling for a wide variety of sarcomere protein mutations (65). The authors genetically engineered murine hearts to systematically perturb the contractile performance of the sarcomere and define the 'tension index' as the difference between the resulting twitch-time integral of genetic variants relative to wild-type. They show that the tension index strongly correlates with the type and severity of the cardiac phenotype for each murine model, as well as for human-induced pluripotent stem cell-derived cardiomyocytes from patients with cardiomyopathy.

Here, we build upon the work of Davis and colleagues to define an experimental analogue of the tension index that can similarly predict the severity of myocardial remodeling in a murine

model of DCM and aid the development of effective preventative interventions. To do so, we investigate the cardiac mechanics and myocardial morphology of a murine model of dilated cardiomyopathy (DCM) that is caused by a point mutation in tropomyosin at the 230th residue (aspartic acid to asparagine, denoted D230N) (7, 228), which has been found to cause DCM in two unrelated families (229). Heterozygous mice expressing D230N tropomyosin present a DCM phenotype within 2-3 months of age, as indicated by thinning of the ventricular walls and reduced end-systolic and end-diastolic pressure-volume relations (230). Furthermore, previous *in vitro* studies have shown that D230N tropomyosin reduces myosin cycling rates and calcium sensitivity of filament sliding in an *in vitro* motility assay (230), and increases the affinity of tropomyosin for actin by nearly 5-fold (231). As such, we hypothesize that: (*i*) contractility and calcium sensitivity of force of cardiac trabeculae from D230N mouse hearts will be reduced compared with wild-type (WT), (*ii*) organ-level function of D230N hearts will be reduced and accompanied by a thinning of the ventricular walls, and (*iii*) these functional assessments can be used to generate a predictive metric that enables us to rationally design a therapeutic intervention to prevent the DCM phenotype.

To test these hypotheses, we measure the twitch force, kinetics, and calcium sensitivity in isolated cardiac muscle preparations from WT and D230N hearts. We then use these measurements, together with an experimental analogue of the tension index, to inform rationally designed therapeutic intervention. We find that contractility of intact trabeculae from D230N hearts is indeed reduced (relative to WT), which is accompanied by a reduction of the calcium sensitivity of force. We therefore implemented a genetic engineering approach to target the calcium sensitivity of the thin filament, in which we incorporated into D230N hearts a calcium sensitizing troponin C mutation (L48Q). Consistent with our expectation, trabeculae from the

L48Q + D230N double-transgenic (DTG) hearts show significantly improved contractility compared with trabeculae from D230N hearts. Furthermore, the tension index calculated from the tension-time integrals of twitches from intact trabeculae from DTG hearts predicted a reduced degree of eccentric hypertrophy (*i.e.*, dilation) of the myocardium compared with the tension index for D230N hearts. This prediction is confirmed by in vivo echocardiographic measurements of the left ventricular dimensions during systole-diastole cycles, which show significantly reduced dilation in DTG hearts compared to D230N hearts. This reduction in dilation is also accompanied by improved ejection fraction and fractional shortening of the left ventricle of DTG hearts compared with D230N hearts.

Thus, the work we present here highlights a significant step towards a precision medicine model to treat DCM by demonstrating the ability to predict and prevent pathological remodeling of the myocardium through targeted and rationally designed therapeutic intervention.

6.2. Methods

6.2.1. Animal use & ethics

Adult male and female mice between 4 and 6 months of age were euthanized following the procedures approved by the Institutional Animal Care and Use Committee for the University of Washington. Mice were sedated by inhalation of isoflurane and an intraperitoneal (IP) injection of 0.1 mL of heparin was administered to minimize blood clotting in the ventricles. Approximately four minutes after the injection of heparin, an IP injection of a lethal dose (0.1 mL) of pentobarbital (Beuthanasia-D) was administered.

6.2.2. Excision of murine hearts

Hearts were rapidly excised via thoracotomy, and immediately immersed in oxygenated (95% O_2, 5% CO_2), room-temperature Krebs buffer containing (in mM) 118.5 NaCl, 5 KCl, 1.2 $MgSO_4$, 2 NaH_2PO_4, 25 $NaHCO_3$, 1.8 $CaCl_2$, and 10 glucose. Hearts were then rinsed via aortic retrograde perfusion with Krebs buffer containing low calcium (0.1 mM $CaCl_2$) and 20 mM 2,3-Butanedione 2-monoxime (BDM) to minimize contraction and subsequent damage during dissection. Conveniently, BDM also acts as a non-specific phosphatase, thereby reducing the degree of phosphorylation of sarcomere proteins (232). This allows us to isolate any off-target phosphorylation-dependent effects on muscle mechanics.

6.2.3. Intact trabeculae mechanics

Thin, unbranched, and intact trabeculae were carefully dissected from the right ventricular wall and mounted between a force transduce (Cambridge Technology, Inc., Model 400A) and a length-controlling motor (Aurora Scientific, Model 300C). Each end of the trabecula was sutured to custom arms attached to the motor and force transducer made from 22-gauge needles. The trabecula was then submerged in a custom experimental chamber that was continuously perfused with modified Krebs buffer (1.8 mM CaCl) at 30° C. Twitches were elicited by field stimulation with custom platinum plate electrodes at 1 Hz with oscillating polarity. Sarcomere length (SL) was set to 2.0 μm using an inverted stereomicroscope with a 40x dry objective lens and a 10x eyepiece. If sarcomeres could not be seen (e.g. if the trabecula was too thick), a SL of 2.0 μm was assumed to be at trabecula slack length (the length of the trabecula at the onset of passive tension development). Trabeculae were allowed to pace at 1 Hz for ~20 minutes at SL 2.0 μm (and 30°C), and then stretched to SL 2.3 μm for data acquisition.

Continuous twitch force traces were recorded using custom LabView software at a sampling rate of 1 kHz and were analyzed with custom code written using MATLAB software (The MathWorks, Natick MA).

6.2.4. Permeabilized trabeculae mechanics

Hearts were permeabilized in 'skinning' solution containing 100 mM KCl, 10 mM MOPS, 5 mM EGTA, 9 mM $MgCl_2$ and either 1 mM dATP or 4 mM ATP (adjusted to pH = 7 with KOH), 1% (by volume) Triton X-100, 1% protease inhibitor (sigma P8340), and glycerol at 4°C overnight. Permeabilized trabeculae were then dissected from the right and left ventricles and mounted between a force transducer and motor using custom aluminum T-clips. Sarcomere length (SL) was measured using a Fourier transform of a digitized image of the sarcomeres using an IonOptix camera connected to a 40x dry objective lens. SL was set to 2.3 μm for the experiments. Trabeculae were submerged in physiological solution at 15°C containing a range of pCa (= $-\log[Ca^{2+}]$) from 9.0 to 4.0, and allowed to reach stead-state tension (T_{SS}) at each pCa. T_{SS}-pCa curves for each genotype were collected and analyzed with custom code using LabView software, and were fit to the Hill equation, as $T_{SS} = T_{SS,Max} \cdot [1 + 10^{n_H \cdot (pCa_{50} - pCa)}]^{-1}$, where $T_{SS,Max}$ is the maximum steady-state tension (at pCa 4.0), pCa_{50} is the pCa at half-maximal tension, and n_H is the Hill coefficient (the slope of the T_{SS}-pCa relation and a measure of the cooperativity of tension).

6.2.5. Echocardiography

Six-month-old male and female mice of each genotype were used for echocardiographic measurements, as previously described (233). Briefly, animals were lightly anesthetized via inhalation of 1% isoflurane, and inner diameters of the left ventricles and the end of diastole and

end of systole were measured using M-mode measurements via the short-axis view of the left ventricle at the mid-papillary level. The fractional shortening was calculated from these data using, the relationship $100*(LVID_d - LVID_s)/LVID_d$, where $LVID_d$ and $LVID_s$ are the left ventricular inner diameters at the end of diastole and systole, respectively.

6.2.6. Data analysis & statistics

All data were analyzed using MATLAB software and built-in statistical packages. Unless stated otherwise, error bars represent the standard error of the mean. A one-way ANOVA with a Tukey post-hoc test of significance was used to compare values across genotype groups, unless stated otherwise.

6.3. Results

6.3.1. Contractility of intact trabeculae from D230N hearts is impaired relative to WT

Given that D230N tropomyosin has been shown to reduce calcium sensitivity of filament sliding and ATPase rates in *in vitro* assays (230, 231), we hypothesized that the twitch force of intact trabeculae from D230N hearts will be reduced compared to trabeculae from WT hearts. To test this hypothesis, intact cardiac trabeculae were isolated from the right ventricle of WT and D230N hearts (as discussed in the Methods section) and electrically paced at 1 Hz (SL 2.3 μm at 30°C). Figure 6.1A shows average twitch traces at from trabeculae from WT and D230N hearts, and Figure 6.1B shows the average peak (maximum) twitch tension (T_P) for each case. Intact trabeculae from D230N hearts produce significantly less maximum tension during a twitch compared to WT. T_P is 61.9 ± 4.6 kPa and 28.3 ± 2.1 kPa for trabeculae from WT and D230N

hearts, respectively (mean ± SEM for n ≥ 6 trabeculae for each group). Similarly, the maximum rate of contraction (Max. d*T*/dt) is significantly reduced for trabeculae from D230N hearts compared with WT (Fig. 6.1C). Interestingly, the time to reach T_P (TT_P; relative to the stimulus), the time to 50% relaxation (RT_{50}), and the time to 90% relaxation (RT_{90}; relative to TT_P) are not different between trabeculae from WT and D230N hearts. (Fig. 6.1D–E, respectively).

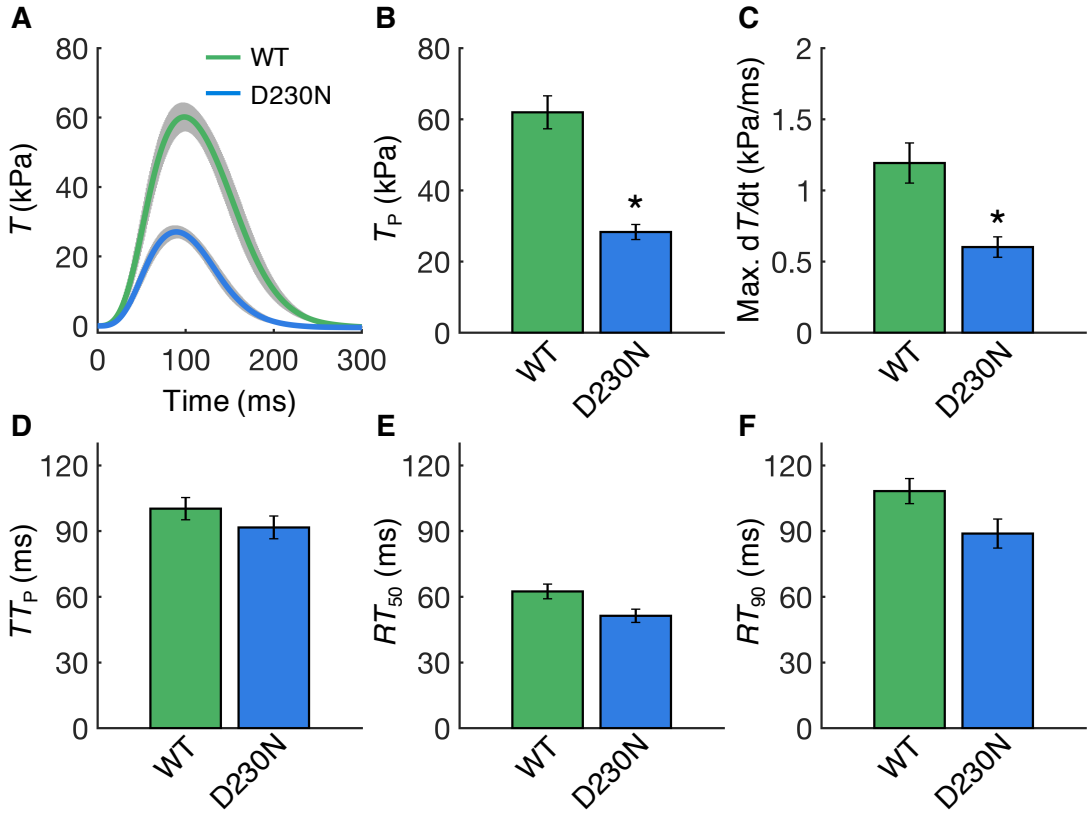

Figure 6.1. D230N tropomyosin reduces twitch tension and the rate of contraction in intact trabeculae.

(A) Average twitch tension (*T*) traces from intact trabeculae from WT (green) and D230N (blue) hearts. Twitch traces are averaged over multiple twitches (1 kHz acquisition rate) from at least 6 trabeculae for each group, and the gray shaded region represents the SEM. The tension at the peak of the twitch (T_P) is significantly reduced in D320N heart compared to WT hearts (**B**), as is the maximum rate of twitch tension development (Max. d*T*/dt; **C**). Conversely, the time to peak twitch tension (TT_P), time to 50% relaxation (RT_{50}), and the time to 90% relaxation (RT_{90}) are not different

between WT and D230N hearts (**D–F**). Relaxation times are relative to TT_P. Error bars represent SEM; *$p < 0.05$ using a one-way ANOVA with a Tukey post-hoc test of significance (see statistical analysis methods section).

6.3.2. D230N tropomyosin alters Ca^{2+} sensitivity of steady-state tension in permeabilized trabeculae without affecting maximum tension

Next, we sought to understand the mechanisms underlying the decreased contractility in intact trabeculae from D230N hearts. In a recent study using a calorimetry-based assay, D230N tropomyosin was found to have increased thermal stability compared to WT, which the authors speculate may hinder Ca^{2+}–mediated activation of thin filaments with D230N compared to WT (230). The authors also found that isolated cardiomyocytes from D230N hearts have increased Ca^{2+} release during contraction, suggesting compensatory response to a primary decrease in Ca^{2+} sensitivity (230) and/or decreased Ca^{2+} buffering by the myofilament lattice (65). These previous studies, together with our finding that the twitch tension is significantly reduced in intact trabeculae from D230N hearts compared to WT (Fig. 6.1), led us to hypothesize that D230N reduces the Ca^{2+} sensitivity of steady-state tension (T_{SS}) in trabeculae permeabilized trabeculae. To test this, we measured T_{SS} as a function of pCa (= –log[Ca^{2+}]) using permeabilized trabeculae from the left ventricle of D230N and WT hearts. Figure 6.2A shows the normalized T_{SS}–pCa relations for trabeculae from D230N (blue traces) and WT (green traces) hearts. Data were fit with the Hill equation (described in the Methods section). The normalized T_{SS}–pCa relation for trabeculae from D230N hearts is right-shifted compared with WT. Additionally, the Hill coefficient (slope) of the force–pCa relations, which is a measure of the cooperativity of the calcium sensitivity of tension

is not different between permeabilized trabeculae from D230N hearts compared with WT at short SL (Fig. 6.2C).

Interestingly, contrary to the peak twitch tension T_P in intact trabeculae, the maximum steady state tension (Max. T_{SS}; determined at pCa 4.0) is not different between trabeculae from D230N and WT hearts (Fig. 6.2D). The discrepancy between T_P and Max. T_{SS} is very likely due to the fact that at the peak of a cardiac twitch, the intracellular calcium concentration is well below the saturating levels of pCa 4.0 [pCa ~5.8–5.6 in human myocardium, depending on the stimulation frequency (55)]. To better visualize the calcium dependence of the tension inhibition by D230N, TSS of trabeculae from D230N hearts were normalized to that of WT at each pCa (Fig. 6.2E). At low levels of Ca^{2+} (pCa = 5.8), permeabilized trabeculae from D230N hearts produce only ~20% of the steady-state tension of trabeculae from WT hearts, while at saturating levels (pCa 4.0), they produce ~80% of the steady-state force of WT trabeculae. For comparison, the peak twitch tension (T_P) produced by intact trabeculae from D230N hearts as a percentage of that from WT hearts is indicated by the dashed horizontal line. This strongly suggests that, given an increase in intracellular calcium concentration or calcium sensitivity of thin filament activation, intact trabeculae from D230N hearts are capable of producing up to ~80% of the force produced in WT trabeculae.

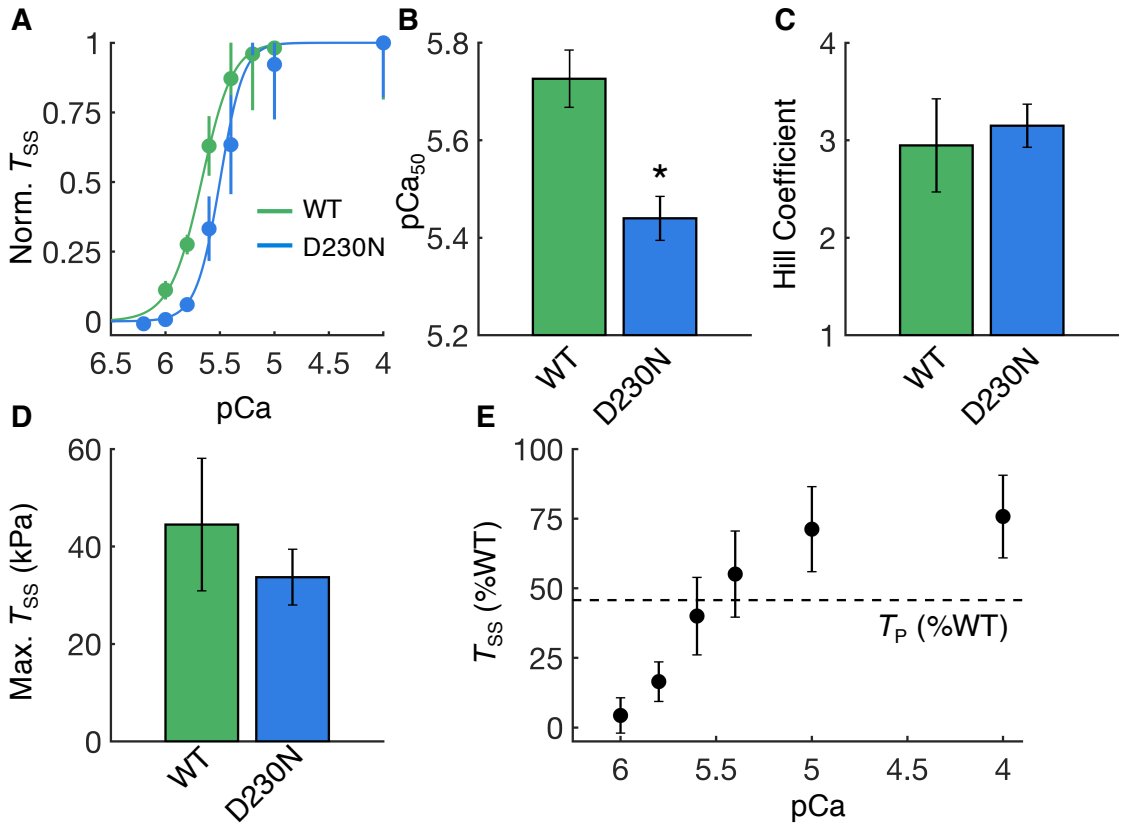

Figure 6.2. D230N reduces the calcium sensitivity of tension of permeabilized trabeculae and causes a strong calcium-dependent depression of steady-state tension.

(A) Normalized steady-state tension (T_{SS}) versus pCa relations for permeabilized trabeculae containing from WT (green) and D230N (blue) hearts. The T_{SS}–pCa relations for preparations from D230N hearts are right-shifted compared to WT, indicating an overall reduction of calcium sensitivity of T_{SS}. **(B)** The right-shift of the T_{SS}–pCa relation is evident by the significantly decreased pCa_{50} (the pCa at half-maximum T_{SS}) for trabeculae from D230N hearts compared with WT hearts. (**C**) The estimated Hill coefficients (a measure of the slope of the fitted Hill equation to the T_{SS}–pCa curves) are not different between trabeculae from WT and D230N hearts. (**D**) The maximum tension (pCa 4.0) is also not different between trabeculae from D230N and WT hearts. (**E**) To better visualize the calcium-dependence of tension inhibition caused by D230N, T_{SS} of trabeculae from D230N hearts was determined as a percentage of T_{SS} of trabeculae from WT hearts at each pCa. At low levels of calcium (pCa = 5.8), T_{SS} is trabeculae of D230N hearts produce only ~20% that of WT, while at saturating levels (pCa 4.0), they produce ~80% of T_{SS} of trabeculae

from WT hearts. For comparison, the dashed line indicates the peak twitch tension (T_P) in trabeculae from D230N hearts as a percentage of T_P in trabeculae from WT hearts.

6.3.3. Incorporating a Ca^{2+}–sensitizing mutation troponin C mutation (L48Q) into D230N hearts augments tension-generating capacity and calcium sensitivity of tension in trabeculae

It is worth pointing out that the decrease in peak twitch tension of intact trabeculae from D230N hearts (< 50% that of WT) occurs despite an increased calcium transient amplitude during a twitch (230). That is, although intact cardiomyocytes from D230N hearts may be operating at a higher peak calcium concentration than WT hearts, the twitch tension is still significantly reduced. This, together with reduced calcium sensitivity of steady-state tension (Fig. 6.2B), strongly suggests that a key determinant of the reduced peak twitch tension in intact trabeculae of D230N hearts is an inhibition of thin filament activation. Therefore, we hypothesize that enhancing the calcium sensitivity of the D230N thin filaments *in vivo* will augment the tension-generating capacity of D230N hearts.

To test this hypothesis, we took a genetic engineering approach that specifically targets the cardiac thin filament protein, troponin C. We crossed the D230N mice with an engineered transgenic mouse line that expresses low levels of the calcium-sensitizing cardiac troponin C variant L48Q. Previous work has demonstrated that L48Q induces a conformational change in the troponin C subunit that ultimately enhances its affinity for both calcium and the troponin I subunit (234, 235), which translates to increased cardiac contractility (236). Furthermore, inclusion of just 16% of L48Q troponin C into the sarcomere has been shown to increase the calcium sensitivity of tension in permeabilized rat trabeculae, and increase the contractility of intact rat cardiomyocytes

(237). Thus, L48Q troponin C serves as a potent calcium-sensitizer and positive inotrope in cardiac muscle.

Trabeculae from the D230N + L48Q double-transgenic (DTG) hearts were isolated and the twitch tension was measured. Figure 6.3A shows the average twitch tension (T) traces for intact trabeculae from WT (green), the L48Q-only controls (gray), D230N (blue), and DTG (red) hearts. The average peak twitch tension (T_P) of trabeculae from DTG hearts is significantly greater than trabeculae from D230N hearts, and is not different from WT (Fig. 6.3B). We also note that T_P of trabeculae from L48Q-only control hearts is not different than the T_P of trabecula from WT nor DTG, but it is significantly greater than T_P of trabeculae from D230N hearts (gray bar, Fig 6.2B). Similarly, the maximum rate of tension development (Max. dT/dt) is significantly reduced in trabeculae from D230N hearts compared with all other groups (Fig. 6.3C), while the time to T_p (TT_P) is not different between any of the groups (Fig 6.3D). Interestingly the only difference in time to 50% relaxation (RT_{50}; Fig. 6.3E) and time to 90% relaxation (RT_{90}) is between L48Q-only controls and other groups. This reduced relaxation of L48Q trabeculae comapred with WT is in agreement with previous work on isolated myofibrils in which native troponin C was exchanged for L48Q troponin C (238) and computational models of the twitch kinetics in L48Q cardiomyocytes (65).

Lastly, to confirm that the calcium handling properties of the DTG hearts were indeed improved compared to D230N hearts, we measured the T_{SS}–pCa relations of trabeculae from each genotype. Figure 6.3G shows the corresponding T_{SS}–pCa relations with the fitted Hill equation. The results of the fits show that, while the pCa50 of trabeculae from D230N hearts is significantly reduced compared to WT, the pCa50 of trabeculae from DTG hearts is not different from trabeculae from WT hearts (Fig. 6.3H). This suggests that the L48Q mutation incorporated in the

sarcomere indeed increases the calcium sensitivity of tension in D230N hearts, which is likely the underlying mechanism of increased twitch tension in intact trabecula from DTG hearts. Finally, the Hill coefficient is not significantly different between trabeculae from WT, D230N, or DTG hearts (Fig. 6.3I). (See table 6.2 for numerical values corresponding to each group of each panel of Figure 6.3.)

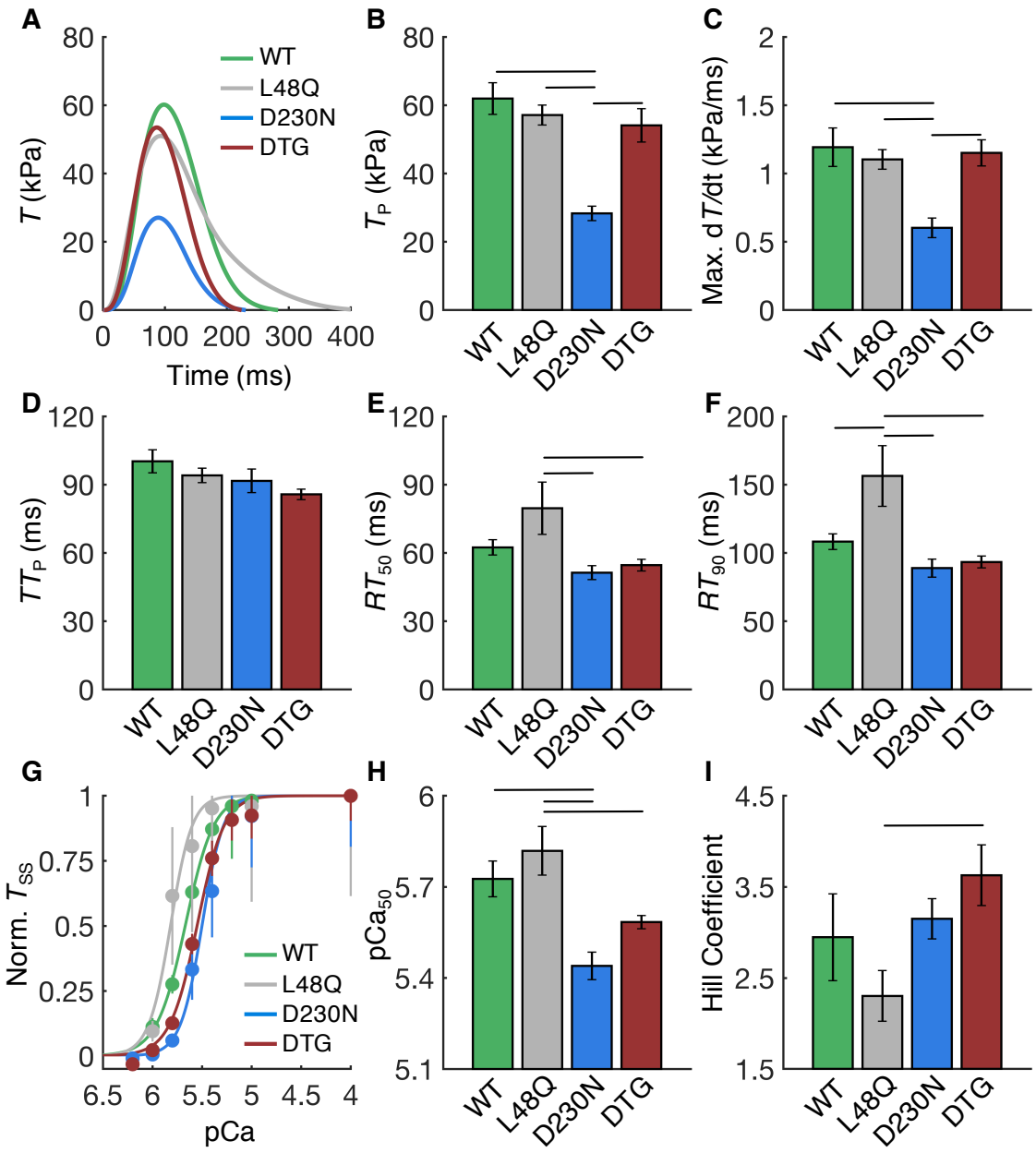

Figure 6.3. Genetically engineering a thin filament calcium sensitizer (the troponin C mutation L48Q) improves function of trabeculae from D230N hearts.

(A) Sample twitches from intact trabeculae from WT (green), L48Q-only controls (gray), D230N (blue), and the L48Q + D230N double transgenic (DTG; red). The SEM of the twitches is excluded for clarity. (**B**) The peak twitch force (T_P) and (**C**) maximum rate of contraction (Max. dT/dt) are not different between trabeculae from WT, L48Q controls, or the DTG hearts, while both parameters are significantly reduced for trabeculae from D230N hearts compared with every other

genotype. (**D**) The time to T_P (TT_P) is not different between trabeculae from each genotype. (**E**) The time to 50% relaxation (RT_{50}) and (**F**) time to 90% relaxation (RT_{90}) are significantly increased in L48Q controls, but are not different for WT, D230N, and DTG genotypes. (**G**) Steady-state tension (T_{SS}) versus pCa relations for trabeculae from heart of each genotype, showing the partial recovery of the calcium sensitivity in the DTG preparations compared to D230N. (**H**) The pCa_{50} for trabeculae from DTG hearts is not significantly different than WT, while (**I**) the Hill coefficient is significantly different only between trabeculae from DTG and L48Q control hearts. WT and D230N data are the same data from Figures 6.1 and 6.2, shown again here for clarity. Error bars represent S.E.M for n=7-9 intact trabeculae and 4-9 permeabilized trabeculae. Black lines above the bars indicate $p < 0.05$ using a one-way ANOVA with a Tukey post-hoc test of significance.

Table 6.1. Intact and permeabilized trabecula mechanics measurements

	WT	**L48Q**	**D230N**	**DTG**
T_P **(kPa)**	61.9 ± 4.6	57.1 ± 2.9	28.3 ± 2.1*	54.1 ± 4.9
Max. d*T*/dt (kPa/ms)	1.19 ± 0.14	1.10 ± 0.07	0.60 ± 0.07*	1.15 ± 0.10
TT_P **(ms)**	100.3 ± 5.1	94.1 ± 3.2	91.7 ± 5.2	85.7 ± 2.3
RT_{50} **(ms)**	62.4 ± 3.4	79.6 ± 11.5	51.3 ± 3.0	54.6 ± 2.5
RT_{90} **(ms)**	108.3 ± 5.7	156.3 ± 22.2*	88.9 ± 6.6	93.4 ± 4.4
pCa_{50}	5.73 ± 0.06	5.82 ± 0.08	5.44 ± 0.05*	5.58 ± 0.02
n_H	2.95 ± 0.48	2.30 ± 0.28	3.15 ± 0.22	3.63 ± 0.33

*$p < 0.05$ compared to WT using a one-way ANOVA with a Tukey post-hoc test of significance. Values represent mean ± S.E.M. for $n \geq 6$ preparations. Data also shown in Fig. 6.3.

6.3.4. Organ-level dysfunction of D230N hearts is prevented by incorporation of L48Q

Given that the incorporation of L48Q troponin C into the thin filament of D230N hearts restores twitch tension and improves the calcium sensitivity of steady-state tension in isolated trabeculae, we wanted to determine whether these functional improvements translate to the whole-organ level. First, because we are able to elicit twitches from intact trabeculae for each of the transgenic murine models, we hypothesized that an experimental analogue of the tension index (Davis *et al. Cell*, 2016) can be generated from each of the averaged twitch tension-time traces, and that it will predict the degree of myocardial remodeling. (65). Davis and colleagues demonstrated that a positive tension index is correlated with hypertrophic/concentric growth, while a negative tension index corresponds to dilated/eccentric growth, and the absolute value corresponds to the degree of hypertrophy (65). Thus, the tension index can be used as a cardiomyocyte-level predictor of the type and severity of myocardial remodeling (65, 66).

To apply this method to the intact trabeculae twitch traces, average twitches of trabeculae from each genotype were normalized to the peak twitch tension of WT trabeculae (Fig. 6.4A) and the force-time integrals were calculated using a point-by-point integration method based on cumulative trapezoidal approximations. We find that the experimental tension index for D230N hearts is -6.62×10^3 (%WT $T \cdot$ms), while it is -1.48×10^3 (%WT $T \cdot$ms) for DTG hearts (Fig. 6.4B). Based on these calculations, we predict that the myocardium of DTG hearts will have less eccentric growth (dilation) than the D230N hearts.

To confirm this prediction, we took echocardiographic measurements of *in vivo* cardiac performance and dimensions for each heart type. The systolic and diastolic left ventricular inner diameters (LVIDs) are significantly increased in D230N hearts compared to WT (Fig. 6.4 C & D, respectively), as predicted based on the large, negative tension index for D230N hearts [Fig 6.4B;

(65)]. Notably, the systolic and diastolic LVIDs DTG hearts are significantly reduced compared to D230N hearts, and are not different from WT. This further confirms the predictions based on the tension index calculation. The fractional shortening and ejection fraction are also significantly reduced in D230N hearts compared to WT, L48Q, and DTG hearts (Fig. 6.4 E & F, respectively). We note again that the fractional shortening and ejection fraction are not significantly different between DTG and WT hearts.

The results shown in Figure 6.4 highlight several important outcomes of this work: (*i*) ability of a trabecula-based tension index to predict organ-level morphology in DCM hearts, (*ii*) the utility of coupling these predictions with measurements of cardiac muscle mechanics to generate precise interventions that mitigate pathological remodeling, and (*iii*) the ability of genetic engineering to deliver targeted therapies that prevents the dysfunction caused by DCM-associated sarcomere protein mutations, from the subcellular to the tissue level.

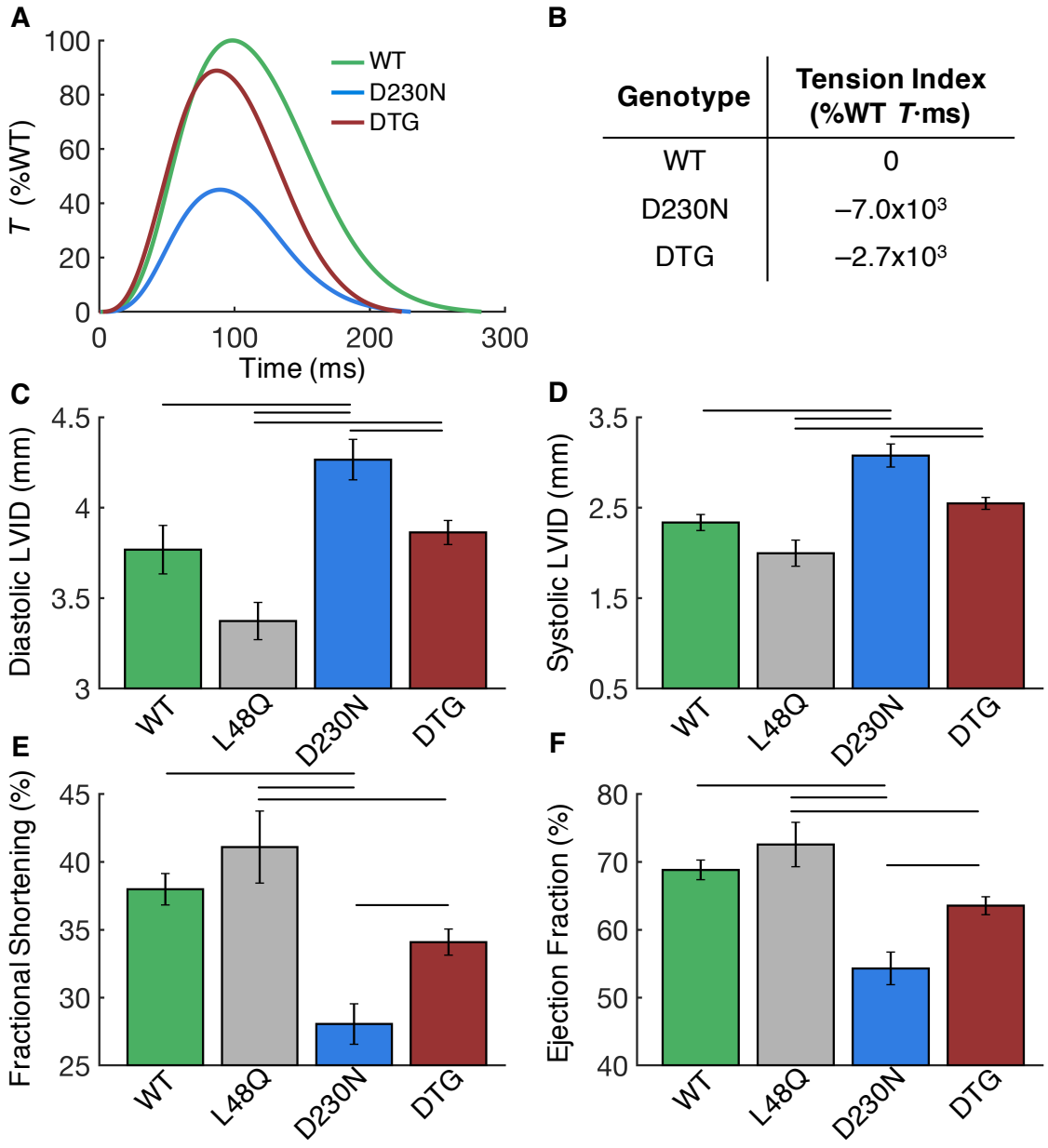

Figure 6.4. Organ-level morphology and dysfunction in D230N hearts is prevented by L48Q, as predicted by tension index calculations.

(A) Twitch force (*T*) traces for trabeculae from D230N (blue) and DTG (red) normalized to WT (green) used to calculate the twitch index (see main text). **(B)** From the normalized twitches, the tension indexes are calculated for each heart type as the difference between the force-time integral of WT and each other heart type (Davis *et al.,* 2016). Echocardiographic measurements from 4-month-old mice reveal that the systolic (**C**) and diastolic (**D**) left ventricular inner diameter (LVID)

correlate with the predictions based on the tension index for each case shown in panel B. The Both the Diastolic and Systolic LVID are significantly increased for D230N hearts compared with WT, while they are not different between WT and DTG hearts. The fractional shortening (**E**) and ejection fraction (**F**) are also improved in the DTG hearts, in that each parameter is significantly greater in DTG hearts compared to D230N and are not different form WT. Horizontal black lines above the bars represent $p < 0.05$ between groups using a one-way ANOVA and a Tukey post-hoc test of significance. Error bars represent the SEM.

Table 6.2. Echocardiographic measurements of ventricle dimensions and cardiac performance *in vivo*

	WT	L48Q	D230N	DTG
Diastolic LVID (mm)	3.77 ± 0.13	3.37 ± 0.10	4.27 ± 0.11*	3.86 ± 0.07
Systolic LVID (mm)	2.34 ± 0.09	2.00 ± 0.14	3.08 ± 0.13*	2.55 ± 0.07
Fractional Shortening (%)	38.0 ± 1.2	41.1 ± 2.7	28.1 ± 1.5*	34.1 ± 1.0
Ejection Fraction (%)	68.8 ± 1.4	72.6 ± 3.3	54.3 ± 2.4*	63.6 ± 1.3

*$p < 0.05$ compared to WT using a one-way ANOVA with a Tukey post-hoc test of significance. Values represent mean ± SEM. Data also shown in Fig. 6.4.

6.4. Discussion

6.4.1. Predicting and preventing myocardial remodeling in a murine model of dilated cardiomyopathy

Approximately 35–40% of genetic DCMs result from mutations in genes that encode sarcomere proteins (44, 61), with a vast diversity of mutations and accompanying functional alterations to the mutated proteins. Moreover, the divergence of phenotype (*e.g.* dilated versus hypertrophic cardiomyopathy) from genotypically similar sarcomere mutations suggests that the molecular underpinnings driving DCM pathogenesis are extremely sensitive to the nature of the mutation. Understanding such specific patho-mechanisms remains a major challenge in cardiac research, and these complications have hampered our ability to design novel therapeutic options to restore function (or prevent dysfunction) of DCM failing hearts.

Here, we address this issue by defining a trabecula-based predictive index of myocardial remodeling in a murine model of dilated cardiomyopathy, and to use this prediction to design a targeted and preventative intervention. To do so, we analyzed intact and permeabilized trabeculae mechanics from mice harboring the point mutation D230N in tropomyosin, which was discovered in two large, unrelated families with DCM (229). Previous *in vitro* characterization of D230N tropomyosin demonstrated that it has a 5-fold higher affinity for actin than WT tropomyosin, which likely limits its azimuthal displacement along the actin (230). We confirm this using demembranated trabeculae and show that the calcium sensitivity of steady-state tension in D230N hearts compared with WT. Thus, the putative inhibition of thin filament activation in D230N hearts likely plays an important role in the DCM pathogenesis, and, as such, we designed a genetically engineered intervention that targets the thin filament. We developed a double-transgenic (DTG) murine model, in which we integrated a calcium-sensitizing troponin C mutation L48Q into the

sarcomere of D230N hearts and found a significant improvement in: (*i*) intact trabeculae contractility, (*ii*) increased calcium sensitivity of steady-state tension in permeabilized trabeculae, and (*iii*) improved myocardial dimension and performance *in vivo* in DTG hearts compared with D230N hearts. Furthermore, by expanding upon the recent work of Davis *et al.* (*Cell*, 2016), we demonstrate that a trabecula-based 'tension index' accurately predicts the degree of myocardial remodeling in the DCM model, as well as the morphological improvements in the myocardium of the DTG model. Thus, the work we present here demonstrates the ability of experimental trabeculae mechanics from myopathic hearts to rationally design targeted interventions to prevent pathological myocardial remodeling interventions, the efficacy of which on can be accurately predicted by a trabecula-based tension index.

6.4.2. Towards a precision medicine model for genetic cardiomyopathies

The use of L48Q troponin C for treating various types of heart failure has been demonstrated previously, using both rat and mouse models of myocardial infarction (236, 237). A recent study by Shettigar *et al.* found that expression of L48Q troponin C in mouse hearts via an adeno-associated virus serotype 9 prior to myocardial infarction (MI) preserves cardiac function and performance post MI, while expression of L48Q after the MI enhances cardiac function (236). Similarly, a study by Feest *et al.* expressed L48Q in intact cardiomyocytes from rat hearts after MI and found significant improvements in contractility compared to untreated cardiomyocytes (237) Here, we find that expression of L48Q has similar beneficial effects on the cardiac performance and morphology of a genetic form of dilated cardiomyopathy. We demonstrate that L48Q has a significant effect on different functional parameters in both WT and D230N hearts from the single

trabecula scale to the whole organ scale—the majority of which are in D230N hearts. These findings are summarized in Figure 6.5.

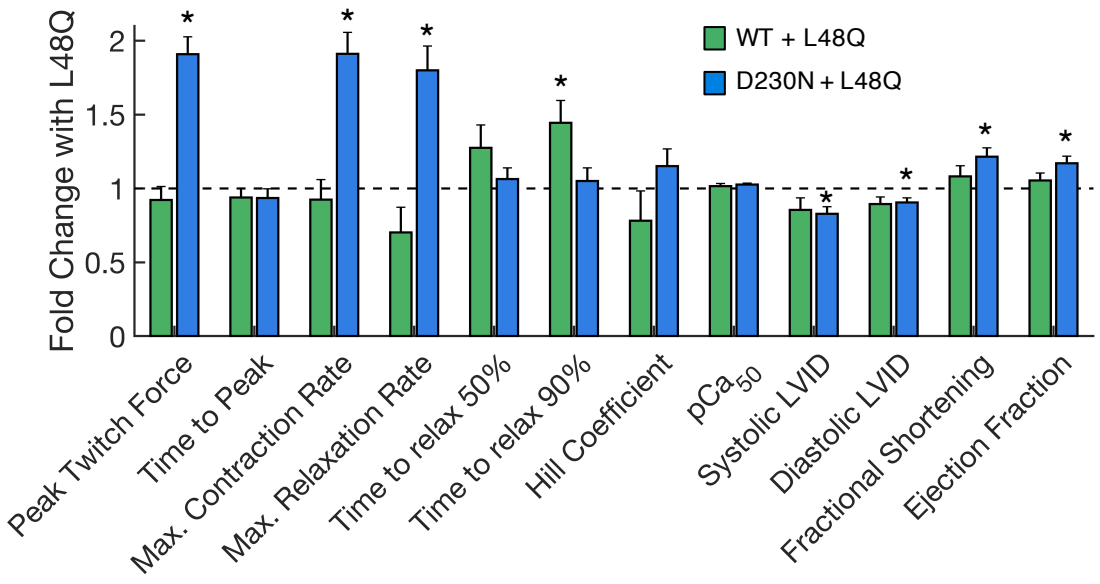

Figure 6.5. Quantitative summary of the functional effects of L48Q troponin C on WT and D230N hearts.

Each parameter for preparations from L48Q controls and the DTG hearts were normalized the value of the same parameter for preparations from WT and D230N hearts, respectively. In doing so, the 'improvement' for each genotype with the addition of L48Q can easily be seen. A value of 1 indicates that there was no change after the incorporation of L48Q into either WT or D230N hearts. The strongest effects of L48Q are on the D230N preparations—specifically on the peak twitch force and maximum rates of contraction and relaxation in which there was nearly a two-fold increase. The systolic and diastolic left ventricular inner diameters (LVID), the fractional shortening, and the ejection fraction of D230N hearts are also significantly increased with the addition of L48Q, whereas the same parameters in WT are unaffected by L48Q. Interestingly, the only parameter significantly affected by L48Q for WT hearts is the time to 90% relaxation. *$p <$ 0.05 comparing L48Q to WT and DTG to D230N.

There is still much work to be done towards a precision medicine model to treat genetic cardiomyopathies. We suspect that L48Q is not the only means by which to restore cardiac function to D230N hearts. It is possible that the small molecule Levosimendan, which interacts with the troponin C subunit and enhances calcium sensitivity (239), may have a similar beneficial effect in DCM hearts of preserving contractility and preventing myocardial remodeling. Moreover, there is a large effort towards developing myosin-targeted positive inotropes to improve contractility in failing hearts. These include small molecules that are already in human clinical trials [*e.g.*, omecamtiv mecarbil (86, 215, 240, 241), or are being heavily investigated for translation to the clinic [*e.g.*, 2-deoxy-ATP (194, 195, 233, 242)]. The naturally occurring nucleotide 2-deoxy-ATP has been shown to improve contraction in myocardial samples isolated from humans with end-stage heart failure (196). Omecamtive mecarbil (OM) was recently shown to increase the myofilament ATPase activity and calcium sensitivity of myofilaments containing a DCM-associated tropomyosin mutation (240). However, the authors did not investigate the long-term effects of OM on preserving myocardial morphology in the mouse model of DCM to assess whether it has a similar preventative capacity as the DTG murine model we report here. Thus, an important next step towards a precision medicine model for treating DCM is to assess whether targeting thick filament proteins to combat thin filament dysfunction has a similar efficacy as we report here.

Finally, if there are compensatory mechanisms that have already developed in the DCM failing heart (*e.g.*, increased Ca^{2+} storage and release in the sarcoplasmic reticulum), then a calcium sensitizer such as L48Q may overcorrect. That is, targeting the myofilament calcium sensitivity may only be efficacious if done early and therefore prevents such compensations. Thus, the timing of intervention likely plays a role in determining the outcome. An important follow-up to the

current study would be to determine if early-stage versus late-stage delivery of L48Q has an impact on the contractile and morphological improvements that we show in the DTG hearts. Lastly, the expression of L48Q used in this study is relatively modest (~20%, unpublished data). Thus, it would be informative to examine a 'dose response' with L48Q to determine if there is an optimized expression level for providing the most effective intervention. Future studies on murine models of DCM are underway to answer these remaining questions.

Chapter 7

Concluding remarks – Summary, remaining challenges, and future research directions

7.1. Summary of current work

Despite significant progress over the past decades towards an understanding of the myofilament basis of striated muscle function, there are still many confounding factors that remain major challenges to overcome. The body of work presented here is aimed at revealing myofilament-based mechanisms that regulate muscle function by leveraging recent advances in structural, mechanical, and computational biology. Specifically, this work focusses on uncovering contributions to regulatory mechanisms of muscle function from each of the three main myofilaments of the sarcomere: the myosin-containing thick filament, the actin-containing thin filament, and the giant filamentous protein titin.

In Chapter 2, we describe a spatially explicit computational model that explores how titin stiffness affects contractile mechanics and energetics. To do so, we modify a previously described model of the half-sarcomere to now include an adjustable I-band spring that extends from the tip of the thick filament to the thin filament-Z-line intersection. By altering the stiffness of the I-band spring, we find that increasing titin stiffness inhibits the ability of myosin motors to energetically compete with the added titin-based strain in the thick filament and are therefore less efficient in generating force compared with motors in series with compliant titin. These findings may also be relevant in cardiac muscle, in which titin isoforms are stiffer than in skeletal muscle, and provide

mechanistic insight into possible patho-mechanisms involving modifications to titin that make it stiffer (*e.g.*, mutations in the I-band region).

Chapter 3 continues the focus on titin, in which measure the contributions of the I-band region of titin to the elasticity of the sarcomere *in-situ* in single intact skeletal muscle fibers throughout the duration of isometric tetanus. By making these measurements at a wide range of sarcomere lengths, we can isolate contributions to the active half-sarcomere elasticity form the A-band and I-band of the sarcomere. Furthermore, we apply to our experimental measurements a rigorous mathematical model of the various elastic elements that contribute to the change in half-sarcomere stiffness during isometric force development. In doing so, we show that titin the I-band region of titin has a dynamic stiffness that is tuned to the length of the sarcomere, likely mediated by load-dependent structural dynamics of the I-band-specific domains. This mechanism is likely important in maintaining sarcomere ultrastructure and preventing inhomogeneities in myofibrils during contractions against high load at long sarcomere lengths.

Chapter 4 highlights work we have done towards understanding the structural basis of force augmentation in response to positively inotropic treatments. Specifically, multiple studies are presented that harness high-intensity synchrotron light to enable Angstrom-level X-ray diffraction-based measurements of the myofilament structure in cardiac muscle. Through this technique, we investigate the structural dynamics of myosin motors in resting and activated cardiac muscle and find that some positively inotropic interventions have no effect on resting sarcomere structure, whereas others perturb the resting state of the thick filament to potentiate the ensuing contraction.

Similarly, Chapter 5 focuses on the effects the naturally occurring nucleotide 2-deoxy-ATP (dATP) on the structure of single myosin motors, and how these structural changes allosterically induce structural changes in the thick filament and sarcomere lattice geometry in resting and

activated permeabilized cardiac muscle. We elucidate the multi-scape structural effects of dATP by applying a multifaceted approach that combines single protein structure, Brownian dynamics simulation, *in vitro* motility assays, and small-angle X-ray diffraction analysis of thick filament structure. We find that a key mechanism driving the cardiac force augmentation with dATP is an electrostatic restructuring of the actin-binding surface of myosin when dADP is bound, that leads to a disruption of the resting state of the thick filament and potentiates strong cross-bridges upon calcium release.

Lastly, Chapter 6 focuses on dysregulation of the cardiac thin filament caused by a dilated cardiomyopathy-related mutation in tropomyosin, and developing a predictive metric based on trabecula mechanics to aid the development of a preventative, targeted therapeutic intervention. We use a transgenic murine model harboring a loss-of-function tropomyosin mutation that causes dilated cardiomyopathy. We show that both sarcomere-level and tissue-level dysfunction can be prevented by incorporating a calcium-sensitizing mutation in troponin C to specifically combat the loss of thin filament activation caused by the tropomyosin mutation.

To summarize, the work presented here highlights results from an integrative approach that aims to understand myofilament-specific mechanisms that govern regulation of both cardiac and skeletal muscle function. As a result, we answer questions that range from a basic understanding of molecular-level regulation of muscle function to developing potential therapeutics that may translate to the clinic for patients with specific types of congenital heart failure.

7.2. Remaining challenges and future directions

7.2.1. Thick filament-based inotropes for thin filament-based cardiomyopathy

There is a large effort towards developing myosin-targeted positive inotropes to improve contractility in failing hearts. These include small molecules that are already in human clinical trials [*e.g.*, omecamtiv mecarbil (86, 215, 240, 241), or are being heavily investigated for translation to the clinic [*e.g.*, 2-deoxy-ATP (194, 195, 233, 242)]. Our group has been focused on developing treatments for heart failure based on the naturally occurring nucleotide 2-deoxy-ATP, which has been shown to improve contraction in myocardial samples from rodents (194, 233), pigs (195), and humans with end-stage heart failure (196). Despite having similar inotropic affects as the calcium sensitizing troponin C mutation L48Q (see Chapter 6), dATP has not yet been tested against genetic dilated cardiomyopathy-induced systolic dysfunction. Interestingly, omecamtive mecarbil (OM) was recently shown to increase the myofilament ATPase activity and calcium sensitivity of myofilaments containing a DCM-associated tropomyosin mutation (240). Thus, a thick filament-targeting positive inotrope (OM) can restore function to a thin filament-based mutation, at least in deconstructed cardiac muscle preparations. Moreover, a similar thick-to-thin filament restorative effect was made when crossing a crossing a loss-of-function troponin C mutation (I61Q) with a hypercontractile myosin heavy chain mutation [R403Q; (66)]. Thus, an important next step towards a precision medicine model for treating DCM is to assess whether targeting thick filament proteins to combat thin filament dysfunction has beneficial outcomes in terms of preventing pathological remodeling and preserving cardiac function.

Unfortunately, delivery of dATP is a current challenge, as it must be generated within the cell. It was recently demonstrated that the dATP content in cardiomyocytes of mouse hearts is ~20 fmol per mg of heart tissue (243). However, we have shown that viral-mediated upregulation of

the dATP-producing enzyme ribonucleotide reductase can improve contractility of isolated rat cardiomyocytes (244), mouse hearts (233), and pig hearts (195). Thus, by virally upregulating ribonucleotide reductase in hearts of a transgenic mouse model harboring a DCM-associated tropomyosin mutation, we examined the ability of increasing dATP levels to preserve function in DCM-induced heart failure.

The work described in Chapter 6 demonstrates that the DCM-associated tropomyosin mutation D230N causes significant dilation of the ventricles, contractile deficiencies in isolated trabeculae, and reduced cardiac output, and that incorporating the calcium-sensitizing troponin C mutation L48Q into the sarcomere of D230N hearts prevents each of these modes of dysfunction. Therefore, we examined whether upregulated levels of dATP has a similar beneficial effect in the same model of DCM. This provides a thick filament correlate of the thin filament intervention described in Chapter 6.

Figure 7.1 shows preliminary results of twitch mechanics and kinetics of intact trabeculae from WT and D230N hearts that were injected with either a virus to promote ribonucleotide reductase-mediated dATP production (+ dATP) or a sham virus (+ sham). Measurements were made at two sarcomere lengths (SL = 2.0 and 2.3 μm) to investigate SL-dependent effects on the D230N mutation and dATP upregulation. Continued efforts are underway to quantify the dATP levels and confirm the efficacy of the virus. In addition, future work will investigate the morphological effects of increased dATP levels using echocardiography, as described in Chapter 6.

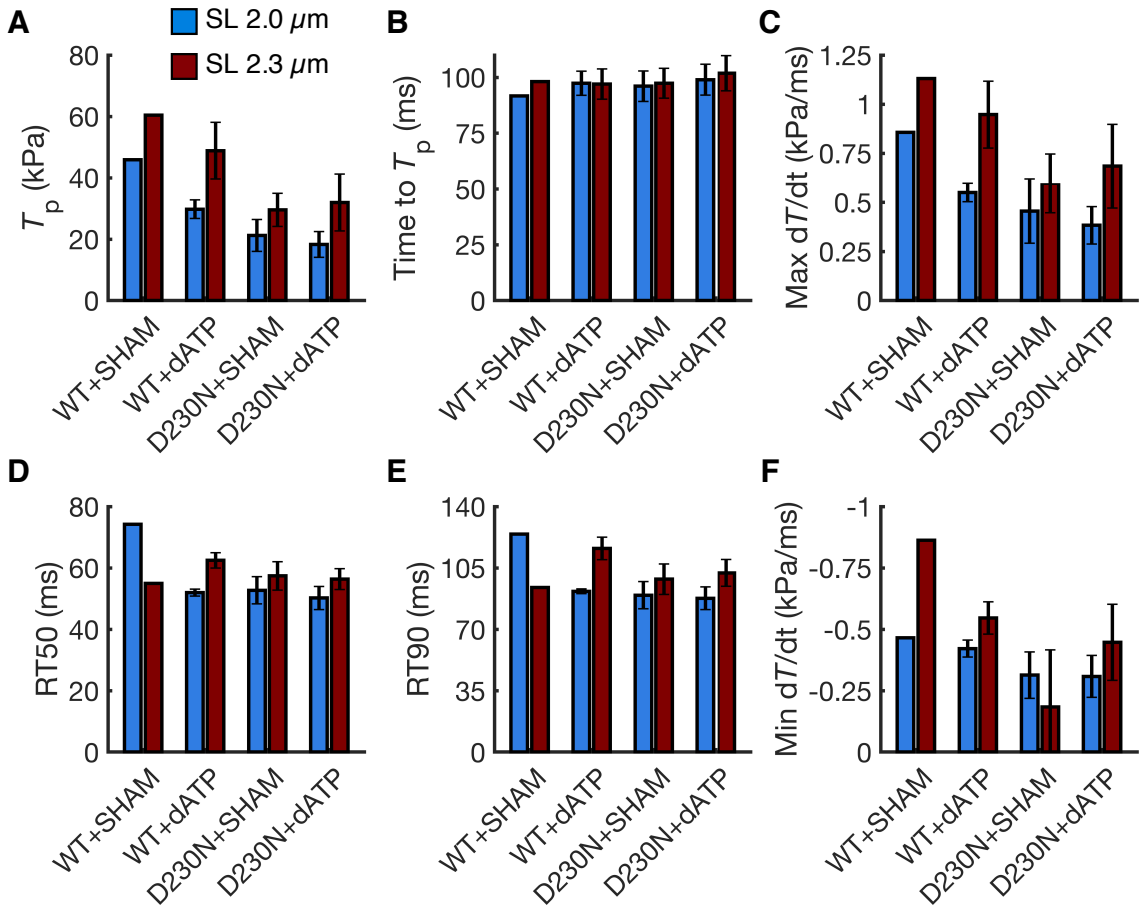

Figure 7.1. Targeting myosin motors in a thin filament-based murine model of DCM

Preliminary data ($n \geq 1$ for each group) for intact trabeculae mechanics from WT and D230N hearts that have been injected with an adeno-associated virus to upregulate the dATP-promoting enzyme ribonucleotide reductase. (**A**) Peak twitch tension (T_P) (B) time to T_P (relative to the stimulus), (**C**) maximum rate of tension development, (**D**) time to 50% relaxation (relative to T_P), (**E**) time to 90% relaxation, (**F**) and maximum rate of relaxation (denoted min. dT/dt). Blue bars and red bars indicate measurements made at SL 2.0 µm and 2.3 µm, respectively. Because of the low biological repeats (only $n = 1$ for WT + SHAM) no statistical comparisons were performed between groups. Error bars represent S.E.M.

7.2.2. What are the functional consequences of altered basal sarcomere length in myopathic hearts?

An interesting and relatively unexplored consequence of some cardiomyopathy-associated sarcomere mutations is an alteration of the basal sarcomere length (SL) of the cardiomyocytes. Interestingly, in some cases, isolated cardiomyocytes from hearts with DCM or HCM have significantly altered resting SL compared to WT (65), while in other cases, the SL is unaffected (230, 245). The latter case implies the addition of sarcomeres longitudinally to increase cell length without affecting SL in eccentric hypertrophy (245), while the former case may impact the Frank-Starling response by changing where on the tension-SL relation the cardiomyocytes are operating. Towards that end, some sarcomere protein mutations cause a diminished Frank-Starling response by altering the sarcomere-length dependent calcium sensitivity and force augmentation (64).

A diminished Frank-Starling response in cardiomyocytes from cardiomyopathic hearts could arise from an altered twitch tension-SL relation, and this would likely translate to a SL-dependent twitch 'tension index' (the twitch tension-time integral of cardiomyopathic cardiomyocytes compared to WT that correlates with the severity of phenotype; see Chapter 6). Therefore, a fundamental question that remains unanswered is whether sarcomere protein mutations that alter basal SL in myopathic hearts is just a consequence of the underlying mutation causing dysregulation of myofilament structure, or a potential compensatory mechanism by which the sarcomeres attempt to modulate contractility by changing the working range of SL. Moreover, if the underlying mutation alters the twitch tension-SL relation, how might that affect the progress of myocardial remodeling?

To address these questions, we set out to establish whether sarcomere protein mutations associated with HCM and DCM have correlative effects on the basal SL, and whether these effects

manifest as SL-dependent tension indexes. Previous work using troponin C modulators in cardiac muscle has established the mutations I61Q and L48Q as models of DCM and HCM (respectively) in hearts from transgenic murine models (65). It was found that isolated cardiomyocytes from I61Q hearts have a significantly increased resting sarcomere length (65), while viral-mediated expression of L48Q does not affect the basal sarcomere length in rat cardiomyocytes (237). Moreover, L48Q has been shown to reduce the sarcomere length dependence of calcium sensitivity and force augmentation due to significantly increased activation at short sarcomere lengths (192). Thus, from these previous studies, we hypothesized that the magnitude of the twitch index of trabeculae from L48Q hearts will be higher at short SL than long SL, while it will be lower at shorter SL than longer SL for trabeculae from I61Q hearts.

To test this hypothesis, we measured twitch tension (*T*) at short (2.0 μm) and long (2.3 μm) in intact trabeculae from WT, L48Q and I61Q hearts (Figure 7.2 A–C). The twitch tension index was calculated by taking the difference between the twitch tension-time integral of trabeculae from each genotype (as a percentage of WT). In agreement with previous work (65), trabeculae from L48Q hearts scored a positive tension index at both SL (indicative of HCM-associated concentric hypertrophy) and trabeculae from I61Q hearts scored a negative twitch index (indicative of DCM-associated eccentric hypertrophy). Furthermore, we find that the tension index for trabeculae from L48Q and I61Q hearts are different at short versus long SL in each group (Figure 7.2 C). As we hypothesized, the tension index from L48Q hearts has a greater magnitude at short SL compared with long SL, while the tension index from I61Q hearts has a greater magnitude at long SL compared with short SL (Fig. 7.2D).

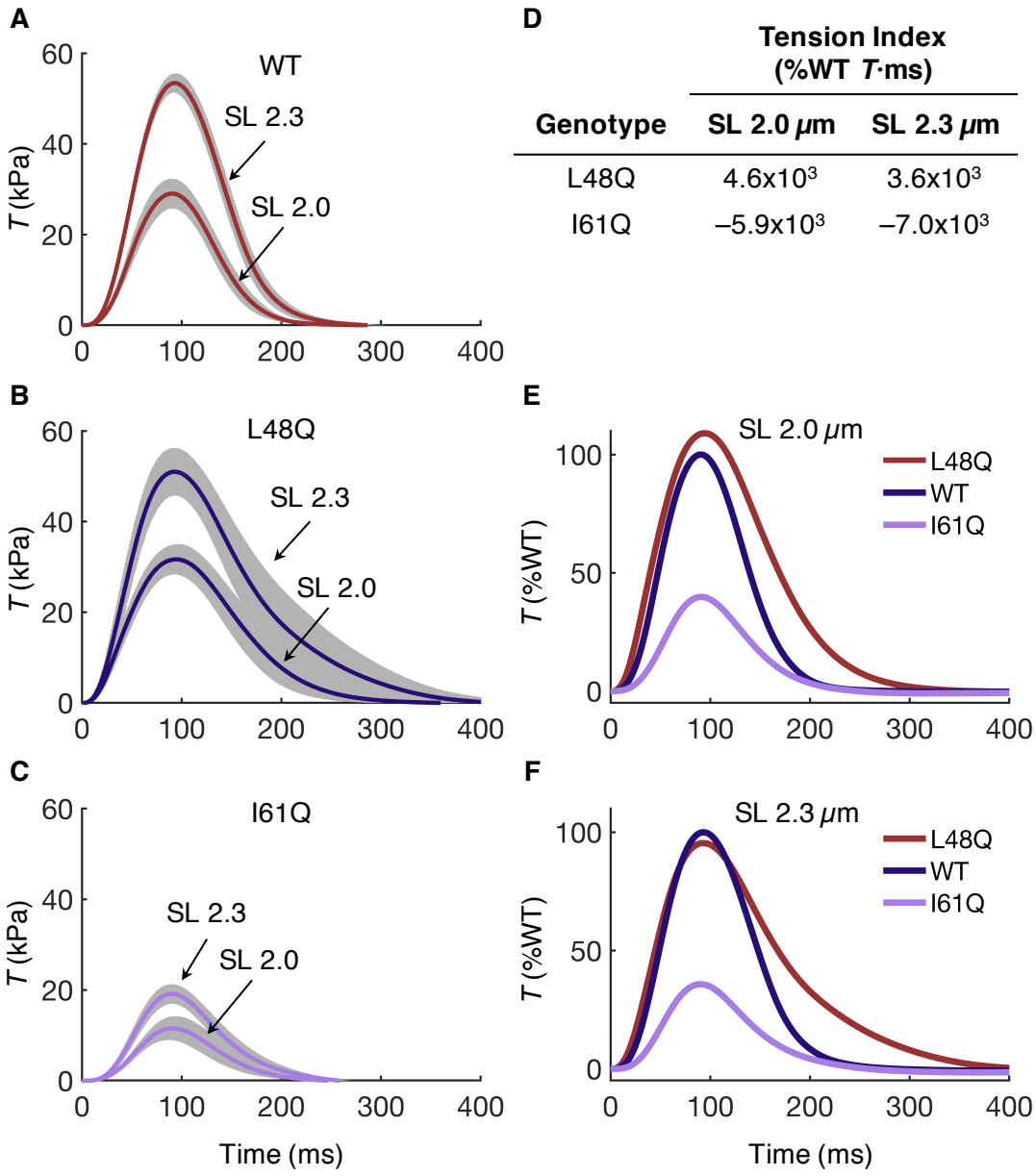

Figure 7.2. Sarcomere length-dependence of twitch force and twitch index of intact trabeculae from mouse hearts with altered thin filament calcium handling

(**A–C**) Twitch tension (*T*) time courses of intact trabeculae paced at 1 Hz (30°C) at either short or long sarcomere length (SL 2.0 and 2.3 μm, respectively) from WT (**A**), L48Q (**B**), and I61Q (**C**) mouse hearts. (**D**) Tension indexes calculated for each genotype based on the normalized twitch traces at SL 2.0 μm (**E**) and 2.3 μm (**F**). Gray shaded region is the S.E.M for $n \geq 7$ animals for each group.

These results suggest that interventions that alter the working SL of myopathic hearts may mitigate pathological remodeling of the myocardium. Future studies will test this idea and focus on determining the molecular mechanisms behind the SL-dependence of the twitch index in each of these cardiomyopathy models.

7.2.3. What is the role of intra- and extracellular mechanotransduction in driving cardiac hypertrophy?

There are many unanswered questions regarding how cardiomyocytes sense and respond to perturbations in mechanical homeostasis, both intracellularly and extracellularly. In a process called mechanotransduction, cardiomyocytes convert mechanical stimuli into biochemical events that affect myocardial structure and function (246). Are there differences in the biochemical and morphological responses of cardiomyocytes undergoing intracellular contractility perturbations (e.g. sarcomere protein mutations) versus extracellular perturbations (e.g. stiffening of the extracellular matrix by myocardial infarction or fibrosis)? This broad question is of great importance to understanding the mechanobiology of cardiomyocytes that maintain its structural organization (247) or drive cardiomyopathy phenotypes.

For example, intracellular molecular mechanosensors likely include many sarcomere and cytoskeletal proteins, including titin, non-muscle myosin (248), and the myosin filament (43, 72, 173, 246, 249), which likely regulate both contractility and changes in myocardial structure. Similarly, microtubules in cardiomyocytes are emerging as important players in mechanobiology

of cardiomyocytes by acting as shock absorbers during contraction that can be tuned by detyrosination, which may be a promising target for treating heart failure (250–253).

Changes in the extracellular environments can also play a role in modulating the mechanotransduction pathways of cardiomyocytes. For example, in cardiac fibrosis is a dangerous condition that cause stiffening of the myocardium and contractile deficiency. Fibrosis can be triggered by cardiac fibroblast activation and differentiation into myofibroblasts that drive excess accumulation of extracellular matrix. This process can be initiated by mechanical stimuli, including stretch and increased tissue stiffness (254, 255), and understanding the mechanobiology that drives it is critical for developing approaches to stop or prevent it.

Finally, there are many questions regarding the physical links that connect mechanotransduction pathways inside and outside of the cardiomyocytes, and how these links influence the relationship between contractility and cell morphology (256). For example, what is dystrophin's link to the contractile apparatus, and how does a disruption of this like affect cardiac contractility in Duchenne Muscular Dystrophy (257, 258)? hat is the role of membrane proteins and protein complexes like integrins and costomeres, in translating the mechanical work of sarcomeres into whole organ-level contraction? These questions, and many others, motivate continued research efforts towards understanding the molecular biophysics and mechanobiology of cardiac muscle, and its role in cardiomyopathy pathogenesis.

References

1. Kendrick-Jones J, Lehman W, Szent-Györgyi AG (1970) Regulation in molluscan muscles. *J Mol Biol* 54(2):313–326.

2. Hu Z, Taylor DW, Reedy MK, Edwards RJ, Taylor K a. (2016) Structure of myosin filaments from relaxed Lethocerus flight muscle by cryo-EM at 6 A resolution. *Sci Adv* 2(9):e1600058–e1600058.

3. Gordon AM, Homsher E, Regnier M (2000) Regulation of contraction in striated muscle. *Physiol Rev* 80(2):853–924.

4. Hoyle G (1983) *Muscles and Their Neural Control* (John Wiley & Sons Inc.).

5. Burgoyne T, Muhamad F, Luther PK (2008) Visualization of cardiac muscle thin filaments and measurement of their lengths by electron tomography. *Cardiovasc Res* 77(4):707–712.

6. Rynkiewicz MJ, et al. (2017) Tropomyosin Must Interact Weakly with Actin to Effectively Regulate Thin Filament Function. *Biophys J* 113(11):2444–2451.

7. Tardiff JC (2010) Tropomyosin and Dilated Cardiomyopathy. Revenge of the Actinomyosin "Gatekeeper." *J Am Coll Cardiol* 55(4):330–332.

8. Orzechowski M, Li X (Edward), Fischer S, Lehman W (2014) An Atomic Model of the Tropomyosin Cable on F-actin. *Biophys J* 107(3):694–699.

9. McKillop D, Geeves M (1993) Regulation of the interaction between actin and myosin subfragment 1: evidence for three states of the thin filamen. *Biophys J* 65(August):693–701.

10. Risi C, et al. (2017) Ca2+-induced movement of tropomyosin on native cardiac thin filaments revealed by cryoelectron microscopy. *Proc Natl Acad Sci* 114(26):201700868.

11. Sousa DR, Stagg SM, Stroupe ME (2013) Cryo-EM structures of the actin:tropomyosin filament reveal the mechanism for the transition from C- to M-State. *J Mol Biol* 425(22):4544–4555.

12. Loong CKP, Badr MA, Chase PB (2012) Tropomyosin flexural rigidity and single Ca2+regulatory unit dynamics: Implications for cooperative regulation of cardiac muscle contraction and cardiomyocyte hypertrophy. *Front Physiol* 3 APR(April):1–10.

13. Loong CKP, Zhou HX, Bryant Chase P (2012) Familial hypertrophic cardiomyopathy related E180G mutation increases flexibility of human cardiac α-tropomyosin. *FEBS Lett* 586(19):3503–3507.

14. Sewanan LR, Moore JR, Lehman W, Campbell SG (2016) Predicting effect of tropomyosin mutations on cardiac muecle contraction through myofilament modeling. *Front Physiol* 7(473):1–13.

15. Matyushenko AM, et al. (2018) The effects of cardiomyopathy-associated mutations in the head-to-tail overlap junction of α-tropomyosin on its properties and interaction with actin. *Int J Biol Macromol*. doi:10.1016/j.ijbiomac.2018.09.105.

16. Redwood C, Robinson P (2013) Alpha-tropomyosin mutations in inherited cardiomyopathies. *J Muscle Res Cell Motil* 34(3–4):285–294.

17. Woodhead JL, et al. (2005) Atomic model of a myosin filament in the relaxed state. *Nature* 436(7054):1195–1199.

18. Lombardi V, et al. (2004) X-ray diffraction studies of the contractile mechanism in single muscle fibres. *Philos Trans R Soc Lond B Biol Sci* 359(1452):1883–93.

19. Reconditi M (2006) Recent Improvements in Small Angle X-Ray Diffraction for the Study

of Muscle Physiology. *Rep Prog Phys* 69(10):2709–2759.

20. Squire J (1981) *The Structural Basis of Muscular Contraction* (Plenum Press, New York, New York).

21. Lombardi V, Piazzesi G, Linari M (1992) Rapid regeneration of the actin-myosin power stroke in contracting muscle. *Nature* 355(February):638–641.

22. Irving M, Lombardi V, Piazzesi G, Ferenczi MA (1992) Myosin head movements are synchronous with the elementary force-generating process in muscle. *Nature* 357(May):156–158.

23. Lombardi V, Piazzesi G, Ferenczi M (1995) Elastic distortion of myosin heads and repriming of the working stroke in muscle. *Nature* 374(April):553–555.

24. Irving M, et al. (2000) Conformation of the myosin motor during force generation in skeletal muscle. *Nat Struct Biol* 7(6):482–485.

25. Piazzesi G, et al. (2007) Skeletal Muscle Performance Determined by Modulation of Number of Myosin Motors Rather Than Motor Force or Stroke Size. *Cell* 131(4):784–795.

26. Previs MJ, et al. (2015) Myosin-binding protein C corrects an intrinsic inhomogeneity in cardiac excitation-contraction coupling. *Sci Adv* 1(1):e1400205–e1400205.

27. Lin BL, et al. (2018) Skeletal myosin binding protein-C isoforms regulate thin filament activity in a Ca2+-dependent manner. *Sci Rep* 8(1):2604.

28. Moss RL, Fitzsimons DP, Ralphe JC (2015) Cardiac MyBP-C regulates the rate and force of contraction in mammalian myocardium. *Circ Res* 116(1):183–192.

29. McNamara JW, Sadayappan S (2018) Skeletal myosin binding protein-C: An increasingly important regulator of striated muscle physiology. *Arch Biochem Biophys*.

doi:10.1016/j.abb.2018.10.007.

30. Harris SP, Belknap B, Van Sciver RE, White HD, Galkin VE (2016) C0 and C1 N-terminal Ig domains of myosin binding protein C exert different effects on thin filament activation. *Proc Natl Acad Sci U S A* 113(6):1558–63.

31. Razumova M V., et al. (2006) Effects of the N-terminal domains of myosin binding protein-C in an in vitro motility assay: Evidence for long-lived cross-bridges. *J Biol Chem* 281(47):35846–35854.

32. Razumova M V., Bezold KL, Tu A-Y, Regnier M, Harris SP (2008) Contribution of the Myosin Binding Protein C Motif to Functional Effects in Permeabilized Rat Trabeculae. *J Gen Physiol* 132(5):575–585.

33. Risi C, et al. (2018) N-Terminal Domains of Cardiac Myosin Binding Protein C Cooperatively Activate the Thin Filament. *Structure*:1–8.

34. Stelzer JE, Dunning SB, Moss RL (2006) Ablation of cardiac myosin-binding protein-C accelerates stretch activation in murine skinned myocardium. *Circ Res* 98(9):1212–1218.

35. Li J, et al. (2018) Sarcomere-based genetic enhancement of systolic cardiac function in a murine model of dilated cardiomyopathy. *Int J Cardiol*. doi:10.1016/j.ijcard.2018.09.073.

36. Granzier HL, Labeit S (2004) The Giant Protein Titin: A Major Player in Myocardial Mechanics, Signaling, and Disease. *Circ Res* 94(3):284–295.

37. Granzier HL, Labeit S (2005) Titin and its associated proteins: The third myofilament system of the sarcomere. *Adv Protein Chem* 71(04):89–119.

38. Linke W, Granzier H (1998) A spring tale: new facts on titin elasticity. *Biophys J* 75(6):2613–2614.

39. Linke WA (2017) Titin Gene and Protein Functions in Passive and Active Muscle. *Annu Rev Physiol* (November 2017):1–23.

40. Maruyama K, et al. (1977) Connectin, an elastic protein of muscle. *J Biochem* 82(2):317–337.

41. Linke WA, Hamdani N (2014) Gigantic business: Titin properties and function through thick and thin. *Circ Res* 114(6):1052–1068.

42. Ait-Mou Y, et al. (2016) Titin strain contributes to the Frank–Starling law of the heart by structural rearrangements of both thin- and thick-filament proteins. *Proc Natl Acad Sci*:201516732.

43. Marcucci L, Washio T, Yanagida T (2017) Titin-mediated thick filament activation, through a mechanosensing mechanism, introduces sarcomere-length dependencies in mathematical models of rat trabecula and whole ventricle. *Sci Rep* 7(1):5546.

44. Herman DS, et al. (2012) Truncations of Titin Causing Dilated Cardiomyopathy. *N Engl J Med* 366(7):619–628.

45. Shih Y-H, et al. (2016) Exon- and contraction-dependent functions of titin in sarcomere assembly. *Development* 143(24):4713–4722.

46. Granzier HL, Irving TC (1995) Passive tension in cardiac muscle: contribution of collagen, titin, microtubules, and intermediate filaments. *Biophys J* 68(3):1027–44.

47. Linke WA, et al. (1998) Nature of PEVK-titin elasticity in skeletal muscle. *Proc Natl Acad Sci* 95(July):8052–8057.

48. Rivas-Pardo JA, et al. (2016) Work Done by Titin Protein Folding Assists Muscle Contraction. *Cell Rep* 14:1–9.

49. Squire JM (2016) Muscle contraction: Sliding filament history, sarcomere dynamics and the two Huxleys. *Glob Cardiol Sci Pract* 11.

50. Huxley AF, Niedergerke R (1954) Structural changes in muscle during contraction: Interference microscopy of living muscle fibres. *Nature* 173(4412):971–973.

51. Huxley HE, Hanson J (1954) Changes in the Cross-Striations of Muscle during Contraction and Stretch and their Structural Interpretation. *Nature* 173(4412):973–976.

52. Telley IA, Denoth J (2007) Sarcomere dynamics during muscular contraction and their implications to muscle function. *J Muscle Res Cell Motil* 28(1):89–104.

53. Gordon A, Huxley A, Julian F (1966) The variation in isometric tension with sarcomere length in vertebrate muscle fibres. *J Physiol*:170–192.

54. Lombardi V, Menchetti G (1984) The maximum velocity of shortening during the early phases of the contraction in frog single muscle fibres. *J Muscle Res Cell Motil* 5(5):503–513.

55. Gwathmey JK, Slawsky MT, Hajjar RJ, Briggs GM, Morgan JP (1990) Role of intracellular calcium handling in force-interval relationships of human ventricular myocardium. *J Clin Invest* 85(5):1599–1613.

56. Campbell SG, Lionetti F V, Campbell KS, McCulloch AD (2010) Coupling of adjacent tropomyosins enhances cross-bridge-mediated cooperative activation in a markov model of the cardiac thin filament. *Biophys J* 98(10):2254–64.

57. Regnier M, et al. (2004) Cross-bridge versus thin filament contributions to the level and rate of force development in cardiac muscle. *Biophys J* 87(3):1815–24.

58. Tanner BCW, Daniel TL, Regnier M (2012) Filament compliance influences cooperative

activation of thin filaments and the dynamics of force production in skeletal muscle. *PLoS Comput Biol* 8(5):e1002506.

59. Chase PB, Macpherson JM, Daniel TL (2004) A spatially explicit nanomechanical model of the half-sarcomere: myofilament compliance affects Ca(2+)-activation. *Ann Biomed Eng* 32(11):1559–68.

60. Daniel TL, Trimble a C, Chase PB (1998) Compliant realignment of binding sites in muscle: transient behavior and mechanical tuning. *Biophys J* 74(4):1611–21.

61. Mcnally EM, Golbus JR, Puckelwartz MJ (2013) Genetic mutations and mechanisms in dilated cardiomyopathy. *J Clin Invest* 123(1). doi:10.1172/JCI62862.the.

62. Seidman JG, Seidman C (2001) The Genetic Basis for Cardiomyopathy. *Cell* 104(4):557–567.

63. Tardiff JC, et al. (2015) Targets for therapy in sarcomeric cardiomyopathies. *Cardiovasc Res* 105(4):457–470.

64. Inoue T, et al. (2013) Depressed Frank-Starling mechanism in the left ventricular muscle of the knock-in mouse model of dilated cardiomyopathy with troponin T deletion mutation δK210. *J Mol Cell Cardiol* 63:69–78.

65. Davis J, et al. (2016) A Tension-Based Model Distinguishes Hypertrophic versus Dilated Cardiomyopathy. *Cell* 165:1147–1159.

66. Dorn GW (2016) Tension-Time Integrals and Genetic Cardiomyopathy: The Force Is with You. *Cell* 165(5):1049–1050.

67. Huxley HE, Brown W (1967) The low-angle X-ray diagram of vertebrate striated muscle and its behaviour during contraction and rigor. *J Mol Biol* 30(2):383-IN16.

68. Reconditi M, et al. (2011) Motion of myosin head domains during activation and force development in skeletal muscle. *Proc Natl Acad Sci U S A* 108(17):7236–40.

69. Zoghbi ME, Woodhead JL, Moss RL, Craig R (2008) Three-dimensional structure of vertebrate cardiac muscle myosin filaments. *Proc Natl Acad Sci* 105(7):2386–2390.

70. Hooijman P, Stewart MA, Cooke R (2011) A new state of cardiac myosin with very slow ATP turnover: A potential cardioprotective mechanism in the heart. *Biophys J* 100(8):1969–1976.

71. Irving M (2017) Regulation of Contraction by the Thick Filaments in Skeletal Muscle. *Biophys J* 113(12):2579–2594.

72. Linari M, et al. (2015) Force generation by skeletal muscle is controlled by mechanosensing in myosin filaments. *Nature*. doi:10.1038/nature15727.

73. Fusi L, Huang Z, Irving M (2015) The Conformation of Myosin Heads in Relaxed Skeletal Muscle: Implications for Myosin-Based Regulation. *Biophys J* 109(4):783–792.

74. Fusi L, Brunello E, Yan Z, Irving M (2016) Thick filament mechano-sensing is a calcium-independent regulatory mechanism in skeletal muscle. *Nat Commun* 7:13281.

75. Piazzesi G, Caremani M, Linari M, Reconditi M, Lombardi V (2018) Thick Filament Mechano-Sensing in Skeletal and Cardiac Muscles: A Common Mechanism Able to Adapt the Energetic Cost of the Contraction to the Task. *Front Physiol* 9(June). doi:10.3389/fphys.2018.00736.

76. Fusi L, et al. (2016) Minimum number of myosin motors accounting for shortening velocity under zero load in skeletal muscle. *J Physiol*. doi:10.1113/JP273299.

77. Reconditi M, et al. (2017) Myosin filament activation in the heart is tuned to the mechanical

task. *Proc Natl Acad Sci*:201619484.

78. Farman GP, et al. (2011) Myosin head orientation: a structural determinant for the Frank-Starling relationship. *Am J Physiol Heart Circ Physiol* 300:H2155–H2160.

79. Farman GP, Allen EJ, Schoenfelt KQ, Backx PH, de Tombe PP (2010) The role of thin filament cooperativity in cardiac length-dependent calcium activation. *Biophys J* 99(9):2978–86.

80. Kampourakis T, Zhang X, Sun Y-B, Irving M (2017) Omecamtiv Mercabil and Blebbistatin modulate cardiac contractility by perturbing the regulatory state of the myosin filament. *J Physiol* 00:1–16.

81. Zhang X, et al. (2017) Distinct contributions of the thin and thick filaments to length-dependent activation in heart muscle. *Elife* 6:1–16.

82. Kampourakis T, Sun Y-B, Irving M (2016) Myosin light chain phosphorylation enhances contraction of heart muscle via structural changes in both thick and thin filaments. *Proc Natl Acad Sci*:201602776.

83. van den Hoogenhof MMG, et al. (2018) RBM20 Mutations Induce an Arrhythmogenic Dilated Cardiomyopathy Related to Disturbed Calcium Handling. *Circulation*:CIRCULATIONAHA.117.031947.

84. Methawasin M, et al. (2014) Experimentally increasing titin compliance in a novel mouse model attenuates the Frank-Starling mechanism but has a beneficial effect on diastole. *Circulation* 129(19):1924–36.

85. Rao VS, et al. (2013) N-terminal phosphorylation of cardiac troponin-I reduces length-dependent calcium sensitivity of contraction in cardiac muscle. *J Physiol* 591(Pt 2):475–90.

86. Greenberg BH, et al. (2015) Safety and tolerability of omecamtiv mecarbil during exercise in patients with ischemic cardiomyopathy and angina. *JACC Hear Fail* 3(1):22–29.

87. Rohde J a, Thomas DD, Muretta JM (2017) A heart failure drug changes the mechano-enzymology of the cardiac myosin powerstroke. *Proc Natl Acad Sci* I(1). doi:10.1073/pnas.1611698114.

88. Nag S, et al. (2017) The myosin mesa and the basis of hypercontractility caused by hypertrophic cardiomyopathy mutations. *Nat Struct Mol Biol* 24(6):525–533.

89. Spudich J a (2015) The myosin mesa and a possible unifying hypothesis for the molecular basis of human hypertrophic cardiomyopathy. *Biochem Soc Trans* 43(1):64–72.

90. Spudich JA (2014) Hypertrophic and Dilated Cardiomyopathy: Four Decades of Basic Research on Muscle Lead to Potential Therapeutic Approaches to These Devastating Genetic Diseases. *Biophys J* 106(6):1236–1249.

91. Yuan C-C, et al. (2018) Sarcomeric perturbations of myosin motors lead to dilated cardiomyopathy in genetically modified *MYL2* mice. *Proc Natl Acad Sci* 115(10):E2338–E2347.

92. Li Y, Lang P, Linke W a. (2016) Titin stiffness modifies the force-generating region of muscle sarcomeres. *Sci Rep* 6(April):24492.

93. Mártonfalvi Z, et al. (2014) Low-force transitions in single titin molecules reflect a memory of contractile history. *J Cell Sci* 127(Pt 4):858–70.

94. Watanabe K, et al. (2002) Molecular mechanics of cardiac titin's PEVK and N2B spring elements. *J Biol Chem* 277(13):11549–11558.

95. Ait Mou Y, Le Guennec JY, Mosca E, De Tombe PP, Cazorla O (2008) Differential

contribution of cardiac sarcomeric proteins in the myofibrillar force response to stretch. *Pflugers Arch Eur J Physiol* 457(1):25–36.

96. Granzier H, Labeit S (2002) Cardiac titin: An adjustable multi-functional spring. *J Physiol* 541(2):335–342.

97. Labeit D, et al. (2003) Calcium-dependent molecular spring elements in the giant protein titin. *Proc Natl Acad Sci U S A* 100(23):13716–13721.

98. Lee E-J, et al. (2013) Calcium sensitivity and myofilament lattice structure in titin N2B KO mice. *Arch Biochem Biophys* 535(1):76–83.

99. Greaser ML, et al. (2005) Developmental changes in rat cardiac titin/connectin: Transitions in normal animals and in mutants with a delayed pattern of isoform transition. *J Muscle Res Cell Motil* 26(6–8):325–332.

100. Patel JR, Pleitner JM, Moss RL, Greaser ML (2012) Magnitude of length-dependent changes in contractile properties varies with titin isoform in rat ventricles. *Am J Physiol Heart Circ Physiol* 302(3):H697-708.

101. Mateja RD, Greaser ML, de Tombe PP (2013) Impact of titin isoform on length dependent activation and cross-bridge cycling kinetics in rat skeletal muscle. *Biochim Biophys Acta* 1833(4):804–11.

102. Nishikawa KC, et al. (2012) Is titin a "winding filament"? A new twist on muscle contraction. *Proc R Soc B Biol Sci* 279(September 2011):981–990.

103. Lindstedt S, Nishikawa K (2017) Huxley's Missing Filament: Form and Function of Titin in Vertebrate Striated Muscle. *Annu Rev Physiol* 79:145–166.

104. Prado LG, et al. (2005) Isoform Diversity of Giant Proteins in Relation to Passive and

Active Contractile Properties of Rabbit Skeletal Muscles. *J Gen Physiol* 126(5):461–480.

105. Tonino P, et al. (2017) The giant protein titin regulates the length of the striated muscle thick filament. *Nat Commun* 8(1):1041.

106. Schoenberg M, Wells JB, Podolsky RJ (1974) Muscle compliance and the longitudinal transmission of mechanical impulses. *J Gen Physiol* 64(6):623–42.

107. Ford L, Huxley A, Simmons R (1977) Tension responses to sudden length change in stimulated frog muscle fibres near slack length. *J Physiol*:441–515.

108. Huxley A, Simmons R (1971) Proposed mechanism of force generation in striated muscle. *Nature* 233(October):533–538.

109. Ford L, Huxley A, Simmons R (1981) The relation between stiffness and filament overlap in stimulated frog muscle fibres. *J Physiol* 311(1):219–249.

110. Ford L, Huxley A, Simmons R (1985) Tension transients during steady shortening of frog muscle fibres. *J Physiol* 361:131–150.

111. Tanner BCW, Daniel TL, Regnier M (2007) Sarcomere lattice geometry influences cooperative myosin binding in muscle. *PLoS Comput Biol* 3(7):e115.

112. Tanner BCW, Regnier M, Daniel TL (2008) A spatially explicit model of muscle contraction explains a relationship between activation phase, power and ATP utilization in insect flight. *J Exp Biol* 211(Pt 2):180–6.

113. Williams CD, Regnier M, Daniel TL (2010) Axial and radial forces of cross-bridges depend on lattice spacing. *PLoS Comput Biol* 6(12):e1001018.

114. Williams CD, Salcedo MK, Irving TC, Regnier M, Daniel TL (2013) The length–tension curve in muscle depends on lattice spacing. *Proc R Soc B* 280(July).

115. Fenwick AJ, Wood AM, Tanner BCW (2017) Effects of cross-bridge compliance on the force-velocity relationship and muscle power output. *PLoS One* 12(12):1–16.

116. Williams CD, Regnier M, Daniel TL (2012) Elastic energy storage and radial forces in the myofilament lattice depend on sarcomere length. *PLoS Comput Biol* 8(11):e1002770.

117. Powers JD, Williams CD (2018) Multifil model including titin (Version v1.0.43). Available at: http://doi.org/10.5281/zenodo.1207224.

118. Campbell KS (2009) Interactions between connected half-sarcomeres produce emergent mechanical behavior in a mathematical model of muscle. *PLoS Comput Biol* 5(11). doi:10.1371/journal.pcbi.1000560.

119. Campbell SG, Hatfield PC, Campbell KS (2011) A mathematical model of muscle containing heterogeneous half-sarcomeres exhibits residual force enhancement. *PLoS Comput Biol* 7(9). doi:10.1371/journal.pcbi.1002156.

120. Powers JD, Williams CD, Regnier M, Daniel TL (2018) A Spatially Explicit Model Shows How Titin Stiffness Modulates Muscle Mechanics and Energetics. *Integr Comp Biol* (August):1–8.

121. George N, Irving T, Williams C, Daniel T (2013) The Cross-Bridge Spring: Can Cool Muscles Store Elastic Energy? *Science (80-)* 340(June):1217–1220.

122. Schappacher-Tilp G, Leonard T, Desch G, Herzog W (2015) A novel three-filament model of force generation in eccentric contraction of skeletal muscles. *PLoS One* 10(3):1–16.

123. Herzog W, Schappacher G, DuVall M, Leonard TR, Herzog J a. (2016) Residual Force Enhancement Following Eccentric Contractions: A New Mechanism Involving Titin. *Physiology* 31(4):300–312.

124. Rassier DE, et al. (2015) Non-crossbridge forces in activated striated muscles: a titin dependent mechanism of regulation? *J Muscle Res Cell Motil* 36(1):37–45.

125. Josephson RK (1985) Mechanical power output from striated muscle during cyclic contraction. *J Exp Biol* 114(4):493–512.

126. Dickinson MH, et al. (2000) How animals move: An integrative view. *Science (80-)* 288(5463):100–106.

127. Hessel AL, Nishikawa KC (2017) Effects of a titin mutation on negative work during stretch-shortening cycles in skeletal muscles. *J Exp Biol* 220:4177–4185.

128. Hinson JT, et al. (2015) Titin mutations in iPS cells define sarcomere insufficiency as a cause of dilated cardiomyopathy. *Science (80-)* 349(6251):982–986.

129. Schafer S, et al. (2016) Titin-truncating variants affect heart function in disease cohorts and the general population. *Nat Genet* (November). doi:10.1038/ng.3719.

130. Huxley AF (1957) Muscle structure and theories of contraction. *Prog Biophys Biophys Chem* 7:255–318.

131. Lymn RW, Taylor EW (1971) Mechanism of Adenosine Triphosphate Hydrolysis by Actomyosin. *Biochemistry* 10(25):4617–4624.

132. Hill A V. (1938) The Heat of Shortening and the Dynamic Constants of Muscle. *Proc R Soc B Biol Sci* 126(843):136–195.

133. Woledge RC, Curtin NA, Homsher E (1985) Energetic aspects of muscle contraction. *Monogr Physiol Soc* 41:1–357.

134. Katz B (1939) The relation between force and speed in muscular contraction. *J Physiol* 96(1):45–64.

135. Linari M, Woledge RC, Curtin NA (2003) Energy storage during stretch of active single fibres from frog skeletal muscle. *J Physiol* 548(2):461–474.

136. Fürst DO, Osborn M, Rüdiger N, Weber K (1988) The Organization of Titin Filaments in the Half-Sarcomere Revealed by Monoclonal Antibodies in Immunoelectron Microscopy: A Map ofTen Nonrepetitive Epitopes Starting at the Z Line Extends Close to the M Line. *J Cell Biol* 106(May):1563–1572.

137. Wang K, McClure J, Tu A (1979) Titin: major myofibrillar components of striated muscle. *Proc Natl Acad Sci* 76(8):3698–3702.

138. Dobbie IM, et al. (1998) Elastic bending and active tilting of myosin heads during muscle contraction. *Nature* 396(November):383–387.

139. Piazzesi G, Reconditi M, Linari M, Lucii L (2002) Mechanism of force generation by myosin heads in skeletal muscle. *Nature* 415(February):659–662.

140. Reconditi M, Linari M, Lucii L, Stewart A (2004) The myosin motor in muscle generates a smaller and slower working stroke at higher load. *Nature* 428(April):578–581.

141. Bagni M, Cecchi G, Colombini B, Colomo F (2002) A Non-Cross-Bridge Stiffness in Activated Frog Muscle Fibers. *Biophys J* 82(June):3118–3127.

142. Bagni MA, Cecchi G, Colombini B (2005) Crossbridge properties investigated by fast ramp stretching of activated frog muscle fibres. *J Physiol* 565:261–268.

143. Colombini B, Nocella M, Bagni MA, Griffiths PJ, Cecchi G (2010) Is the cross-bridge stiffness proportional to tension during muscle fiber activation? *Biophys J* 98(11):2582–90.

144. Fusi L, Brunello E, Reconditi M, Piazzesi G, Lombardi V (2014) The non-linear elasticity of the muscle sarcomere and the compliance of myosin motors. *J Physiol* 592(Pt 5):1109–

18.

145. Nocella M, Colombini B, Bagni MA, Bruton J, Cecchi G (2012) Non-crossbridge calcium-depednent stiffness in slow and fast skeletal fibres from mouse muscle. *J Muscle Res Cell Motil* 32(6):403–409.

146. Cornachione AS, Rassier DE (2012) A non-cross-bridge, static tension is present in permeabilized skeletal muscle fibers after active force inhibition or actin extraction. *Am J Physiol Physiol* 302(3):C566–C574.

147. Percario V, et al. (2018) Mechanical parameters of the molecular motor myosin II determined in permeabilised fibres from slow and fast skeletal muscles of the rabbit. *J Physiol* 596(7):1243–1257.

148. Lombardi V, Piazzesi G (1990) The contractile response during steady lengthening of stimulated frog muscle fibres. *J Physiol*:141–171.

149. Bagni M a, Cecchi G, Colomo F, Tesi C (1988) Plateau and descending limb of the sarcomere length-tension relation in short length-clamped segments of frog muscle fibres. *J Physiol* 401:581–595.

150. Offer G (1973) C-Protein and the Periodicity in the Thick Filaments of Vertebrate Skeletal Muscle. *Cold Spring Harb Symp Quant Biol* 37(0):87–93.

151. Moos C, Mason CM, Besterman JM, Feng INM, Dubin JH (1978) The binding of skeletal muscle C-protein to F-actin, and its relation to the interaction of actin with myosin subfragment-1. *J Mol Biol* 124(4):571–586.

152. Luther PK, et al. (2011) Direct visualization of myosin-binding protein C bridging myosin and actin filaments in intact muscle. *Proc Natl Acad Sci* 108(28):11423–11428.

153. Pertici I, Caremani M, Reconditi M (2018) A mechanical model of the half-sarcomere which includes the contribution of titin. *BioRxiv*. doi:http://dx.doi.org/10.1101/435420.

154. Huxley AF, Lombardi V (1980) A sensitive force transducer with resonant frequency 50 kHz. *J Physiol* 305:15–16.

155. Huxley AF, Lombardi V, Peachey LD (1981) A system for recording sarcomere longitudinal displacements in a striated muscle fibre during contraction. *J Physiol* 317:12P–13P.

156. Fusi L, et al. (2017) Minimum number of myosin motors accounting for shortening velocity under zero load in skeletal muscle. *J Physiol* 595(4):1127–1142.

157. Brunello E, et al. (2014) The contributions of filaments and cross-bridges to sarcomere compliance in skeletal muscle. *J Physiol* 592(Pt 17):3881–99.

158. Brunello E, et al. (2006) Structural changes in the myosin filament and cross-bridges during active force development in single intact frog muscle fibres: stiffness and X-ray diffraction measurements. *J Physiol* 577(Pt 3):971–84.

159. Huxley HE, Stewart A, Sosa H, Irving T (1994) X-ray diffraction measurements of the extensibility of actin and myosin filaments in contracting muscle. *Biophys J* 67(6):2411–21.

160. Wakabayashi K, et al. (1994) X-ray diffraction evidence for the extensibility of actin and myosin filaments during muscle contraction. *Biophys J* 67(6):2422–2435.

161. Linari M, et al. (1998) The stiffness of skeletal muscle in isometric contraction and rigor: the fraction of myosin heads bound to actin. *Biophys J* 74(5):2459–73.

162. Mobley B a, Eisenberg BR (1975) Sizes of components in frog skeletal muscle measured

by methods of stereology. *J Gen Physiol* 66(1):31–45.

163. Reconditi M, et al. (2014) Sarcomere-length dependence of myosin filament structure in skeletal muscle fibres of the frog. *J Physiol* 592(5):1119–37.

164. Labeit S, Kolmerer B (1995) Titins: giant proteins in charge of muscle ultrastructure and elasticity. *Science (80-)* 270(5234):293–296.

165. Nagy A, et al. (2005) Hierarchical extensibility in the PEVK domain of skeletal-muscle titin. *Biophys J* 89(1):329–336.

166. Trombitás K, et al. (1998) Titin extensibility in situ: Entropic elasticity of permanently folded and permanently unfolded molecular segments. *J Cell Biol* 140(4):853–859.

167. Mártonfalvi Z, et al. (2014) Low-force transitions in single titin molecules reflect a memory of contractile history. *J Cell Sci* 127(Pt 4):858–70.

168. Marino M, et al. (2005) Poly-Ig tandems from I-band titin share extended domain arrangements irrespective of the distinct features of their modular constituents. *J Muscle Res Cell Motil* 26(6–8):355–365.

169. Stewart MA, Franks-Skiba K, Chen S, Cooke R (2010) Myosin ATP turnover rate is a mechanism involved in thermogenesis in resting skeletal muscle fibers. *Proc Natl Acad Sci* 107(1):430–435.

170. Brunello E, et al. (2007) Skeletal muscle resists stretch by rapid binding of the second motor domain of myosin to actin. *Proc Natl Acad Sci* 104(501):20114–20119.

171. Fusi L, et al. (2010) The mechanism of the resistance to stretch of isometrically contracting single muscle fibres. *J Physiol* 588(Pt 3):495–510.

172. Huxley HE (2004) Recent X-ray diffraction studies of muscle contraction and their

implications. *Philos Trans R Soc Lond B Biol Sci* 359(1452):1879–82.

173. Reconditi M, et al. (2017) Myosin filament activation in the heart is tuned to the mechanical task. *Proc Natl Acad Sci U S A* 114(12):3240–3245.

174. Colson BA, et al. (2010) Differential roles of regulatory light chain and myosin binding protein-C phosphorylations in the modulation of cardiac force development. *J Physiol* 588(6):981–993.

175. Kampourakis T, Yan Z, Gautel M, Sun Y-B, Irving M (2014) Myosin binding protein-C activates thin filaments and inhibits thick filaments in heart muscle cells. *Proc Natl Acad Sci* 111(52):18763–18768.

176. Colson BA, et al. (2012) Myosin binding protein-C phosphorylation is the principal mediator of protein kinase A effects on thick filament structure in myocardium. *J Mol Cell Cardiol* 53(5):609–616.

177. Colson B a, et al. (2008) Protein kinase A-mediated phosphorylation of cMyBP-C increases proximity of myosin heads to actin in resting myocardium. *Circ Res* 103(3):244–51.

178. Harris SP, et al. (2002) Hypertrophic cardiomyopathy in cardiac myosin binding protein-C knockout mice. *Circ Res* 90(5):594–601.

179. Kensler RW, Craig R, Moss RL (2017) Phosphorylation of cardiac myosin binding protein C releases myosin heads from the surface of cardiac thick filaments. *Proc Natl Acad Sci* 114(8):E1355–E1364.

180. Narayanan T, et al. (2018) A multipurpose instrument for time-resolved ultra-small-angle and coherent X-ray scattering. *J Appl Crystallogr* 51(6):in press.

181. Caremani M, et al. (2016) Size and speed of the working stroke of cardiac myosin in situ.

Proc Natl Acad Sci:201525057.

182. Millman BM (1998) The filament lattice of striated muscle. *Physiol Rev* 78(2):359–391.

183. Martyn D, et al. (2004) Response of Equatorial X-Ray Reflections and Stiffness to Altered Sarcomere Length and Myofilament Lattice Spacing in Relaxed Skinned Cardiac Muscle. *Biophys J* 86(February):1002–1011.

184. Piazzesi G, et al. (2014) The myofilament elasticity and its effect on kinetics of force generation by the myosin motor. *Arch Biochem Biophys* 552–553:108–16.

185. Holmes KC, Angert I, Kull FJ, Jahn W, Schröder RR (2003) Elechron cryo-microscopy shows how strong binding of myosin to actin releases nucleotide. *Nature* 425(6956):423–427.

186. de Tombe PP, et al. (2010) Myofilament length dependent activation. *J Mol Cell Cardiol* 48(5):851–8.

187. Caremani M, et al. (2017) Structural Changes in the Thick Filaments during Activation of Demembranated Skeletal Muscle Fibers. *Biophys J* 112(3):181a.

188. Luther PK (2009) The vertebrate muscle Z-disc: Sarcomere anchor for structure and signalling. *J Muscle Res Cell Motil* 30(5–6):171–185.

189. Alamo L, et al. (2017) Effects of myosin variants on interacting-heads motif explain distinct hypertrophic and dilated cardiomyopathy phenotypes. *Elife* 6:1–31.

190. Konhilas JP, Irving TC, de Tombe PP (2002) Myofilament Calcium Sensitivity in Skinned Rat Cardiac Trabeculae: Role of Interfilament Spacing. *Circ Res* 90:59–65.

191. Konhilas JP, et al. (2003) Troponin I in the murine myocardium: influence on length-dependent activation and interfilament spacing. *J Physiol* 547(2003):951–961.

192. Korte FS, Feest ER, Razumova M V, Tu A-Y, Regnier M (2012) Enhanced Ca2+ binding of cardiac troponin reduces sarcomere length dependence of contractile activation independently of strong crossbridges. *Am J Physiol Heart Circ Physiol* 303(7):H863-70.

193. Nowakowski SG, Regnier M, Daggett V (2017) Molecular mechanisms underlying deoxy-ADP.Pi activation of pre-powerstroke myosin. *Protein Sci* 26(4):749–762.

194. Regnier M, Rivera a. J, Chen Y, Chase PB (2000) 2-Deoxy-ATP Enhances Contractility of Rat Cardiac Muscle. *Circ Res* 86(12):1211–1217.

195. Kadota S, et al. (2015) Ribonucleotide reductase-mediated increase in dATP improves cardiac performance via myosin activation in a large animal model of heart failure. *Eur J Heart Fail*:1–10.

196. Moussavi-Harami F, et al. (2014) 2-Deoxy adenosine triphosphate improves contraction in human end-stage heart failure. *J Mol Cell Cardiol*. doi:10.1016/j.yjmcc.2014.12.002.

197. Regnier M, Martyn D a, Chase PB (1998) Calcium regulation of tension redevelopment kinetics with 2-deoxy-ATP or low [ATP] in rabbit skeletal muscle. *Biophys J* 74(4):2005–15.

198. Regnier M, Homsher E (1998) The effect of ATP analogs on posthydrolytic and force development steps in skinned skeletal muscle fibers. *Biophys J* 74(6):3059–71.

199. Regnier M, Lee DM, Homsher E (1998) ATP analogs and muscle contraction: mechanics and kinetics of nucleoside triphosphate binding and hydrolysis. *Biophys J* 74(6):3044–58.

200. Huber GA, McCammon JA (2010) Browndye: A Software Package for Brownian Dynamics. *Comput Phys Commun* 118(11):1896–1905.

201. Fischetti R, et al. (2004) The BioCat undulator beamline 18ID: A facility for biological non-

crystalline diffraction and X-ray absorption spectroscopy at the Advanced Photon Source. *J Synchrotron Radiat* 11(5):399–405.

202. Dolinsky TJ, Nielsen JE, McCammon JA, Baker NA (2004) PDB2PQR: An automated pipeline for the setup of Poisson-Boltzmann electrostatics calculations. *Nucleic Acids Res* 32(WEB SERVER ISS.):665–667.

203. Baker NA, Sept D, Joseph S, Holst MJ, McCammon JA (2001) Electrostatics of nanosystems: Application to microtubules and the ribosome. *Proc Natl Acad Sci* 98(18):10037–10041.

204. Kron SJ, Toyoshima YY, Uyeda TQP, Spudich JABT-M in E (1991) Assays for actin sliding movement over myosin-coated surfaces. *Molecular Motors and the Cytoskeleton* (Academic Press), pp 399–416.

205. Gordon AM, LaMadrid MA, Chen Y, Luo Z, Chase PB (1997) Calcium regulation of skeletal muscle thin filament motility in vitro. *Biophys J* 72(3):1295–1307.

206. Homsher E, Wang F, Sellers JR (1992) Factors affecting movement of F-actin filaments propelled by skeletal muscle heavy meromyosin. *Am J Physiol* 262(3):C714–C723.

207. Furch M, Geeves MA, Manstein DJ (1998) Modulation of actin affinity and actomyosin adenosine triphosphatase by charge changes in the myosin motor domain. *Biochemistry* 37(18):6317–6326.

208. Schoffstall B, Clark A, Chase PB (2006) Positive inotropic effects of low dATP/ATP ratios on mechanics and kinetics of porcine cardiac muscle. *Biophys J* 91(6):2216–26.

209. Irving TC, Konhilas JP, Perry D, Fischetti R, de Tombe PP (2000) Myofilament lattice spacing as a function of sarcomere length in isolated rat myocardium. *Am J Physiol - Hear*

Circ Physiol 279:H2568–H2573.

210. Alamo L, et al. (2008) Three-Dimensional Reconstruction of Tarantula Myosin Filaments Suggests How Phosphorylation May Regulate Myosin Activity. *J Mol Biol* 384(4):780–797.

211. Brenner B, Yu LC, Podolsky RJ (1984) X-ray diffraction evidence for cross-bridge formation in relaxed muscle fibers at various ionic strengths. *Biophys J* 46(3):299–306.

212. Xu S, Martyn D, Zaman J, Yu LC (2006) X-ray diffraction studies of the thick filament in permeabilized myocardium from rabbit. *Biophys J* 91(10):3768–3775.

213. Xu S, Gu J, Belknap B, White H, Yu LC (2006) Structural characterization of the binding of myosin·ADP·Pi to actin in permeabilized rabbit psoas muscle. *Biophys J* 91(9):3370–3382.

214. Malik FI, et al. (2011) Cardiac myosin activation: A potential therapeutic approach for systolic heart failure. *Science (80-)* 331(March):1439–1443.

215. Winkelmann DA, Forgacs E, Miller MT, Stock AM (2015) Structural basis for drug-induced allosteric changes to human β-cardiac myosin motor activity. *Nat Commun* 6:7974.

216. Nagy L, et al. (2015) The novel cardiac myosin activator omecamtiv mecarbil increases the calcium sensitivity of force production in isolated cardiomyocytes and skeletal muscle fibres of the rat. *Br J Pharmacol* 172(18):4506–4518.

217. Liu C, Kawana M, Song D, Ruppel KM, Spudich JA (2018) Controlling load-dependent kinetics of β-cardiac myosin at the single-molecule level. *Nat Struct Mol Biol* 25(6):505–514.

218. Teerlink JR, et al. (2016) Chronic Oral Study of Myosin Activation to Increase Contractility

in Heart Failure (COSMIC-HF): a phase 2, pharmacokinetic, randomised, placebo-controlled trial. *Lancet* 388(10062):2895–2903.

219. Kolwicz SC, et al. (2016) AAV6-mediated cardiac-specific overexpression of ribonucleotide reductase enhances myocardial contractility. *Mol Ther* 24(2):240–250.

220. Anderson RL, et al. (2018) Deciphering the super relaxed state of human β-cardiac myosin and the mode of action of mavacamten from myosin molecules to muscle fibers. *Proc Natl Acad Sci U S A* 115(35):201809540.

221. Adhikari AS, et al. (2016) Early-Onset Hypertrophic Cardiomyopathy Mutations Significantly Increase the Velocity, Force, and Actin-Activated ATPase Activity of Human β-Cardiac Myosin. *Cell Rep* 17(11):2857–2864.

222. Cheng Y, Hogarth KA, O'Sullivan ML, Regnier M, Pyle WG (2016) 2-Deoxyadenosine triphosphate restores the contractile function of cardiac myofibril from adult dogs with naturally occurring dilated cardiomyopathy. *Am J Physiol - Hear Circ Physiol* 310(1):H80–H91.

223. Chang AN, Potter JD (2005) Sarcomeric protein mutations in dilated cardiomyopathy. *Heart Fail Rev* 10(3):225–235.

224. Hershberger RE, Morales A, Siegfried JD (2010) Clinical and genetic issues in dilated cardiomyopathy: A review for genetics professionals. *Genet Med* 12(11):655–667.

225. Hershberger RE, Siegfried JD (2011) Update 2011: clinical and genetic issues in familial dilated cardiomyopathy. *J Am Coll Cardiol* 57(16):1641–9.

226. Willott RH, et al. (2010) Mutations in Troponin that cause HCM, DCM AND RCM: what can we learn about thin filament function? *J Mol Cell Cardiol* 48(5):882–92.

227. Parvari R, Levitas A (2012) The mutations associated with dilated cardiomyopathy. *Biochem Res Int* 2012(Dcm):639250.

228. Tardiff JC (2011) Thin filament mutations: developing an integrative approach to a complex disorder. *Circ Res* 108(6):765–82.

229. Lakdawala NK, et al. (2010) Familial Dilated Cardiomyopathy Caused by an Alpha-Tropomyosin Mutation. The Distinctive Natural History of Sarcomeric Dilated Cardiomyopathy. *J Am Coll Cardiol* 55(4):320–329.

230. Lynn ML, et al. (2017) The structural basis of alpha-tropomyosin linked (Asp230Asn) familial dilated cardiomyopathy. *J Mol Cell Cardiol* 108:127–137.

231. Gupte TM, et al. (2015) Mechanistic heterogeneity in contractile properties of α-tropomyosin (TPM1) mutants associated with inherited cardiomyopathies. *J Biol Chem* 290(11):7003–7015.

232. Coulombe A, Lefevre IA, Deroubaix E, Thuringer D, Coraboeuf E (1990) Effect of 2,3-Butanedione 2-Monoxime on slow inward and transient outward currents in rat ventricular myocytes. *J Mol Cell Cardiol* 22:921–932.

233. Nowakowski SG, et al. (2013) Transgenic overexpression of ribonucleotide reductase improves cardiac performance. *Proc Natl Acad Sci U S A* 110(15):6187–92.

234. Parvatiyar MS, Pinto JR, Liang J, Potter JD (2010) Predicting cardiomyopathic phenotypes by altering Ca2+ affinity of cardiac troponin C. *J Biol Chem* 285(36):27785–27797.

235. Wang D, et al. (2012) Structural and functional consequences of the cardiac troponin C L48Q Ca(2+)-sensitizing mutation. *Biochemistry* 51(22):4473–87.

236. Shettigar V, et al. (2016) Rationally engineered Troponin C modulates in vivo cardiac

function and performance in health and disease. *Nat Commun* 7:10794.

237. Feest ER, et al. (2014) Thin filament incorporation of an engineered cardiac troponin C variant (L48Q) enhances contractility in intact cardiomyocytes from healthy and infarcted hearts. *J Mol Cell Cardiol*. doi:10.1016/j.yjmcc.2014.03.015.

238. Kreutziger KL, et al. (2011) Calcium binding kinetics of troponin C strongly modulate cooperative activation and tension kinetics in cardiac muscle. *J Mol Cell Cardiol* 50(1):165–74.

239. Sorsa T, Pollesello P, Solaro RJ (2004) The contractile apparatus as a target for drugs against heart failure: Interaction of levosimendan, a calcium sensitiser, with cardiac troponin c. *Mol Cell Biochem* 266(1–2):87–107.

240. Utter MS, Ryba DM, Li BH, Wolska BM, Solaro RJ (2015) Omecamtiv mecarbil, a cardiac myosin activator, increases Ca2+-sensitivity in myofilaments with a dilated cardiomyopathy mutant tropomyosin E54K. *J Cardiovasc Pharmacol* 66(4):1.

241. Shen Y-T, et al. (2010) Improvement of cardiac function by a cardiac Myosin activator in conscious dogs with systolic heart failure. *Circ Heart Fail* 3(4):522–527.

242. Lundy SD, et al. (2014) Cell-based delivery of dATP via gap junctions enhances cardiac contractility. *J Mol Cell Cardiol* 72:350–359.

243. Olafsson S, Whittington D, Murray J, Regnier M, Moussavi-Harami F (2017) Fast and sensitive HPLC–MS/MS method for direct quantification of intracellular deoxyribonucleoside triphosphates from tissue and cells. *J Chromatogr B Anal Technol Biomed Life Sci* 1068–1069(June):90–97.

244. Korte FS, et al. (2011) Upregulation of cardiomyocyte ribonucleotide reductase increases

intracellular 2 deoxy-ATP, contractility, and relaxation. *J Mol Cell Cardiol* 51(6):894–901.

245. Wei H, Jin J-P (2014) A dominantly negative mutation in cardiac troponin I at the interface with troponin T causes early remodeling in ventricular cardiomyocytes. *Am J Physiol Cell Physiol* 307(4):C338-48.

246. Lyon RC, Zanella F, Omens JH, Sheikh F (2015) Mechanotransduction in Cardiac Hypertrophy and Failure. *Circ Res* 116(8):1462–1476.

247. Kresh JY, Chopra A (2011) Intercellular and extracellular mechanotransduction in cardiac myocytes. *Pflugers Arch Eur J Physiol* 462(1):75–87.

248. Pandey P, et al. (2018) Cardiomyocytes Sense Matrix Rigidity through a Combination of Muscle and Non-muscle Myosin Contractions. *Dev Cell* 44(3):326–336.e3.

249. Marcucci L, Reggiani C (2016) Mechanosensing in myosin filament solves a 60 years old conflict in skeletal muscle modeling between high power output and slow rise in tension. *Front Physiol* 7(September):1–14.

250. Chen CY, et al. (2018) Suppression of detyrosinated microtubules improves cardiomyocyte function in human heart failure. *Nat Med*. doi:10.1038/s41591-018-0046-2.

251. Robison P, et al. (2016) Detyrosinated microtubules buckle and bear load in contracting cardiomyocytes. *Science (80-)* 352(6284):aaf0659-aaf0659.

252. Kerr JP, et al. (2015) Detyrosinated microtubules modulate mechanotransduction in heart and skeletal muscle. *Nat Commun* 6:8526.

253. Prosser BL, Ward CW (2014) Mechano-chemo transduction tunes the heartstrings. *Sci Signal* 7(317):1–4.

254. Herum K, Lunde I, McCulloch A, Christensen G (2017) The Soft- and Hard-Heartedness

of Cardiac Fibroblasts: Mechanotransduction Signaling Pathways in Fibrosis of the Heart. *J Clin Med* 6(6):53.

255. Herum KM, Choppe J, Kumar A, Engler AJ, McCulloch AD (2017) Mechanical regulation of cardiac fibroblast profibrotic phenotypes. *Mol Biol Cell* 28(14):1871–1882.

256. Sequeira V, Nijenkamp LLAM, Regan JA, Van Der Velden J (2014) The physiological role of cardiac cytoskeleton and its alterations in heart failure. *Biochim Biophys Acta - Biomembr* 1838(2):700–722.

257. Shirokova N, Niggli E (2013) Cardiac phenotype of Duchenne Muscular Dystrophy: Insights from cellular studies. *J Mol Cell Cardiol* 58(1):217–224.

258. Wagner S, et al. (2012) The heart in Duchenne muscular dystrophy: Early detection of contractile performance alteration. *J Cell Mol Med* 16(12):3028–3036.

Supplement & Appendices

Derivation of the overlap correction factor for filament compliance at SL > 2.15 μm for the predicted curves of Figure 3.2 in the main text of Chapter 3.

List of parameters:

$C_F \equiv$ Total filament compliance
$c_A \equiv$ Compliance of actin filament per unit length
$c_M \equiv$ Compliance of myosin filament per unit length
$l_A \equiv$ Length of actin filament
$l_M \equiv$ Length of myosin filament
$l_{hs} \equiv$ Length of half-sarcomere
$\xi = l_A + l_A - l_{hs} \equiv$ Length of overlap region

From Ford, Huxley & Simmons (1981), the filament compliance (C_F) is defined as:

$$C_F = c_A\left(l_A - \frac{2}{3}\xi\right) + c_M\left(l_M - \frac{2}{3}\xi\right) \tag{1}$$

At "full overlap" (i.e. SL=2.15 μm), $\xi = \xi_0$, and $C_F = C_{F,0}$, so

$$C_{F,0} = c_A\left(l_A - \frac{2}{3}\xi_0\right) + c_M\left(l_M - \frac{2}{3}\xi_0\right) \tag{2}$$

Now, add and subtract $\frac{2}{3}c_A\xi_0$ and $\frac{2}{3}c_M\xi_0$ from (1).

$$C_F = c_A\left(l_A - \frac{2}{3}\xi\right) + c_M\left(l_M - \frac{2}{3}\xi\right) + \frac{2}{3}\xi_0 c_A - \frac{2}{3}\xi_0 c_A + \frac{2}{3}\xi_0 c_M - \frac{2}{3}\xi_0 c_M$$

$$= c_A l_A - \frac{2}{3}\xi c_A + c_M l_M - \frac{2}{3}\xi c_M + \frac{2}{3}\xi_0 c_A - \frac{2}{3}\xi_0 c_A + \frac{2}{3}\xi_0 c_M - \frac{2}{3}\xi_0 c_M$$

$$= c_A\left(l_A - \frac{2}{3}\xi_0\right) + c_M\left(l_M - \frac{2}{3}\xi_0\right) - \frac{2}{3}\left(c_A + c_M\right)\left(\xi - \xi_0\right)$$

$$C_F = C_{F,0} - \frac{2}{3}\left(c_A + c_M\right)\left(\xi - \xi_0\right) \tag{3}$$

Now, recall that

$$C_{F,0} = c_A\left(l_A - \frac{2}{3}\xi_0\right) + c_M\left(l_M - \frac{2}{3}\xi_0\right) = -\frac{2}{3}\xi_0\left(c_A + c_M\right) + c_A l_A + c_M l_M \tag{4}$$

We can re-write $c_A l_A + c_M l_M$ as $0.5(c_A + c_M)(l_A + l_M) + 0.5(c_A - c_M)(l_A - l_M)$ such that (4) becomes

$$C_{F,0} = -\frac{2}{3}\xi_0\left(c_A + c_M\right) + 0.5(c_A + c_M)(l_A + l_M) + 0.5(c_A - c_M)(l_A - l_M)\ . \tag{5}$$

From (FHS, 1981), we can assume that the term $0.5(c_A - c_M)(l_A - l_M)$ is negligible with respect to $0.5(c_A + c_M)(l_A + l_M)$ because $c_A \approx c_M$ and $l_A \approx l_M$. Therefore, (5) becomes

$$C_{F,0} \approx -\frac{2}{3}\xi_0\left(c_A + c_M\right) + 0.5(c_A + c_M)(l_A + l_M) \tag{6}$$

and thus

$$\left(c_A + c_M\right) \approx \frac{C_{F,0}}{0.5(l_A + l_M) - 2\xi_0 / 3}\ . \tag{7}$$

Now, substitute (7) into (3) to get

$$C_{\mathrm{F}} \approx C_{\mathrm{F},0} - \frac{(2/3)C_{\mathrm{F},0}(\xi - \xi_0)}{0.5(l_{\mathrm{A}} + l_{\mathrm{M}}) - 2\xi_0/3}$$

$$C_{\mathrm{F}} \approx C_{\mathrm{F},0}\left[\frac{l_{\mathrm{A}} + l_{\mathrm{M}} - \frac{4}{3}\xi}{l_{\mathrm{A}} + l_{\mathrm{M}} - \frac{4}{3}\xi_0}\right] \tag{8}$$

Now, from Brunello *et al.* (2014) we have ζ_0 = 0.7 μm, and, for SL > 2.15μm, $l_{\mathrm{A}} = 1.0\mu\mathrm{m}$ and $l_{\mathrm{M}} = 0.8\mu\mathrm{m}$, such that [from (8)], for SL > 2.15 μm

$$C_{\mathrm{F}} \approx C_{\mathrm{F},0}(2.077 - 1.538\zeta) .$$

Curriculum Vitae

Education

- **Ph.D. – Bioengineering, 2018**
  University of Washington
  Dissertation Topic: Molecular mechanics of striated muscle contraction
  Advisors: Michael Regnier, PhD & Thomas L. Daniel, PhD

- **M.S. – Biomedical Engineering, 2013**
  University of Minnesota
  Thesis Topic: Steric-specific reactions in crowded environments
  Advisor: David J. Odde, PhD

- **B.S. – Biomedical Engineering, 2012**
  University of Minnesota
  Emphasis: Biomedical Transport Phenomena

- **B.S. – Physics, 2012**
  University of Wisconsin – La Crosse
  Minor: Mathematics

Employment & Experiences

2017 – 2018	**Doctoral Candidate in Bioengineering,** *University of Washington* (Seattle, WA), Department of Bioengineering & Biology - Regnier & Daniel research groups
2017	**Teaching Assistant,** *University of Washington* (Seattle, WA), Special Topics Course: Advanced Cardiac Engineering - Department of Bioengineering
2015 – 2016	**Visiting Graduate Research Fellow,** *Università degli studi di Firenze* (Florence, Italy), Department of Biology - Lombardi & Piazzesi research group
2014 – 2016	**Graduate Research Assistant**, *University of Washington* (Seattle, WA), Department of Bioengineering & Biology - Regnier & Daniel research groups
2013 – 2014	**Rotating Graduate Research Assistant**, *University of Washington* (Seattle, WA), Department of Bioengineering - Wiggins & Carothers research groups

2012 – 2013	**Graduate Student Researcher,** *University of Minnesota* (Minneapolis, MN), Department of Biomedical Engineering - Odde research group
2012	**Teaching Assistant,** *University of Minnesota* (Minneapolis, MN), Coding in MATLAB for Biomedical Engineers - Department of Biomedical Engineering
2011	**Biomedical Engineer Intern,** *Medtronic Inc.* (Minneapolis, MN), Cardiovascular group, Mechanical heart valve engineering
2009 – 2010	**Undergraduate Researcher,** *University of Wisconsin – La Crosse* (La Crosse, WI), La Crosse Institute for Movement Sciences - Ragan research group

Academic Awards & Fellowships

- Experimental Pathology of Cardiovascular Disease Training Grant – National Institute of Health (National Heart, Lung, and Blood Institute, NIH T32-HL007312) & University of Washington (2017-2019)
- Young Researcher's Travel Grant – Alpbach Myosin Motors Conference, 2016 (Alpbach, Austria)
- Visiting Graduate Research Fellowship (2015-2016) – University of Florence (Italy), Laboratory of Physiology – Advisors: Professor Vincenzo Lombardi and Professor Gabriella Piazzesi
- COMAP International Mathematical Competition in Modeling Finalist (ranked top 1% worldwide) (2010)

Publications

1. **Powers JD**, Bianco P, Reconditi M, Lombardi V, & Piazzesi G (*in prep. for PNAS*). Titin is a dynamic I-band spring with a stiffness that is tuned to the length of the active muscle sarcomere.
2. **Powers JD**, Kooiker K, Flint G, Tardiff J, Regnier M, Moussavi-Harami F, & Davis J, (*in prep*). Targeting sarcomere dysfunction in dilated cardiomyopathy by genetically engineering myofilament-specific interventions.

3. **Powers JD***, Yuan C-C*, McCabe K, Murray JD, Flint G, Mohran S, Castillo R, Zuzek C, Ma W, McCulloch AD, Irving TC, & Regnier M. (*in prep*). Electrostatic restructuring of myosin by 2-deoxy-ATP actuates sarcomeres in resting cardiac muscle. **Co-first author.*

4. Caremani M, Pinzauti F, **Powers JD**, Governali S, Narayanan T, Stienen GJM, Reconditi M, Linari M, Lombardi V, & Piazzesi G. (*in press*). The regulatory state of the cardiac thick filament in diastole during inotropic intervention. *Journal of General Physiology*

5. Choi Y, Jang J, Yi H, Chae S, Kim S, Corbett DC, **Powers JD**, Pabon LM, Yoo DC, Lee S, Ahn M, Kim HJ, Park MN, Ha D, Shim J, Yun W, Rengier M, Murry CE, Stevens KR, & Cho D. (*in review, Nature Protocols*). Decellularized extracellular matrix-based Bioinks for printing functional human muscular tissues.

6. **Powers JD**, Williams CD, Regnier M, & Daniel TL. (2018). A spatially explicit model shows how titin stiffness modulates muscle mechanics and energetics. *Integrative & Comparative Biology,* icy055, DOI: 10.1093/icb/icy055.

7. Leonard A, Bertero A, **Powers JD**, Bhandari S, Regnier M, Murry CE, & Sniadecki NJ. (2018). Afterload promotes matutration of human induced pluripotent stem cell-derived cardiomyocytes in engineered heart tissues. *Journal of Molecular and Cellular Cardiology* **118,** 147-158.

8. Reconditi M, Caremani M, Pinzauti F, **Powers JD**, Narayanan T, Stienen GJM, Linari M, Lombardi V, & Piazzesi G. (2017). Myosin filament activation in the heart is tuned to the mechanical task. *Proceedings of the National Acadamy of Science* 201619484.

9. Fusi L, Percario V, Brunello E, Caremani M, Bianco P, **Powers JD**, Reconditi M, Lombardi V, & Piazzesi G. (2017). Minimum number of myosin motors accounting for shortening velocity under zero load in skeletal muscle. *Journal of Physiology* **595.4,** 1127-1142.

10. **Powers JD**, Castle BT, & Odde DJ. (2015). The predicted role of steric specificity in crowding-mediated effects on reversible biomolecular association. *Physical Biology* **12,** 066004.

Presentations

1. "The role of titin in modulating muscle mechanics and energetics" (*invited symposium speaker*), **Society for Integrative & Comparative Biology Meeting**, San Francisco, CA, USA (2018).

2. "Engineered thin filament mutations to study the sarcomere length dependence of cardiac muscle contractility" (*poster presentation*), **62nd Annual Biophysical Society Meeting**,

San Francisco, CA, USA (2018).

3. "The nonlinear mechanical properties of titin modulate striated muscle contraction efficiency" (*poster presentation*), **62nd Annual Biophysical Society Meeting**, San Francisco, CA, USA (2018).

4. "Elucidating the mechanism of reduced length-dependent activation due to a dilated cardiomyopathy-associated tropomyosin mutation" (*poster presentation*), **American Heart Association Conference for Basic Cardiovascular Science**, Portland, OR, USA (2017).

5. "Evidence for an I-band spring that is tuned to the length of the skeletal muscle sarcomere" (*platform talk*) **61st Annual Biophysical Society Meeting**, New Orleans, LA, USA (2017).

6. "The Frank-Starling mechanism is attenuated by a dilated cardiomyopathy-associated tropomyosin mutation" (*poster presentation*) **61st Annual Biophysical Society Meeting**, New Orleans, LA, USA (2017).

7. "A study of the nature of the parallel elasticity in the active sarcomere" (*platform talk*), **15th Alpbach Myosin Motors Research Conference**, Alpbach, Austria (2016).

8. "Investigating the role of troponin in modulating sarcomere length dependence of thin filament activation in cardiac muscle" (*platform talk*), Società Italiana di Fisiologia – **9th Meeting of Young Researchers in Physiology**, Florence, Italy (2015).

9. "No Sting in Your Swing: A Mathematical Model of the 'Sweet Spot' on a Baseball Bat" (*invited talk*), **Mathematical Association of America Conference**, Oshkosh, WI, USA (2010).

Other Conference Proceedings

1. **Powers JD**, Glint G, Tardiff J, Regnier M, Moussavi-Harami F, & Davis J. Predicting and preventing myocardial remodeling in a meurine model of dilated cardiomyopathy. (Expected 2019). *63rd Biophysical Society Meeting*, Baltimore, MD.

2. Kooiker KB, **Powers JD**, Tardiff J, Reginer M, Davis J, Moussavi-Harami F. Engineered thin fialment mutations to increase calcium sensitivity of force in tropomyosin mutation of dilated cardiomyopathy. (Expected 2019). *63rd Biophysical Society Meeting*, Baltimore, MD.

3. Yuan CC, **Powers JD**, McCabe KJ, Murray JD, Morhan S, Castillo R, Zuzek C, Ma W, McCulloch AD, Iring TC, & Regnier M. Enhanced cross-bridge binding with 2-deoxy-ATP results from increased electrostatic interactions between myosin and actin in cardiac muscle. (Expected 2019). *63rd Biophysical Society Meeting*, Baltimore, MD.

4. Yuan CC, **Powers JD**, Murray JD, Mohran S, Ma W, Luttrell SM, Irving TC, Regnier M, & Mack DL. Time-resolved X-ray studies of skeletal muscle from a Duchene Musular Dystrophy rat model. (Expected 2019). *63rd Biophysical Society Meeting*, Baltimore, MD.

5. Mijailovich SM, Nedic D, Stojanovic B, **Powers JD**, Davis J, Geeves MA, & Regnier M. Influence of cTn Ca^{2+} binding properties and cooperative mechanisms on cardiac muscle contractile dynamics. (Expected 2019). *63rd Biophysical Society Meeting*, Baltimore, MD.

6. Piazzesi G, Caremani M, Reconditi M, **Powers JD,** Governali S, Pinzauti F, Stienen GJM, Narayanan T, Linari M, & Lombardi V. Inotropic interventions that almost double the systolic force of a cardiac trabecula do not affect the OFF state of the thick filament in diastole. (2018). *The Europhysiology Meeting.* London, England.

7. Piazzesi G, Caremani M, Reconditi M, **Powers JD,** Governali S, Pinzauti F, Stienen GJM, Narayanan T, Linari M, & Lombardi V. Thick filament mechanosensing in skeletal and cardiac muscles: A common mechanism for different tasks. (2018) *The Myofilament Meeting,* Madison, WI.

8. Yuan C, McCabe K, Murray J, **Powers JD,** Ma W, Daggett V, McCulloch A, Irving TC, & Regnier M. Structure and simulation studies on cardiac muscle contraction by using dATP (2018) *The Myofilament Meeting 2018,* Madison, WI.

9. Yuan C, McCabe K, Murray J, **Powers JD**, Ma W, Daggett V, McCulloch A, Irving TC, & Regnier M. Structural studies of cardiac muscle contraction with dATP (2018) *The European Muscle Conference*, Budapest, Hungary.

10. Chiao YA, Moussavi-Harami F, Cheng Y, **Powers JD**, Razumova M, Granzier H, Regnier M, & Rabinovitch P. Rapamycin treatment promotes myofibril relaxation kinetics and reduces myocardial stiffness to improve diastolic function in old murine hearts. (2018) *Experimental Biology Meeting*.

11. Caremani M, Linari M, Pinzauti F, **Powers JD**, Lombardi V, & Piazzesi, G. The off state of thick filament is not affected by inotropic interventions like the increase in diastolic sarcomere length or the addition of a β-adrenergic effector. (2018) *62nd Biophysical Society Meeting*, San Francisco, CA.

12. Yuan C, **Powers JD**, Murray JD, Ma W, Dagget V, Irving TC, Regnier M. X-ray studies of rat cardiac msucle with ATP versus dATP (2018) *62nd Biophysical Society Meeting*, San Francisco, CA.

13. Mijailovich SM, Nedic D, Stojanovic B, **Powers JD**, Davis J, Geeves MA, & Regnier M. Infulence of cTn Ca^{2+} binding properties and cooperative mechanisms in the dynamics of cardiac muscle contraction and relaxation. (2018) *62nd Biophysical Society Meeting*, San Francisco, CA.

14. Linari M, Caremani M, Pinzauti F, **Powers JD**, Narayanan T, Stienen G, Reconditi M, Piazzesi G, & Lombardi V. (2017). Thick filament mechanosensing in cardiac muscle drives to a new concept of the Frank-Starling Law. *68th Meeting of the Italian Society of Physiology,* Pavia, Italy.

15. Piazzesi G, Caremani M, Pinzauti F, **Powers JD**, Narayanan T, Stienen G, Linari M, Reconditi M, & Lombardi V. (2016). Micrometer-nanometer scale X-ray diffraction to study the molecular mechanisms of heart regulation. *15th Alpbach Myosin Motors Research Conference,* Alpbach, Austria.

16. Piazzesi G, Caremani M, Pinzauti F, **Powers JD**, Narayanan T, Stienen G, Linari M, Reconditi M, & Lombardi V. (2016). Interference X-ray diffraction in intact trabeculae from rat ventricle. *67th Meeting of the Italian Society of Physiology,* Catania, Italy.

17. Fusi L, Percario V, Brunello E, **Powers JD**, Reconditi M, Lombardi V, & Piazzesi G. (2015). Sources of nonlinear elasticity of the muscle sarcomere. *66th Meeting of the Italian Society of Physiology,* Genoa, Italy.

18. Klaiman JM, Razumova MV, **Powers JD**, Turtle CW, Moussavi-Harami F, Gillis TE & Regnier M (2015). The role of calcium affinity and C-I interaction in length-dependent activation. *Biophys J* **110,** 465a.